Government of Western Australia

Department of
Mines and Petroleum

REPORT 144

GREENFIELDS GEOCHEMICAL EXPLORATION IN A REGOLITH-DOMINATED TERRAIN: THE ALBANY–FRASER OROGEN/ YILGARN CRATON MARGIN

by
I González-Álvarez, RR Anand, R Hough, W Salama, C Laukamp, MT Sweetapple, Y Ley-Cooper, I Sonntag, M Lintern, T Abdat, M leGras, and J Walshe

mriwa
Minerals Research Institute of Western Australia

National Research FLAGSHIPS
Minerals Down Under
CSIRO

ROYALTIES FOR REGIONS
EXPLORATION INCENTIVE SCHEME

Geological Survey of Western Australia

Government of **Western Australia**
Department of **Mines and Petroleum**

REPORT 144

GREENFIELDS GEOCHEMICAL EXPLORATION IN A REGOLITH-DOMINATED TERRAIN: THE ALBANY–FRASER OROGEN/ YILGARN CRATON MARGIN

by
I González-Álvarez*, RR Anand*, R Hough*, W Salama*, C Laukamp*, MT Sweetapple*, Y Ley-Cooper*, I Sonntag*, M Lintern*, T Abdat*, M leGras*, and J Walshe*

*** CSIRO Minerals Down Under Flagship, Australian Resources Research Centre, 26 Dick Perry Avenue, Kensington WA 6151**

Perth 2014

Geological Survey of Western Australia

REFERENCE
The recommended reference for this publication is:
González-Álvarez, I, Anand, RR, Hough, R, Salama, W, Laukamp, C, Sweetapple, MT, Ley-Cooper, Y, Sonntag, I Lintern, M, Abdat, T, leGras, M, and Walshe J 2014, Greenfields geochemical exploration in a regolith-dominated terrain: the Albany–Fraser Orogen/Yilgarn Craton margin: Geological Survey of Western Australia, Report 144, 213p.

National Library of Australia Cataloguing-in-Publication entry:

Title:	Greenfields geochemical exploration in a regolith-dominated terrain : the Albany-Fraser Orogen/Yilgarn Craton margin / I. González-Álvarez, R. R. Anand, R. Hough, W. Salama, C. Laukamp, M. T. Sweetapple, Y. Ley-Cooper, I. Sonntag, M. Lintern, T. Abdat, M. leGras and J. Walshe.
ISBN:	9781741685985 (ebook)
Subjects:	Geochemical prospecting--Western Australia--Albany Region. Geochemical prospecting--Western Australia--Yilgarn Craton. Regolith--Western Australia--Albany Region. Regolith--Western Australia--Yilgarn Craton.
Other Authors/Contributors:	González-Álvarez, Ignacio, author. Anand, R. R. (Ravinder Raj) author. Hough, Rob, author. Salama, W., author. Laukamp, Carsten, author. Sweetapple, Marcus T., author. Ley-Cooper, Yusen, author. Sonntag, Iris, author. Lintern, M. J., author. Abdat, Tania, author. Legras, Monica, author. Walshe, John L., author.
Dewey Decimal Classification:	622.13
ISSN	0508–4741

Grid references in this publication refer to the Geocentric Datum of Australia 1994 (GDA94). Locations mentioned in the text are referenced using Map Grid Australia (MGA) coordinates, Zone 50. All locations are quoted to at least the nearest 100 m.

This Record presents the results of the Minerals and Energy Research Institute of Western Australia (MERIWA) Project M411 Greenfields geochemical exploration in a regolith-dominated terrain: the Albany–Fraser Orogen/Yilgarn Craton margin Project. The Geological Survey of Western Australia (GSWA) is releasing the Report as part of its Report Series to ensure a wider distribution. Although GSWA provided support to the project from the Exploration Incentive Scheme (EIS), the scientific content of the Report and the drafting of figures has been the responsibility CSIRO. No editing has been undertaken by GSWA.

Published 2014 by Geological Survey of Western Australia
The PDF of this Report, the plates and its accompanying appendices are available to download from <www.dmp.wa.gov.au/GSWApublications>.

Further details of geological publications and maps produced by the Geological Survey of Western Australia are available from:
Information Centre
Department of Mines and Petroleum | 100 Plain Street | EAST PERTH | WESTERN AUSTRALIA 6004
Telephone: +61 8 9222 3459 Facsimile: +61 8 9222 3444 **www.dmp.wa.gov.au/GSWApublications**

Cover image: Field view at the NE Albany–Fraser Orogen – SE Yilgarn Craton margin. Photo courtesy of Ignacio Gonzalez-Alvarez.

mriwa
Minerals Research Institute
of Western Australia

REPORT NO. 305

Greenfields geochemical exploration in a regolith-dominated terrain: the Albany-Fraser Orogen/Yilgarn Craton margin

Results of research carried out as MRIWA Project No. M411

at

CSIRO Minerals Down Under Flagship

by

I. González-Álvarez, R. R. Anand, R. Hough, W. Salama, C. Laukamp, M. T. Sweetapple, Y. Ley-Cooper, I. Sonntag, M. Lintern, T. Abdat, M. leGras and J. Walshe

February 2014

Distributed by: MRIWA

Mineral House

100 Plain Street

Perth WA 6000

to which all enquiries should be addressed

ISBN 1920981667

Division CESRE/Mineral Resources National Flagship

Citation

González-Álvarez, I., Anand, R.R., Hough, R., Salama, W., Laukamp, C., Sweetapple, M., Ley-Cooper, Y., Sonntag, I., Lintern, M., Abdat, T., leGras, M., Walshe, J., 2014. Greenfields geochemical exploration in a regolith-dominated terrain: the Albany-Fraser Orogen/Yilgarn Craton margin. Internal report for CSIRO, Australia, M411, Mineral Resources National Flagship, EP1312271, 213 pp.

Copyright and disclaimer

Important disclaimer

Geological Survey of Western Australia

ROYALTIES FOR REGIONS

EXPLORATION INCENTIVE SCHEME

Foreword

This report presents a summary of research funded in part by CSIRO's strategic investment in greenfields mineral exploration along cratonic boundaries in Western Australia. This research applies a multi-scale approach, which aims to support the prospectivity assessments of small to medium exploration companies during greenfields exploration, by the development of efficient exploration proxies. It also follows up on the recent Tropicana-Havana Au and the Nova magmatic Ni-Cu discoveries, by building on previous exploration experience in the south-east Yilgarn Craton margin. This project was jointly undertaken by MRIWA, GSWA and CSIRO.

Chapters presented in this report are summaries of complete studies carried out on the different aspects of this project. Complete independent reports are attached as digital Appendices.

Ignacio González-Álvarez
Project Leader

Contents

Figures

Tables

Acknowledgments

We would like to thank GSWA through the EIS program for their financial support, as well as MRIWA and Creasy Group, Silver Lake Resources, Sipa Resources and AngloGold Ashanti who fully supported this project; as well as to Beadell Resources, International Goldfields and Triton Gold for their partial support of this project.

We specially thank Charles Butt for editorial advice.

Executive summary

The Albany-Fraser Orogen (AFO) is a regolith-dominated terrain with some significant differences in regolith evolution compared with its neighbouring Yilgarn Craton. These unknowns in the regolith framework pose significant challenges for greenfields exploration in the region. Two major discoveries: the Tropicana-Havana Au system (with a Au resource of 6.41 M oz) in 2005, and the Nova Ni-Cu deposit in the Fraser Range in 2012 - have sparked mineral exploration interest in the AFO.

In this region, regolith covers about 85% of the total surface area and can reach thicknesses of up to 150 m. The palaeoclimatic evolution of the exposed AFO ranged from humid and sub-tropical during the Mesozoic to the Pliocene, shifting during the Quaternary to arid and semi-arid. Consequently, weathering profiles in the AFO are the result of successive climatic overprinting. In this terrain, weathering profiles obscure the surface expression of the basement geochemistry, and therefore blur or obliterate the geochemical footprints of mineral systems at depth.

Regolith framework of the Albany-Fraser Orogen and southeast Yilgarn Craton margin

A conceptual model of the AFO as a palaeocoast with numerous islands and estuarine zones driven by transgression-regression events is proposed. 'On inland' and 'on island' weathering profiles vary in maturity and saprolite development, with or without transported cover derived from exotic marine sedimentary rocks and limestones, and clastic detritus from the Yilgarn Craton. These areas are more reliable for understanding geochemical anomaly-basement relationships, whereas the 'marine inundated' areas would require a more-detailed investigation, due to the role of marine reworking of weathering profiles (Fig. A).

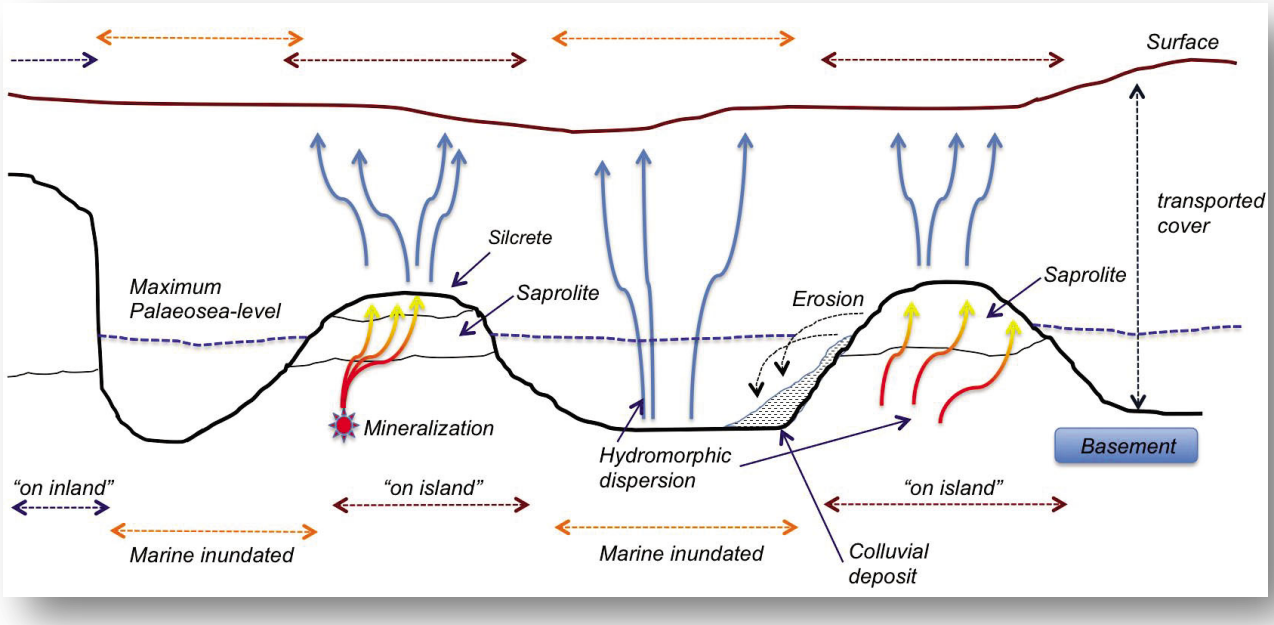

Figure A. Sketch of the effect of sea marine transgressions and regressions generating 'on inland' and 'on island' areas together with 'marine inundated' zones, and its implications for vertical trace element dispersion of the basement geochemical signature.

Within the above framework, the following four contrasting regolith settings have been identified: (1) Albany; (2) Kalgoorlie-Norseman margin; (3) Esperance; and (4) Neale. The landscape changes from a topographically high, dissected Yilgarn surface geomorphology with thick saprolite and topographic-inverted palaeochannels, to a nearly flat dominated by sand dunes and thin saprolite towards the coast.

Mapping the palaeocoasts, islands and estuarine zones, as well as the region of influence of marine limestones and sedimentary rocks, significantly improves the planning and implementation of exploration campaigns in the region, as these features have been shown to have a severe impact on conventional regolith development and vertical trace element mobility.

Au anomaly in calcrete: the displaced anomaly at Woodline

The Woodline Au Project (Sipa Resources), about 110 km north-east of Norseman, is within the Kalgoorlie-Norseman margin setting. This site was selected to study and understand the formation of Au anomalies in calcrete displaced from mineralization in the region. This anomaly was previously described as *in situ*. Results from this study indicated a transported anomaly in younger colluvium overlying Tertiary marine sediments, with no Au mineralization beneath.

Neale area: regolith stratigraphy and trace element mobility

The main study site selected was the Neale area (Hercules and Atlantis Au prospects; 60 km north-east of the Tropicana–Havana Au system), for the purpose of improving understanding of trace element mobility from the basement through the regolith profile.

Basement lithologies at Neale contain two styles of Au mineralization: a disseminated style related to altered felsic to intermediate intrusive rocks, and a dilational quartz vein hosted style associated with mylonite zones. Gold is associated with Cu minerals, mostly chalcopyrite. Gold and sulfide species are interpreted to have a relatively late paragenesis.

Silver-rich Au at the Hercules Au prospect is found as fine inclusions in pyrite, and is hosted in mica-altered felsic to intermediate granitoids, granofels, and discrete quartz veins. At the Atlantis prospect, Au is identified as crystalline grains of about 10 µm size with no Ag, within a chlorite-sericite-altered granite, spatially associated with and typically hosted in mylonitized units, with subordinate mica-altered felsic to intermediate intrusives granites.

Regolith developed above the Neale mineralized area has a total thickness of about 75 m, including about 25 m of transported cover that overlies a silcrete unit (Fig. B). The silcrete unit (from 4 to 20 m thick) is widely distributed, capping the kaolinitic upper saprolite. Cementation of the unit varies, with more permeable areas, resulting from more-intense vertical weathering. Surface geochemical sampling above these permeable areas has the potential to deliver more reliable geochemical basement signatures (Fig. B).

The residual regolith is divided into ferruginized lower saprolite, sandy kaolinitic upper saprolite and silcrete. Weathering at Neale occurred under oxidizing, acidic conditions with low-salinity groundwaters, and display is minor vertical hydromorphic dispersion of Rare Earth Elements (REE; from La to Lu), High Field Strength Elements (HFSE; Zr, Hf, Nb, Ta, Th) and transition metals (V, Cr, Co, Cu, Ni, Sc) within the upper saprolite and through most of the transported cover except for the eolian sand in which there is no

detectable expression. Drill core and Reverse Circulation (RC) drill chip samples from the lower saprolite preserve the main geochemical features (REE and transition element patterns, Light REE/Heavy REE, Zr/Hf, Nb/Ta, Th/Sc ratios) of the basement, and therefore can be used in geochemical exploration targeting (Fig. B).

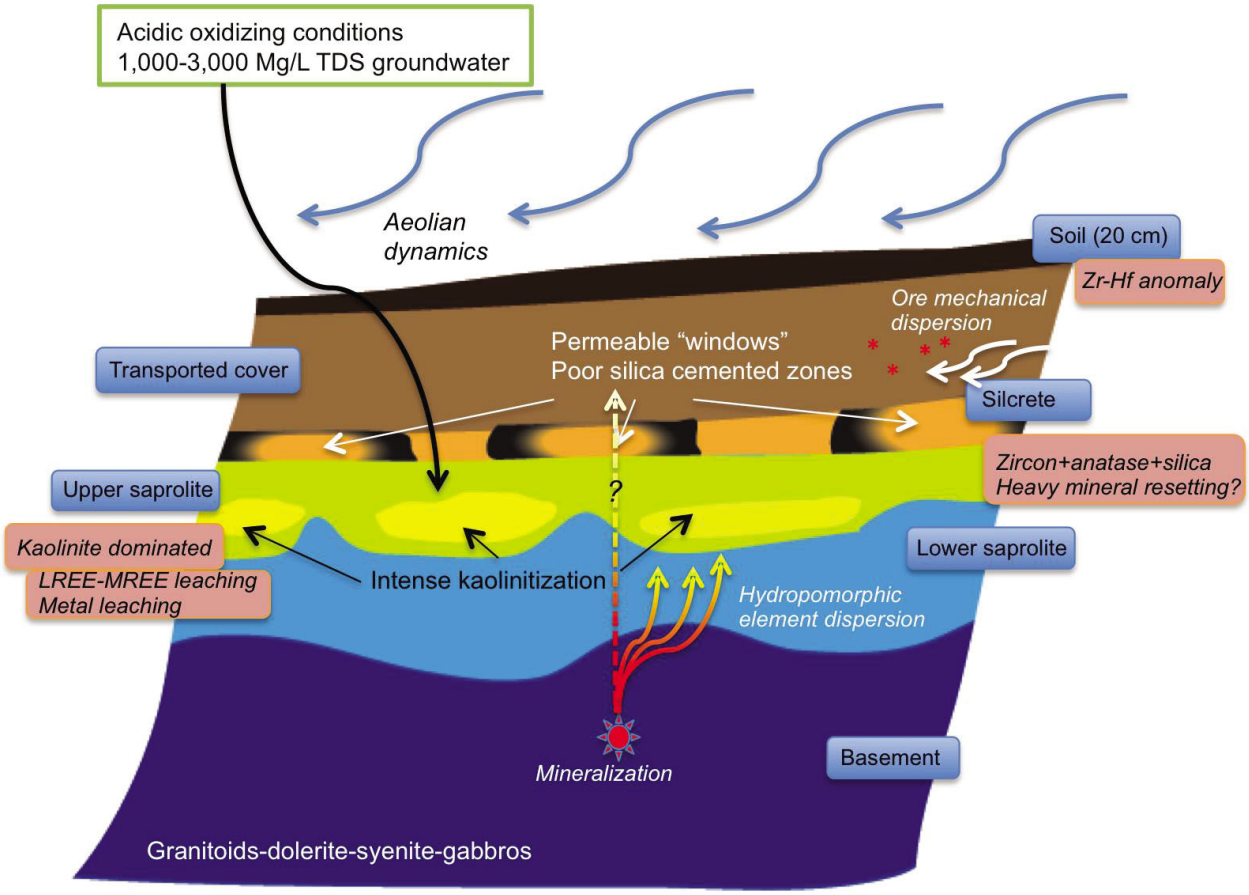

Figure B. Basement-regolith geochemical dispersion model, based on study of the Neale area.

New exploration technologies in the AFO: ASTER, HyLogging™ and AEM

Advanced Spaceborne Thermal and Reflection Radiometer (ASTER) Geoscience products were used for geological mapping at district and camp scales, where spectral patterns in single regolith units enable differentiation between regolith domains. Spatially dense HyLogging™ data (1 cm steps) from seven drill holes from the Hercules and Atlantis prospects successfully interpreted primary lithologies, alteration and regolith mineralogy, enabling mapping of narrow (cm-wide) carbonate-altered or cherty layers by using kaolinite crystallinity, Hylogging™ was able to accurately segregate residual *versus* transported material in regolith profiles at Salmon Gums and Neale. This was confirmed by manual logging. Spatially dense HyLogging™ data (1 cm steps) from seven drill holes from the Hercules and Atlantis prospects successfully interpreted primary lithologies, alteration and regolith mineralogy, enabling mapping of narrow (cm-wide) carbonate-altered or cherty layers.

Airborne electromagnetic (AEM) datasets from the Tropicana Au system were examined to determine their potential for assisting exploration through cover. The historical AEM data collected using a fixed wing airborne time domain EM system (TEMPEST) were reinterpreted based on the regolith context and groundwater salinity constraints. The fully inverted dataset permitted better definition of basement topography and regolith architecture (saprolite and transported cover). This result highlights the usefulness of revisiting historical AEM surveys and their transforms, by subjecting them to a full inversion, which permits a better understanding of the weathered landscape and regolith in the AFO.

ASTER images appear promising for tenement-scale regolith mapping; HyLogging™ for distinguishing between residual and transported cover from drill hole samples. AEM has considerable potential as a tool to assist in characterizing local geomorphological-sedimentary environments and regolith architecture, subject to constraints imposed by variations in groundwater salinity.

Introduction

Regolith-dominated terrains extend throughout Australia. Many of these areas display deeply weathered profiles, that have been developing for at least the last 65 Ma, reaching depths of up to 150 m (e.g., Anand and Paine, 2002; Anand and Butt, 2010). The rocks exposed within the Yilgarn Craton in Western Australia originally date back to the Palaeozoic and Mesozoic (~300 Ma and <145 Ma respectively; Anand, 2005; Pillans, 2007). Thus this region represents an ancient, stable and weathered landscape.

Sedimentary packages with exotic mineral and geochemical features contribute to increase the total thickness of the regolith profile. These overburden units act as filters or even impermeable barriers to geochemical vertical dispersion, which can reduce significantly, if not prevent, any ore pathfinder element or anomalous geochemical proxy from reaching the surface and being detectable in exploration campaigns. Therefore, even if regolith thickness is strongly linked to basement geology, deeply and intensely weathered profiles coupled with sedimentary cover obscure the surface expression of the geochemical features of the basement, and therefore blur and in some cases obliterate the geochemical footprints of mineral systems at depth.

The Albany-Fraser Orogen is a regolith-dominated terrain adjacent to the Yilgarn Craton. Cratonic margin complexities of basement lithologies, such as reworking and remelting of mixed rock suites of diverse ages, and high grades of metamorphism variably affecting basement units, enhance the difficulties of mineral exploration in this region. This makes the AFO a particularly challenging environment for mineral exploration.

This study builds on previous work of the CRC LEME reports of Anand and De Broekert (2005) and Butt et al. (2005), bringing novel data to the regolith framework at orogen scale for the region (Fig. 1). In addition, this project explores the geomorphological framework of the area, exploring correlations between regolith formation and basement geology along the cratonic boundary, and identifying the key processes that have dominated the evolution of the surface landscape. Orogenic scale multi-component datasets were integrated to identify key control elements of geomorphology to answer these questions.

Next page:

Figure 1. Location map combined with a Landsat image, with UTM coordinates, of the Albany-Fraser Orogen/Yilgarn Craton margin. The study area is shaded in green.


SATELLITE IMAGE
(Microsoft Bing, 2008)
Town
Geological Region
Road
Study site
Ore deposit
Officer Basin
Eucla Basin
Neale
Tropicana Au deposit
Beachcomber
Nova Ni-Cu Deposit
Woodline
FRASER RANGE
Albany-Fraser Orogen
KALGOORLIE-BOULDER
NORSEMAN
Salmon Gums
ESPERANCE
RAVENSTHORPE
Yilgarn Craton
Southern Ocean
Bremer Region
ALBANY
DENMARK
WALPOLE
KOJONUP
BRIDGETOWN
BUNBURY
PERTH
Perth Region
N
S
E
W
0 25 50 100 km
116°
118°
120°
122°
124°
-30°
-32°
-34°

Figure 1.

Geological and regolith setting

Regional geology and main geophysical features

The Yilgarn Craton (~3.0 and ~2.6 Ga; with a minor >3.7 Ga component) and the Mesoproterozoic Albany-Fraser Orogen (~1.35-1.26 Ga) comprise the basement of a cratonic-mobile belt margin in the southern Western Australia. This margin is the result of collision between the West Australian and the East Antarctic-South Australian cratons, resulting in the assemblage of Archaean-Proterozoic terranes (Fig. 2; Condie and Myers, 1999; Kirkland et al., 2010), with an intracratonic reactivation (~1215-1140 Ma), that involved oblique fault movement and a northwestward transport of thrust slices (Jones, 2006; Kirkland et al., 2011 and references therein).

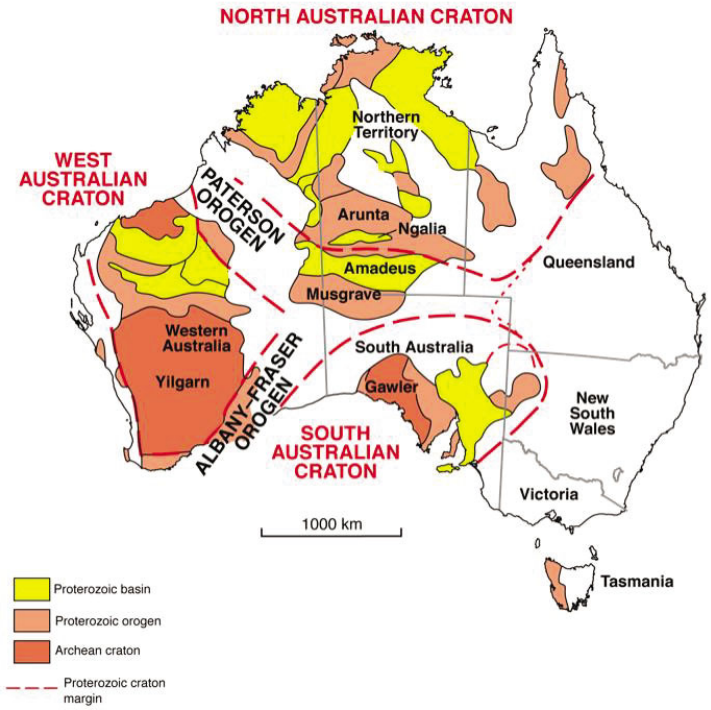

Figure 2. Map of Australia displaying the main cratonic, orogens and Proterozoic basins (adapted from Smithies et al., 2011).

The Yilgarn Craton was an extensional region spanning ~650,000 km^2, which stabilized before 2.4 Ga. The craton is formally subdivided into six terranes: (1) Narryer Terrane in the northwest; (2) South-West Terrane in the south-west; (3) Youanmi Terrane in the centre which is an amalgamation of the Murchison and Southern Cross domains; (4) Kalgoorlie; (5) Kurnalpi; and (6) the Burtville terranes in the eastern part of the craton. The last three terranes are bounded by an interlinked fault system and jointly comprise the Eastern Goldfields superterrane (Cassidy et al., 2006).

These terranes consist primarily of metavolcanic and metasedimentary rocks, together with granites and granitic gneiss, with a formational age span between ~3.0 and ~2.6 Ga. Magmatic events resulted in large granite intrusions at ~2.7-2.6 Ga, which stitched together the diverse tectonic units within the Yilgarn Craton (Cassidy et al., 2006 and references therein).

The Albany-Fraser Orogen is subdivided into fault-bounded zones with distinct lithotectonic character. This orogen has dominant lithologies of amphibolite to granulite facies paragneisses and orthogneisses, subsequently intruded by late tectonic granitic plutons (e.g., Myers, 1995; Spaggiari et al., 2009, 2011; Kirkland et al., 2011). These zones are (Fig. 3):

(1) The Northern Foreland (Archaean-Proterozoic metagranitic and metamafic rock suites, metagranite with Biranup Zone intrusions);
(2) The Kepa Kurl Booya Province (Proterozoic metasyenogranite interlayered with mingled metadiorite-metagabbro and remnants of Archaean suite rocks, which include the Biranup Zone, the 1.7 Ga magmatism of the Bobbie Point metasyenogranite, the Fraser Zone and the Nornalup Zone);
(3) The Recherche and Esperance supersuites (Mesoproterozoic, strongly deformed metagranites and undeformed to moderately deformed granitic rocks respectively); and
(4) Various Mesoproterozoic cover sedimentary units. Eastwards Phanerozoic sedimentary and volcanic units of the Eucla basin largely cover the AFO.

The Yilgarn Craton and the AFO are regolith-dominated terrains, which meet at the sharp boundary of the Cundeelee fault. The geological trend drastically changes from southwestern-northeastern in the Albany-Fraser Orogen, to northwestern-southeastern in the Yilgarn Craton (Fig. 3). Geophysical datasets suggest that materials from these two regions have distinct physical properties that differentiate the Yilgarn Craton and the AFO (Figs. 4, 5 and 6).

Next pages:

Figure 3. Simplified geological map of the Albany-Fraser Orogen and Yilgarn Craton margin based on the Geological Survey of Western Australia (GSWA) 500K geological map of GSWA (2008) and Spaggiari et al. (2011).

Figure 4. Gravimetric Bouger data for the Albany-Fraser Orogen and Yilgarn Craton margin from Geosciences Australia (GA) 2012 dataset. The Fraser Range displays the most significant gravity anomaly. The Ni-Cu Nova deposit is located on the edge of the Fraser Range anomaly.

Figure 5. Interpreted total magnetic intensity map for the Albany-Fraser Orogen and Yilgarn Craton margin from Geosciences Australia (GA) 2012 dataset. The geological trends in the southwestern and northeastern AFO are highlighted by intense positive magnetic anomalies (shaded in red).

Figure 6. Radiometric data (U-Th-K) for the Albany-Fraser Orogen and Yilgarn Craton margin from Geosciences Australia (2012) dataset. Drainage sedimentary patterns are highlighted by the presence of K in the south-west, and by Th in areas of the Yilgarn Craton. The sedimentary surface of the Eucla basin displays a complex colour pattern that differentiates it from the adjacent Albany-Fraser Orogen.

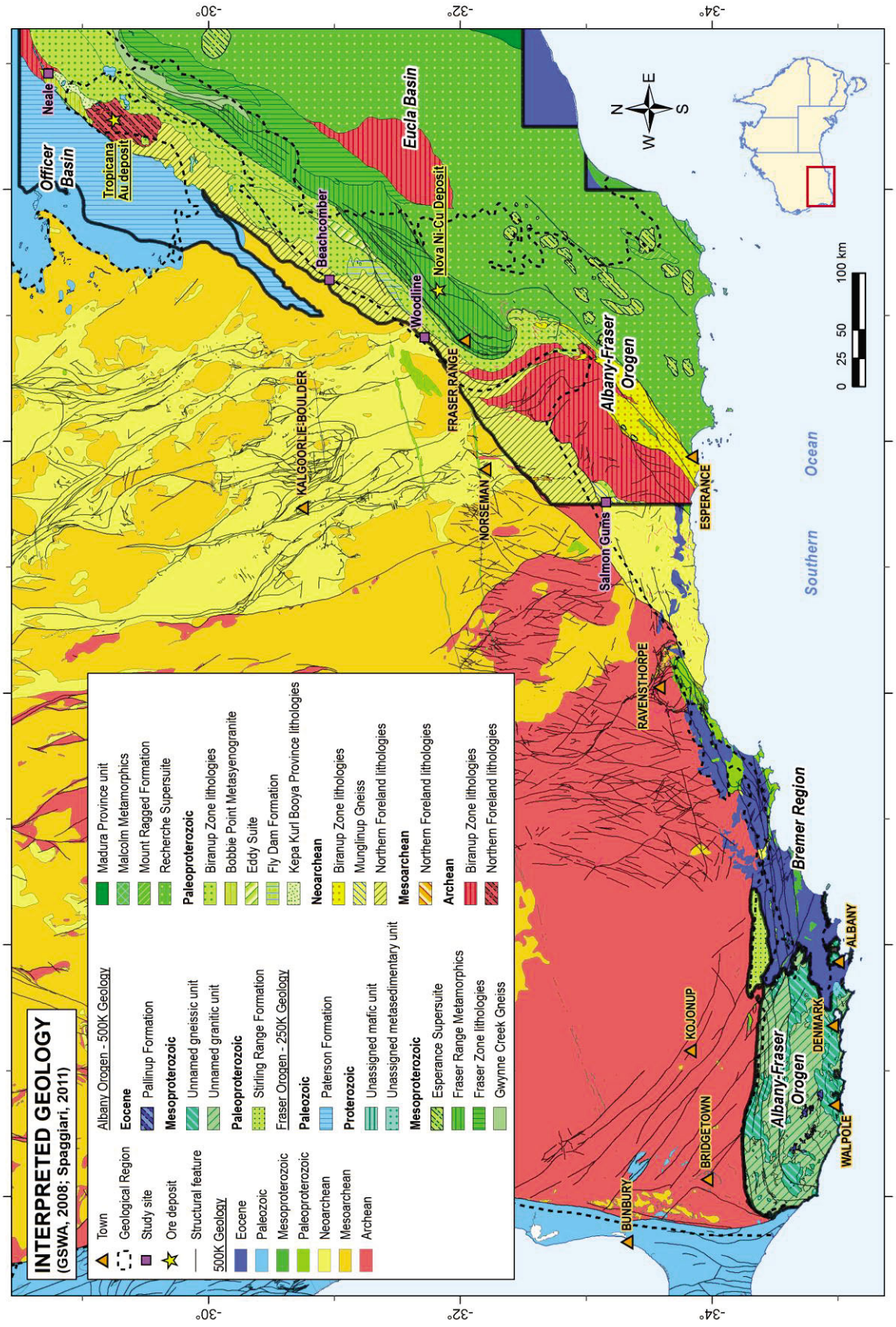
INTERPRETED GEOLOGY
(GSWA, 2008; Spaggiari, 2011)
Town
Geological Region
Study site
Ore deposit
Structural feature
500K Geology
Eocene
Paleozoic
Mesoproterozoic
Paleoproterozoic
Neoarchean
Mesoarchean
Archean
Albany Orogen - 500K Geology
Eocene
Pallinup Formation
Mesoproterozoic
Unnamed gneissic unit
Unnamed granitic unit
Paleoproterozoic
Stirling Range Formation
Fraser Orogen - 250K Geology
Paleozoic
Paterson Formation
Proterozoic
Unassigned mafic unit
Unassigned metasedimentary unit
Mesoproterozoic
Esperance Supersuite
Fraser Range Metamorphics
Fraser Zone lithologies
Gwynne Creek Gneiss
Madura Province unit
Malcolm Metamorphics
Mount Ragged Formation
Recherche Supersuite
Paleoproterozoic
Biranup Zone lithologies
Bobbie Point Metasyenogranite
Eddy Suite
Fly Dam Formation
Kepa Kurl Booya Province lithologies
Neoarchean
Biranup Zone lithologies
Munglinup Gneiss
Northern Foreland lithologies
Mesoarchean
Northern Foreland lithologies
Archean
Biranup Zone lithologies
Northern Foreland lithologies
Officer Basin
Neale
Tropicana Au deposit
Eucla Basin
Beachcomber
Nova Ni-Cu Deposit
Woodline
FRASER RANGE
Albany-Fraser Orogen
KALGOORLIE-BOULDER
NORSEMAN
Salmon Gums
ESPERANCE
RAVENSTHORPE
Southern Ocean
Bremer Region
ALBANY
DENMARK
WALPOLE
KOJONUP
BRIDGETOWN
BUNBURY
Albany-Fraser Orogen
N
S
W
E
0 25 50 100 km
116°
118°
120°
122°
124°
-30°
-32°
-34°

Figure 3.

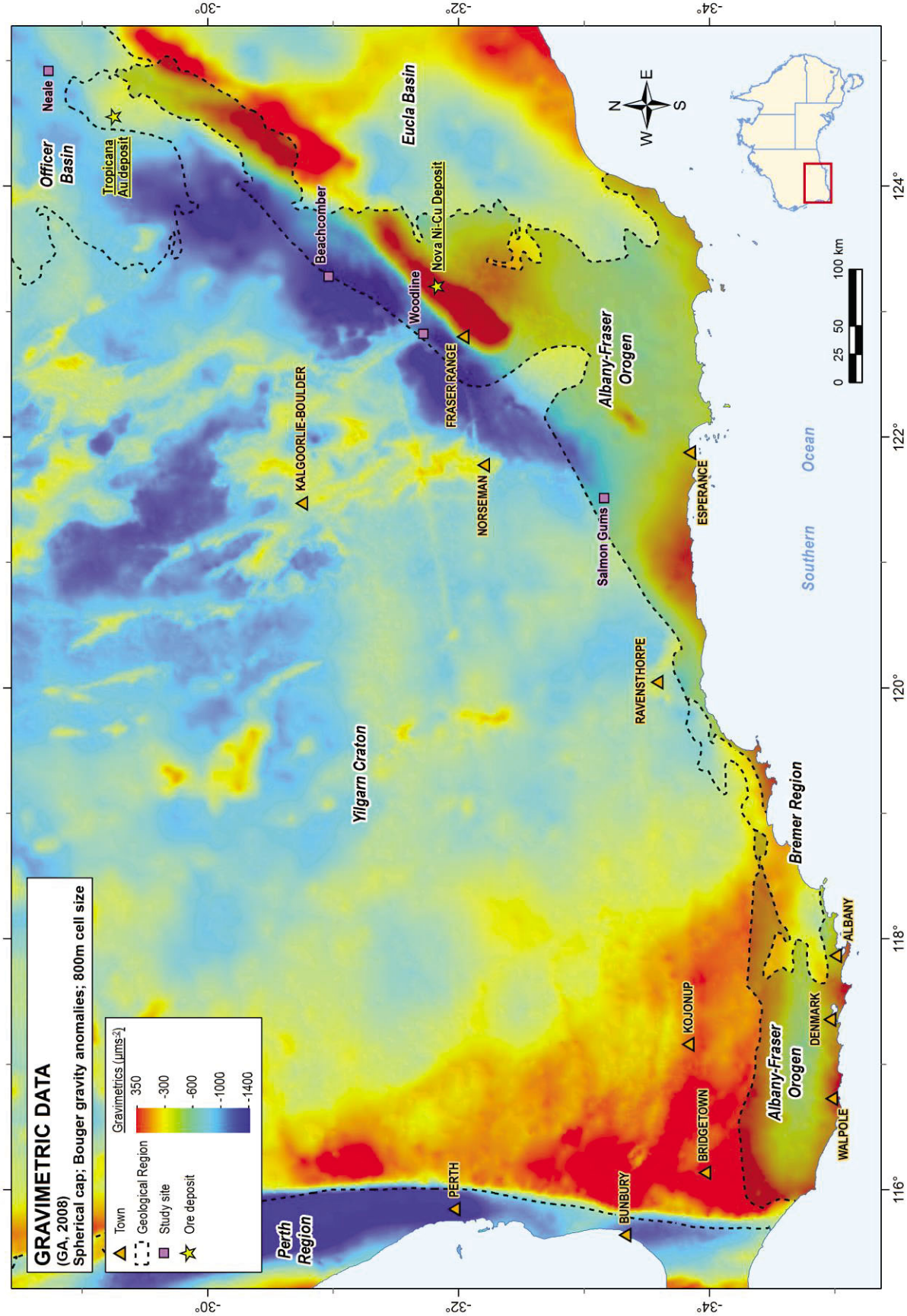
GRAVIMETRIC DATA
(GA, 2008)
Spherical cap; Bouger gravity anomalies; 800m cell size
Gravimetrics (μms-2)
350
-300
-600
-1000
-1400
Town
Geological Region
Study site
Ore deposit
Officer Basin
Eucla Basin
Yilgarn Craton
Albany-Fraser Orogen
Albany-Fraser Orogen
Albany-Fraser Orogen
Bremer Region
Perth Region
Southern Ocean
Neale
Tropicana Au deposit
Beachcomber
Woodline
Nova Ni-Cu Deposit
FRASER RANGE
KALGOORLIE-BOULDER
NORSEMAN
Salmon Gums
ESPERANCE
RAVENSTHORPE
PERTH
BUNBURY
BRIDGETOWN
KOJONUP
DENMARK
ALBANY
WALPOLE
N
S
E
W
0 25 50 100 km
116°
118°
120°
122°
124°
-30°
-32°
-34°

Figure 4.

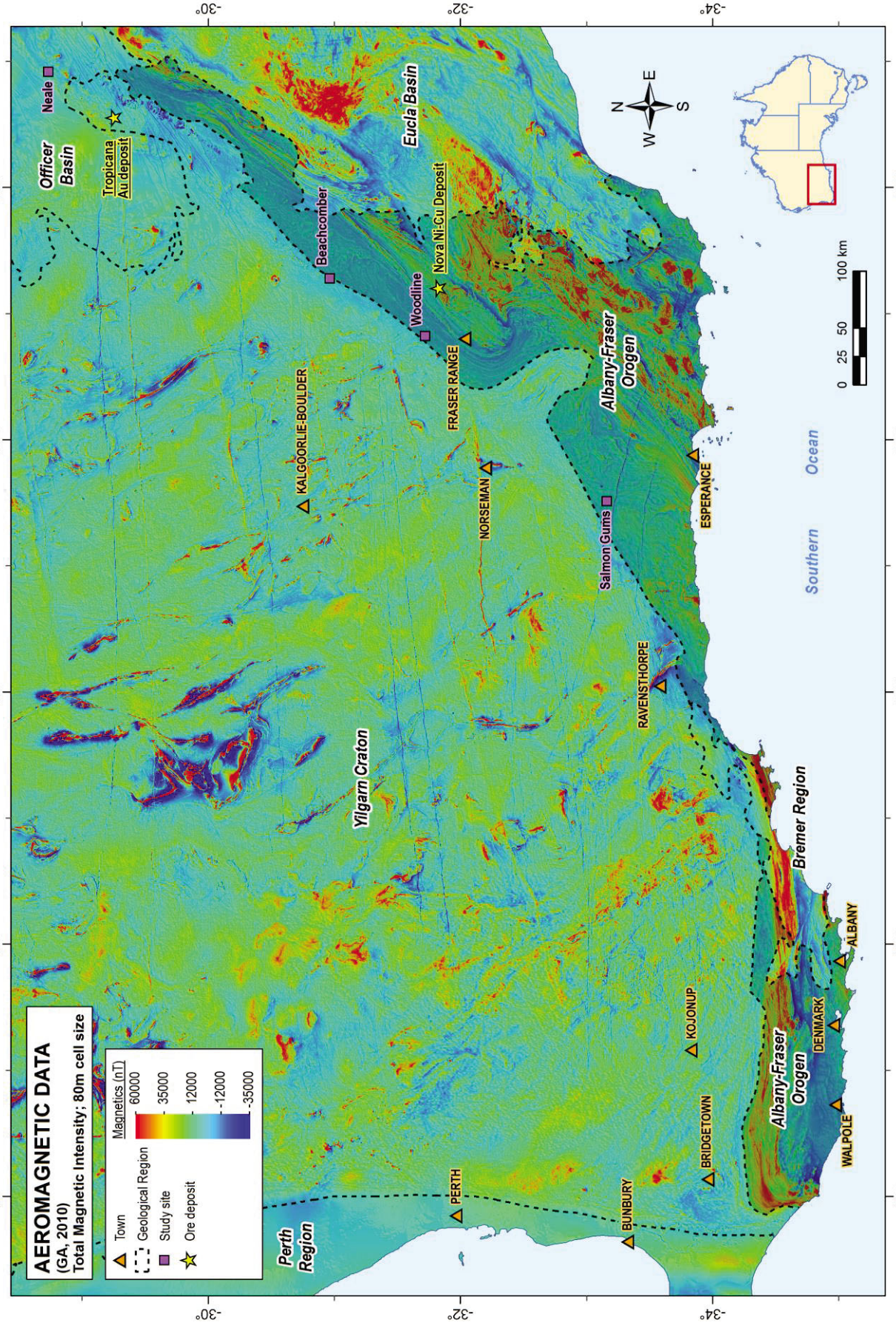
AEROMAGNETIC DATA
(GA, 2010)
Total Magnetic Intensity; 80m cell size
Magnetics (nT)
60000
35000
12000
-12000
-35000
Town
Geological Region
Study site
Ore deposit
Officer Basin
Eucla Basin
Yilgarn Craton
Albany-Fraser Orogen
Bremer Region
Perth Region
Southern Ocean
Neale
Tropicana Au deposit
Beachcomber
Nova Ni-Cu Deposit
Woodline
FRASER RANGE
KALGOORLIE-BOULDER
NORSEMAN
Salmon Gums
ESPERANCE
RAVENSTHORPE
KOJONUP
BRIDGETOWN
DENMARK
ALBANY
WALPOLE
BUNBURY
PERTH
116°
118°
120°
122°
124°
-30°
-32°
-34°
N
S
E
W
0 25 50 100 km

Figure 5.

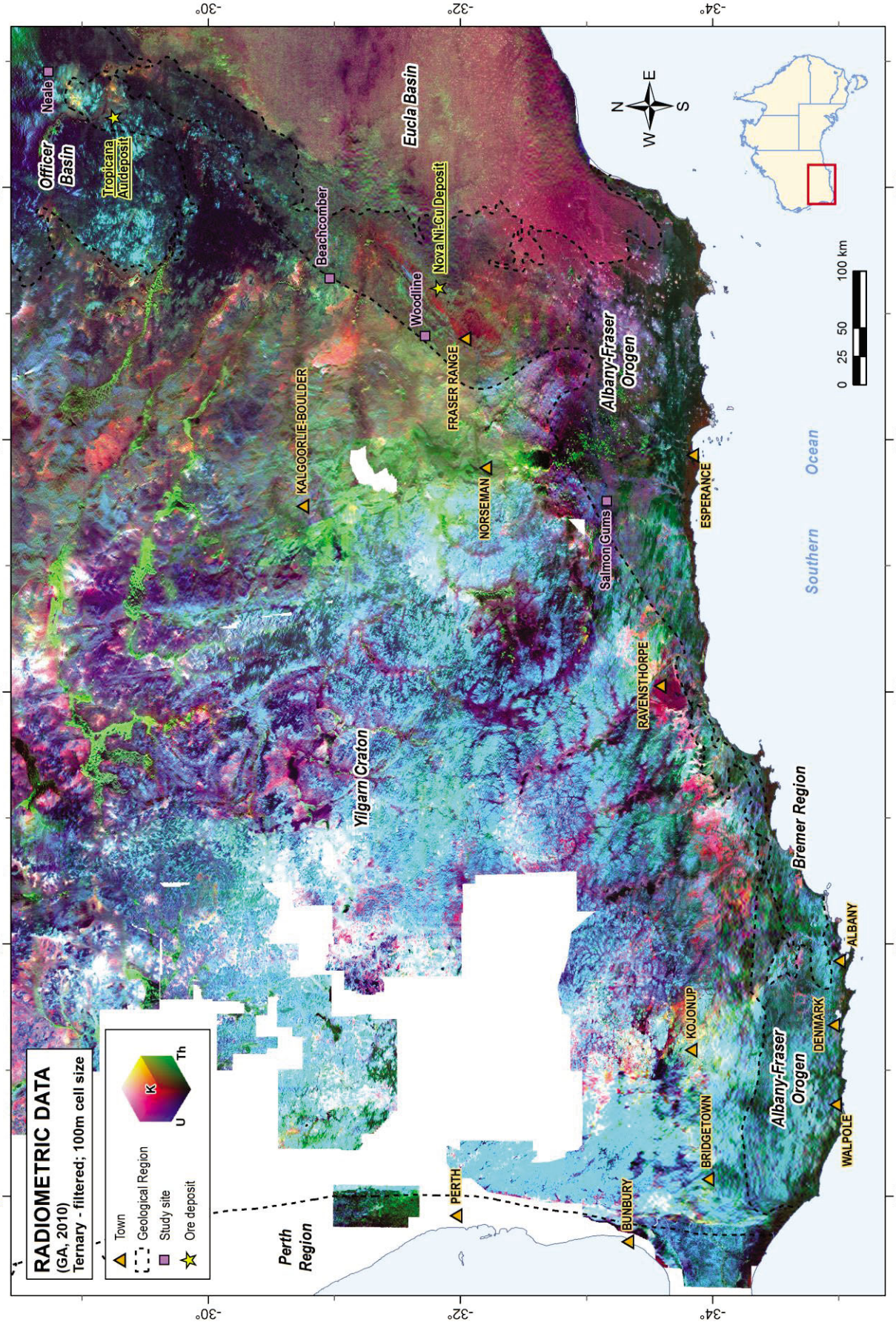
RADIOMETRIC DATA
(GA, 2010)
Ternary - filtered; 100m cell size
K
Th
U
Town
Geological Region
Study site
Ore deposit
Officer Basin
Eucla Basin
Albany-Fraser Orogen
Yilgarn Craton
Perth Region
Bremer Region
Southern Ocean
Neale
Tropicana Antideposit
Beachcomber
Nova Ni-Cu Deposit
Woodline
FRASER RANGE
KALGOORLIE-BOULDER
NORSEMAN
Salmon Gums
ESPERANCE
RAVENSTHORPE
PERTH
BUNBURY
BRIDGETOWN
KOJONUP
DENMARK
ALBANY
WALPOLE
N
S
E
W
0 25 50 100 km
116°
118°
120°
122°
124°
-30°
-32°
-34°

Figure 6.

Mineral systems in the Yilgarn Craton/Albany-Fraser Orogen margin

Two major deposits have recently been discovered in the Albany-Fraser Orogen/Yilgarn Craton margin: (1) the Tropicana-Havana Au system with a resource of 6.41 Moz Au (http://www.tropicanajv.com.au, September 2013) and (2) The Nova Ni-Cu deposit (http://www.siriusresources.com.au, resource of 10.2Mt at 2.4% Ni).

Tropicana is located 330 km north-east of Kalgoorlie (Fig. 1). It was discovered in 2005 after AngloGold Ashanti Australia followed up on a Au anomaly in soil associated with a palaeochannel. The neighbouring Havana deposit (south of Tropicana) was discovered in 2006 as the result of a follow up of an unexplained Au-in-soil anomaly. The Nova Ni-Cu deposit in the Fraser Range was discovered in 2012. These two discoveries highlight the importance of the AFO as an emerging metal-rich province.

Based on the initial Tropicana discovery, and the proximity of Yilgarn-like greenstone belt outcrops, the area was considered prospective for deposits with Yilgarn lode-Au style affinities. Subsequent work on the Tropicana deposit has proven that this mineralization is not a counterpart of Yilgarn style Au deposits (Doyle et al., 2007), but was formed by hydrothermal activity in the AFO marginal to the Yilgarn Craton. It was also shown not to be the result of metamorphism of a pre-existing Archaean Au deposit (Blenkinsop and Doyle, 2013a and b).

The mineralized zones at Tropicana and Havana are principally hosted within rocks of quartzofeldspathic gneiss and pegmatite facies affiliation. Two mineralization styles are distinguished:

(1) Disseminated and pyrite-dominant bands and crackle breccia veins within altered quartzofeldspathic gneiss and rare garnet gneiss intervals; and

(2) Patchy vein style pyrite-pyrrhotite selectively replacing thin intervals of metasediments spatially associated and interlayered with a hanging wall of garnet gneiss (Doyle et al., 2007; Spaggiari et al., 2011). Gold is concentrated in quartzofeldspathic gneiss within the so-called “favourable horizon”.

Higher Au grades (up to 6.6 g/t) are associated with anastomosing biotite-sericite fracture infill and crackle breccia zones. Sulfides within the mineralized zones consist mainly of pyrite (2-8%, <0.2 mm). Visible Au has not been recorded. Quartz veining and pervasive carbonate alteration is absent (Doyle et al., 2007; Spaggiari et al., 2011).

The Tropicana Project area (Fig. 2A) lies adjacent to a north-east trending magnetic feature, which extends over 550 km in length. This feature is interpreted to be the major tectonic suture between the Yilgarn Craton and the Proterozoic Albany-Fraser Orogen. The Atlantis and Hercules Au prospects can be interpreted as expressions of the Tropicana-Havana Au system further to the north-east (Fig. 2).

Shortly after the discovery of the Tropicana Au deposit in 2005, the Nova Ni-Cu deposit was discovered in 2012 from a Ni soil anomaly. It was confirmed by an EM survey that indicated sulfide mineralization beneath overburden in the Fraser Range. The discovery drill hole intersected a 4 metre thick zone of semi-massive pyrrhotite-pentlandite-chalcopyrite containing 3.8% Ni and 1.42% Cu. Further drilling intersected 13 m @ 4.3% Ni, 1.83% Cu and 0.12% cobalt. The Nova Ni-Cu deposit is hosted in granulite facies metamorphic rocks (Sirius Resources website, http://www.siriusresources.com.au, February 2013).

Palaeogeographical and palaeoclimatological development

Since the last tectonic event affecting the Albany-Fraser Orogen at ~1.15 Ga, this cratonic boundary has been considered largely stable (Spaggiari et al., 2011 and references therein). Erosion during this period of long-term stability has produced a very characteristic near-flat surface for the region, and weathering generated a deeply regolith-dominated terrain (e.g., ferruginous laterite and/or saprolite).

Since the Early Triassic (230 Ma), the Australian continent has drifted within a short latitude span (between 30-60 degrees; Fig. 7). Latitude changes affected palaeoclimatic conditions, which resulted in diverse weathering intensities throughout the Albany-Fraser Orogen/Yilgarn Craton margin. Increasing aridity throughout the orogen has been the main palaeoclimatic change since the Middle Eocene (50 Ma).

This palaeoclimate evolution can be summarized in five main stages, during which the sedimentary dynamics were dominated by fluvial systems in the Palaeozoic and Mesozoic, whereas, in the Cretaceous and Eocene, changes in sea-level led to reduced erosion and deep weathering under humid sub-tropical to tropical climates, followed in the Late Tertiary by semi-arid conditions. These five stages are presented in Table 1 and Fig. 7.

Table 1. The weathering framework of the Albany-Fraser Orogen (after Anand and Butt, 2010).

(1) Weathering of the pre-existing geomorphologic features that had undergone glacial erosion during the Early Permian by the subsequent Palaeozoic and Mesozoic river systems, which eroded many of the previously formed geomorphologic features;
(2) Late Cretaceous humid and sub-tropical conditions promoted intense chemical weathering;
(3) Late Cretaceous-Mid Eocene sea-level changes which resulted in erosion and sedimentary events that reshaped the landscape;
(4) Mid to Late Tertiary weathering under humid tropical-sub tropical conditions resulting in intense alteration, converting smectite into poorly crystalline kaolinite; and
(5) Late Tertiary and Quaternary changes in climatic conditions from arid to semi-arid. These had a large impact in terms of sedimentation and weathering environments, resulting in increased groundwater salinity.

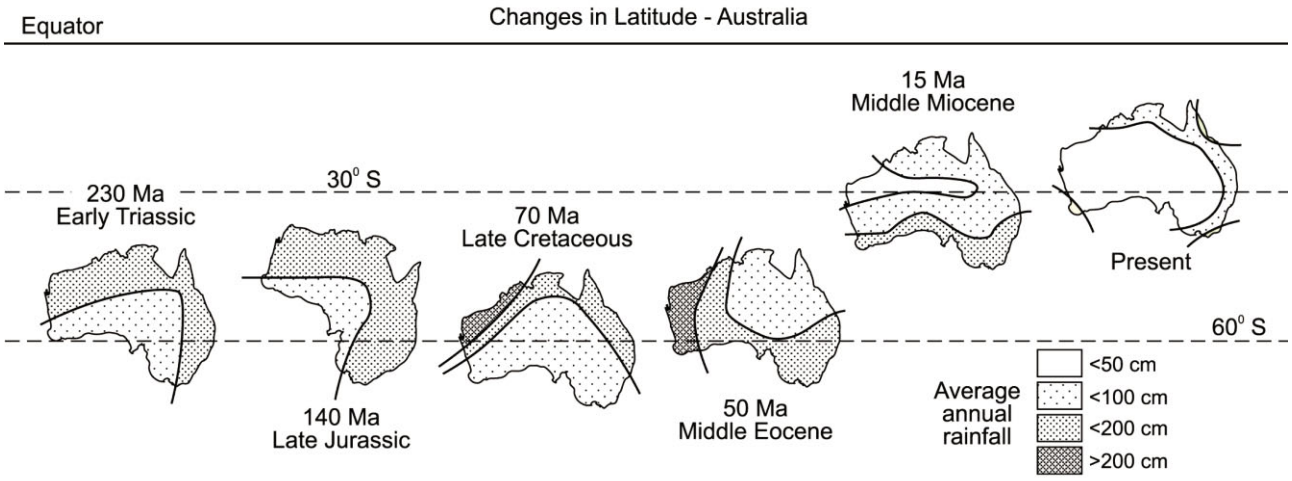

Figure 7. Palaeogeographic drift of Australia from the Palaeozoic to the present (Tardy and Roquin, 1998).

Weathering geochronology and landscape preservation

Burial and exhumation are key elements in the preservation of ancient landscapes in Australia (Pillans, 2005). Landscape evolution in the Yilgarn Craton presents evidence of stable and regular geomorphological features and weathering as early as late Carboniferous in the Laverton and Meekatharra areas (~300 Ma; Pillans, 2007). This implies low denudation rates and a long-term tectonic stability lacking any dynamic sedimentary systems for some specific areas. Palaeozoic and Mesozoic weathering profiles are recorded throughout Western Australia, suggesting the possibility that similar ages could be recorded for the Albany-Fraser Orogen (Fig. 8).

This long exposure of the surface implies a complex history of weathering. Residual weathering profiles result from the overprinting of several climatic changes, including water table fluctuations, together with variations in salinity and groundwater residence times. This uninterrupted weathering can produce overprinting features over the original geochemical signatures and/or mineralogy, resulting in the unreliability of the profiles as primary proxies to describe weathering evolution, such as using the degree of alteration of feldspars and ferromagnesian minerals. When comparing data extracted from different minerals and/or methods, the overprinting can result in different weathering ages being obtained from the same unit in a regolith profile.

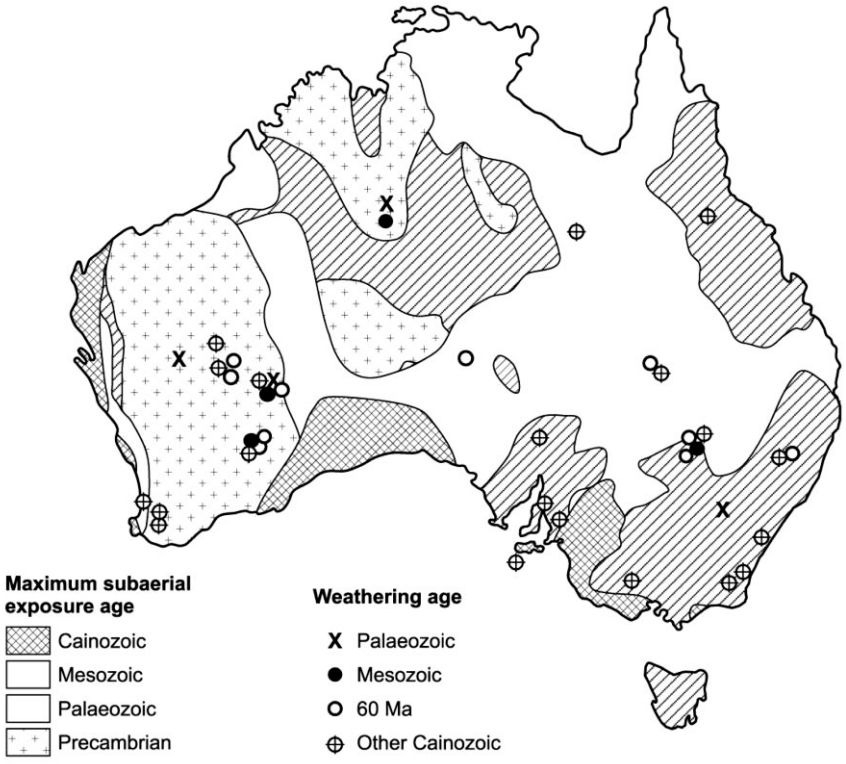

Figure 8. Map of the maximum subaerial exposure ages cross-referenced to weathering age (After from Pillans, 2005).

In southwestern Western Australia, low relief landforms cover ~95% of the landscape (Finkl, 1979). During the Late Mesozoic-Early Tertiary, lateritic deep chemical weathering developed widely throughout this region (Anand and Butt, 2010). The weathering profiles were preserved due to sea-level regression during the Oligocene: water tables dropped due to increased aridity, resulting in induration of the weathering profiles. Subsequent climatic changes produced varying degrees of erosion, truncating the lateritic profiles, and distributing the detritus as sedimentary packages in the surrounding areas. This process aided in flattening the landscape by filling in the low areas. Finkl (1979) interpreted the low relief landforms in the south-west of Western Australia as a series of plains, where lower plains were successively stripped (etchplain) from of higher plains to produce a step-like topography (Fig. 9).

The south of the Albany-Fraser Orogen/Yilgarn Craton margin is characterized by an area where most of the deeply weathered profiles were eroded, so that less than 10 m of the original residual regolith is preserved in in only about 10% of the surface area (Fig. 9). However, a large area in the most southwestern region is characterized by a largely preserved regolith sequence, with a thickness of 30-50m.

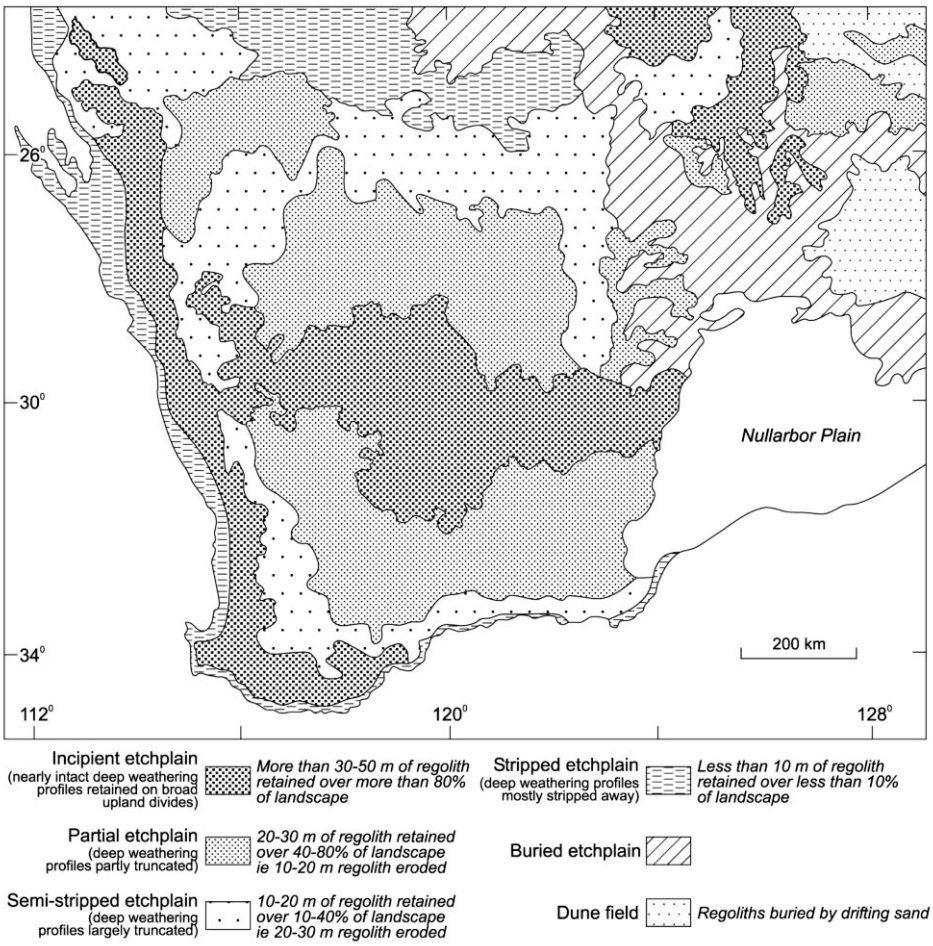

Figure 9. Stepped land surfaces in south Western Australia (excerpt from Anand and Paine, 2002; Anand and Butt, 2010, after Finkl, 1979).

The study area has been previously described by the Geological Survey of Western Australia as comprising regolith that is divided into three major domains: (1) sand plains that developed extensively in the north-east across to Esperance, (2) colluvium and residual ground in the Fraser Range-Beachcomber and Denmark areas, and (3) outcropping and coastal plains around Ravensthorpe and along the coastline from Esperance to Albany (Fig. 10).

These regolith domains are strongly related to the topographic variability of the region, which changes from >500 m in the Yilgarn Craton to the low plains of the Nullarbor, Eucla basin and the coast (Fig. 11). The complexities of the drainage patterns change significantly from Kalgoorlie, where they are dominated by main channels, to the Fraser Range and Salmon Gums areas, where the drainage patterns are much more open, forming large flat areas containing broken landscape highs.

The study area has vegetation zones, varying from native grasslands and minimally modified pastures in the north-east, to native forests and woodlands in the central east area. Farmland spans from Esperance to Denmark, with patches of native forests and woodlands in the south western and Ravensthorpe areas (Fig. 12).

Vegetation distribution follows annual average precipitation, which varies from 200 mm for the Tropicana-Neale prospect areas, to 500 mm in the interior, south and parallel to the coastline, rising to 800 mm in Esperance and up to 1,600 mm in the south-west corner of the Albany-Fraser Orogen (Fig. 13). Variations in annual precipitation averages for different areas have a fundamental effect on the calcrete development and carbonate sedimentary unit erosional processes. Calcrete tends to dissolve when average yearly rainfall exceeds 800 mm.

Next pages:

Figure 10. Interpreted regolith cover of the Albany-Fraser Orogen/Yilgarn Craton (500K; Geological Survey of Western Australia, 2008).

Figure 11. Digital elevation model of the Albany-Fraser Orogen/Yilgarn Craton (Geosciences Australia, 2009).

Figure 12. Interpreted vegetation cover of the Albany-Fraser Orogen/Yilgarn Craton (CSIRO, 2007).

Figure 13. Annual average precipitation of the Albany-Fraser Orogen/Yilgarn Craton (Bureau of Meteorology, 2005).

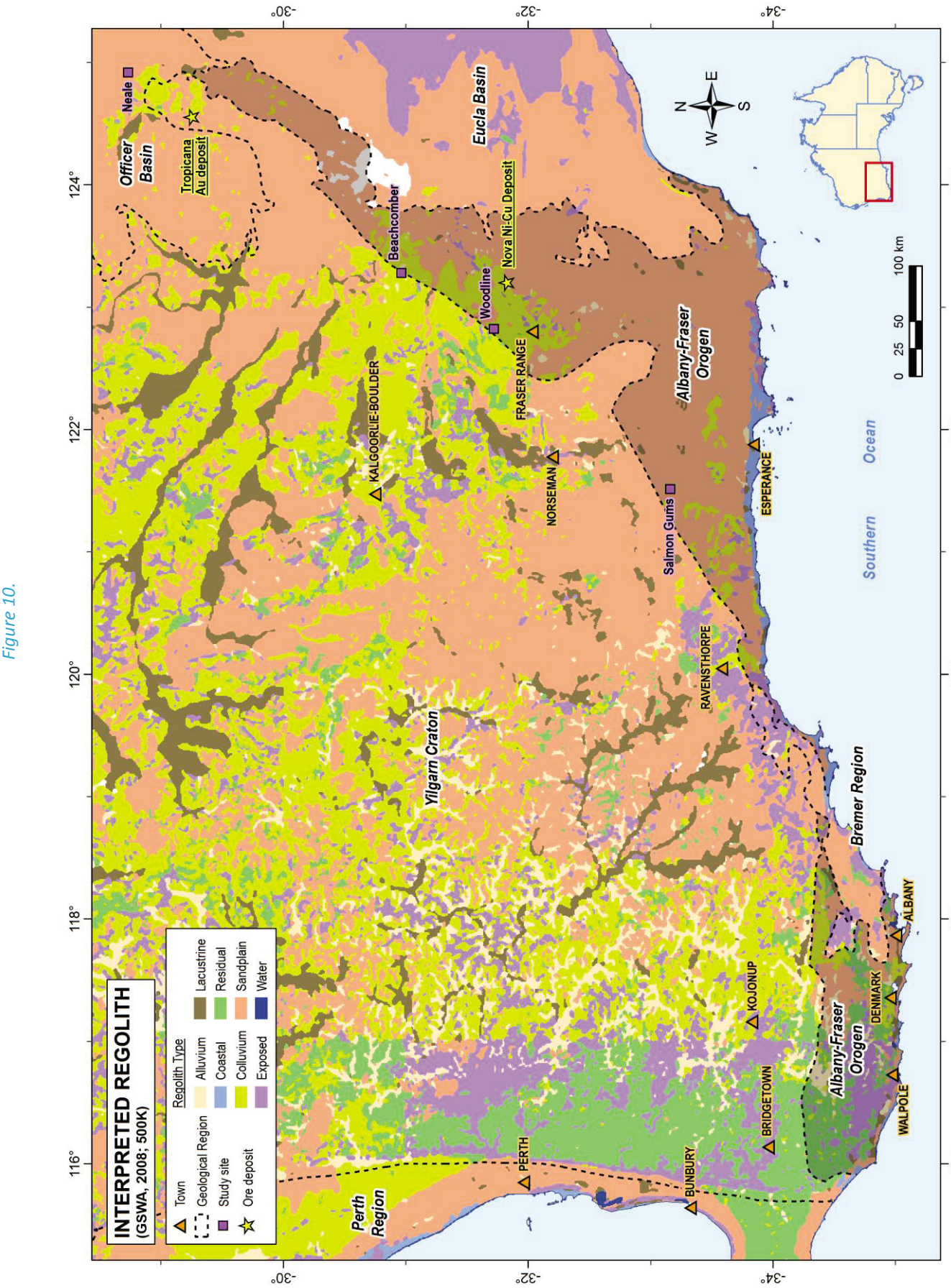
INTERPRETED REGOLITH
(GSWA, 2008; 500K)
Town
Geological Region
Study site
Ore deposit
Regolith Type
Alluvium
Coastal
Colluvium
Exposed
Lacustrine
Residual
Sandplain
Water
Officer Basin
Eucla Basin
Yilgarn Craton
Albany-Fraser Orogen
Albany-Fraser Orogen
Bremer Region
Perth Region
Southern Ocean
Neale
Tropicana Au deposit
Beachcomber
Woodline
Nova Ni-Cu Deposit
KALGOORLIE-BOULDER
FRASER RANGE
NORSEMAN
Salmon Gums
ESPERANCE
RAVENSTHORPE
ALBANY
DENMARK
WALPOLE
KOJONUP
BRIDGETOWN
BUNBURY
PERTH
N
S
E
W
0 25 50 100 km
116°
118°
120°
122°
124°
-30°
-32°
-34°

Figure 10.

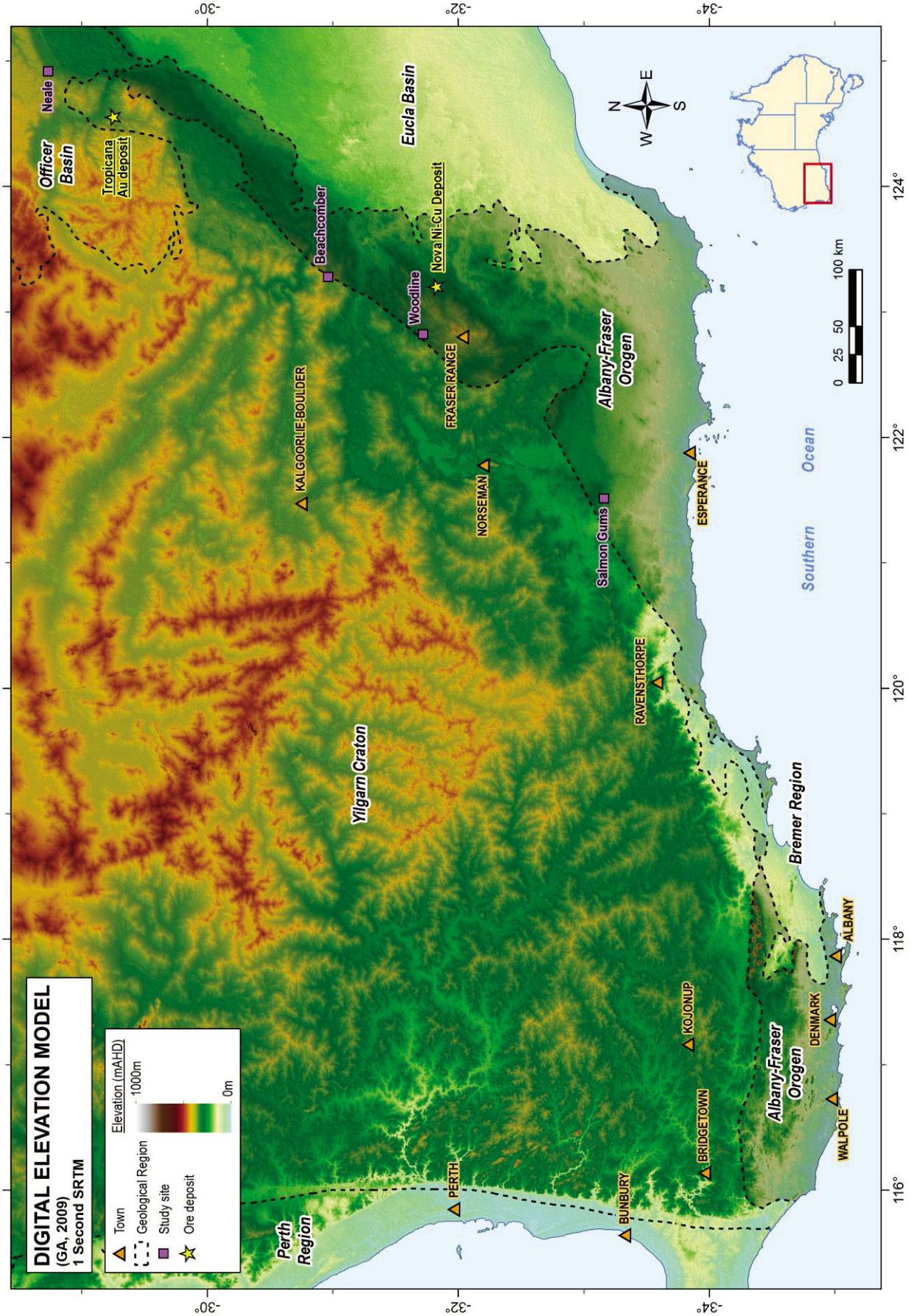
DIGITAL ELEVATION MODEL
(GA, 2009)
1 Second SRTM
Elevation (mAHD)
1000m
0m
Town
Geological Region
Study site
Ore deposit
Neale
Officer Basin
Tropicana Au deposit
Eucla Basin
Beachcomber
Nova Ni-Cu Deposit
Woodline
FRASER RANGE
Albany-Fraser Orogen
KALGOORLIE-BOULDER
NORSEMAN
Salmon Gums
ESPERANCE
Southern Ocean
RAVENSTHORPE
Yilgarn Craton
Bremer Region
ALBANY
DENMARK
WALPOLE
KOJONUP
BRIDGETOWN
BUNBURY
PERTH
Perth Region
Albany-Fraser Orogen
116°
118°
120°
122°
124°
-30°
-32°
-34°
N
S
E
W
0 25 50 100 km

Figure 11.

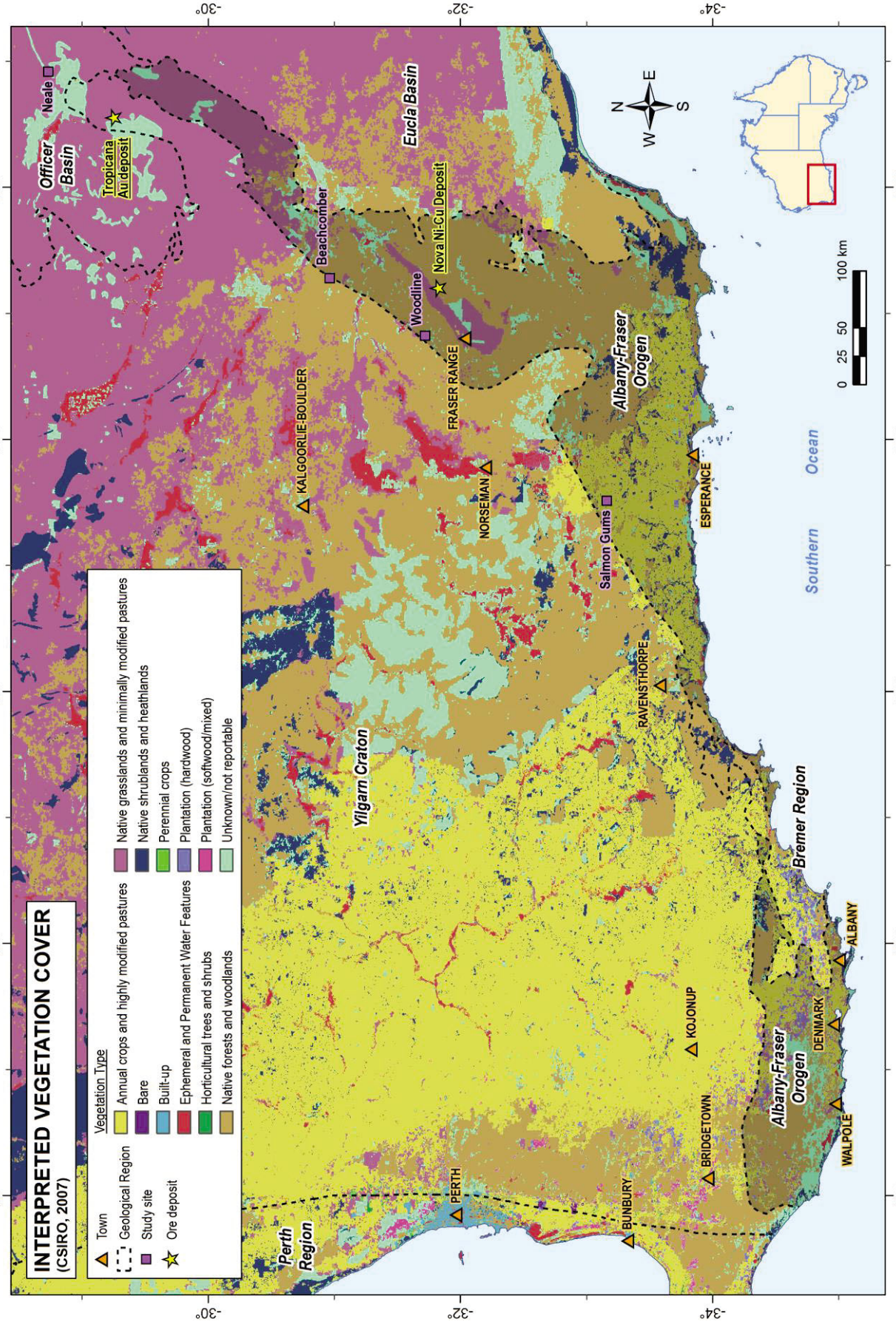
INTERPRETED VEGETATION COVER
(CSIRO, 2007)
Vegetation Type
Annual crops and highly modified pastures
Bare
Built-up
Ephemeral and Permanent Water Features
Horticultural trees and shrubs
Native forests and woodlands
Native grasslands and minimally modified pastures
Native shrublands and heathlands
Perennial crops
Plantation (hardwood)
Plantation (softwood/mixed)
Unknown/not reportable
Town
Geological Region
Study site
Ore deposit
Officer Basin
Neale
Tropicana Au deposit
Eucla Basin
Beachcomber
Nova Ni-Cu Deposit
Woodline
FRASER RANGE
KALGOORLIE-BOULDER
NORSEMAN
Albany-Fraser Orogen
Salmon Gums
ESPERANCE
Southern Ocean
RAVENSTHORPE
Yilgarn Craton
Bremer Region
KOJONUP
BRIDGETOWN
DENMARK
ALBANY
WALPOLE
BUNBURY
PERTH
Perth Region
116°
118°
120°
122°
124°
-30°
-32°
-34°
N
S
E
W
0 25 50 100 km

Figure 12.

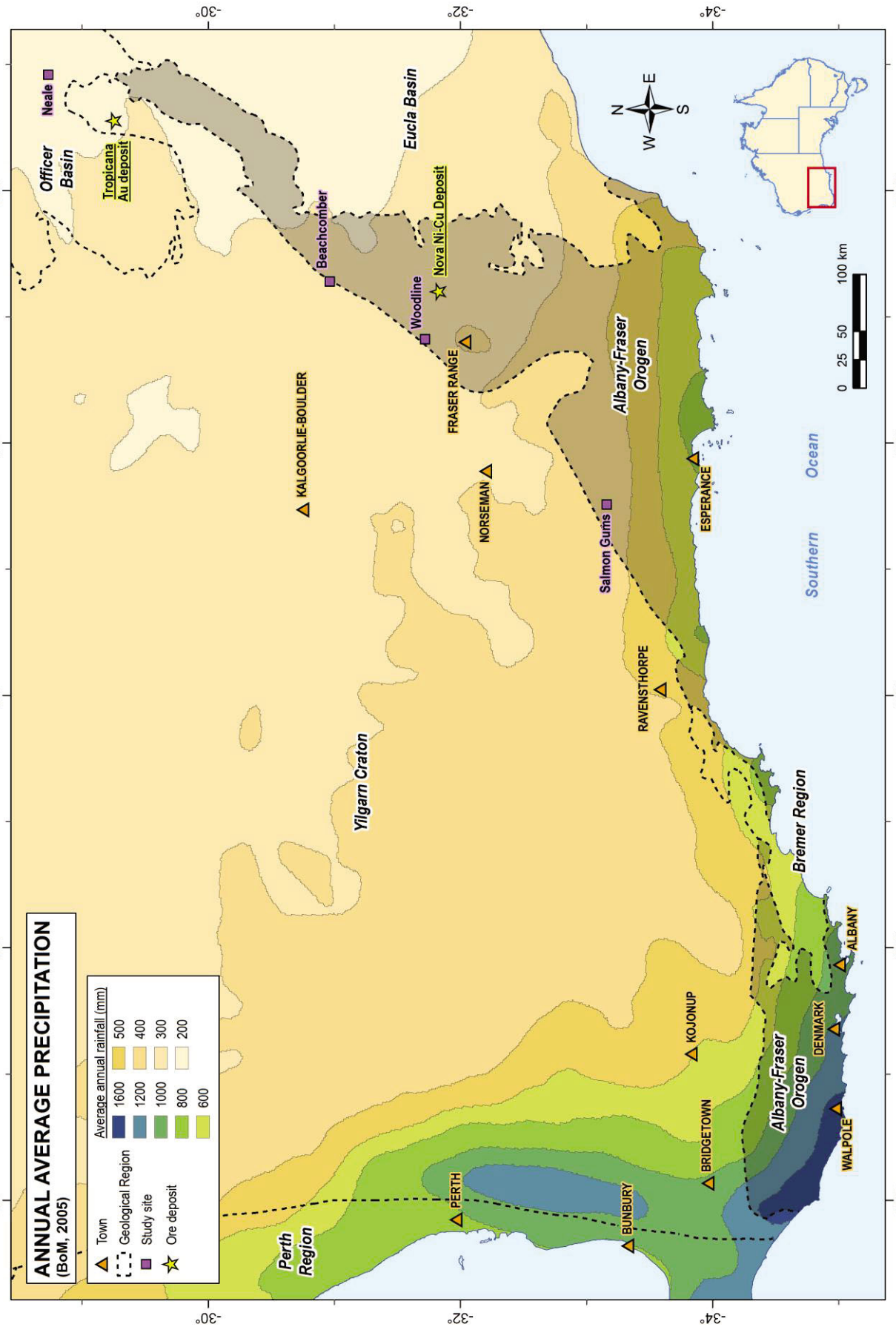
ANNUAL AVERAGE PRECIPITATION
(BoM, 2005)
Town
Geological Region
Study site
Ore deposit
Average annual rainfall (mm)
1600
1200
1000
800
600
500
400
300
200
Officer Basin
Eucla Basin
Yilgarn Craton
Albany-Fraser Orogen
Perth Region
Bremer Region
Southern Ocean
Neale
Tropicana Au deposit
Beachcomber
Nova Ni-Cu Deposit
Woodline
FRASER RANGE
KALGOORLIE-BOULDER
NORSEMAN
Salmon Gums
ESPERANCE
RAVENSTHORPE
PERTH
BUNBURY
BRIDGETOWN
KOJONUP
DENMARK
ALBANY
WALPOLE
116°
118°
120°
122°
124°
-30°
-32°
-34°
N
S
E
W
0 25 50 100 km

Figure 13.

1 Regolith framework model *(Appendix A)*

Summary

A new conceptual model of the Albany-Fraser Orogen/Yilgarn Craton margin as a palaeocoastline with numerous islands and estuarine zones is proposed, based on an integrated interpretation of the data presented within this report. The model involves extensive erosion, sedimentation and saprolite development taking place in different styles of regolith development.

"On inland" and "on island" weathering profiles may vary in maturity and saprolite development, with or without a transported cover derived from exotic marine sediments and/or limestones, and also from a sedimentary contribution from the Yilgarn Craton. Such areas are more reliable for understanding geochemical anomaly-basement relationships, whereas the "sea-flooded" areas require a more thorough and detailed investigation due to the combined effects of sediment mixing, mechanical dispersion, rejuvenated weathering profiles and short-term vertical element dispersion processes.

Within the above framework, the following four different regolith settings of diverse regolith architecture have been identified and defined. The settings have been named on the type locations where they are best developed.

(1) Albany setting is dominated by shallow weathered profiles with minimal regolith thickness (>0-15 m) and abundant basement outcrop. The regolith stratigraphy is mainly developed at elevations >200 m above sea-level. Below this level, erosional features and transported deposits are more abundant, thereby completely removing the saprolite.

(2) Kalgoorlie-Norseman setting is dominated by intensely and deeply weathered profiles, with relict landscape having abundant erosional breaks and variable thick regolith profile >20 m. Abundant inverted channels produced by the differential resistance to erosion of the ferruginized channel deposits of palaeodrainage networks. Saline lakes, as remnants of palaeodrainage are common, concentrating saline groundwater as modern landscape water collectors in combination with elevated evaporation rates.

(3) Esperance setting: regolith is dominated by sand dunes with thin exposure of surface regolith stratigraphy (<5 m). An increased transported cover of sand dune systems at the shoreline, of up to ~20 m thickness. Saprolite is developed from granitic gneisses at depth and progresses upwards to the formation of pisolitic units, which are in turn overlain by transported sand packages <2 m thick. In this regolith setting, newly formed units of ferruginous sandstone occur within transported sand dune packages. This horizon accumulates transition metals, whereas Au is anomalous in the transported upper sandy units.

(4) Neale setting: relict, deeply weathered saprolitic profile with the regolith commonly comprising residual deeply weathered profiles overlain by a transported blanket (2-25m thick). The residual regolith profile consists of four units from base to top, namely, saprock, dominated by partially weathered granitoids, gneisses and mafic rocks; lower ferruginous saprolite (3-25 m thick) dominated by quartz, feldspars, kaolinite, and goethite after ferromagnesian and sulfide minerals; upper kaolinitic saprolite (10-40 m) dominated by quartz and kaolinite; and a silcrete/grit layer (4-20 m thick).

Calcrete horizons have formed within the transported sand packages such as those at Salmon Gums (Esperance setting). Metal dispersion within the transported sands concentrates Au within the calcrete horizon, and other transition metals (V, Cr, Co, Ni and Sc) in the sand unit immediately above. In addition to this, post-depositional units of ferruginous sandstone occur within the transported sand dune packages (Esperance setting). This horizon accumulates transition metals (V, Cr, Co, Cu, Ni and Sc), whereas Au is anomalous in the upper sandy units. Currently forming calcrete and ferruginous sandstone units within the modern sand dune systems present excellent sampling media for exploration purposes.

In summary, any geochemical sampling, data interpretation and remote sensing technique applied to the region should be framed, and its efficacy evaluated, taking into account regional groundwater salinity, pH-Eh, geomorphological-sedimentary environments and average annual precipitation patterns.

Mapping the palaeocoastlines, islands and estuarine zones, as well as the region of marine limestone/sediment influence, would have a significant remarkable impact on planning and implementation of exploration campaigns in the region.

1.1 Introduction

This Chapter explores the geomorphological framework of the AFO. In particular, it addresses whether there is a major correlation between regolith formation/features and basement geology along the cratonic boundary, and/or if regolith formation is mainly dominated by surface landscape evolution. Orogenic scale multi-component datasets were integrated to identify key controls of regolith geomorphology to answer these questions.

A new conceptual model of the Albany-Fraser Orogen/Yilgarn Craton margin as a palaeocoastline with numerous islands and estuarine zones is proposed based on an integrated interpretation of the data presented in this report. The model involves extensive erosion, sedimentation and saprolite development taking place in different styles of regolith development. Full details of the findings of this chapter may be found in Appendix A.

1.2 Sample strategy: regional transects

Five regional surface transects were carried out at different latitudes as displayed in Figs. 14 and 15. These transects were designed to cross-cut geomorphological features along the boundary between the Yilgarn Craton and the AFO, in order to characterize the landscape evolution through these two geological regions.

Surface observations from each traverse were compiled and summarized as stations (Figs. 14 and 15). In selected stations, rock/soil/regolith samples were collected for whole-sample geochemistry to evaluate the geochemical features of key stratigraphic units of the regolith stratigraphy (Figs. 14 and 15; Appendix A).

(1) Transect A, in yellow from Kojonup to near Albany with a length of ~400 km, with a total of 19 surface stations.
(2) Transect B, in red from Bridgetown to Albany with a length of ~250 km, with a total of 11 surface stations.
(3) Transect C, in blue from Kalgoorlie to Esperance with a length of ~900 km, with a total of 40 surface stations.
(4) Transect D, in yellow from Kalgoorlie to Esperance via Balladonia with a length of ~800 km, with a total of 29 surface stations.
(5) Transect E, in yellow from Albany to Esperance with a length of ~650 km, with a total of 39 surface stations.

All information compiled in this report has been geo-referenced and integrated with other datasets in a GIS platform using ArcGIS 10.0 software.

Next page:

Figure 14. Transects of the south-west Albany-Fraser Orogen/Yilgarn Craton margin area with the location of the surface stations on the digital elevation model (DEM; in UTM coordinates). The locations of the stratigraphic type sequences studied are highlighted in blue ovals.


DIGITAL ELEVATION MODEL
(GA, 2009)
1 Second SRTM
Town
Geological Region
Traverse station
Bri-Alb Traverse
Koj-Alb Traverse
Alb-Esp Traverse
Elevation (mAHD)
1000
750
500
250
0
Yilgarn Craton
Albany-Fraser Orogen
Bremer Region
KOJONUP
KATANNING
TAMBELLUP
CRANBROOK
MOUNT BARKER
ALBANY
DENMARK
WALPOLE
NORTHCLIFFE
PEMBERTON
MANJIMUP
BRIDGETOWN
BOYUP BROOK
B1
B2
B3
B4
B5
B6
B7
B8
B9
B10
B11
E01
E02
E03
E04
E05
E06
E07
A1
A2
A3
A4
A5
A6
A7
A8
A9
A10
A11
A12
A13
A14
A15
A16
A17
A18
A19
N
S
E
W
0
10
20 km
400000
450000
500000
550000
600000
650000
615000
620000
625000

Figure 14.

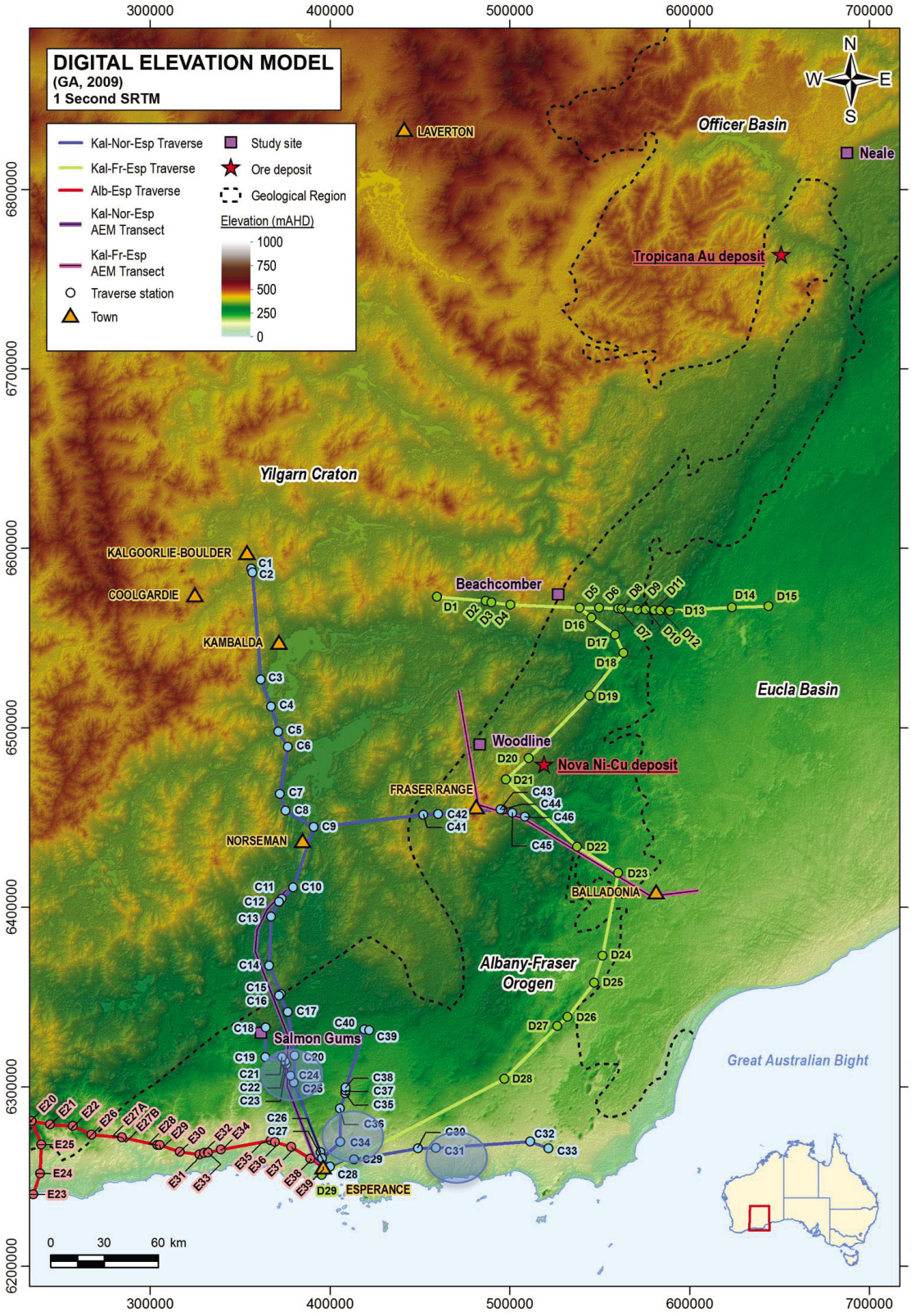

Figure 15. Transects in the north-east Albany-Fraser Orogen/Yilgarn Craton margin with the location of the surface stations on the digital elevation model (in UTM coordinates) included, and geographic location of the two AEM regional lines flown with Spectrem$_{2000}$ (Appendix A). Highlighted in blue circles are the locations of stratigraphic type sequences.

1.3 Regional traverses and key regolith profiles

Based on the observations from five regional traverses covering a total length of ~3,000 km, and ~140 observation stations within six regolith stratigraphic type sequences, the regolith framework of the Albany-Fraser Orogen/Yilgarn Craton margin can be subdivided into four domains. Each setting may be a composite formed from more than one transect, and their regional boundaries remain to be determined:

1.3.1 Region dominated by shallow weathered profiles: Albany setting (Figs. 14 and 16; Appendix A)

The Albany setting features saprolite with a laterally continuous pisolitic unit (0.5-3 m in thickness; Figs. 14) over the Yilgarn Craton. These units change into a very thin saprolite package overlain by colluvial deposits after 100 km. This cover package changes into transported cover. At 80 km from the coast the setting becomes dominated by a sand dune system (Appendix A).

Regolith profiles characteristically have a thickness of ~0-15 m with abundant basement outcrop. There is a *maximum* of ~150 m difference between the regolith topographic highs and lows in the landscape (Appendix A). The transported packages are generally <5 m thick inland and thicken to ~10 m close to the coast as the result of the accumulation of active sand dune systems (Appendix A).

In many locations the pisolitic unit has been transported over the underlying saprock units (Appendix A). This regolith stratigraphy is mainly developed at >200 m above sea-level. Below this topographic high, erosional features and colluvial deposits are more abundant, completely removing the saprolite package or colluvium covering it. Transported laterite accumulates V and Cr (Appendix A). It is uncertain if the metal anomalies are due to lateral or vertical dispersion processes. The most remarkable geochemical feature of this profile is the erratic ratios of Zr/Hf, Nb/Ta and Y/Ho. This supports differentiation between the saprock and the overlying transported cover with an exotic composition (Appendix A).

Within 30 km of the shoreline, beach deposits covering saprock were reported on slopes facing inland (Appendix A). These deposits are indicative of palaeoshorelines with different erosional regimes and sedimentary dynamics.

1.3.2 Region dominated by deeply weathered profiles: Kalgoorlie-Norseman setting (Figs. 15-18; Appendix A)

This is the typical “Yilgarn environment” has been described in previous studies (e.g., Anand and Butt, 2010).

Relict landscape with abundant erosional breaks and thick regolith profile >20 m (Appendix A) characterizes the Kalgoorlie-Norseman setting. Abundant inverted channels at local scale are present, produced by differential erosion of the ferruginized channel deposits of palaeodrainage networks for the first 100 km of the transect (Appendix A). Saline lakes in valleys represent remnants of palaeodrainages concentrating saline groundwater. Salinities are further increased by elevated evaporation rates. After 180 km, the saprolite develops a pisolitic unit and calcrete, until 60 km from the coast where sand dunes and calcrete on marine limestone are established. This setting ends transitionally into the Esperance setting a few kilometres south from Norseman.

1.3.3 Regolith-dominated by sand dunes: Esperance setting (Figs. 15, 16 and 17; Appendix A)

The laterally continuous pisolitic unit at ~130 km from the transect D (Fig. 15), and south of Norseman in transect C10-C46, becomes calcrete-dominated at surface for ~60 km; shifting into colluvial sediments in direct contact with basement, and thence evolving into a calcrete unit for ~180 km. Outcropping limestone is noted at the coast.

In this setting, the general regolith profile is <5 m thick, with an increase of the transported cover thickness (sand dunes systems) at the shoreline up to ~20 m (Appendix A). Saprolite and overlying pisolitic units (up to 1 m thick) developed from weathering of granitic-gneisses at depth and develops, and are overlain by transported sand packages <2 m in thickness (Appendix A).

Calcrete horizons are generated within the transported sand packages (e.g., Salmon Gums; Appendix A). Dispersion within the transported sand concentrates Au within the calcrete horizon (Appendix A), as well as transition metals in the sand unit immediately above it (V, Cr, Co, Cu, Ni and Sc). This implies that the transported sand cover has enough residence time to produce accumulations of metals in horizons that post-date the residual saprolite. These represent an excellent sampling *medium* for the identification of anomalous elements during mineral exploration campaigns at regional scale.

In addition, in the Esperance regolith setting, newly formed units of ferruginous sandstone within the transported sand dune packages have been identified (Appendix A). These horizons accumulate transition metals (V, Cr, Co, Ni and Sc), whereas Au is anomalous in the upper sandy units (Appendix A).

Marine limestone is abundant in outcrop along the coast and inland. Calcrete horizons up to 3 m thick are well developed in limestones from Esperance to Balladonia (Appendix A).

1.3.4 Relict deeply weathered saprolitic profile: Neale setting (60 km north-east Tropicana deposit; Figs. 15 and 16; Appendix A)

The regolith in this area comprises a residual deeply weathered profile without landscape breaks and inverted channels. The saprolite is overlain by a transported blanket of ferruginous sands, gravels and lateritic pisoliths and nodules (2-25 m). The thickness of the transported cover increases up to 75 m when associated with palaeodrainage sedimentary features.

The residual regolith profile consists of four units, from base to top: (1) saprock, dominated by partially weathered granitoids, gneisses and mafic rocks; (2) lower ferruginous saprolite (3-25 m thick), dominated by quartz, feldspars, kaolinite, goethite after ferromagnesian minerals, and sulfide minerals; (3) upper kaolinitic saprolite (10-40 m thick), dominated by quartz and kaolinite; and (4) silcrete/grit layer (4-20 m thick), dominated by quartz, with accessory anatase and zircon.

The lower ferruginous saprolite displays the same geochemical signatures as the basement rocks. This saprolitic horizon has the potential to develop anomalous geochemical halos associated with basement mineralization.

Implications for drilling and geochemical sample *media* are summarized in Fig. 16. Thick regoliths in the Kalgoorlie-Norseman and Neale settings can form barriers to metal mobility from the basement due to transported cover and the depleted section of the upper saprolite, whereas the thinner “rejuvenated” regolith profiles of the Albany and Esperance settings, lacking the depleted upper saprolite and/or thin transported cover, will require shallower drilling to sample the basement and to test for vertical metal dispersion.

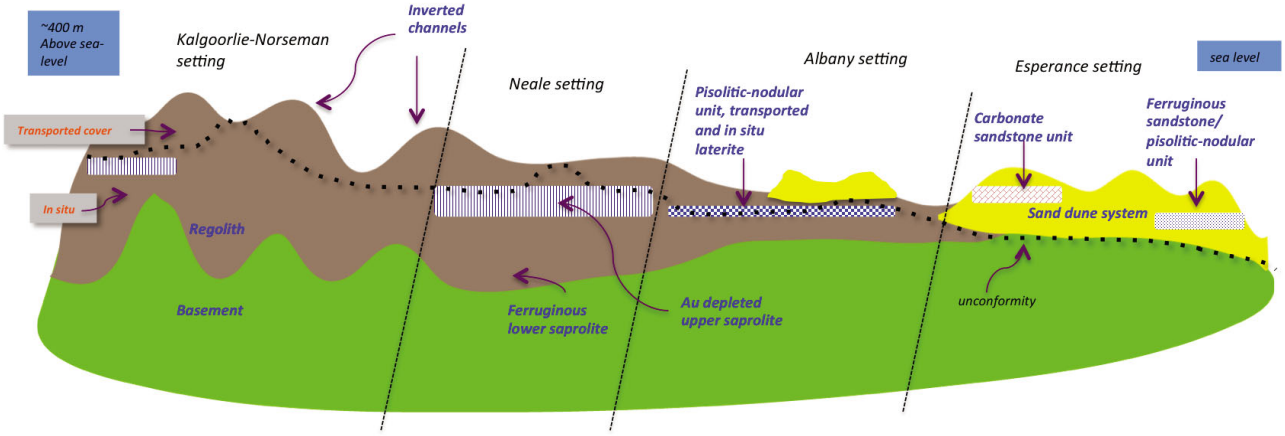

Figure 16. Schematic summary of the four-regolith settings defined in this study.

Next pages:

Figure 17. Schematic regional traverse C from Kalgoorlie to Esperance, with vertical exaggeration. From Kalgoorlie to Norseman, inverted channels are the predominant relict regolith feature in the landscape, coupled with erosional features that display the regolith profile of the area (station C4). Inverted channels are filled with ferruginized sediment with distinctive magnetic properties. These channels form hills due to erosional resistance. Inverted channels were not encountered further south of Norseman. At ~250 m above sea-level, pisoliths and calcrete units are more abundant. Close to the shoreline, limestone outcrops, active sand dune systems and calcrete are common.

Figure 18. Regolith sequence displaying ferruginous sandstone unit developed within the sand dune system, Esperance, station C34. In a sequence of ~3 m thickness, a ferruginous sandstone is developed residual, composed of 60% silica and 40% goethite. Above the sandstone unit, two further units of sand units are developed, capped by an organic-rich soil.

Figure 19. Geochemical plots of major oxides and transition metals for the sequence from Fig. 18 (station C34). Units were analyzed for two grain size fractions: <1/250 mm and >1/250 mm, plotted in red and blue respectively. (A) Displays mirrored concentrations of silica and alumina for the >1/250 mm size fraction, whereas Fe is enriched in the ferruginous sand unit. (B) Transition metals are concentrated in the ferruginous unit, but still at lower values that UCC (Upper Continental Crust), whereas Au is concentrated in the sandy upper units.

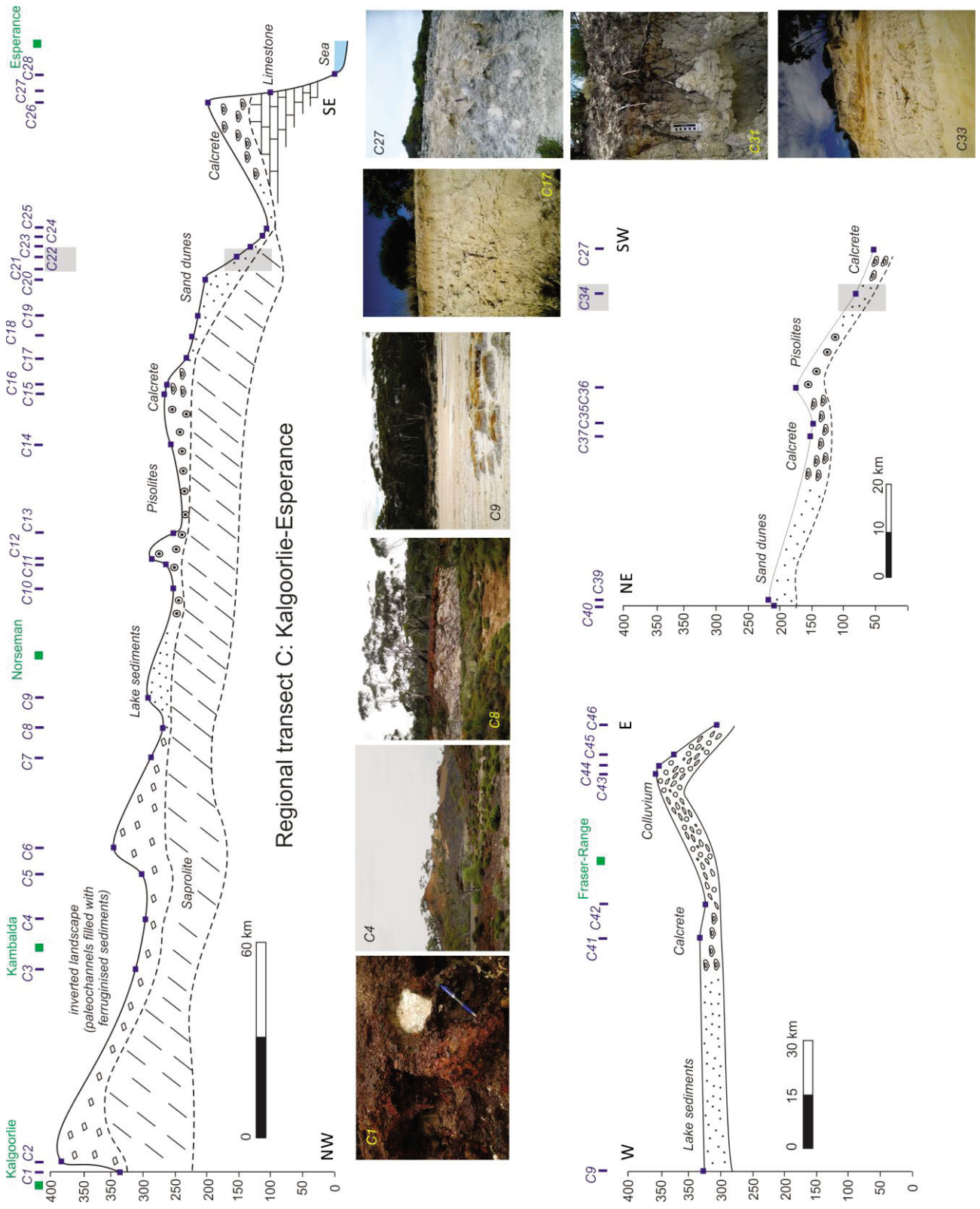
Regional transect C: Kalgoorlie-Esperance
Kalgoorlie
Kambalda
Norseman
Fraser-Range
Esperance
inverted landscape (paleochannels filled with ferruginised sediments)
Saprolite
Lake sediments
Pisolites
Calcrete
Sand dunes
Limestone
Sea
NW
SE
0 60 km
C1
C4
C8
C9
C17
C27
C31
C33
W
E
NE
SW
Colluvium
0 15 30 km
0 10 20 km

Figure 17.

Figure 18.

Ferruginous sandstone unit developed within the sand dune system, Esperance

Profile C, *Station C34*

Field observations

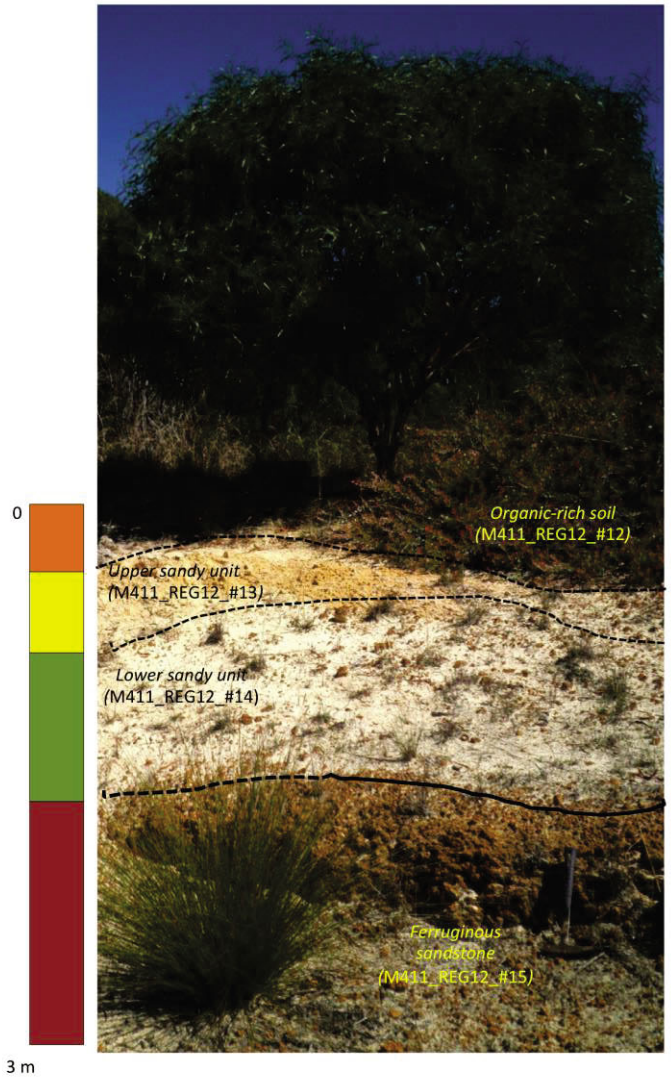

HyLogger analyses

Unit	*Quartz*	*Goethite*
Organic-rich soil	X	
Upper sandy unit	X	
Lower sandy unit	X	
Ferruginous sandstone		X

Mineralogy

99 % quartz and 1 % zircon, rutile and ilmenite

99 % quartz and 1 % zircon, rutile and ilmenite

99 % quartz and 1 % orthoclase, biotite, zircon, rutile and ilmenite

60 % quartz and 40% goethite

Petrography

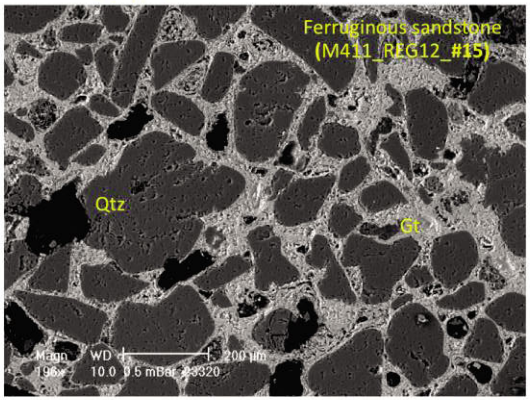

Figure 19.

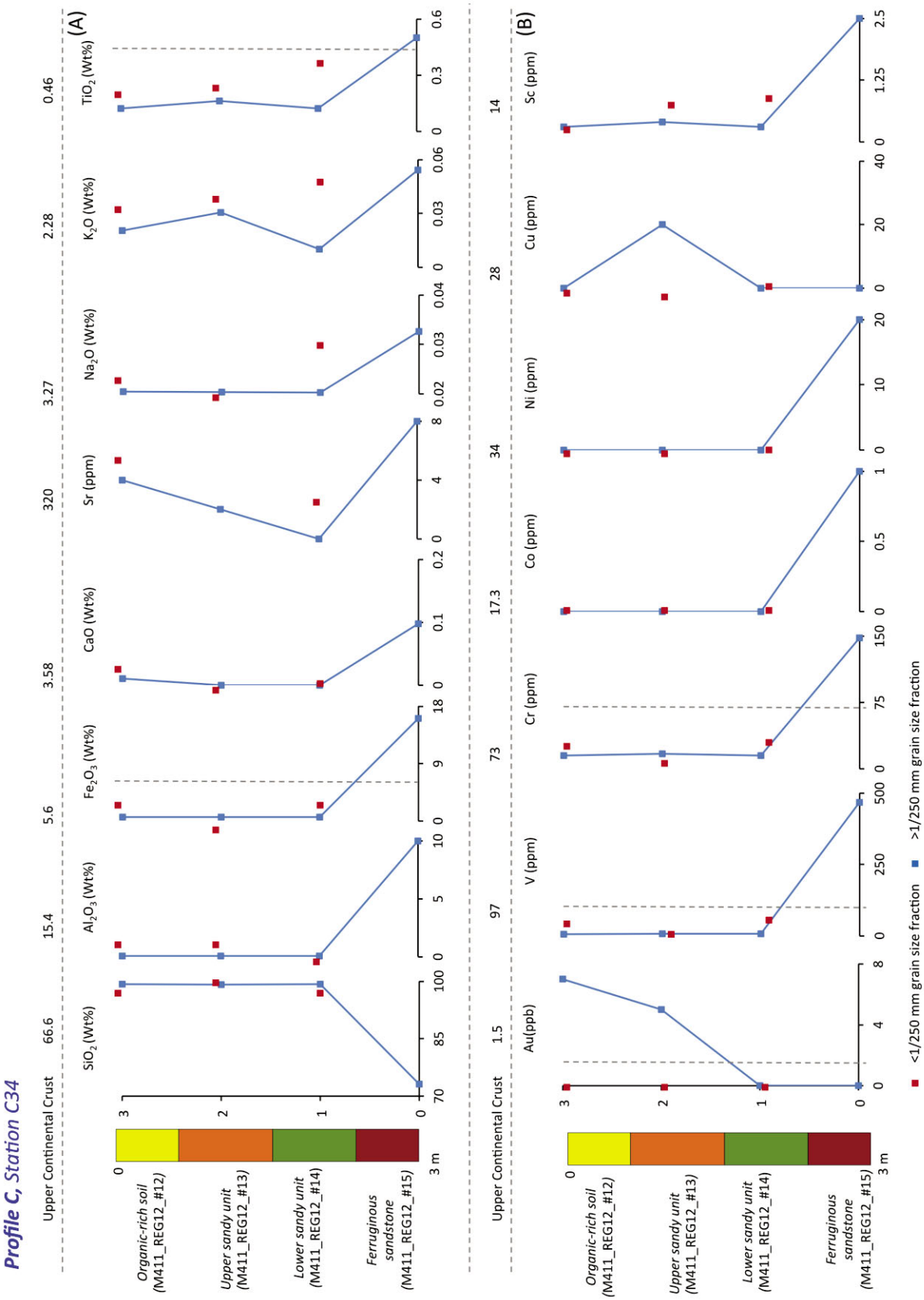
Profile C, Station C34
Upper Continental Crust
66.6
15.4
5.6
3.58
320
3.27
2.28
0.46
SiO2 (Wt%)
Al2O3 (Wt%)
Fe2O3 (Wt%)
CaO (Wt%)
Sr (ppm)
Na2O (Wt%)
K2O (Wt%)
TiO2 (Wt%)
(A)
Organic-rich soil (M411_REG12_#12)
Upper sandy unit (M411_REG12_#13)
Lower sandy unit (M411_REG12_#14)
Ferruginous sandstone (M411_REG12_#15)
3 m
Upper Continental Crust
1.5
97
73
17.3
34
28
14
Au(ppb)
V (ppm)
Cr (ppm)
Co (ppm)
Ni (ppm)
Cu (ppm)
Sc (ppm)
(B)
<1/250 mm grain size fraction
>1/250 mm grain size fraction

1.4 Contextualization of the data

1.4.1 Metal mobility: key variables

Mineral exploration protocols vary based on the chemical element targets (based on the ore or/and pathfinder minerals) and *media* sampled. When geochemistry is applied to soil or/and regolith exploration, sample collection strategies and data interpretation will vary significantly depending on trace element mobilities in the area explored. The following parameters should be defined through sampling to assist in data interpretation: (1) groundwater salinity; (2) soil pH-Eh; (3) average annual rainfall; and (4) geomorphology-sedimentary dynamics. This section presents a regional data compilation for these variables.

(1) The oldest geomorphological feature preserved in the Albany-Fraser Orogen/Yilgarn Carton margin is the palaeochannel network. Between the late Tertiary and Quaternary, semi-arid to arid climatic conditions were widespread throughout the Yilgarn. This resulted in the failure of major river systems, which turned into a sequence of lakes. At the same time, surface and groundwaters became increasingly saline.

Saline water is concentrated in areas with higher porosity within the river sedimentary sequences, and therefore can be used as a tracer in defining palaeochannels from groundwater salinity maps (Fig. 20). In large regions north-east of the Albany-Fraser Orogen, Commander (1989) recorded groundwater salinity values >35,000 g/L, that are interpreted to be associated with the confluence of large palaeochannels.

Hypersalinity has significant effects on the mobility of many trace elements within the regolith and their expression at surface, since element dispersion is driven mainly by the fluid conditions of salinity, acidity (pH) and oxidation-reduction potential (Eh). Differences in groundwater salinity require significantly different frameworks for the operation of geochemical methods and interpretations of surveys in different areas. Similarly, different protocols need to be considered for ground responses to technologies such as AEM.

(2) In addition to salinity, Fig. 21 presents a pH dataset from Gray (2001, unpublished CSIRO dataset) for groundwater. Acidic pH values are widely distributed in the Kalgoorlie-Norseman-Fraser Range-Esperance zone, as well as at the Beachcomber prospect and in the vicinity of Albany (Fig. 21).

Gold dispersion and mobility are strongly affected by local groundwater salinity and acidity as well as other transition metals and pathfinder elements (e.g., acidic oxidizing environments enhance the mobility of Au; e.g., Anand and Butt, 2010). This has a significant effect on both geochemical protocols for exploration, and the interpretation of data, since a diverse range of elements can be pathfinders or otherwise depending on their relative mobility (e.g., Anand and Butt, 2010). No regional data on Eh variability is available at present.

(3) Distribution and intensity of average annual rainfall, presented in Fig. 13, controls the recharge of the aquifers, and affects the salinity of the groundwater. Low rainfall, vegetation type and groundwater fluctuations are important factors in the formation and development of calcareous soils, which is important sample *medium* for Au. However, it is essential to distinguish between pedogenic calcrete (whether powdery, nodular to pisolitic, or massive) developed in the upper regolith from that developed on limestone, and/or marine sediments, since the latter may obscure or destroy any metal anomaly associated with the basement.

(4) In combination with the above, geomorphology and sedimentary/drainage dynamics are essential factors for the understanding of fluid flow and trace element redistribution and dispersion. Figure 22 displays valley elevations as gradients, derived from the Gallant and Dowelling (2003) algorithm. This algorithm describes the landscape-enhancing bottom features of valleys, which discriminates between uplands (dark grey colours) and lowlands (whiter colours).

The multi resolution index of valley bottom flatness (MrVBF) identifies areas that are low and flat relative to their surroundings and hence likely to have more accumulated sediment. Larger values of the MrVBF index indicate broader and flatter valley bottoms and hence thicker sediment deposits. This procedure has the potential to map the main depositional areas and describe geomorphological domains in relation to palaeovalleys and palaeochannels throughout the study area. It indicates the sedimentary dynamics of the area, and therefore where the thickest sedimentary packages could be expected, information that can lead to better interpretation of geochemical data by linking them to transported cover features and sedimentary dynamics.

In conclusion, any exploration protocol applied in the Albany-Fraser Orogen/Yilgarn Craton margin must account for the variability and combination of the groundwater salinity, pH-Eh, regional average annual rainfall and geomorphological-sedimentological dynamics of the area to optimize sampling and geochemical data interpretation.

Next pages:

Figure 20. Groundwater salinity map of Commander (1989). Palaeodrainage features present the highest saline concentrations.

Figure 21. Groundwater pH map based on data from Gray (2001, unpublished CSIRO dataset). Acidity or alkalinity of the groundwater table may determine the mobility of most elements utilized in mineral exploration, including dispersion of pathfinder elements.

Figure 22. Digital elevation model data presented after being filtered with the algorithm of Gallant and Dowling (2003) describing the landscape and enhancing the valley bottom features. Dark greys represent steeper areas. Light grey colours may indicate the presence of palaeochannels, which represent the flattest areas.

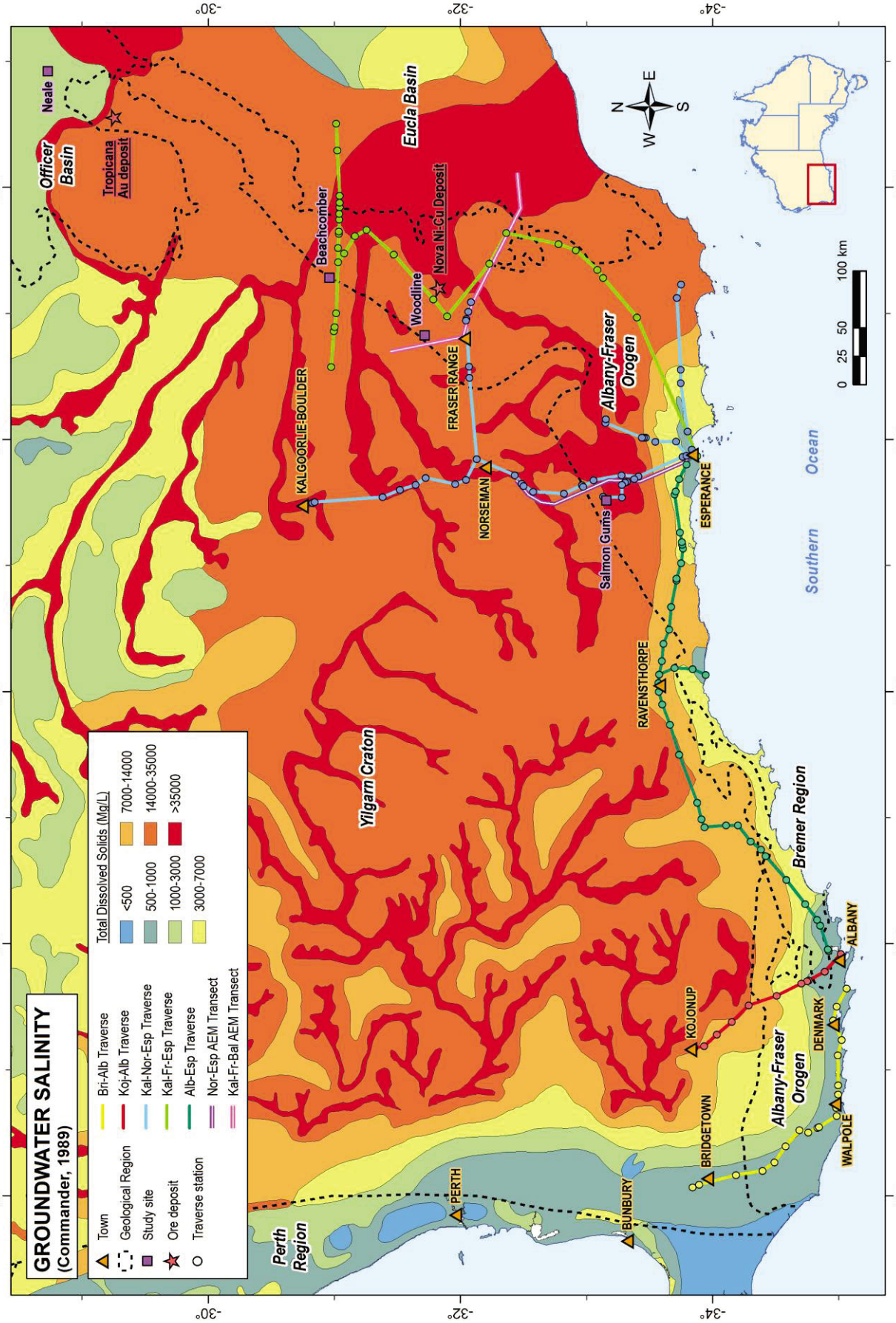
GROUNDWATER SALINITY
(Commander, 1989)
Town
Geological Region
Study site
Ore deposit
Traverse station
Bri-Alb Traverse
Koj-Alb Traverse
Kal-Nor-Esp Traverse
Kal-Fr-Esp Traverse
Alb-Esp Traverse
Nor-Esp AEM Transect
Kal-Fr-Bal AEM Transect
Total Dissolved Solids (Mg/L)
<500
500-1000
1000-3000
3000-7000
7000-14000
14000-35000
>35000
Officer Basin
Eucla Basin
Yilgarn Craton
Albany-Fraser Orogen
Albany-Fraser Orogen
Bremer Region
Perth Region
Southern Ocean
Neale
Tropicana Au deposit
Beachcomber
Woodline
Nova Ni-Cu Deposit
KALGOORLIE-BOULDER
FRASER RANGE
NORSEMAN
Salmon Gums
ESPERANCE
RAVENSTHORPE
KOJONUP
BRIDGETOWN
DENMARK
ALBANY
WALPOLE
BUNBURY
PERTH
116°
118°
120°
122°
124°
-30°
-32°
-34°
N
S
E
W
0 25 50 100 km

Figure 20.

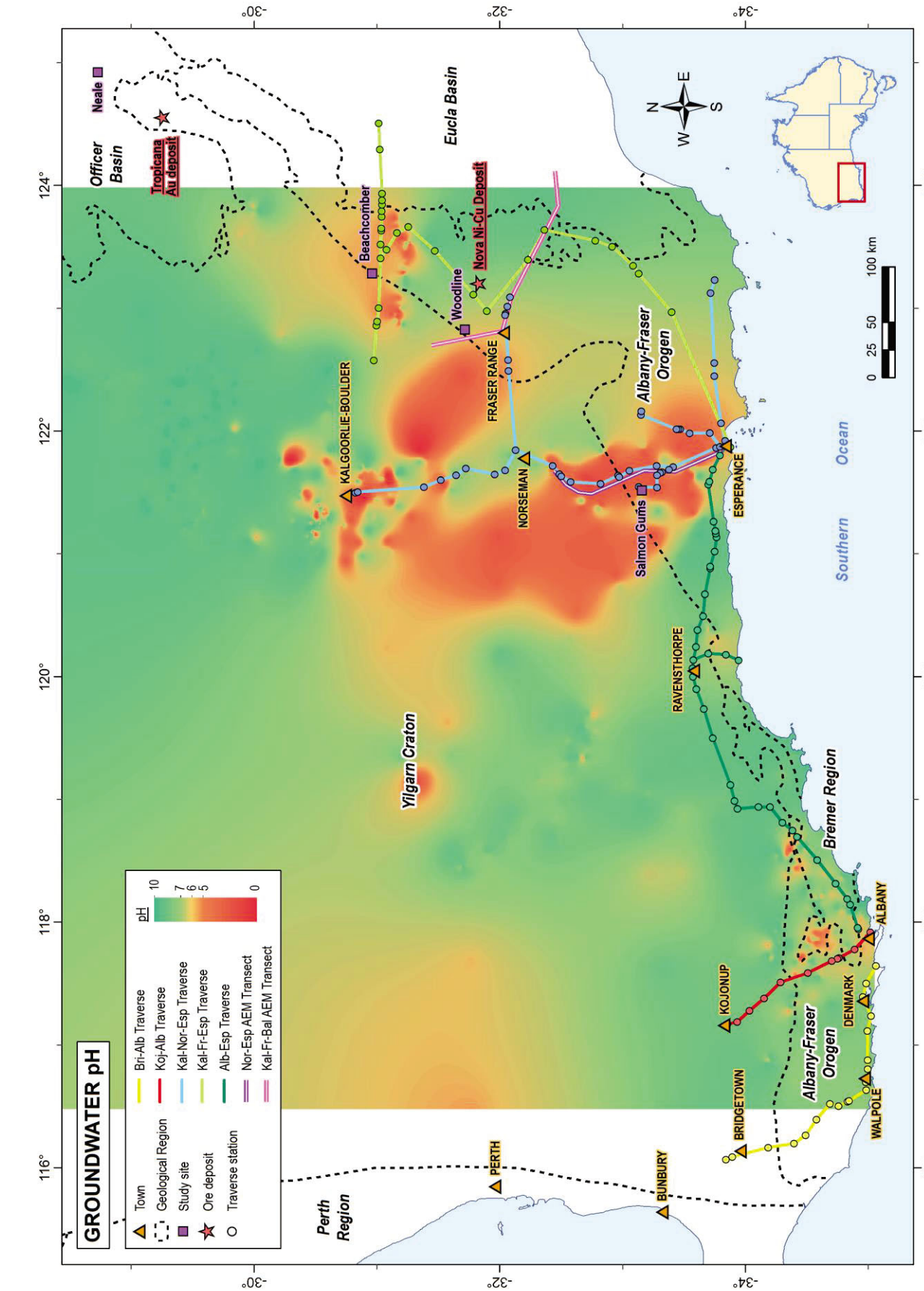
GROUNDWATER pH
pH
10
7
6
5
0
Town
Geological Region
Study site
Ore deposit
Traverse station
Bri-Alb Traverse
Koj-Alb Traverse
Kal-Nor-Esp Traverse
Kal-Fr-Esp Traverse
Alb-Esp Traverse
Nor-Esp AEM Transect
Kal-Fr-Bal AEM Transect
Officer Basin
Eucla Basin
Yilgarn Craton
Albany-Fraser Orogen
Bremer Region
Perth Region
Southern Ocean
Neale
Tropicana Au deposit
Beachcomber
Woodline
Nova Ni-Cu Deposit
KALGOORLIE-BOULDER
FRASER RANGE
NORSEMAN
Salmon Gums
ESPERANCE
RAVENSTHORPE
KOJONUP
BRIDGETOWN
DENMARK
ALBANY
WALPOLE
PERTH
BUNBURY
0 25 50 100 km
N
S
E
W
116°
118°
120°
122°
124°
-30°
-32°
-34°

Figure 21.

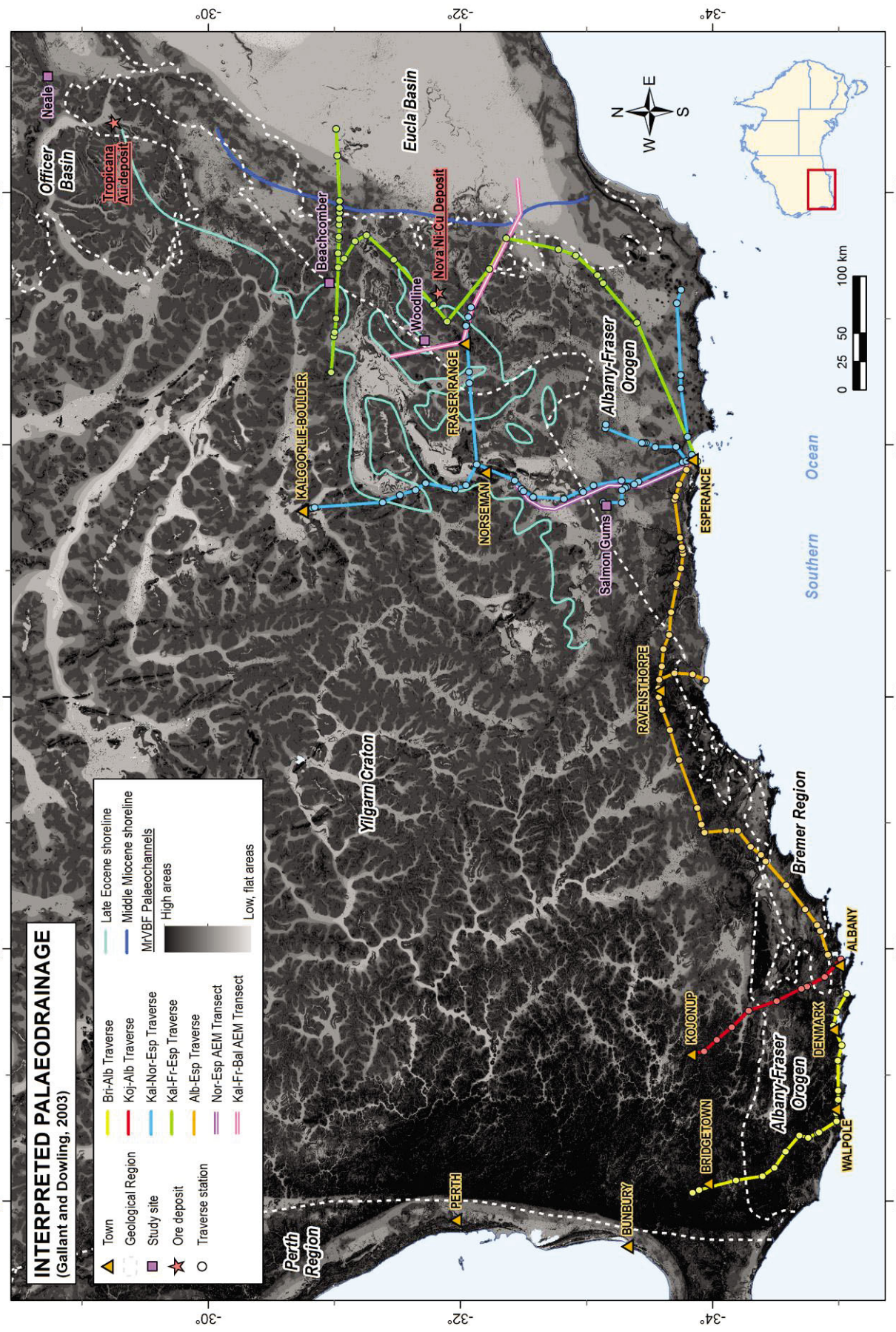
INTERPRETED PALAEODRAINAGE
(Gallant and Dowling, 2003)
Town
Geological Region
Study site
Ore deposit
Traverse station
Bri-Alb Traverse
Koj-Alb Traverse
Kal-Nor-Esp Traverse
Kal-Fr-Esp Traverse
Alb-Esp Traverse
Nor-Esp AEM Transect
Kal-Fr-Bal AEM Transect
Late Eocene shoreline
Middle Miocene shoreline
MrVBF Palaeochannels
High areas
Low, flat areas
Officer Basin
Eucla Basin
Yilgarn Craton
Albany-Fraser Orogen
Bremer Region
Perth Region
Southern Ocean
Neale
Tropicana Au deposit
Beachcomber
Nova Ni-Cu Deposit
Woodline
KALGOORLIE-BOULDER
FRASER RANGE
NORSEMAN
Salmon Gums
ESPERANCE
RAVENSTHORPE
KOJONUP
BRIDGETOWN
DENMARK
ALBANY
WALPOLE
BUNBURY
PERTH
0 25 50 100 km
116°
118°
120°
122°
124°
-30°
-32°
-34°

Figure 22.

1.4.2 Sea-level changes

The most significant complexity from the point of view of mineral exploration in the AFO is understanding the data collected from the regolith cover sequences. In addition to the challenges posed, and approaches developed for the Yilgarn Craton (e.g., Anand and Butt 2010 and references therein), an additional key element is the development and deposition of regional overburden by sea-level changes during the last ~65 Ma (e.g., Haine et al., 2010).

Transgressive-regressive cycles affecting coastal areas produced variations in basin architecture that significantly affected sedimentation: (1) during transgression events, transgressed weathered areas were eroded and became flattened by wave action; (2) sediment produced by sea erosion on the "platform" was redistributed along the new shoreline; (3) new exotic marine sediment could be deposited by coastal currents; (4) different chemical sediments such as carbonates were deposited subaqueously; and (5) sediments derived from continental drainage catchments play only a minor role, since ocean transgression may overcome fluvial erosional processes (Fig. 23).

When sea-level drops, a new sedimentary dynamic results. This results in a rejuvenation of the residual weathering profile and the deposition of a new sequence of marine sediments. The active drainage networks on land are reactivated by the increased gradient, resulting in larger volumes of sediment transported to the new shoreline by rivers that cut deeper and further into their upper catchment zones (Fig. 23). This complicated sedimentary pattern mixes the different geochemical footprints of the continental-derived sediments (inland geochemical signatures), the residual weathering profile of the AFO, and the marine limestone.

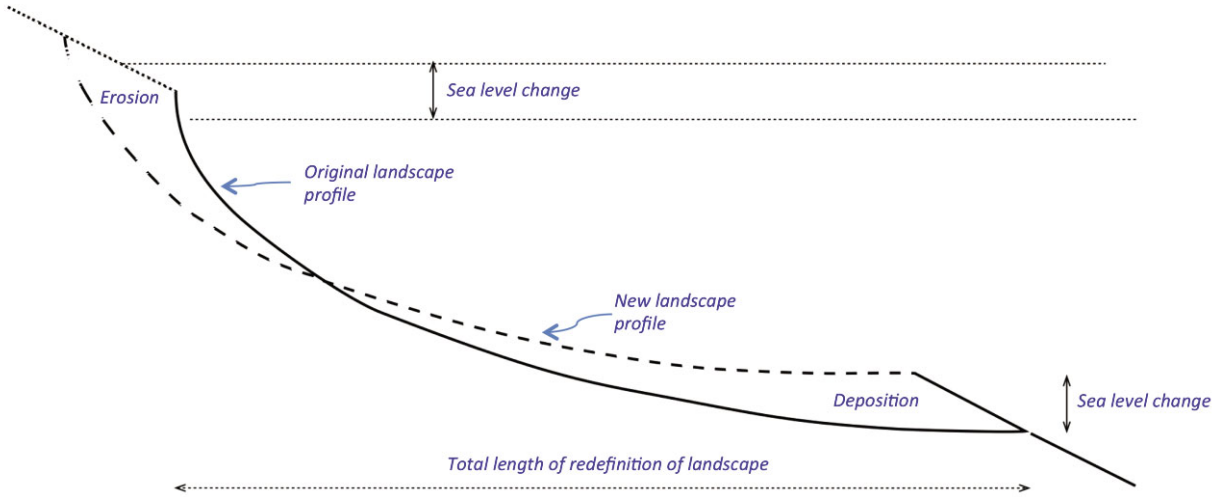

Figure 23. Schematic modelling of the changes in the sedimentary/erosional dynamics produced by sea-level changes in any landscape.

In the last ~65 Ma sea-level changes (Figs. 24 and 25) ranged from +100 m down to -50 m relative to the present. This is referenced to the actual sea-level high, when large areas of the Albany-Fraser Orogen/ Yilgarn Craton margin were flooded and drained, distributing limestone deposits and exotic marine sediments. The mixing of Yilgarn sediments during sea-level regressions followed this event.

Three main periods for sedimentation are identified: (1) Middle to Late Eocene; (2) Middle Eocene-Early Pliocene; and (3) Quaternary, coupled with three stages of main weathering alteration: (1) Cretaceous-Early Eocene, (2) Oligocene-Early Miocene, and (3) Late Pliocene (Hou et al., 2008).

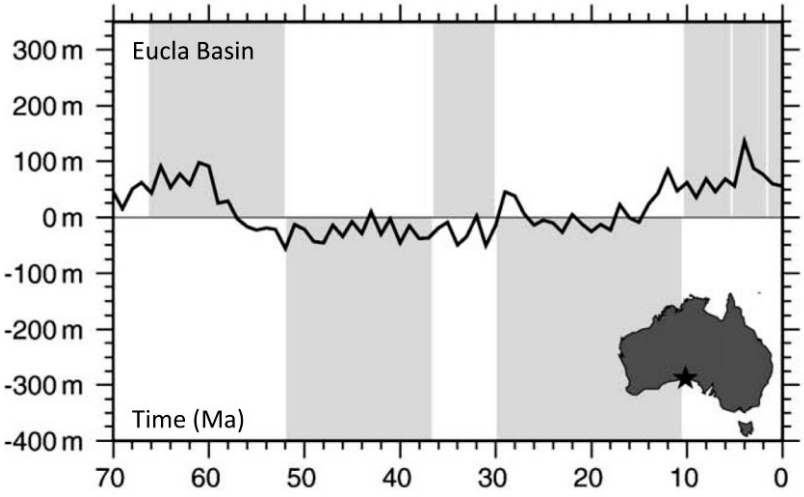

Figure 24. Elevation history relative to sea-level of wells in Australia, integrating dynamic topography, plate kinematics and eustatic sea-level correction. Grey rectangles below 0m elevation indicate flooding, and above 0m indicate exhumation for the marked location at the indicated time (Heine et al., 2010 and references therein).

This resulted in erosion of the residual regolith, redistributing sedimentary cover and mixing the transported cover with marine sediments and Yilgarn and Albany-Fraser sediments. This has substantial implications for mineral exploration, and specifically for interpretation of regolith geochemical signatures.

This mixing of sediments in the transported cover leads to the potential generation of numerous false geochemical anomalies due to mechanical or chemical concentrations of metals unrelated to any mineralization in the local basement rocks. In addition, the lower residence time of sediment after deposition can result in less vertical dispersion of trace element and, therefore, the absence of valuable surface geochemical anomalies.

This underscores the importance of the interpretation of the geomorphological landscape to target the most appropriate *medium* for geochemical sampling, and to understand the significance of the element anomalies reported.

The calcrete horizons within the transported sand packages, such as those at Salmon Gums described above, and the ferruginous sandstone within the transported sand dune packages identified in the Esperance setting, become of fundamental importance for mineral exploration. In addition, abundant Middle Eocene spicular sandstones were widely deposited along the marginal marine areas, tidal-estuarine environments and drowned palaeovalleys (Clarke et al., 1996; Hou et al., 2008). In addition, carbonate units were deposited within the marine-flooded palaeovalleys, where they were protected from the higher energy environment of the open marine zone.

Marine transgressions during the Middle and Late Eocene in the south-east margin of the Yilgarn Craton have been suggested to be drivers of deep weathering associated with acid leaching, and in determining the age, style and distribution of metal traps within the regolith (Worrall and Clarke, 2004).

1.5 Conceptual regolith framework: tracking anomalies and implementing exploration protocols

The regolith of the Albany-Fraser Orogen/Yilgarn Craton margin displays a complex variability in total thickness and distribution of transported cover. Marine transgressions and regressions, and their associated erosional action over the platform, do not produce a smooth large scale down dip slope of the platform towards the sea (Appendix A).

The Albany-Fraser Orogen has different drainage patterns to those on the Yilgarn Craton (Fig. 22) due to the influence of repeated sea-level changes (Figs. 23 and 24). The Yilgarn Craton drainage patterns are typical dendritic river-like patterns, whereas in the Albany-Fraser these patterns are blurred without a main drainage direction. However, topographically higher areas, >100-150m above sea-level, display similar drainage patterns to the Yilgarn Craton (Appendix A). They also have thicker saprolite (Appendix A) and beach deposits are only found on some of the slopes (Appendix A). These observations are consistent with a disrupted transgression, where the land remained emergent and was not covered or was much less affected by erosion and sedimentation than most of the flooded inland areas.

Positive relief of the landscape can be produced by the ferruginization of channel deposits, which produce inverted landscapes after erosion (e.g., Anand and Butt, 2010). Such inverted landscapes are not reported south of Norseman (Appendix A).

A preliminary understanding of the effects of diverse regression-transgression cycles on the geomorphology and sedimentary dynamics of the area can be obtained by considering the consequences of inundation of the present relief by incremental rises of sea-level rise (Fig. 25):

(1) In a transgression with a 100 m rise of sea-level, the coastline would be similar to the present in the east and north-east, whereas, in the south-west, large estuaries and shallow bays would develop (Fig. 25A);

(2) For a 150 m sea-level rise, the east-north-east coast line becomes complex, and would be dominated by an archipelago up to ~50 km long. In the south-west, the bays widen (Fig. 25B);

(3) For a 225 m rise, a large complex of island-peninsulas and estuarine areas would be developed to the south-east of the Fraser Range (Fig. 25C);

(4) For a rise of 275 m, the sea floods the large tracts around Norseman; these would be protected from marine erosion and favour deposition of cool-water carbonate deposits. This scenario is consistent with the formation of the carbonate sediments of Norseman Formation (Clarke et al., 1996).

Next page:

Figure 25. Theoretical sea-flooding of the AFO at (A) +100 m, (B) +150 m, (C) +225 m and (D) +275 m above the present sea-level. Continental tilting of the block has not been taken into account.

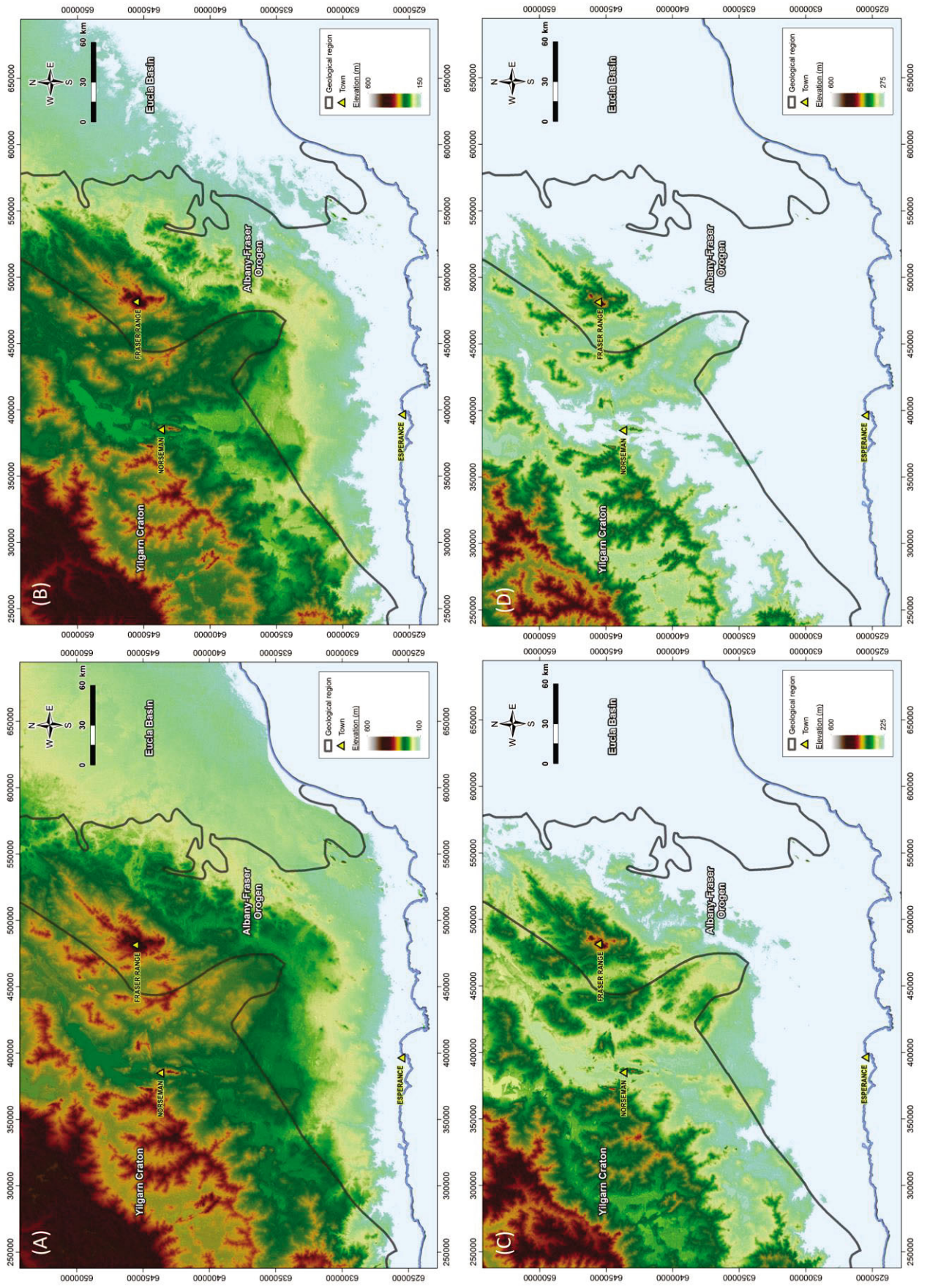
(A)
(B)
(C)
(D)
Yilgarn Craton
Albany-Fraser Orogen
Eucla Basin
FRASER RANGE
NORSEMAN
ESPERANCE
Geological region
Town
Elevation (m)
600
100
150
225
275
0
30
60 km
N
S
E
W
250000
300000
350000
400000
450000
500000
550000
600000
650000
6250000
6300000
6350000
6400000
6450000
6500000

Figure 25.

Based on the integration of field observations presented in this study with the theoretical effect of the sea-level rises, the conceptual model proposed for the Albany-Fraser Orogen/Yilgarn Craton margin is the evolution of a coastline-dominated marine environment with drowned palaeovalleys, abundant islands, and estuarine zones (Fig. 26), where extensive erosion, sedimentation and saprolite formation took place in three main phases of transgression and emergence.

Figure 26. Graphic regolith framework suggested for the Albany-Fraser Orogen/Yilgarn Craton margin (Image from the Broken Group Islands, Western Vancouver Island, Canada; www.uclueletwildpacific.com/vslideshowucluele tbrokengroupislands.html). A combination of a main shoreline, islands and estuarine areas are suggested to have been partly responsible for regolith depth and variability in distribution in the region.

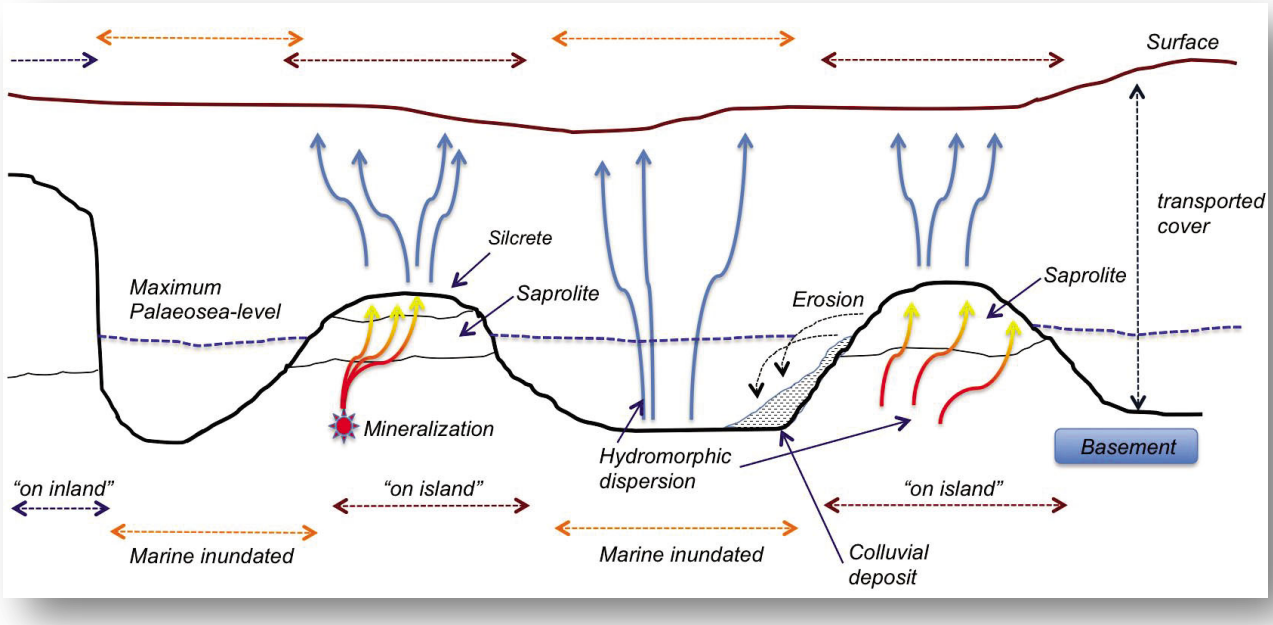

Figure 27. Sketch of the effect of marine transgressions and regressions generating "on inland" and "on island" areas together with "marine inundated" zones, and its implications for vertical trace element dispersion for the geochemical signature of the basement. Vertical and horizontal scales may vary from 100 m to 10 km.

This island-coastline geomorphological scenario has substantial implications for greenfields and brownfields mineral exploration. Geochemical exploration *medium* and interpretation of the landmasses inland, or on islands, should be treated and approached differently from those with a flat marine inundated landscape, reworked by wave action, with a more diverse sedimentary provenance.

"On inland" and "on island" weathering profiles may vary in maturity and saprolite development, with or without transported cover derived from exotic marine sediments and/or limestones, and also with contributions from sediments of the Yilgarn Craton. Such areas are more reliable for understanding geochemical anomaly - basement relationships, whereas the "sea-flooded" areas require a more thorough and detailed investigation due to the mixing of sediment sources, mechanical dispersion, rejuvenated weathering profiles and short-term vertical element dispersion processes (Fig. 27).

1.6 Implications for mineral exploration

Based on the results of this study, at least six significant implications for mineral exploration were discovered, which may contribute to a more effective utilization of geochemical exploration datasets obtained from drilling in this region, and towards more effective regional exploration targeting:

(1) Four different regolith settings with diverse regolith architecture have been defined: the Albany, Kalgoorlie-Norseman, Esperance and Neale settings. Mineral exploration protocols, sampling *medium* and interpretation of geochemical data should be carefully linked with the characteristics of the regolith-landform setting.

(2) Deep weathering profiles will present obstacles to metal mobility from the basement due to transported cover and the depleted section of the upper saprolite (Kalgoorlie-Norseman and Neale settings); whereas "rejuvenated" regolith profiles, lacking the depleted upper saprolite and/or thin transported cover, will require shallower drilling to sample the basement and will present thinner regolith horizons for vertical metal dispersion (Albany and Esperance settings).

(3) Any geochemical sampling, data interpretation and remote sensing techniques applied in the region should be put in context and, their efficiency evaluated within regional datasets, including data regarding groundwater salinity, pH-Eh, average annual rainfall and local geomorphological-sedimentary environments.

(4) In the Esperance setting post-depositional units of ferruginous sandstone occur within the transported sand dune packages. This horizon accumulates transition metals (V, Cr, Co, Cu, Ni and Sc), whereas Au is anomalous in the upper sandy units.

(5) Calcrete horizons are produced within the transported sand packages, such as at Salmon Gums (Esperance setting). Element dispersion within the transported sand packages concentrates Au within the calcrete horizon and transition metals (V, Cr, Co, Ni and Sc), in the overlying sand unit. The post-depositional pisolitic carbonate unit within the modern sand dune system is an excellent sample *media* for exploration purposes.

(6) The regolith framework is the result of the evolution of a coastline with numerous islands and estuarine areas, where extensive erosional processes, sedimentary deposition and saprolite development took place.

(7) “On inland” and “on island” weathering profiles may vary in maturity and saprolite development, with or without a transported cover derived from exotic marine sediments and/or limestones, and also from sediments of the Yilgarn Craton. Such areas are more reliable for understanding geochemical anomaly - basement relationships, whereas the marine inundated areas would require a more thorough and detailed investigation as a result of sediment mixing, mechanical dispersion, rejuvenated weathering profiles and short-term vertical element dispersion processes.

(8) Mapping the palaeocoastlines, coupled with the islands and estuarine zones, and the extension of the marine limestone/sediment influence inland, would have an extensive impact on more efficient planning and interpretation of exploration campaigns and their results in the region.

2 Calcrete Au anomaly: the displaced anomaly at Woodline *(Appendix B)*

Summary

The Woodline Project (owned by Sipa Resources) is located in the southern Albany-Fraser Orogen, an underexplored area lying to the east of the Yilgarn Craton about 110 km north-east of Norseman, comprising a number of Au prospects including Leucippus, Theofrastos and Heraclitus. The principal objective of this project was to understand the distribution of Au in the soil and to interpret the formation of Au anomalies in calcrete at Leucippus, some of which are displaced from areas of known mineralization.

A regolith-landform map was constructed using field data, aerial photography and other imagery (e.g., DEM). Regolith stratigraphy of a transect selected across Leucippus indicated that marine sediments (spongolite) up to 14 m thick were present in an inverted landscape. This transect crossed Au mineralization and had a significant (*maximum* 27 ppb), but displaced, Au in calcrete anomaly. The presence of a weak (<200 ppb Au) supergene Au layer was interpreted at about 30 m depth near the current water table with higher grades (>1 ppm) in saprolite beneath this.

A series of profiles were selected primarily based on Au data from a calcrete survey and drill hole data previously undertaken by Sipa; four profiles were selected across the transect. A series of 2 m pits were dug to access the soil profiles. This enabled detailed sampling (at 10 cm intervals), photography and description. Multi-element geochemistry (including Au and a suite of 57 other elements) and X-ray diffraction (XRD) was done on the bulk profile samples.

A number of interesting results were found:

1) Gold is very closely associated with calcrete in the soil profile; calcrete was ubiquitous;

2) The displaced Au in calcrete anomaly on the Leucippus transect was located in younger colluvium overlying Tertiary marine sediments. As there was no Au beneath the surficial anomaly the most likely explanation is that it was transported to this position;

3) The absence of an anomaly over mineralization on the Leucippus transect was due either to ongoing erosion of material (containing accumulated Au), or the weakness and/or depth of the mineralization itself; and

4) Other elements (e.g., Ni) were anomalous over mineralization at Leucippus, some of which were related to the presence of Mn oxides.

The results showed that some Au in calcrete anomalies is transported. Care should be taken when sampling calcrete and soil, and in interpreting the data. The highest Au concentrations are not at the surface but are located a few tens of centimetres below this where the calcrete is more abundant. A number of recommendations are made for further studies in this area.

2.1 Introduction

Within the Kalgoorlie-Norseman margin setting, the Woodline Au project (Sipa Resources) located ~110km north-east of Norseman (Fig. 28), was selected to understand the formation of Au anomalies in calcrete displaced from mineralization in the region. This anomaly was explained previously by exploration in the area as residual. Results from this study indicated a transported anomaly in younger colluvium overlying Tertiary marine sediments, with no Au mineralization beneath.

Calcrete is widely used a sample *medium* for Au exploration in the Eastern Goldfields and the Gawler Craton, in particular. Calcrete is a generic name applied to pedogenic carbonate commonly consisting of calcite and/or dolomite. It is formed as a result of accession of salts of marine origin through dust, aerosol and meteoric processes with minor contributions from local bedrock (Lintern et al., 2006).

In the soil the alkaline earth metals combine with CO_2 produced by respiration, and through pedogenic processes carbonate accumulates in specific and predictable horizons with the soil profile. This vadose calcrete is distinguished from groundwater calcrete formed by phreatic processes related to high water tables and evaporation.

The Woodline calcrete study was undertaken at Leucippus, Heraclitus and Theofrastos prospects at the Woodline project area (Fig. 28).

Calcrete at the Woodline project prospects is ubiquitous and occurs in various forms. Calcrete samples were uncovered residual from soil profiles by excavation using a back hoe. The exposure of the undisturbed calcrete profile in this way enabled detailed photography, documentation and subsequently, precise sampling. It enabled the examination of the inter-relationship between calcrete, other soil components, landscape and mineralization. Sipa Resources provided a database including Au in calcrete data, mineralization and location of drill holes.

A specific question addressed at the Woodline for this Chapter is: why are some calcrete anomalies displaced from mineralization rather directly above it? This is not a problem unique to the Albany-Fraser Orogen (e.g., Lintern et al., 2011). An example of this “transported anomaly” was found at Leucippus and was specifically addressed by this study. Briefly, an anomalous mineralized Au corridor, orientated in a north-west/south-east direction, at Leucippus has a Au in calcrete anomaly associated with it, which is displaced to the east. There appears to be low Au concentrations in calcrete directly over the mineralized corridor.

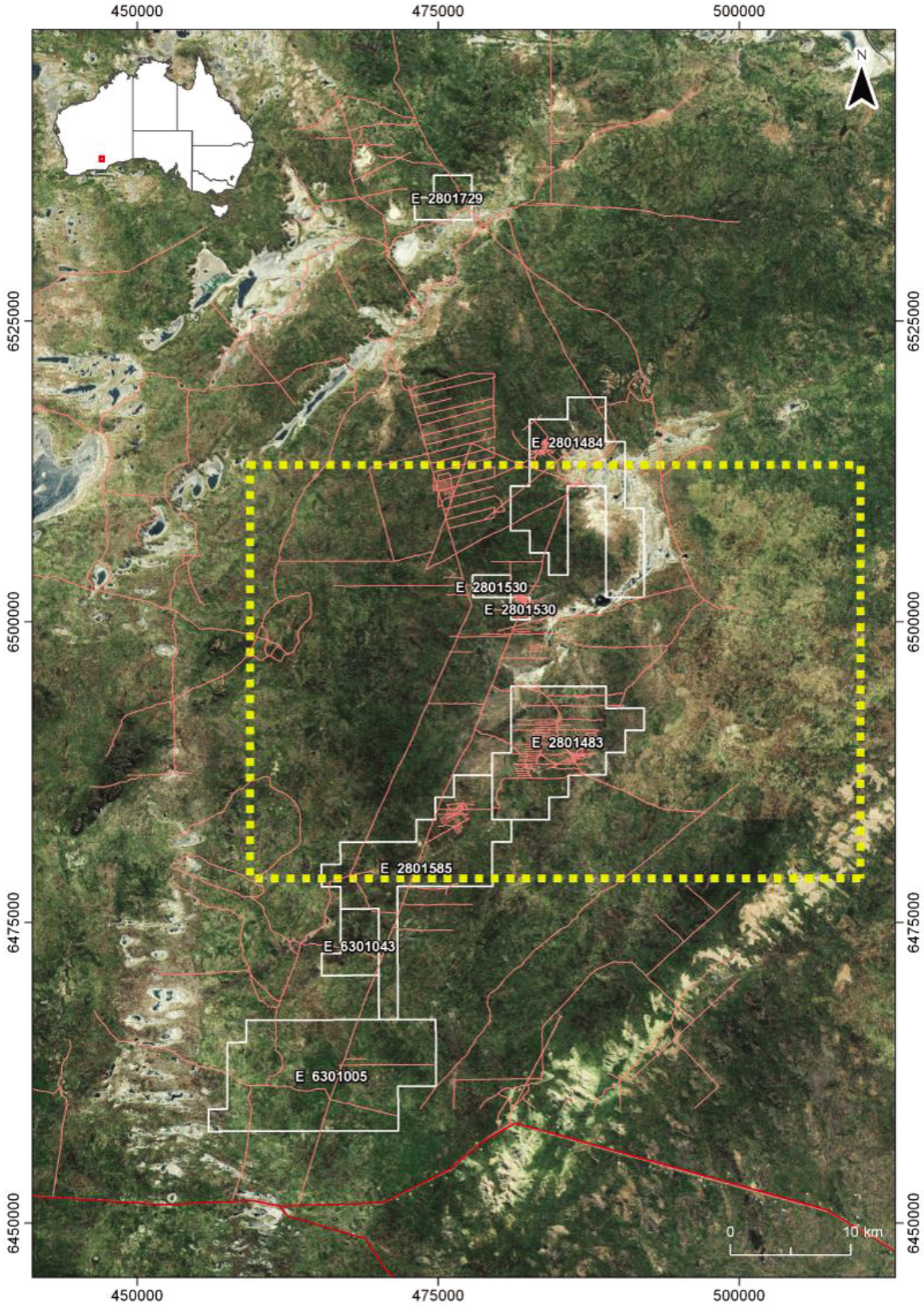

Figure 28. Location plan with named prospects and exploration leases for the Woodline project (Sipa Resources). The yellow box marks the area focused on by study. Image courtesy of Sipa Resources.

The general relief of the Woodline area is from 250-400 m ASL (Figs. 29 and 30). The landscape consists of hill tops, hillslopes and plains. Vegetation communities are strongly related to landform, although general observations of these were restricted to the access roads. Woodlands of Eucalyptus, Acacia and Casuarina dominate the hill tops, slopes and calcareous plains (except for the clay pans which had sparse vegetation cover) and vary in height (some up to 15 m). An understorey of shrubs including perennial grasses and herbs were noted beneath the woodland, together with small trees and larger shrubs (Fig. 31).

Norseman has hot, dry to humid summers and mild, dry to moist winters. The nearest climate recording station is at Norseman. Rainfall is 289 mm spread evenly throughout the year (Bureau of Meteorology website, 2012). More reliable rainfall occurs in winter, and irregular large amounts may fall in summer as a result of rain-bearing depressions sourced from north-west Australian cyclonic activity. Mean highest, *maximum* daily, mean lowest and *minimum* daily temperatures recorded are 32.4°C, 45.6°C, 17.3°C and 10.1°C, respectively.

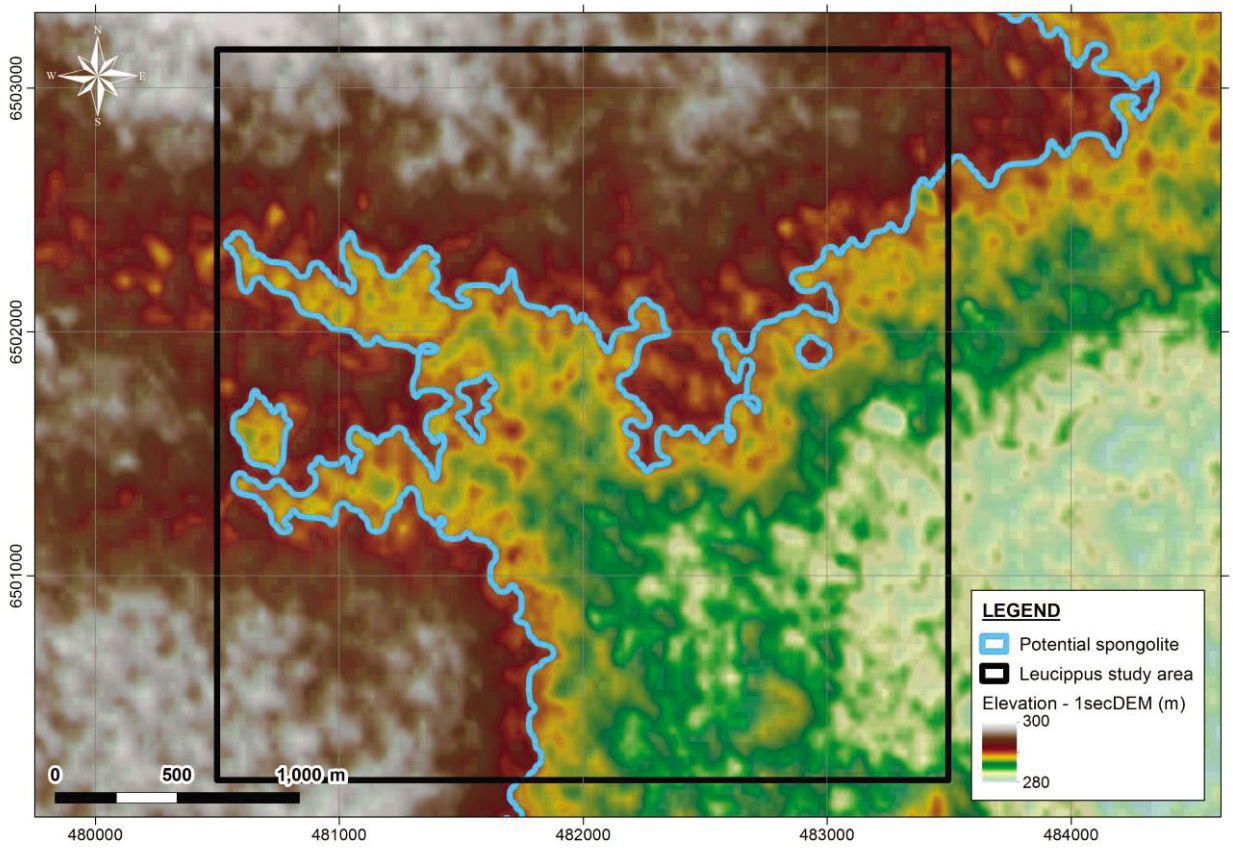

Figure 29. Regional DEM of the Woodline area showing location of Leucippus, Theofrastos and Heraclitus prospects. The boxed area outlines the regolith map study area at Leucippus.

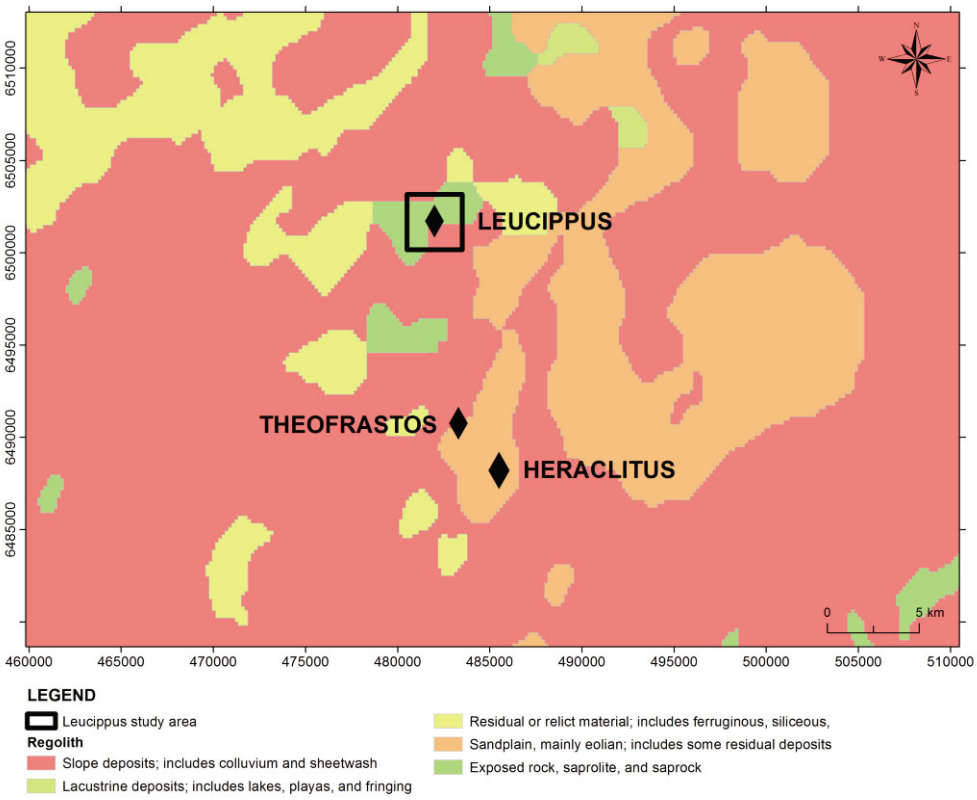

Figure 30. Regolith-landforms of the Woodline area (data courtesy of Sipa Resources).

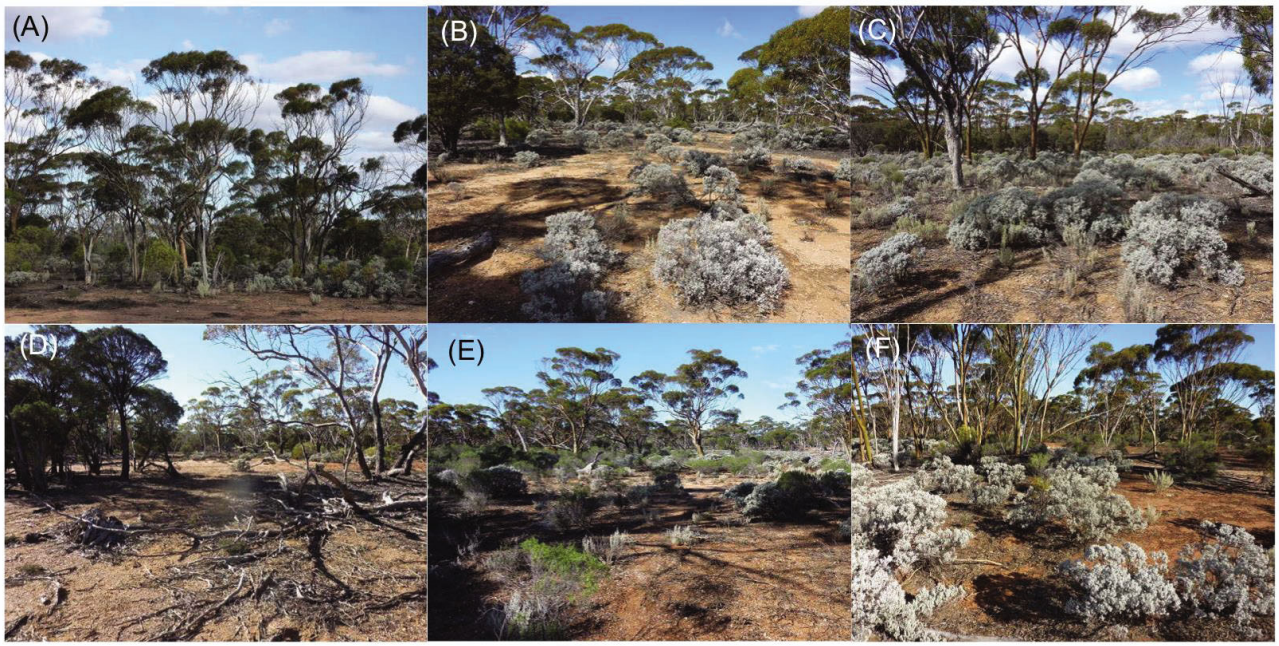

Figure 31. Landscape images from Woodline showing the stature of the vegetation. (A) Salmon gum woodland (485521E 6488214N); (B) mixed eucalypt woodland with false bluebush (483310E, 6490777N); (C) Gimlet with false bluebush (486393E, 6488591N); (D) mixed eucalypt and melaleuca woodland (482297E, 6501806N); (E) Salmon gum woodland (482023E, 6501816N); and (F) Gimlet with false bluebush (481779E, 6501810N).

2.2 Calcrete geochemistry (Sipa Resources data)

Gold concentrations range from less than detection limit (1 ppb) to an outlier of 300 ppb in the Leucippus study area. The highest concentrations of Au are generally in the >20 ppb. Gold concentrations in calcrete are negatively skewed (Fig. 32). Two areas are anomalous in Au and are highlighted in the hotter colours. The central area is centred on a rise that is at least partly underlain by alluvium-colluvium overlying spongolite (Figs. 33, 34, 35 and 36). Separating the two areas is an S-shaped east-west drainage channel. This drains from the north-west of the image to the south-east. The anomalous area in the south-west is also on a rise but has not been investigated as part of this project. It is recommended that a thorough statistical appraisal of the Sipa Au in calcrete data is undertaken if it has not been already undertaken.

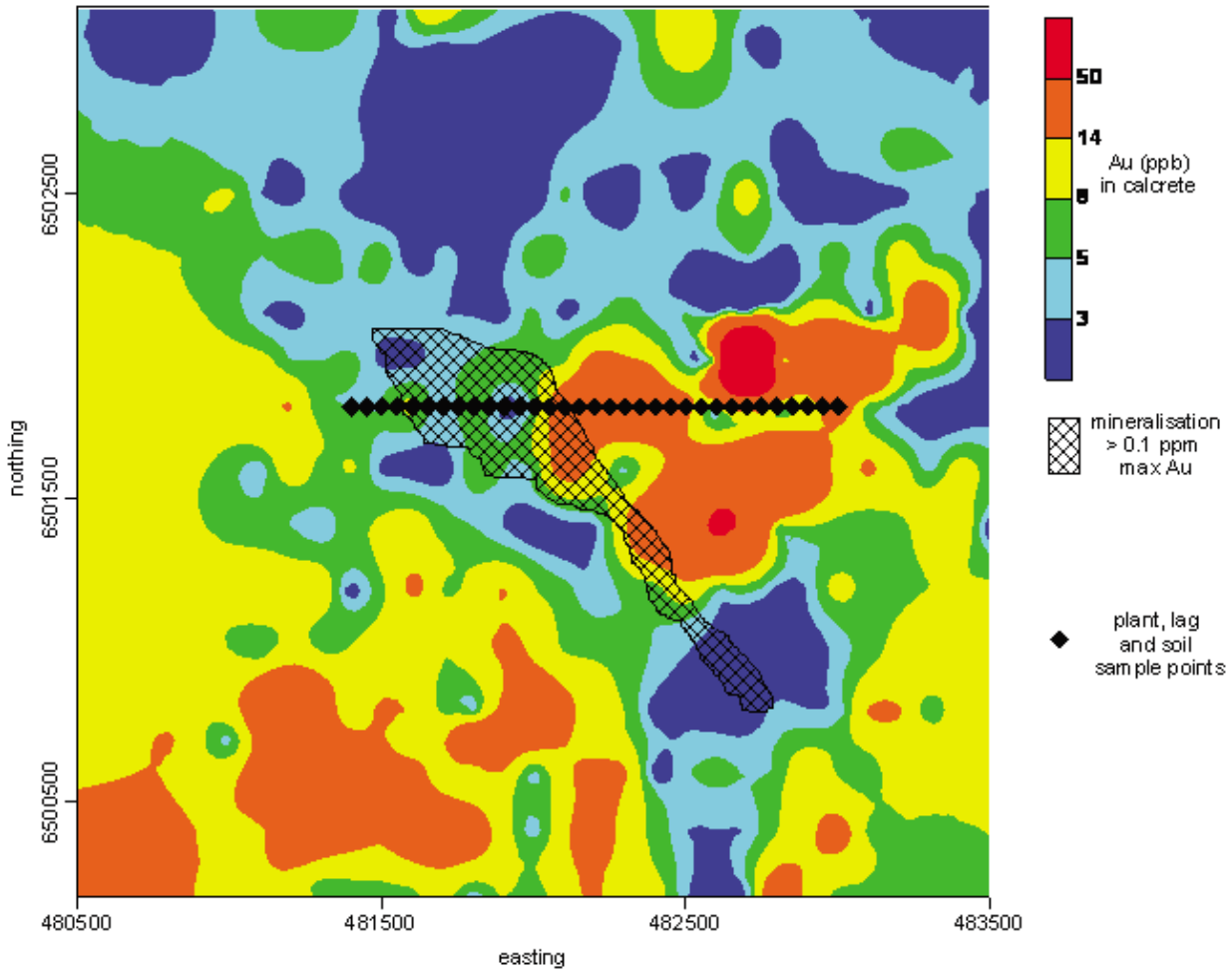

Figure 32 Location of sampling at Leucippus in relation to mineralization and Au in calcrete anomalies. Calcrete data (supplied by Sipa Resources) was kriged. Outline of mineralization was interpreted from data supplied by Sipa Resources.

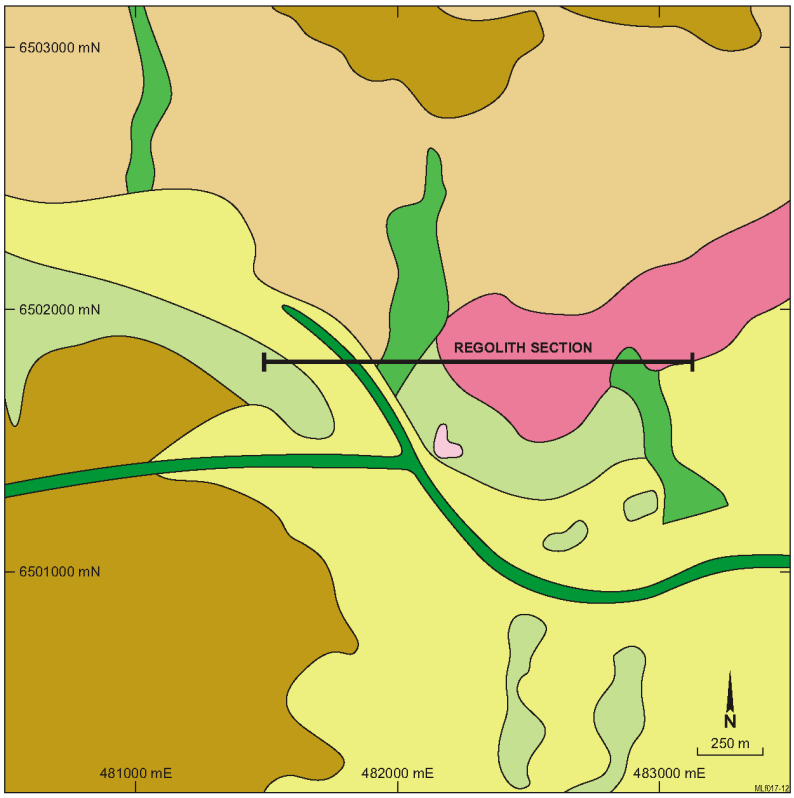

Figure 33. Regolith transect cross-cutting different geological units and the surface Au anomaly (as above).

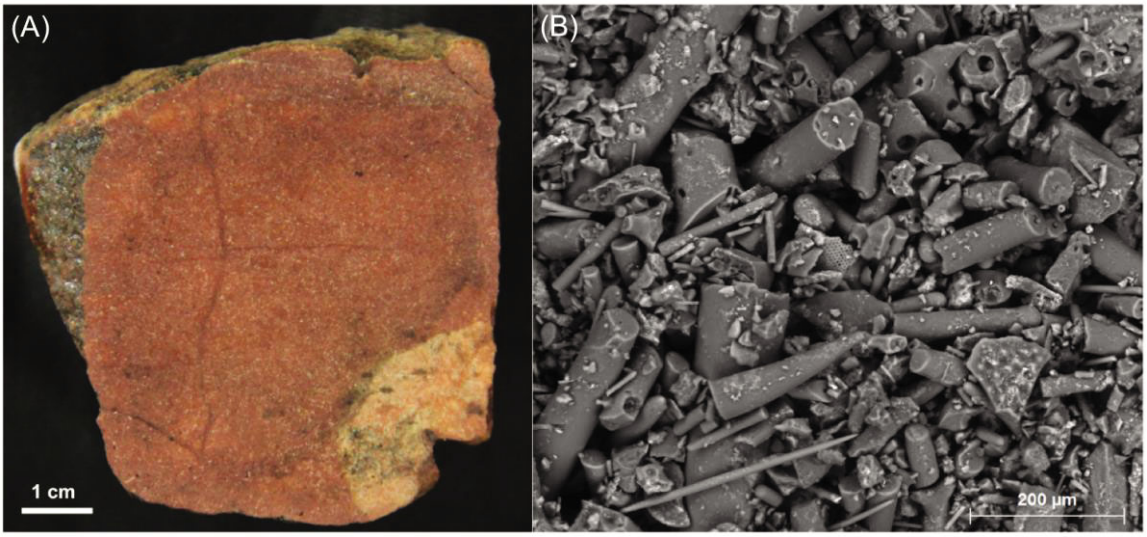

Figure 34. Spongolite images: (A) from a rock sample and (B) SEM image of spongolite from drill cuttings.

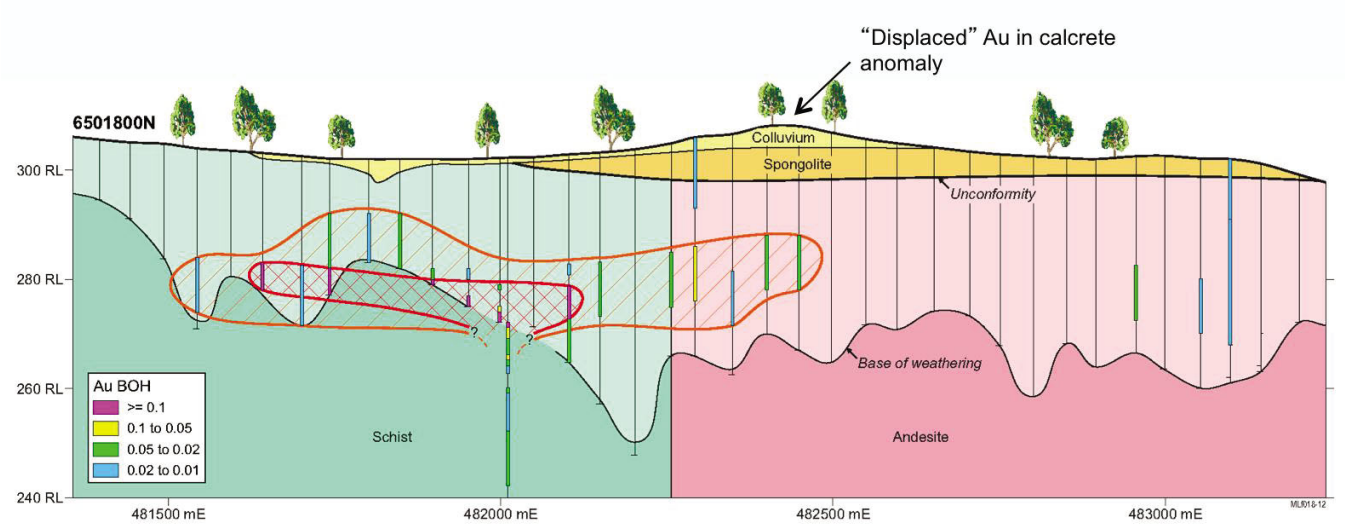

Figure 35. Schematic regolith section on 6501800N at Leucippus prospect, with gross vertical exaggeration. Vertical drill holes are indicated, with Au intercepts. Note the presence of spongolite and colluvium on the topographically higher areas to the east of mineralization.

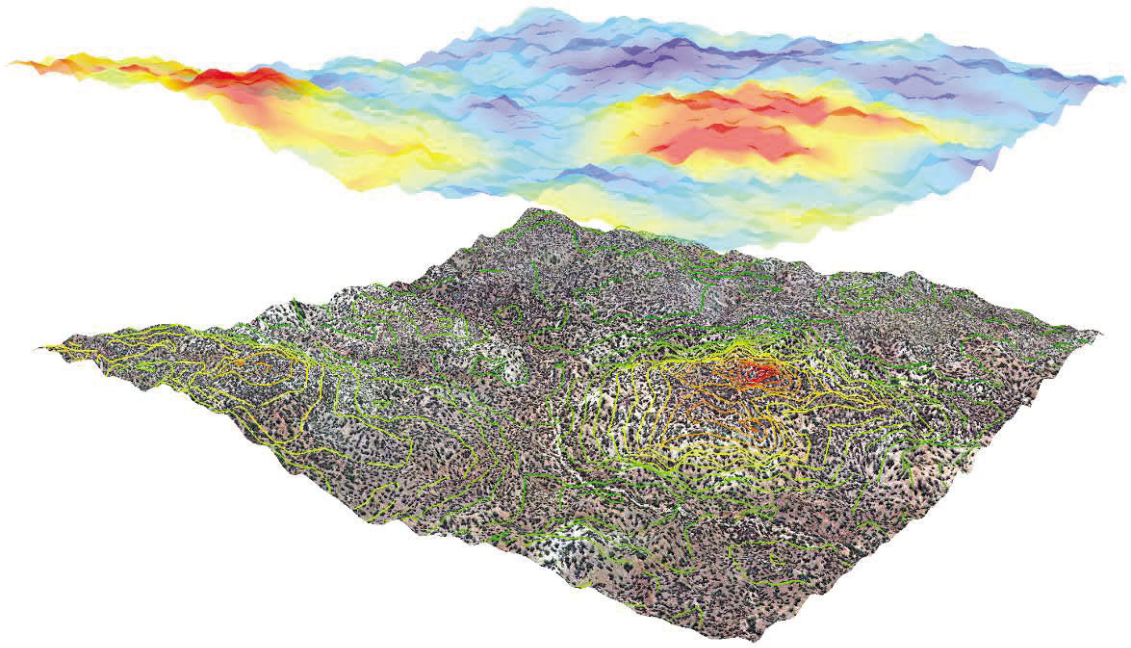

Figure 36. Gold in calcrete geochemistry draped in 3D landform and airphoto terrain models at the Leucippus prospect. The nearest corner in view is the south-east. Hotter (red) colours signify higher Au concentrations; the Au in calcrete anomaly near the centre is located within colluvium over spongolite. Calcrete data are courtesy of Sipa Resources.

2.3 Leucippus transect

Gold in calcrete sampling has previously shown that there are only near-background Au concentrations directly over mineralization at Leucippus (5 ppb), but on adjacent higher ground, devoid of mineralization, a significant anomaly (27 ppb) has developed (Sipa Resources data; Figs. 35 and 36). The calcrete data from Sipa Resources is limited to the elements Au, As, Ca, Cr, Cu, Fe, Mg, Mn, Mo, Ni, Pb, U and Zn. Calcium is more abundant on the eastern part of the transect corresponding with the higher ground (inverted landscape) of colluvium and spongolite (Fig. 34), as well as where calcrete is better developed (Fig. 35). The Au anomaly is displaced slightly to the west of the higher Ca concentrations, but to the east of mineralization. Normalizing Au with respect to Ca does not improve the anomaly strength over mineralization (Fig. 35).

The Mn in calcrete shows a broad weak anomaly over mineralization. Nickel and Zn concentrations broadly correspond with those of Mn, but the anomalous zone shows greater contrast of these elements over mineralization. The other calcrete data do not show any particular trends of interest.

2.3.1 Down hole geochemistry

Drill cuttings and field observations reveal the Leucippus transect on 6501800N to be deeply weathered to 10-30 m; the residual weathered section of the profile is comprised of mica schist and andesite saprolite (less weathered to the west; Fig. 35). At Leucippus the water table is at about 30 m depth (Sipa data) coinciding with a supergene Au layer. Importantly, multi-element analytical data of samples (*aqua regia* digest, ICP-OES/MS) from the Au supergene zone do not show strong enrichment in other potential pathfinder elements (e.g., maxima of As 9 ppm, Bi 2.5 ppm, Cu 54 ppm, Mo 1.1 ppm, Ni 50 ppm, Sb 0.08 ppm, W 3.5 ppm, Zn 139 ppm). Deeper mineralization is centred around 482000E where *maximum* Au concentrations in four adjacent drill holes are in excess of 1 ppm over a metre spread (*maximum* of 3.83 ppm) at about 30 m depth. Above the supergene layer there are at least 20 m (from 10 m composites) of Au concentrations <10 ppb Au. Colour, mineralogy (ASD and HyChips) and major element geochemistry (by portable XRF) of selected drill hole cuttings from Leucippus prospect vary considerably, but discussion of these data is beyond the scope of this study.

2.3.2 Leucippus Pit (482297E, 6501806N)

Leucippus pit LP1 is located in *colluvium-alluvium* above the spongolite and coincident with the Au-in calcrete anomaly (Fig. 37). The colour of the soil from the surface to the base of the profile varies from a light red to pink (within the calcrete horizon), then back to light red, and then finally red at the base. Soil texture is variable from predominantly clayey sand near the surface, to clay loam at depth. Abundant ferruginous granules and quartz occur throughout the profile and form a deflation lag on the surface. The mineralogy is dominated by quartz, hematite, maghemite, calcite, dolomite, kaolinite and feldspar. The surface lag consists of magnetic and non-magnetic ferruginous lag with angular and sub-rounded quartz, which would account for the hematite recorded by XRD. Lenses of alluvial ferruginous granules (partly magnetic) occur lower in the profile coincident with abundant hematite and greater Fe concentrations. The pedogenic carbonate minerals calcite and dolomite occur in the upper part of the profile with calcite occurring above dolomite. Feldspars are present in small amounts and reflect unweathered minerals associated with detrital rock fragments.

Aqua regia: extractable Fe concentrations are strongly related to the occurrence of the ferruginous (hematitic) alluvium. Iron concentrations are partly diluted by calcrete and clay minerals. Iron controls the distribution of As, V and several other elements but not Zn, Ni and Cu (Fig. 38). The ratio of Fe to As varies with depth suggesting that the lenses of gravels may have different provenance as seen in other colluvial deposits nearby at Higginsville (Lintern et al., 2001). Aluminium and K are strongly associated, and related to, the abundance of clay minerals and appear to partially control Mn, REE and Ni. Calcium and Mg concentrations are strongly correlated with the appearance of (Mg-rich) calcite and dolomite. Gold concentrations are strongly associated with the calcrete and thus the concentrations of Ca and Mg. Gold shows no erratic spikes in concentration suggesting that it is finely particulate or ionic in nature. Small amounts of Au appear below the calcrete, appearing to be associated with Mg concentrations. Peak Au concentrations (75 ppb) correspond with peak Ca at about 40 cm depth, whereas Au concentrations near the surface are ~20 ppb. Concentrations of Au in the Fe-rich gravels near the surface are <5 ppb.

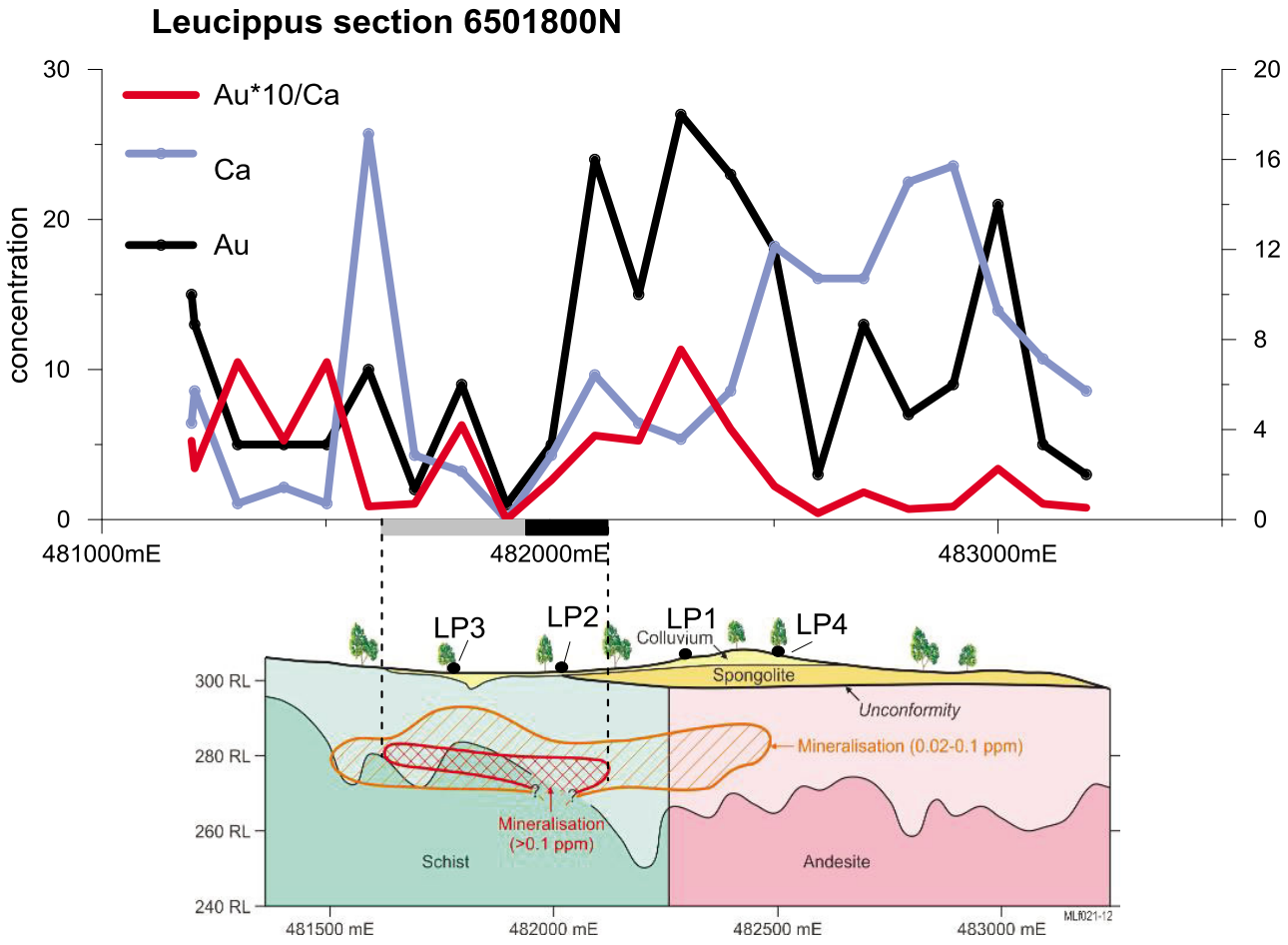

*Figure 37. Calcrete geochemistry of the Leucippus transect for Ca, Au and Au*10/Ca. Gold is not correlated with Ca and is displaced from subsurface mineralization. Iron and arsenic are weakly related in these bulk calcrete samples. Black and shaded rectangles locate bedrock and supergene mineralization, respectively.*

2.4 Soil profiles- major elements

There is a geochemical similarity between the soil profiles at Leucippus, Heraclitus and Theofrastos, which reflects the mineralogy and the soil descriptions. Soil geochemistry is dominated by three principal factors: ferruginous granules, pedogenic carbonate and (in some cases) weathered bedrock. Abundant pedogenic carbonates and bedrock are easily identified by their mineralogy but magnetic lag, at lower concentrations, is best quantified geochemically.

Concentrations of Fe in the profiles reflect the abundance of ferruginous granules noted in the soil descriptions. These granules have a strong influence on many minor elements (including potential pathfinders to base metal and Au mineralization). Typically, the Fe concentrations reflecting ferruginous granules concentrate a near the surface, to form deflation lag, and in lenses within the alluvium-colluvium (Fig. 28). They are present in alluvium and may give rise to transported anomalies and longer (though diluted) dispersion trains. The highest concentrations of Fe are found in profiles LP1, LP2 and LP4, which are in colluvium-alluvium. Profile LP4 finishes in spongolite and HP1-TP1 in weathered mica schist, which are both relatively low in Fe oxides.

The Al concentrations are all below about 3%, indicating that the *aqua regia* digest is poor at extracting the abundant kaolinite identified by XRD. The strong correlation (r^2=0.65, $p<0.05$) with K suggests that either some micas are being extracted, or adsorbed K and/or Al is being extracted. For LP3 the correlation is poorer towards the base of the profile indicating a change in colluvium source; Ce and Mn correlations also change in this part of the profile. For LP2, where mica dominates, the relationship breaks down entirely. Other elements that are correlated with Al (and K) are Cs (r^2=0.73), Rb (r^2=0.75) and, to a lesser extent, Sn (r^2=0.48).

Calcium and Mg concentrations are strongly related to the occurrence of calcite and dolomite, respectively (Fig. 30). Their distribution is important for Au exploration as has been previously demonstrated. The alkaline earth elements are abundant in all profiles. High concentrations of Mg (without corresponding Ca) in LP4 are due to smectite and possibly Mg-rich mica minerals. Strontium is also correlated with Ca (r^2=0.87) and Mg (r^2=0.69) as it can readily substitute for the former in crystal lattices. Copper is correlated with Ca (r^2=0.76). Magnesium concentrations are typically higher in the lower part of the profile (mostly in dolomite).

2.4.1 Soil profiles-minor elements

Many minor elements are associated with *aqua regia* extractable Fe. The more strongly correlated elements include: As (r^2=0.74), Bi (0.71), Cr (0.75), Ga (0.87), Hf (0.77), In (0.89), Mo (0.9), Ni (0.53), Pb (0.93), Sb (0.91), Sc (0.82), Th (0.95), V (0.94), W (0.58) and Zr (0.88). The slopes of the regression lines for the scatter plots of Fe *versus* these elements is location dependent; differences are possibly due to provenance or weathering processes related to the ferruginous granules within which most of the Fe (as oxides and oxyhydroxides) is contained. For example, for Fe *versus* As, samples from profile LP1 are on a different trend to LP3. The ferruginous granules from LP3 are sourced from the north-west whilst those from LP1 (located in alluvium above the spongolite) are sourced from elsewhere. Manganese minerals are an important host for Co, Ni, REE and Zn.

2.4.2 Soil profiles-Au

Gold is correlated with Ca (r^2=0.57) and Mg (r^2=0.63) and therefore associated with calcite and dolomite. In some saprolite-dominated samples in the lower profile, it is also found in other materials suggesting residual Au associated with mineralization. The peak Au concentration is commonly between 0.4 and 0.6 m depth. Calcareous samples nearer the surface are lower in Au. Gold concentrations are relatively low in samples from profiles over mineralization (LP1, TP1 and HP1) regardless of the depth at which the samples are taken.

2.5 Interpretation of Au anomaly at Leucippus

Geochemical studies at Woodline focused on addressing two questions pertaining to the distribution of Au in near surface materials at Leucippus prospect:

(1) Why are Au concentrations low in calcrete and other regolith-*media* over mineralization?

(2) Why is there a false positive Au anomaly in calcrete, apparently displaced from the mineralization?

In considering (1) above, the Au distribution in the full regolith profile needs to be considered. The soil profiles studied at Woodline are principally developed in erosional terrain (over leached saprolite) or in depositional terrain. Although calcretes are well developed and Ca concentrations are high in the soil profiles, their Au concentrations are not anomalous (compared to the entire regional dataset). Gold has been leached (or is naturally low) from the underlying saprolite and/or is located deep in the weathered profile, as at Leucippus (LP2) where a supergene layer occurs at about 30 m depth. Whilst this may present an enlarged target for drilling, the absorption of elements by tree roots from this depth is an unlikely mechanism by which significant amounts of Au may be brought to the surface. The supergene layer is probably too deep (and/or low) in Au for the roots of vegetation to absorb and translocate Au to the surface in any significant amount. Higher concentrations of Au (in saprock) are even deeper. Consequently, the only available Au that can be potentially be absorbed by trees are the small amounts occurring in soil that have been transported to their current position by other processes such as sheetwash or soil creep. Gold that is present in calcrete may also be derived from relict Au that has residually accumulated and subsequently leached from detrital rock fragments or quartz. The position of the profile on a gentle slope and the presence of only thin colluvial cover suggest that erosion is active in this area. Thus in the unlikely scenario that small amounts of Au have accumulated in this position by biogenic processes, or have accumulated by weathering of rock fragments, it will be subject to dispersion down slope.

Addressing question (2), the most important factor here is the alluvium-colluvium and the stability of the land surface in this locality. A 10 m thick, Si-rich layer of spongolite separates the *colluvium-alluvium* from the underlying weathered crystalline basement. The *colluvium-alluvium* is anomalous in Au (within the calcrete) but this appears to be unrelated to the underlying Au in the spongolite and supergene layer that have much lower Au concentrations. The Au in this profile was most likely sourced from upslope at the time of deposition and has been redistributed within the calcrete following pedogenic processes.

Not apparent in geochemical data, but noted in from field observations, is the abundant angular quartz in the *colluvium-alluvium* that forms a depositional lag (within ferruginous gravels and granules). Encapsulated Au within the quartz may be the immediate source of Au to the soil at LP1, which is released during weathering of the quartz, and then subsequently re-distributed by groundwater in the soil. The ultimate source of Au in the transported anomaly probably will be from upslope in the direction from where the *colluvium-alluvium* was sourced, but this needs more investigation. The stability of the locality (on indurated spongolite) and the flat nature of the landscape here ensure that any Au leached from the alluvium and colluvium accumulates in the calcrete within the profile.

Further work is required to test these hypotheses in different settings of mineralization and regolith. For example, the Au response in the calcrete should be examined where mineralization is stronger and/or nearer to the surface. Investigations should be undertaken to understand the origins of the ferruginous granules at Leucippus, as this may provide an easily traceable vector to the possible origin(s) of the Au.

2.6 Conclusions

Investigations of the distribution of the Au and other elements have been conducted on soil profiles, regolith profiles and calcrete principally at the Leucippus prospect at Woodline; other soil profiles were investigated at Heraclitus and Theofrastos. Gold in the soil profiles was almost exclusively located in the calcrete, which is comprised of calcite with some dolomite. Some Au was associated with other phases.

Possible mechanisms for the dispersion and accumulation of Au were investigated. This was principally driven by an attempt to understand false positive and negative Au in calcrete anomalies at Leucippus. Abiotic processes such as mechanical dispersion driven by gravity and landscape position are probably the principal drivers for the accumulation and dispersion of Au anomalies in calcrete at Leucippus (Figs. 38 and 39). In addition, although there is some mineralization at Leucippus, it is deep, sub-economic and separated from the surface by very low Au abundances.

Although Au is not anomalous in calcrete, a number of other elements were found to be so. Mn in calcrete shows broad weak anomalies over mineralization. Nickel and Zn concentrations in calcrete broadly correspond with those of Mn, but the anomalous zone shows s greater contrast over mineralization. The other calcrete data do not show any particular trends of interest.

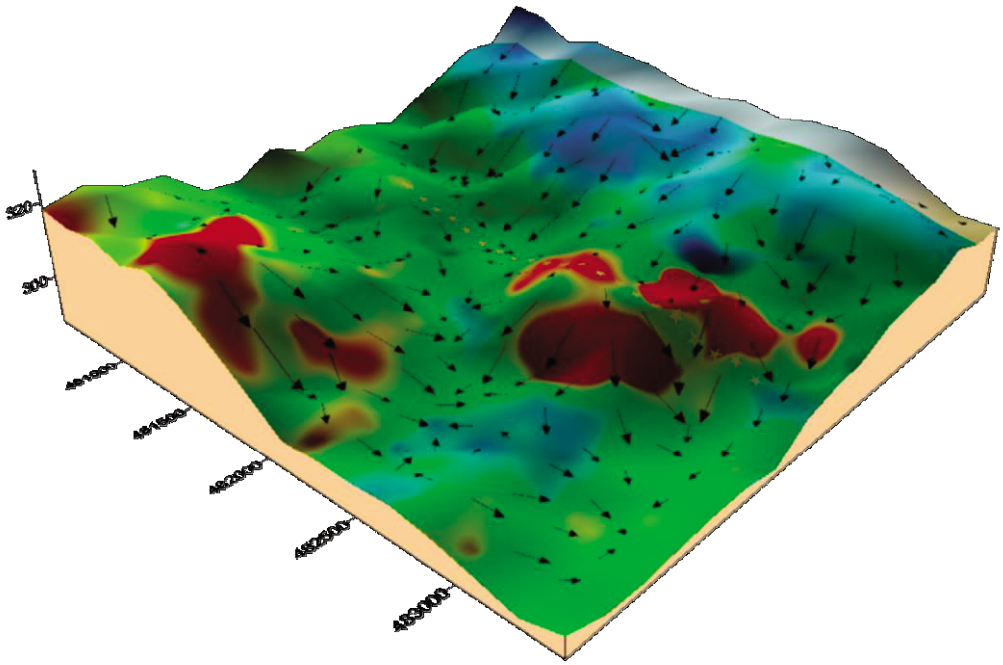

Figure 38. Calcrete Au geochemistry contours for Leucippus Au anomaly dispersion.

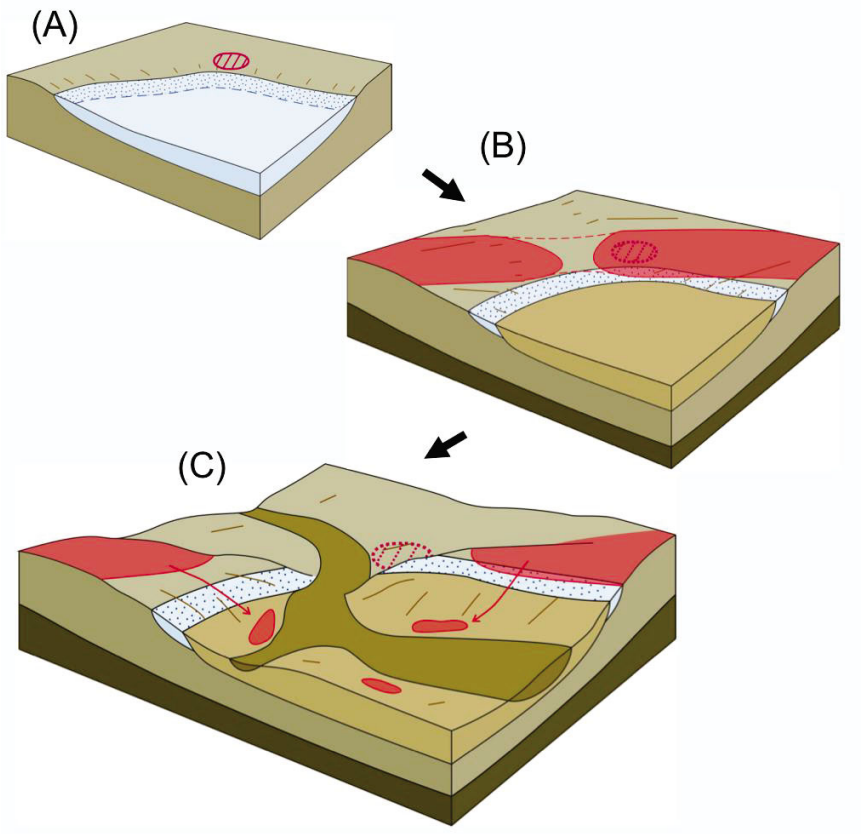

Figure 39. Dispersion model for the calcrete Au anomaly at Leucippus.

3 Geochemistry, mineralogy and petrology of the basement rock suites at the study sites *(Appendix C)*

Summary

Results indicate complex basement geology with mainly Archaean (Yilgarn Craton) and re-worked Archaean rocks (Northern Foreland) displaying mafic (SiO_2 <55 wt%), mostly tholeiitic, units with flat rare earth element patterns and felsic (SiO_2 >65 wt%) units with steep REE patterns. Proterozoic lithologies tend to have intermediate to felsic compositions and moderately inclined rare earth element patterns with local positive Eu anomalies. Some units carry distinctive minerals such as tourmaline or Ba-rich feldspar, which can be related to elevated B and Ba contents in whole-rock geochemistry.

Geochemical observations are combined with mineralogy, and show a distinctive enrichment of carbonate in most rock units, especially around areas of mineralization. Portable XRF (pXRF) studies can be used to define rock types, especially in zones were rocks are leached or colour and texture are obscured. Elevated Cu values were detected with pXRF in the mineralized zone of Salmon Gums, which is compatible with petrological observations of chalcopyrite. The alteration zones appear to be not distinctive enough to define more specific groupings of pathfinder elements related to mineralization; with most geochemical trends strongly influenced by the composition of the different rock types. Stable isotope analysis did not provide clear results related to mineralization, however, positive values for sulfur isotopes appear to be related to mineralization and/or rock type. Mineralogy is an indicator of differing metamorphic grade in the different study areas: Woodline displays mainly epidote, albite and chlorite indicative of lower greenschist facies; Beachcomber contains more Ca-rich plagioclase end members and garnet, more typical of amphibolite facies; and Salmon Gums exhibits local epidote and/or garnet, suggestive of different P-T conditions ranging between higher greenschist and amphibolite facies.

Paragenetic investigations point out at least two distinctive styles of Au mineralization indicating different physio-chemical conditions, and probably structural settings, which are likely related to different mineralizing events, or may be linked to the same event at differing depths and/or structures. Principally, Au mineralization is associated with quartz veins, and displays visible Au in white quartz veins, and common chalcopyrite in host rock proximal to finer quartz veins. Chalcopyrite is occurs with pyrite and/or pyrrhotite. Minerals spatially associated with this mineralization style are chlorite and carbonate. The second style of mineralization occurs in mafic tholeiites, rocks and is spatially associated with chalcopyrite, Bi-sulfides, sphalerite, galena and scheelite. Broad pyrite veins cross-cut the gneissic fabric close to these mineralized areas.

3.1 Introduction

This section focusses on the whole-rock geochemistry of the different basement units in the Yilgarn margin related to four study areas: Salmon Gums, Woodline, Beachcomber and Neale (Fig. 40; datasets and details in Appendix C), providing the basis for understanding Yilgarn margin geology, and potential pathfinder elements for Au exploration. Samples from Salmon Gums, Beachcomber and Neale were taken from diamond drill core, whereas drill chips from the bottom of percussion drill holes were analyzed for the Woodline area. Rocks were classified according to their major and trace element distribution with a special focus on REE systematics. Furthermore, a detailed mineralogical study, including the paragenesis of mineralization was performed on selected samples from the Salmon Gums, Woodline and Beachcomber areas. The Geological Survey of Western Australia dated and analyzed data from the Salmon Gums and Woodline areas. Handheld pXRF was used to analyse profiles over Au mineralized zones of drill core from one Salmon Gums and two Beachcomber diamond drill holes. In addition, stable isotope studies were performed on sulfides and carbonates from samples of two drill holes from Salmon Gums.

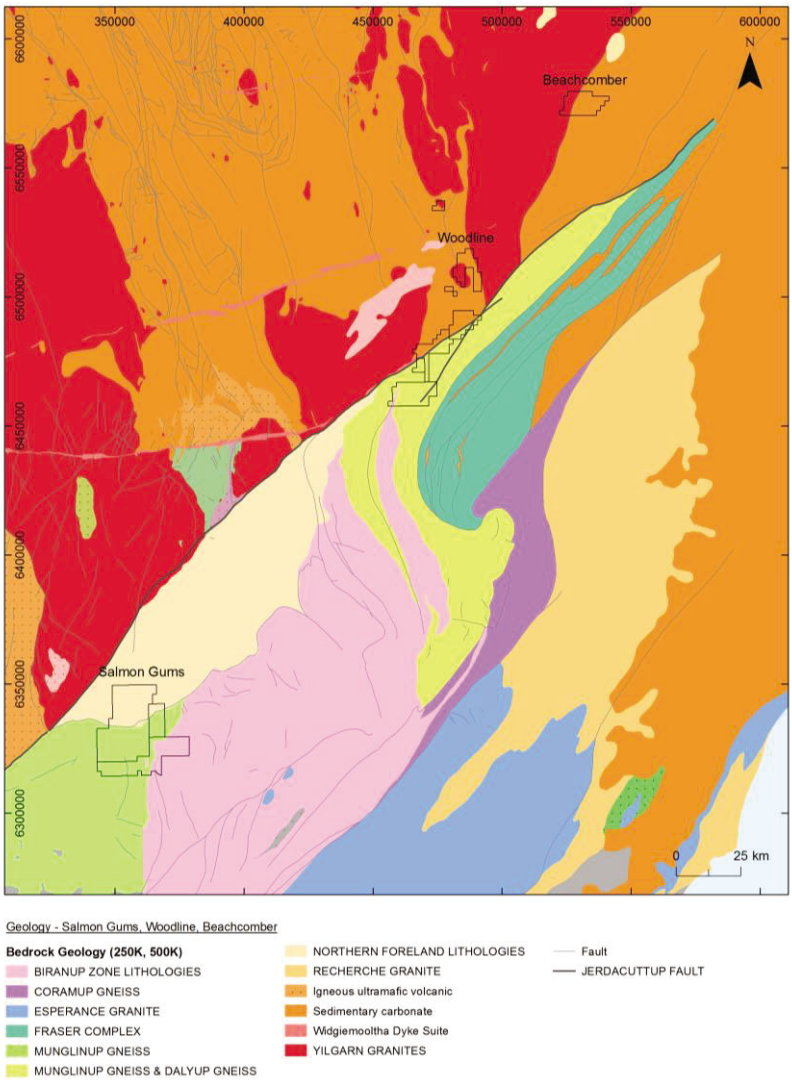

Figure 40. Basement geology map of the Albany-Fraser Orogen/Yilgarn margin displaying the study areas from south-west to north-east: Salmon Gums, Woodline and Beachcomber (map is based on a synthesis of the bedrock geology maps 250K and 500K by the Geological Survey of Western Australia).

3.2 Geochemistry of basement lithologies

In the four study areas, three different SiO_2 groups can be distinguished and be separated into mafic units below 55 wt% SiO_2, an intermediate to felsic group with 55 to 75 wt% SiO_2 and a felsic group with SiO_2 above 75 wt% SiO_2. Most samples appear to be of igneous origin, with rocks inferred geochemically to have a potential sedimentary origin are close in composition to proximal igneous source rock. This sedimentary geochemical signature may represent partially digested rafts or xenoliths incorporated in igneous rock types, and/or these compositions may represent modifications in composition due to deformational processes, such as shearing. The inferred separation between igneous and sedimentary groups is not shown in the following diagrams. On classification diagrams, samples from the Woodline area tend to be more mafic to intermediate (basaltic/gabbroitic to andesitic/dioritic) in composition in comparison with the other prospects, which tend to have more intermediate to felsic (andesitic/dioritic to rhyolitic/granitic) compositions (Fig. 41A, C). Some samples from Neale and Salmon Gums plot into the field of trachy-andesites/syeno-diorite to trachytes/syenites (Fig. 41A, B) indicating a slightly more alkaline character. Komatiitic basalt samples are present in the Beachcomber, Woodline and Neale area, but are absent at Salmon Gums (Fig. 41D). The wide range of data at Neale, especially with respect to SiO_2 content (Fig. 41A) is likely to at least due to widely varying extents of deformation, including mylonitization. Observation of drill core and petrology (Appendix C) supports the presence of a sedimentary component (source?) to some granitoids, as well as a wide range of igneous compositions, including many lithologies of intermediate composition (Figs. 42 and 43).

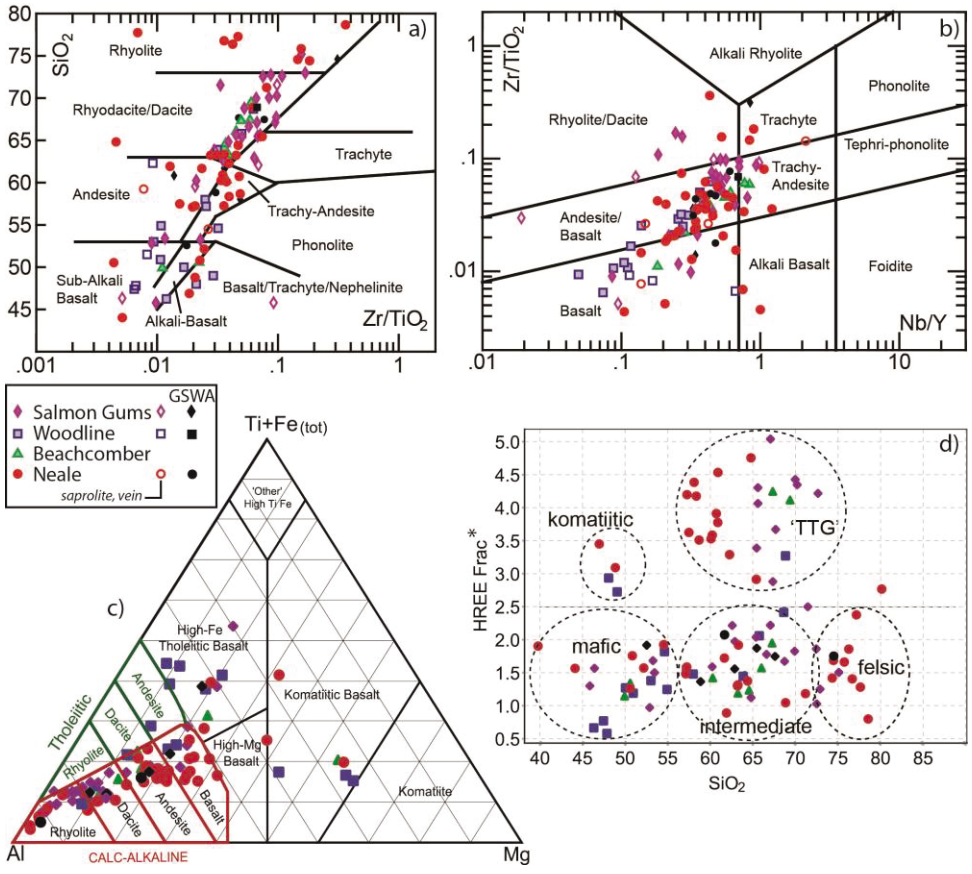

Figure 41. Geochemical classification diagrams for the four prospect areas. (A) (B) and (C) Classical classification diagrams; and (D) geochemical classification of this study using various fractionation of heavy REE (normalized after Boynton 1983) versus SiO2 contents for the Salmon Gums, Woodline, Beachcomber and Neale sites.

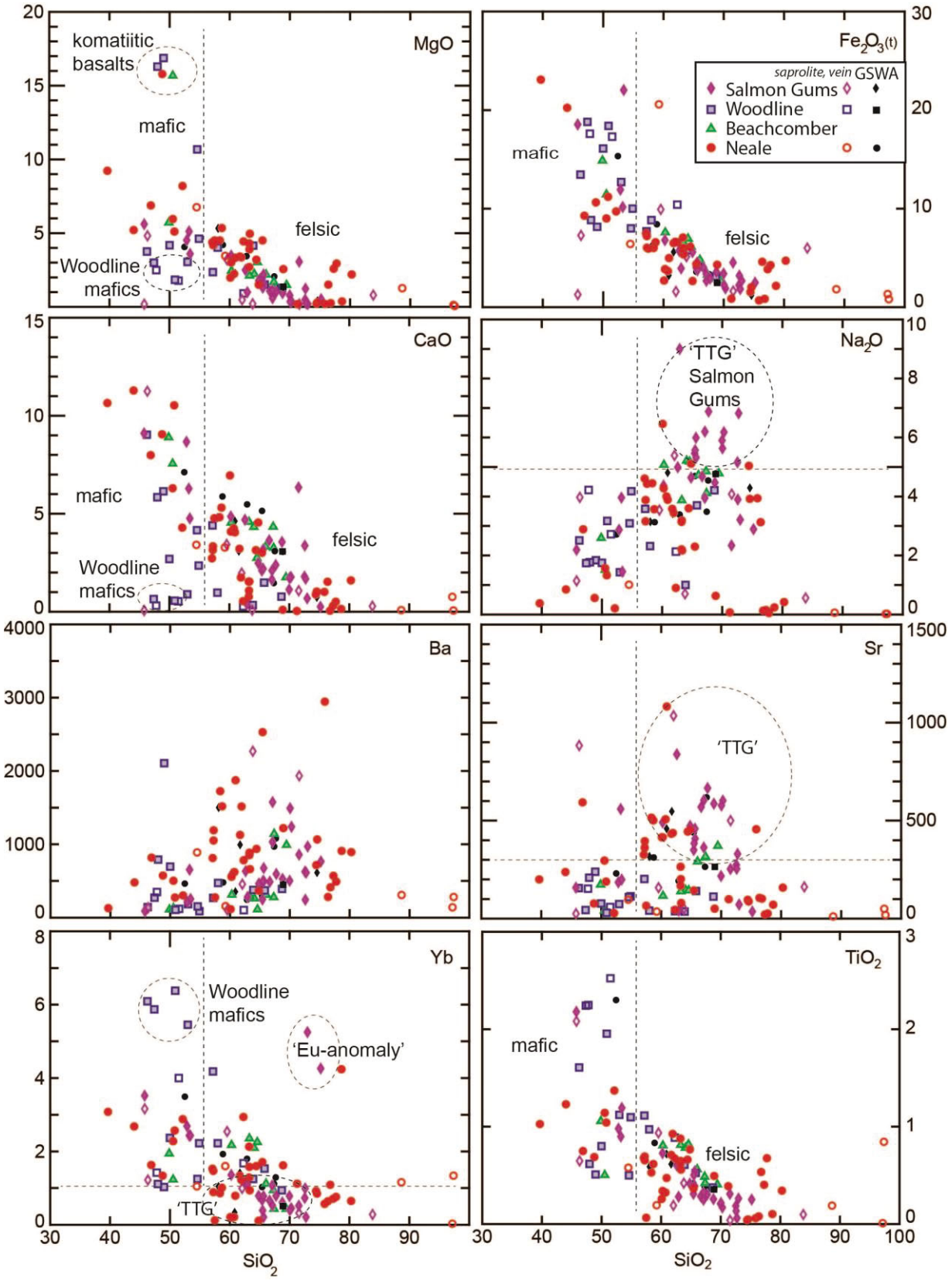

Figure 42. Binary plots of major (wt%) and trace element (ppm) versus SiO_2 for whole-rock geochemistry of all study areas.

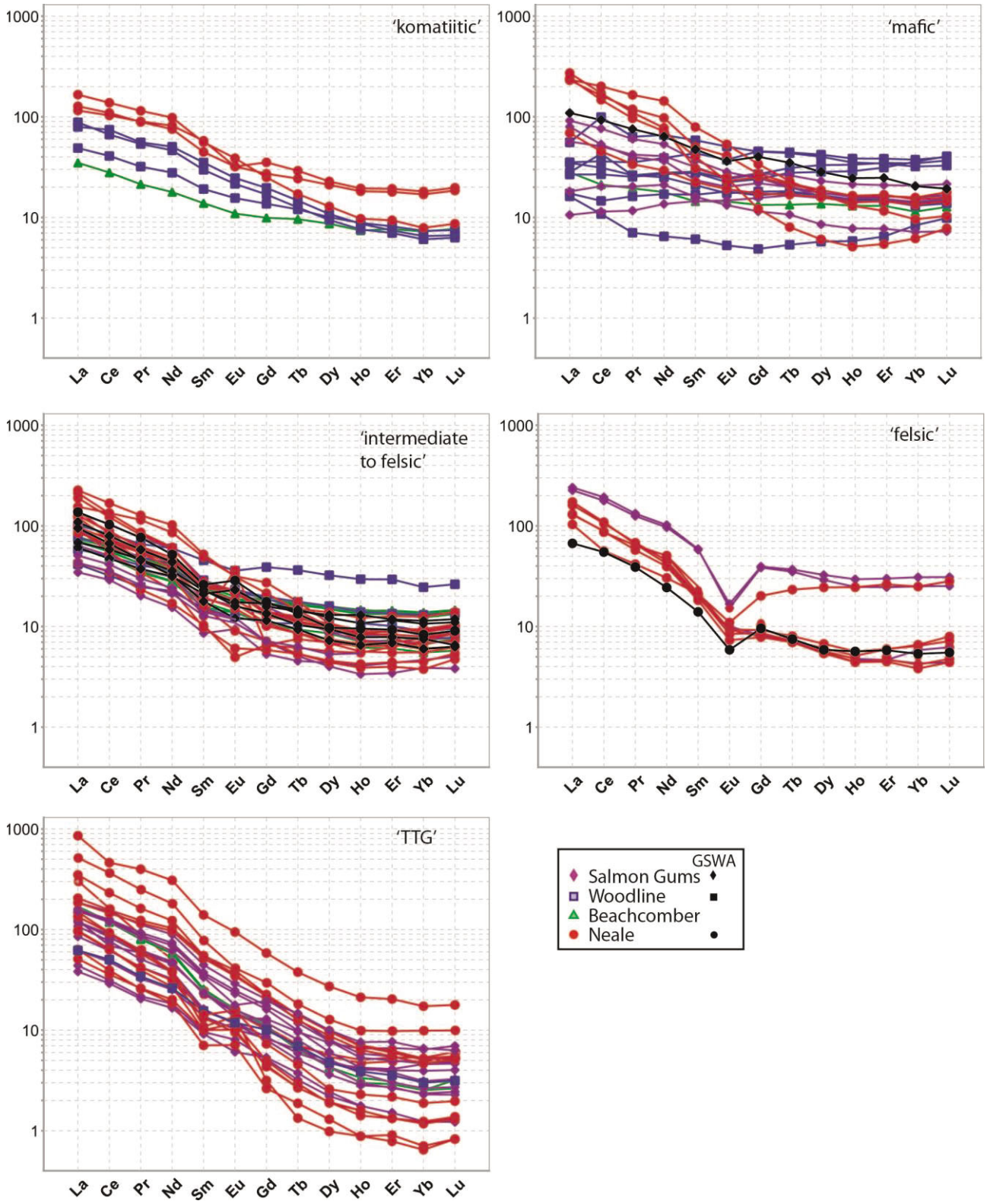

Figure 43. Log-normal REE plots for all study areas, with data grouped by geochemical rock classification. Rare earth element data normalized to Primitive Mantle (PM) from Sun and McDonough (1995).

On binary plots of major element, and trace element ratio diagrams *versus* SiO_2, the two previously defined generalized groups, i.e. mafic and felsic rocks, can be identified, showing mafic rocks with SiO_2 contents below 55 wt% and trends toward elevated MgO, Fe_2O_3, CaO and TiO_2 contents. The komatiitic basalts of the Woodline, Beachcomber and Neale area have distinctly higher MgO contents than the other mafic units. Some mafic Woodline samples display higher Fe_2O_3, lower MgO and distinctly lower CaO contents than mafic units of any other study area (Fig. 42). This may be related to the more oxidized character of the shallow depths of the drill chip samples taken for whole-rock analyses. Furthermore these samples have the highest Yb contents of all areas.

Overall, almost all of the observed rock types across the different study areas can be divided based on their REE patterns, into:

(1) Rare ultramafic to mafic komatiitic samples (absent in the Salmon Gums area) with SiO_2 values below 55 wt% and high Mg, Ni and Cr values, mostly displaying steeply inclined REE patterns with $(Gd/Yb)_N$ (Gd/Yb normalized to chrondrite) ratios above 2.5, with the exception of two Neale and one Beachcomber samples, which have flatter REE patterns and $(Gd/Yb)_N$ ratios below 2.5 (Fig. 41D);

(2) Mafic units with SiO_2 values below 55 wt%, commonly Fe-rich tholeiites, with flat (Woodline, Beachcomber and Salmon Gums) to inclined (Salmon Gums and Neale) REE patterns. Two Neale samples display higher enrichment in light REE than the other mafic samples;

(3) Common intermediate to felsic gneisses with SiO_2 contents between mainly 55 and 70 wt% (two samples with 72 wt%), showing inclined light REE and relatively flat heavy REE patterns;

(4) Scarce felsic gneisses (absent at the Woodline and Beachcomber areas) with SiO_2 values between 70 and 75 wt%, showing inclined light REE and relatively flat heavy REE, with a pronounced negative Eu anomaly; and

(5) Widespread felsic tonalite-trondhjemite-granodiorite (TTG) gneisses (nearly absent in Woodline) with SiO_2 values between 57 and 72 wt%, very steep REE patterns and distinctively high $(Gd/Yb)_N$ ratios above 2.5 (normalized after Boynton, 1984) or Gd/Yb ratios above 3.5 (Figs. 41D and 43). Neale samples display relatively low SiO_2 contents, between 55 and 65 wt%, and have relatively high MgO, CaO and TiO_2 contents when compared to TTG samples from the other areas. In contrast, Salmon Gums and Beachcomber samples display clearly higher SiO_2 contents between 65 and 72 wt%. All TTG samples display higher Sr (>200 ppm) contents, with trends to lower Yb (<1 ppm) and lower Y (<10 ppm) contents compared to most samples across all types and localities (Fig. 42). The Salmon Gums area displays characteristically higher Na_2O contents (>5 wt%) for TTG-type rocks when compared to all other samples.

The tholeiitic mafic gneisses of the Salmon Gums and Woodline area are dated by GSWA as Neoarchaean (preliminary age; Spaggiari, 2013, personal communication). However, it is difficult to infer this age for samples from other areas based solely in chemical composition, but, as greenstone terranes border all study areas, it is likely that the mafic units generally belong to the Northern Foreland/Yilgarn Craton. The Northern Foreland lithologies, and especially the Munglinup unit, consist of orthogneisses metamorphosed to amphibolite and granulite facies, but can also contain mafic metamorphosed lenses, amphibolite schist and metamorphosed ultramafic rocks (Spaggiari et al., 2011). Therefore, it may be difficult to distinguish between Yilgarn and re-worked Northern Foreland rock suites.

All intermediate to felsic Salmon Gums gneisses, which have undergone low-heavy REE fractionation, have been sampled and dated as Palaeoproterozoic (preliminary age, Spaggiari, 2013, personal communication). They probably belong to the Biranup Zone lithologies, comprised of mid-crustal rocks, including intensely deformed orthogneisses, metagabbros and paragneisses (Spaggiari et al., 2011). The intermediate to felsic gneiss group in the Neale and Beachcomber area are very similar in composition, but also display different trends to more alkaline trachitic/syenitic compositions. Therefore a clear Proterozoic geochemical fingerprint may not be produced, and further dating is required to confirm a link between geochemistry and age.

The TTG gneisses likely represent (re-worked) Archaean Yilgarn material, as these patterns are typical for Archaean units, together with komatiites. This group shares common low Yb and steep REE patterns. The variation in major elements (SiO_2 and Na_2O) between the Salmon Gums and Neale TTG group may indicate variations in fractionation of the magmatic protolith or in relation to metamorphism (i.e., albite more dominant at lower grade, but Ca-rich feldspars dominate at higher grades). It could also indicate the presence of completely different units, especially considering the positive Eu anomaly in the Neale area. Therefore, it is unclear if these units are related, or if they just indicate similar petrogenetic conditions unrelated in time and space.

Each prospect area shows some distinctive rock types. The Salmon Gums and Neale area displays some felsic gneisses with distinct positive Eu anomalies and in the case of Salmon Gums, also high Y and Yb values. The Neale area also displays REE patterns with a positive Eu-anomaly. Furthermore, Salmon Gums displays a rare mafic unit with depleted light REE (middle oceanic ridge basalt, MORB, type pattern).

The Woodline area appears to be mostly influenced by greenstone material and is mainly comprised of Yilgarn and Northern Foreland lithologies, whereas the Salmon Gums area also contains Biranup rock types. The Beachcomber area has been mapped as mainly being comprised of Northern Foreland lithologies, but also contains displays komatiitic suites, which are also indicative of Yilgarn basement. The relatively homogenous intermediate gneisses of the Beachcomber area may be part of the Proterozoic Albany-Fraser Orogeny, being very similar to the Salmon Gums intermediate gneisses, showing neat and overlapping REE patterns (Fig. 43).

3.3 Petrology of basement units

Mineralogy also reflects metamorphic grade and illustrates that the Woodline area, showing mainly chlorite, albite and epidote, has a lower metamorphic grade (lower greenschist facies) than the Beachcomber area (amphibolite facies), which has calcic plagioclase and high abundance of garnet. The Salmon Gums area appears to be somewhere intermediate between the other two study areas, having minor garnet, common epidote, mostly albite and high amounts of biotite. Samples from Beachcomber and Woodline area are much more enriched in carbonate when compared to the Salmon Gums area. However, all basement study areas contain siderite and calcite in zones, which display higher Au assays. Tholeiitic mafic rocks have a greater abundance of amphibole, whereas komatiitic ultramafic rocks contain pyroxene. Tholeiitic rock suites from all study areas appear to be similar in composition, whereas komatiitic rocks may show some variation in mineralogy, displaying different proportions of pyroxene *versus* amphibole (e.g., Woodline is more amphibole rich, and Beachcomber is very pyroxene-rich), which could indicate a difference in metamorphic grade or the nature of the protolith.

Pyrite is the most common sulfide in all study areas, and occurs displayed in two textural forms, presumably related to two different generations. The first generation consists of larger pyrite grains, which become patchy and later disappear close to mineralization. They are commonly crossed cut by chlorite and may contain Ni-Co sulfide inclusions (in drill holes Woodline WDR774 and Salmon Gums SGD002). The second generation is flaky in appearance, located along cracks, cleavage planes, and within veins, and is probably linked to partial recrystallization of the first pyrite generation. This second generation pyrite may be crystallize early during the mineralization event, and is commonly associated with siderite and Mg-rich chlorite. All study areas display higher amounts of chalcopyrite in the mineralized areas, with chalcopyrite being locally associated with higher amounts of pyrrhotite (Salmon Gums SGD005 and Beachcomber) or pyrite (at Woodline and Beachcomber).

The mineral and sulfide assemblages in the three study areas are ambiguous, but partly similar. All study areas display a second generation of chlorite in the mineralized zones, which is typically Mg-rich, and displays strong disequilibrium textures in the Salmon Gums and Beachcomber area. This patchy to skeletal chlorite contains garnet in the Salmon Gums area and calcite in the Beachcomber area. It could be related to a previous Fe-Mg rich mineral such as amphibole, biotite or clinopyroxene that has been destroyed by the mineralizing fluid at lower temperatures. In Beachcomber and Salmon Gums, this chlorite is also associated with calcite and/or siderite, indicating CO_2-rich fluids. In contrast, at Woodline, Mg-rich chlorite is absent in the mineralized mafic unit (WDR774), but a Mg-rich dolomite rim is associated with pyrite/chalcopyrite. A very different mineral assemblage is also present in the tholeiitic mafic amphibole-rich mineralized rock of SGD005. The tholeiitic mafic units in the Beachcomber and Woodline area display similar mineralogy to the Salmon Gums units, but are not mineralized. The rock is mainly comprised of amphibole and quartz, with Mg-rich chlorite absent, but pyroxene is observed along sulfide rims. The transformation of amphibole into pyroxene may be related to higher temperatures and the loss of H_2O indicating a relatively hot dry mineralizing fluid related to higher degrees of metamorphism (amphibolite towards granulite facies). In the Salmon Gums area, these two mineralization types may indicate completely separate events. Conversely, the two parageneses may simply relate to spatial chemical variations related to temperature, fluid composition, and especially fO_2, H_2S and CO_2 activity leading to an assemblage with scheelite, pyrrhotite and Bi-sulfides in a amphibole matrix, or lower temperature mineral assemblages such as chlorite, sphalerite, galena in quartz veins.

In summary, various mineral and sulfide assemblages in all study areas may be explained by two different events, not necessarily affecting all areas, related to different P-T, chemical conditions (and fluid compositions, or by a single event over a continuum of time producing different assemblages related to depth, with deeper rock units being metamorphosed to higher grades than shallower units.

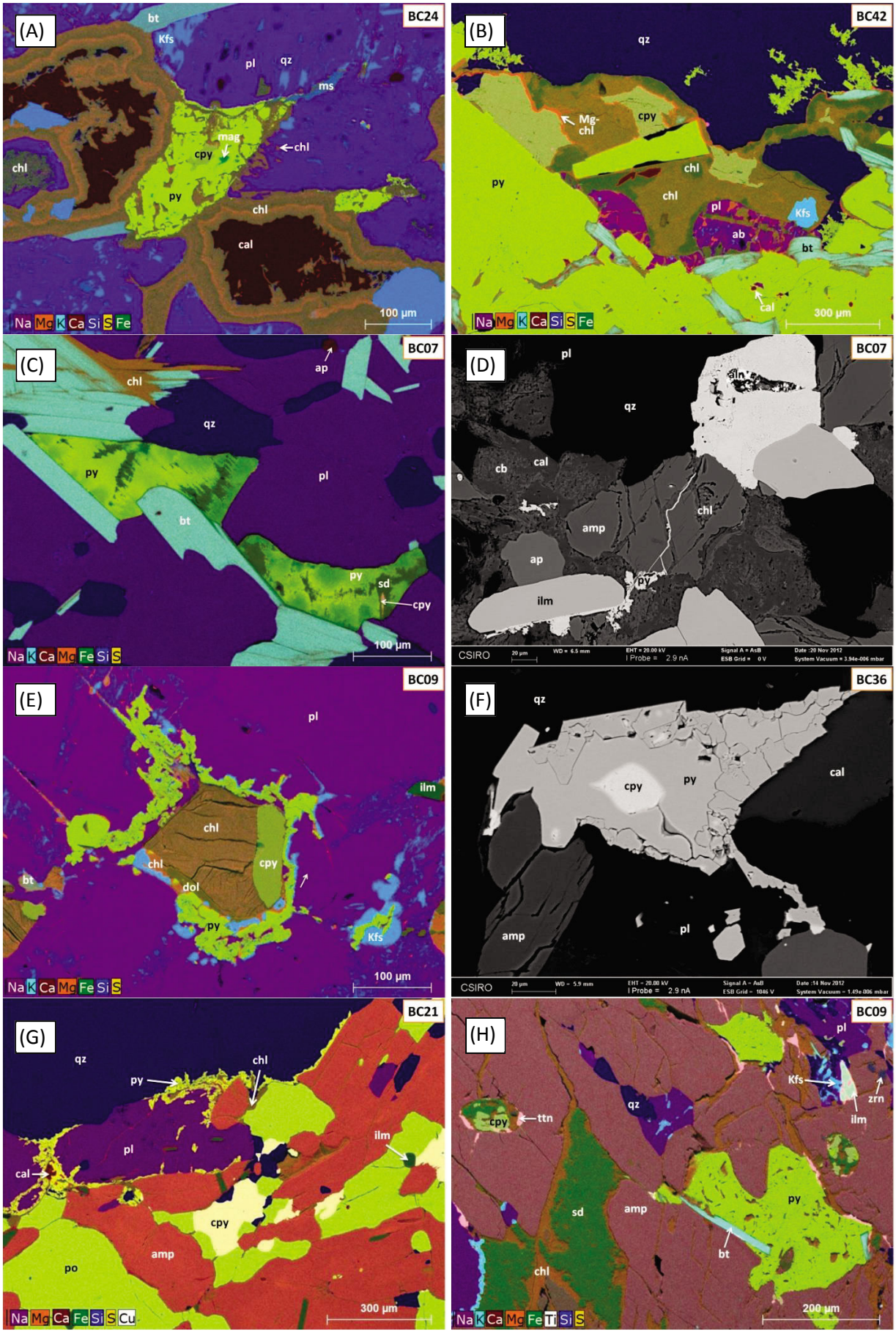

Figure 44. Backscattered SEM images and false coloured SEM images with element maps for pyrite and sulfide textural relationships illustrative of paragenesis in the Beachcomber area. (A)-(B)-(C) Energy Dispersive Spectrometry (EDS) maps showing pyrite associated with chlorite, carbonate and chalcopyrite; (D) Back Scattered Electromicroprobe (BSE) image of pyrite forming along cracks; (E) EDS map of flaky pyrite; (F) BSE image of brittle pyrite with chalcopyrite inclusion; and (G)-(H) chalcopyrite with pyrrhotite and siderite.

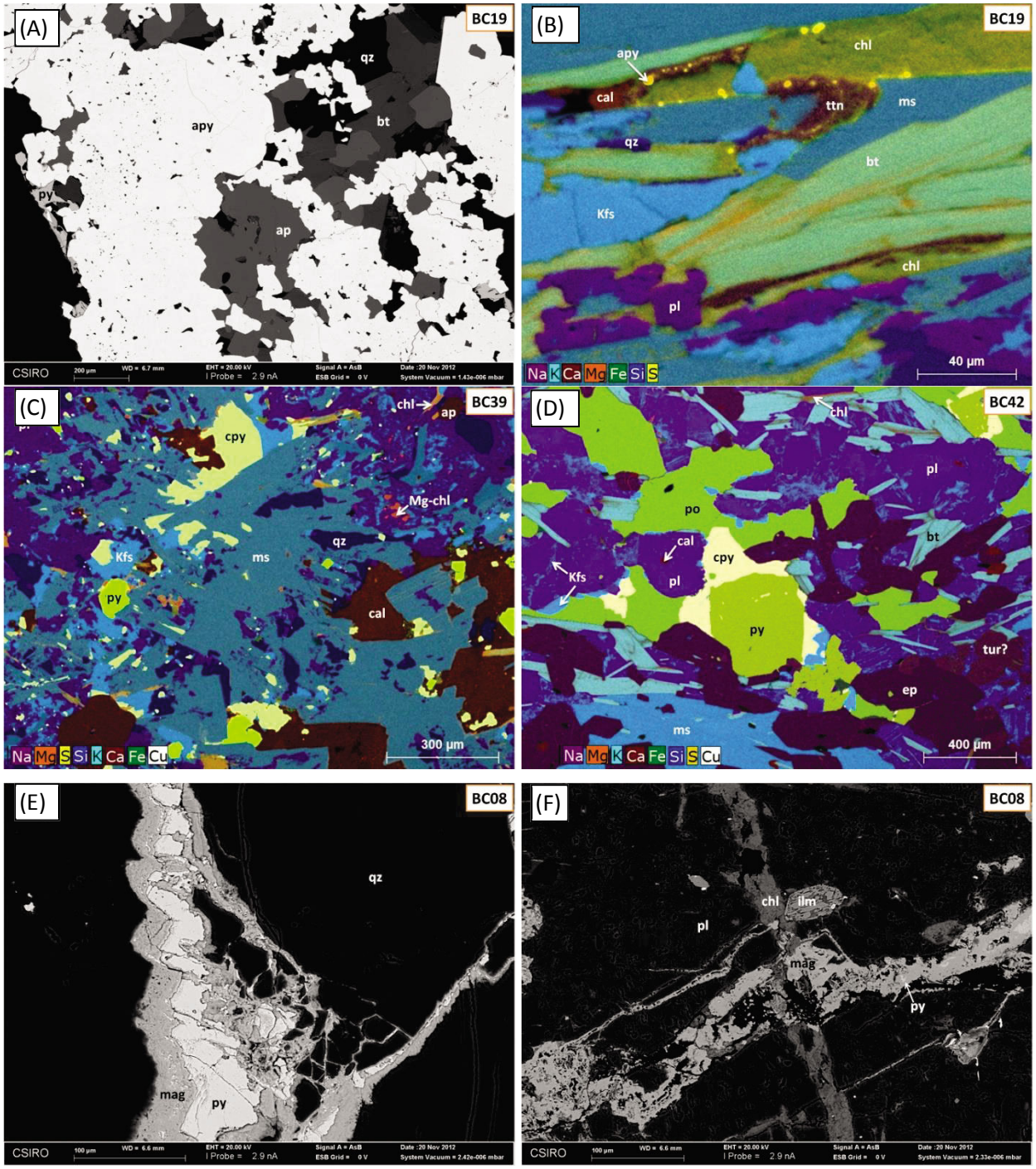

Figure 45. Backscattered SEM images and false coloured SEM images with element maps for sulfide parageneses of the Beachcomber area: (A) BSE image of arsenopyrite overgrowing biotite; (B) EDS map of arsenopyrite observed within titanite and chlorite; (C) EDS maps showing pyrite and chalcopyrite with muscovite and calcite; (D) EDS map of chalcopyrite together with early pyrite and associated with pyrrhotite; (E) and (F) BSE image of pyrite surrounded and intruded by magnetite (BC08), which grows together with chlorite.

3.4 Conclusions

The complex basement geology of the Yilgarn margin area comprises at least five different types of metasedimentary and metaigneous rocks. These have characteristic trace element patterns that belong to the Yilgarn Craton, Northern Foreland and the Biranup Zone. Mafic gneisses, with SiO_2 below 55 wt%, can be divided in a tholeiitic Fe-rich or calc-alkaline mafic groups, with an uncommon group of komatiitic affinity (high MgO, Ni, and Cr contents), and a very rare group of light REE depleted MORB-type metamafic rocks (at Salmon Gums only). The tholeiitic and komatiitic mafic gneisses together with the felsic TTG group, display very steep REE patters and $(Gd/Yb)_N$ values >2.5, presumably representing re-worked Archaean rock types, relating to the Yilgarn Craton or Northern Foreland (Munglinup Gneiss). Gneisses with an intermediate to felsic composition (65-70 wt% SiO_2) with relatively inclined REE patterns and felsic gneisses (SiO_2 >70 wt%) with inclined light REE, flat heavy REE patterns and a distinctive Eu-anomaly, probably belong, at least partly, to the Biranup lithologies of Proterozoic age. The Salmon Gums and Beachcomber areas have very similar geochemistry and rock units. Woodline comprises generally more mafic rocks, but all of the metamorphic rock units are comparable to the Salmon Gums and Beachcomber area. The Neale study area located to the far north-east displays a greater range of trace element patterns, with positive Eu anomalies and generally more inclined REE patterns when compared to Salmon Gums, Woodline and Beachcomber.

Portable XRF studies supported the identification of different rock suites in drill core, especially in zones with strong alteration, but also indicated that the alteration halo is not distinctive enough to define pathfinder elements.

Metamorphic grades vary between study areas from greenschist to amphibolite facies, with lower grades in the Woodline area, intermediate in Salmon Gums and the highest grades in the Beachcomber area, based on the relative abundance and presence of albite/plagioclase, epidote/garnet and chlorite/biotite. Meta-igneous rocks with komatiitic affinity contain mainly pyroxene and plagioclase. Mafic gneisses are mainly comprised of amphibole and plagioclase, with minor of K-feldspar, chlorite, and biotite; tholeiitic gneisses contain high garnet content. Intermediate to felsic gneisses contain little or no amphibole, higher amounts of biotite and chlorite, plagioclase and K-feldspar. Those classified as TTG gneisses locally contain Ba-enriched feldspars, which may be an indication of contact metamorphism, but are unrelated to mineralization. Tourmaline is observed in some gneisses (Woodline and Beachcomber) also does not appear to have any relationship to mineralization.

Mineralization appears to be generally independent of the rock-type when it is related to quartz veins, but may also have a relationship to mafic tholeiitic units, although these do not display distinctive quartz veining. In areas with Au mineralization, in quartz veins (with >1 ppm Au), high abundances of chlorite, carbonate, chalcopyrite, locally pyrite, sphalerite and galena are detected. Pyrite appears in two generations, both appearing to have crystallized before the other sulfides. They may be related to the Au mineralization event, and potentially may provide vectors to assist exploration. The other type of mineralization, unrelated to quartz veins, in amphibole-rich rocks, displays pyroxene overgrowing, and intergrouped with chalcopyrite, pyrrhotite, sphalerite, scheelite and Pb-Bi sulfides. Shear zones favour mineralization as they provide fluid pathways and are indicated by enrichment of chlorite, especially within mafic units. It is unclear if these different mineral assemblages simply relate to different geochemical conditions and buffering systems, but formed within a single event, or whether they indicate completely different mineralization events. Chalcopyrite in the Salmon Gums area displays higher $\delta^{34}S$ values in the zone of Au mineralization than in unmineralized intervals.

3.5 Implications for exploration

(1) All study areas along the Albany-Fraser Orogen/Yilgarn Craton corridor show similar rock types, comprised of at least two of the five different distinctive basement lithologies/units, and these may be related back to characteristic REE patterns.

(2) Two types of mineralization are observed, with a dominant type (A) related to quartz veins, and an uncommon type (B) related to meta-mafic rock units and shear zones. Type (B) is typically occurs with chalcopyrite, and therefore elevated Cu contents are indicative of this type of. However all assay data needs to be levelled, as mafic units tend to contain generally higher background Cu contents compared to felsic units. Type (B) mineralization also contains Bi-sulfides, scheelite and minor sphalerite, with Bi having a positive correlation to higher Au-values. Arsenopyrite is noted in some mineralized areas and As contents can be positively correlated with Au values, but the paragenetic timing of arsenopyrite is unclear.

(3) Chlorite and carbonate species (i.e., calcite, dolomite and siderite) are alteration minerals spatially related to mineralization.

(4) Elevated Ba and locally observed high B contents are unlikely to be indicators of mineralization, but high Ba contents are typical of zones of alternating rock types, especially in and proximal to TTG-type gneisses. High B contents are related to tourmaline-rich gneisses. Contact zones between different rock types and especially shear zones, are considered to be favourable pathways for fluid flow.

4 Petrography and mineralogy of mineralized samples from the Hercules/Atlantis prospects, *(Appendix D)*

Summary

Petrographic studies have identified traces of Au are present in both the northern area (Hercules prospect) of the Neale project area, and the southern area (Atlantis project). The Au in the two areas has distinctly different modes of occurrence. Gold in both areas is associated with traces of Cu minerals, mostly chalcopyrite. Gold and sulfide species are interpreted to have a relatively late paragenesis with respect to the rest of the mineralogy of the samples.

Gold at the Hercules prospect occurs as very fine (<25 µm) inclusions in pyrite, present in three of eight samples. This Au has Ag content of 12-46 wt%. The highest grade Au was hosted in a micro scale chloritic dilational jog structure within a quartz vein. Gold at Hercules has a broad spatial geochemical association of LREE-Ba-Cu-Pb-Zn-Ni-Pb-Bi-Te-As-Ag-Mo-W, based on the suite of accessory minerals present. Samples studied are hosted in mica-altered felsic to intermediate granitoids, granofels, and discrete quartz veins. Quartz veins typically contain chlorite ± 'sericite' ± carbonate filled fractures.

Gold identified at the Atlantis prospect has been reported as a crystalline grain of ~10 µm size, within a chlorite-'sericite' altered granitoid. It has no detectable Ag content. Based on the suite of accessory minerals present, a geochemical signature of LREE-Ba-Cu-Zn-Ni-Mo-Bi-Te is spatially associated with anomalous Au bearing samples. Boron bearing minerals (axinite and tourmaline) are proximal to some samples. Samples from Atlantis are typically hosted in mylonitic lithologies, with subordinate mica altered felsic to intermediate granitoids.

Two styles of Au mineralization are inferred to be present: a disseminated style related to altered felsic to intermediate intrusives, and a quartz vein hosted style associated with major structures, including mylonite zones and dilational structures and veins.

4.1 Introduction

This Chapter presents results from the petrographic and mineralogical studies of a suite of fifteen petrographic sections selected from sampling of 7 diamond drill holes from the Neale Project, within the AFO, held by Beadell Resources (Fig. 46). The Neale project area is located approximately 400 km north-east of Kalgoorlie, lying to the north-east of Tropicana in the eastern Biranup Zone of the north-eastern Albany-Fraser Orogen (Kirkland et al., 2011). These samples are representatives of anomalous auriferous intercepts from diamond drill holes representing the two prospect areas (Hercules and Atlantis) within the project area, separated by approximately 5 km. Two diamond drill holes were sampled from the northern prospect area, Hercules (NLD097 and NLD210), and five diamond drill holes were sampled from the Atlantis site (NLD046, NLD069, NLD070, NLD071, NLD080). All samples from these drill holes are located within basement lithologies of the McKay Creek Metasyenogranite of the Neoarchaean to Palaeoproterozoic Kepa Kurl Booya Province, as documented by Spagiarri et al. (2009), Spaggiari and Pawley (2012) and in this Chapter. Spaggiari and Pawley (2012) described this host rock unit as weakly foliated to mylonitic in texture, and is mingled with metagabbro, and forms minor hybrid rocks with metagranodiorite and metadiorite. It may contain intrusions of Bobbie Point Metasyenogranite and Archaean remnants. The distribution of host rock units is shown in Figs. 47A and 48A.

The regional geological setting, and the geochemistry of 43 samples related to mineralization in the Neale project area and their regional context may be found in Appendix D. Interpretation and assessment of Visible and Infrared Reflectance Spectroscopy (VIRS) HyLogging^{TM} in Appendix D.

This Chapter aims to provide detailed petrological, mineralogical and paragenetic information regarding these samples, as a module of the larger study of the geochemical expression of Au and mineralization in the project areas, in an exploration context.

Polished thin sections from all samples studied here were prepared in-house at CSIRO laboratories, Kensington, Western Australia. All polished thin sections were examined and photographed using both transmitted and reflected light microscopic techniques, followed by study using SEM imaging and EDS analyses. X-ray diffraction studies were undertaken on selected portions of material extracted from the slabs used to prepare two of the samples. Results from these studies are presented here.

A summary of petrographic samples examined is presented in Table 2, with names derived from original core logging as well as from petrography (this Chapter).

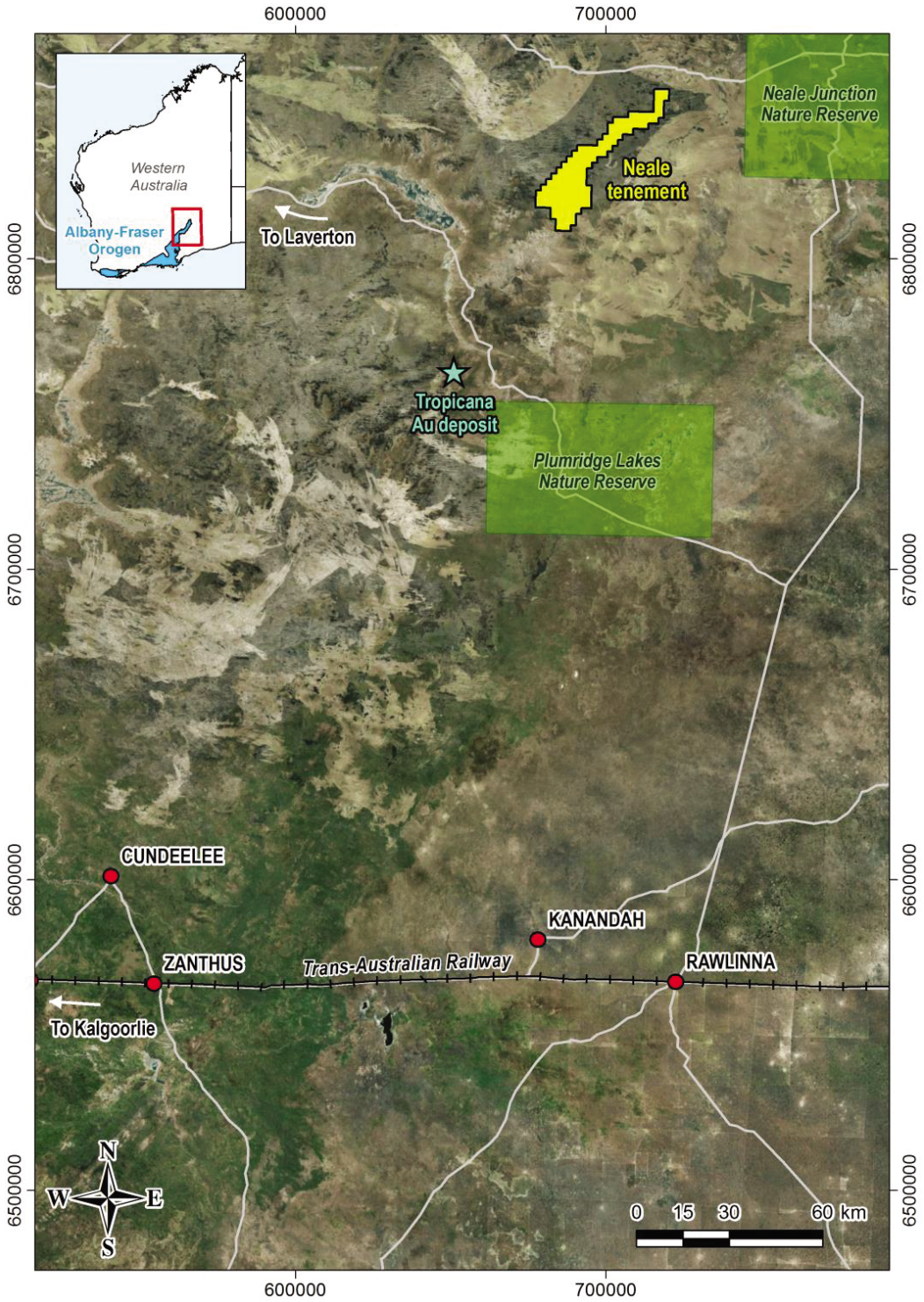

Figure 46. Geographic location plan, combined with a Landsat image, displaying the location of the Neale tenement of Beadell Resources, and the Tropicana Au deposit of AngloGold Ashanti.

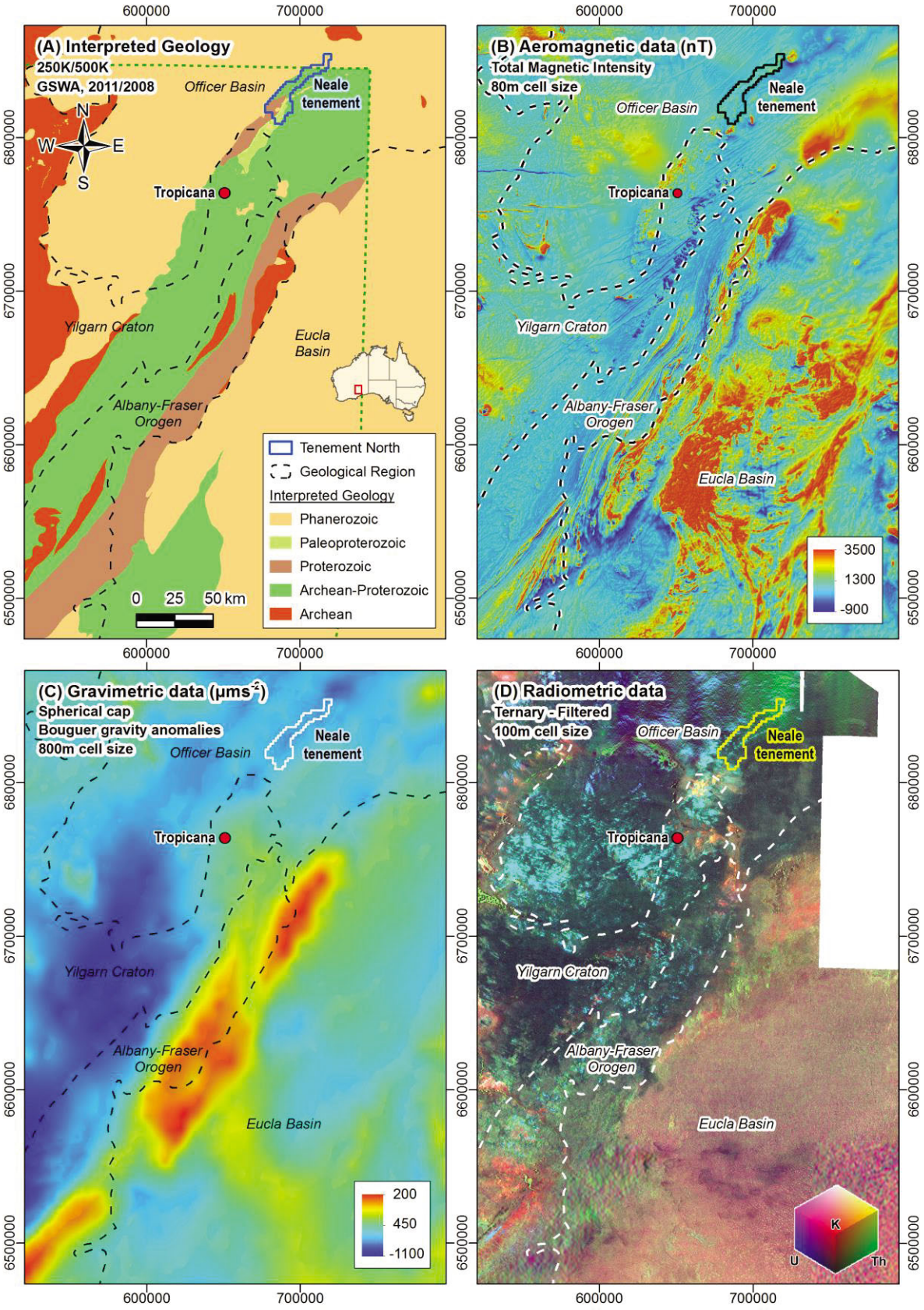

Figure 47. Maps of the regional geological and geophysical context of the Neale tenement: (A) geology, 500K, GSWA (2008 and 2011); where the Archaean-Proterozoic geology corresponds to undifferentiated Archaean-Proterozoic units; the black dashed line marks the boundaries of the geological datasets for GSWA (2008 and 2011); (B) Aeromagnetic data (as total magnetic intensity); (C) gravimetric data (Bouguer gravity anomaly); and (D) radiometric data. Datasets downloaded from the GSWA (2013) (A) and Geoscience Australia websites (B), (C) and (D), Geoscience Australia (2013).

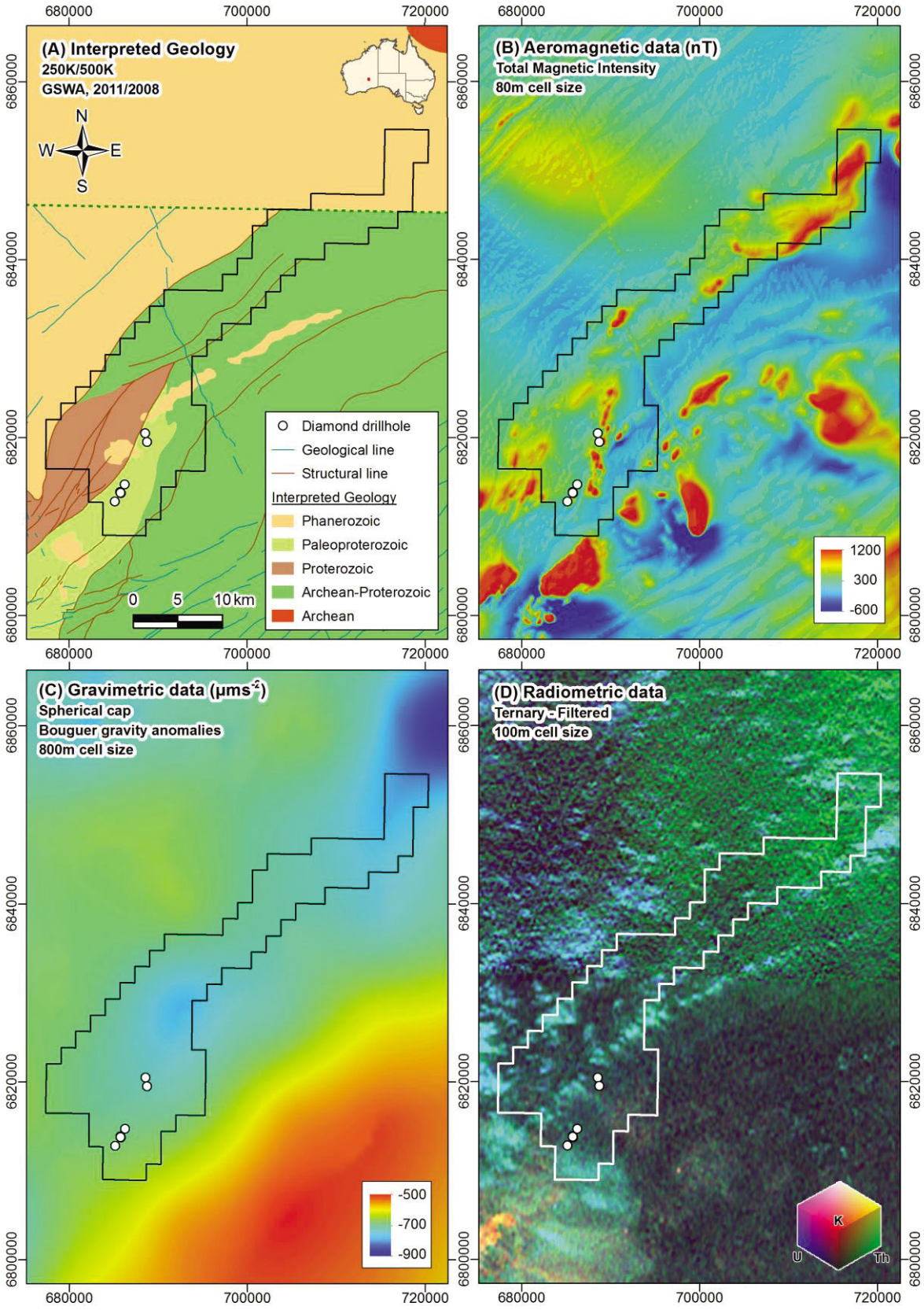

Figure 48. Maps of the local geological and geophysical context of the Neale tenement. (A) Interpreted basement geology (GSWA, 250K/500K, (2008 and 2011); (B) magnetic data (total magnetic intensity); (C) gravimetric data (Bouguer gravity anomaly); and (D) radiometric data. (B), (C) and (D) datasets from Geosciences Australia (GA, 2013).

4.2 The Neale tenement: Hercules and Atlantis prospects local geology

The Neale tenement is located 60 km north-east of the Tropicana-Havana Au system. The former is found above the Kepa Kurl Booya Province and Archaean Biranup lithologies to the north and east, with outcropping patches of the Carboniferous-Permian Paterson Formation to the west (Figs. 46, 47).

The Hercules prospect is located in the Bobbie Point metasyenogranite, outcrops about 30 km north-east of the Tropicana (Figs. 47A and 48A), whereas the Atlantis prospects are located in the Palaeoproterozoic Kepa Kurl Booya lithologies of metagranites interlayered with metamafics. According to the terminology of Spaggiari et al. (2011), the Tropicana-Havana system is located in Archaean-Proterozoic Northern Foreland lithologies. The main geological trend in this tenement is north-east/south-west, which is marked by the geometry of the main lithological units, together with structural shear zones and magnetic trends (Figs. 47, 48A-C and 49).

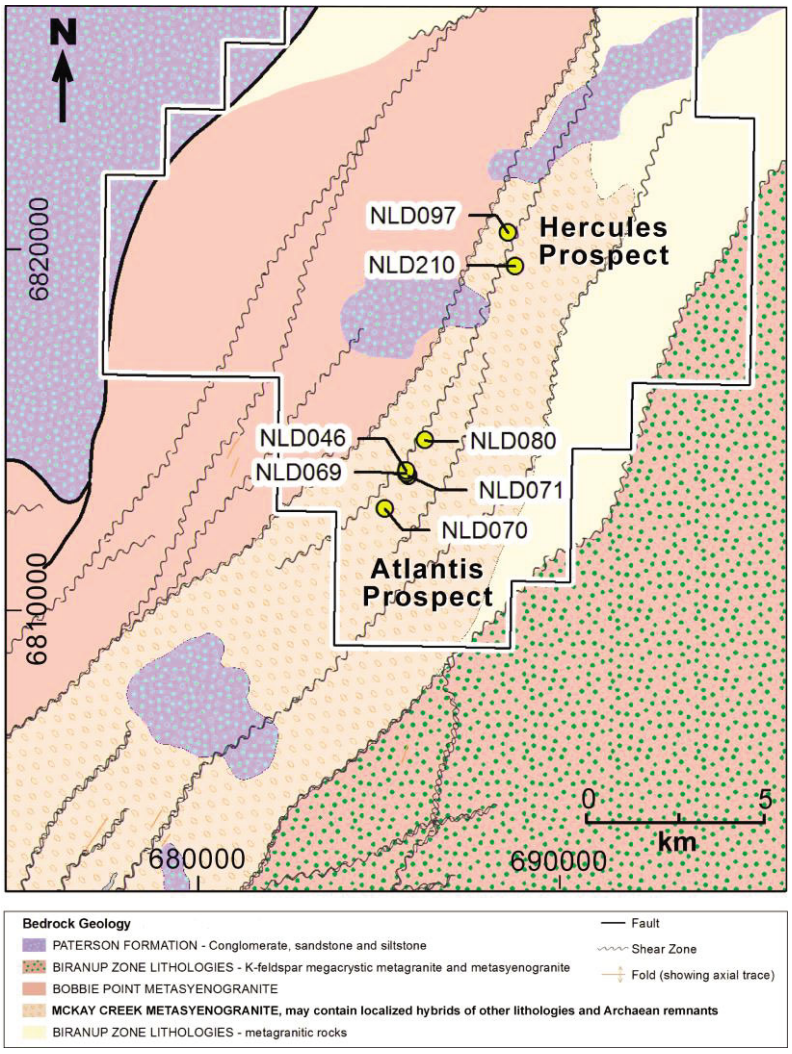

Figure 49. Basement geology of the Neale project region, adapted from Spagiarri and Pawley (2012), shown with tenement boundary and diamond drill hole collar locations. Basement lithologies belong to the Kepa Kurl Booya Province of the Albany-Fraser Orogen, with the exception of the Palaeozoic Paterson Formation (shaded violet).

Table 2. Summary of samples investigated, with original logging description based upon hand specimen observations, and corresponding name derived from petrological and mineralogical studies here.

Lab sample label	*from (m)*	*to (m)*	*Gold Assay (ppm)*	***Interval logged as**	***Petrologic name of sample represented***
NLD046_01	129.90	130.10	~0.5	*Talc carbonate schist*	Muscovite-biotite-quartz mylonite
NLD069_20	74.20	74.40	0.336	*Alkali granite (Kspar+qtz), fractured*	Altered ('sericite'±hematite) intermediate intrusive with apatite? vein
NLD070_31	102.80	103.00	0.308	*Dolerite; pyrite noted*	Vein quartz, with pyrite (± quartz ± chlorite) veinlet
NLD070_34	125.75	125.95	0.576	*Talc carbonate schist*	Quartz-muscovite protomylonite, with minor pyrite bands.
NLD071_41	81.20	81.40	0.121	*interval missing (granite/paragneiss?)*	'Sericite' ± chlorite altered (cataclasitic) granitoid
NLD080_48	60.70	60.85	0.3	*Talc carbonate schist*	Quartz-muscovite-biotite (meso)mylonite
NLD080_51	83.88	84.05	0.133	*Talc carbonate schist*	Quartz-'sericite'± chlorite ± biotite ± carbonate mylonite
NLD097_55	90.00	90.15	0.3	*Orthogneiss, alkali K-feldspar*	Leucocratic monzogranite
NLD097_57	90.45	90.65	0.3	*Orthogneiss; epidote-tourm-garnet 5 m below*	Biotite-'sericite' altered granodiorite, with biotite ± clinozoisite shear
NLD097_59	122.50	122.70	0.3	*Orthogneiss, alkali K-feldspar*	White mica altered granitoid with a quartz-'sericite'± chalcopyrite vein
NLD097_61	133.50	133.70	0.3	*Dioritic orthogneiss w. pyrite-chlorite (fractures)*	Protomylonitic biotite-quartz-plagioclase ± 'sericite' metagranitoid
NLD210_71	95.30	95.50	0.367	*Diorite, foliated; below mafic schist*	'Sericite'-actinolite±chlorite±clinozoisite altered intermediate intrusive
NLD210_75	165.90	166.05	0.478	*Talc carbonate schist; pyrite*	'Sericite'-chlorite- quartz ± clinozoisite granofels, adjoins a sheared quartz-pyrite ± chlorite vein
NLD210_76	166.60	166.80	0.477	*Recrystallized quartzite; pyrite*	Quartz vein, with chlorite-'sericite'-carbonate segregations
NLD210_77	167.90	168.00	4.806	*Recrystallized quartzite; pyrite; talc schist below*	Quartz vein, with chlorite ± 'sericite' ± carbonate filled fractures
				*based on a company code system	

4.3 Petrography of key thin sections

The petrographic descriptions of three key samples with Au occurrences associated with inclusions of pyrite and K-feldspar are presented in this section:

(1) NLD210-75 'Sericite'-chlorite- quartz ± clinozoisite granofels, adjoining a sheared quartz-pyrite ± chlorite vein.

Hand specimen: the sample is comprised of the contact between a very fine grained foliated micaceous lithology, with minor disseminated sulfide and a milky quartz vein, where the contact between these hosts a ~1 cm wide band of fine to coarse disaggregated, partly brecciated pyrite in a quartz-chlorite matrix, partially flowing into the vein quartz part of the slide.

As in hand specimen, this sample may be subdivided into three domains, i.e.:

A. Quartz domain comprised of near mono-mineralic recrystallized quartz

B. Pyrite domain with a strained quartz ± chlorite ± carbonate matrix; pyrite is fine to coarse grained, with prominent fibrous quartz strain fringes aligned oblique to the contact with domain C.

C. Hazy very fine mass of 'sericite'-chlorite- quartz ± clinozoisite(?) with lithofabric development. The fabric seen in hand specimen appears to be obliquely truncated by the contact with domain B, and there is an earlier(?) (weak cryptic) foliation defined by aligned quartz and mica grains as microlithons roughly orthogonal to this later (dominant) fabric, formed by partly orientated fine mica aggregates (Fig. 50A).

Domain A.

This domain is almost entirely composed of aggregates of recrystallized inequigranular polygonal quartz (effectively 100% of domain), mostly 50-250 µm in size, interspersed with larger highly strained grains, with strongly undulose extinction, of ~0.25-2 mm in *maximum* dimension. These latter (anhedral) grains are presumably representative of original vein quartz. Some of these grains display an internal preferred orientation of incipient recrystallized quartz subgrains, sub-parallel to the orientation of the later fabric seen in domain C (Fig. 50A).

This domain also contains traces (<<1%) of anhedral calcite, chlorite, subhedral-euhedral pyrite and anhedral chalcopyrite as grains or grain aggregates <200 µm in *maximum* dimension. These minerals occur as infillings between recrystallized quartz grains. The sulfides occur adjacent to chlorite-calcite masses associated with a branching fracture connected to domain B. SEM imaging indicated the presence of very fine (≤5 µm sized) galena inclusions in pyrite. EDS analysis of calcite indicated minor MgO (2.05 wt%), MnO (0.8 wt%) and FeO (0.6 wt%) content. A pyrite EDS analysis indicated a content of 0.45 wt% ZnO.

This domain partially grades to domain B, where a branching portion of this latter domain transgresses domain A, accompanying increasing sulfide content and orientated mica and quartz aggregates.

Domain B.

This domain is comprised by: pyrite: (~40%) anhedral to subhedral grains (rarely euhedral for the finer grain sizes) ranging in size from ~20 µm to ~4 mm in *maximum* dimension (median size ~1.2 mm) (Fig. 50A). Larger grains often show fracturing, with some degree of 'jigsaw' brecciation to produce at least some of the finer grain population. Jagged, consertal-type grain boundaries are typical of larger pyrite grains (>~0.3 mm), which may suggest some degree of dissolution by later fluids. Rare (<100 µm) pyrite grains are contained within quartz strain fringes.

An EDS analysis of this pyrite indicated a Zn content of 1.57 wt%. Scanning Electron Microscope (SEM) imaging along the margin of this grain, further revealed an anhedral inclusion of pyrrhotite ~75 µm across, which contains 0.32 wt% NiO and 1.36 wt% ZnO; a grain of galena ~5 µm across was also close to this grain (Zn content of 1.2 wt%; Fig. 50B). The former anhedral grain has a dull yellow appearance in plane polarized reflected light.

Scanning electron microscope imaging indicated the presence of elongate to microplaty molybdenite adjoining, or proximal to, these pyrite crystals (Fig. 27b). Molybdenite ranged in size from <1-20 µm sized grains, with the finest grains disseminated in the quartz-carbonate matrix.

Two anhedral grains of Au, ~10x25 µm and <2 µm size were identified as inclusions in pyrite (Fig. 27c). An EDS analysis indicated an Ag content of 11.92 wt%.

Chalcopyrite: (<1%) anhedral brassy yellow grains (in reflected light), often shardy in appearance, ~50-225 µm in *maximum* dimension; these grains may display marginal oxidation. Chalcopyrite is spatially associated with finely recrystallized quartz.

Hematite/goethite: (<1%) minor anhedral to subhedral grains, and oxidation coatings on sulfides; rarely as subhedral platy to acicular grains with microscale boxwork textures, <200 µm in *maximum* dimension, associated with very fine micas and clinozoisite(?). These grains were confirmed as Fe oxide by EDS analyses.

Carbonate: (~3%) typically occurs as localized masses of interlocking hazy anhedral grains (<200 µm grains) up to 1 mm or more across, overprinting fibrous quartz and chlorite adjoining coarse pyrite. Carbonate tends to be present where strain shadows are out of alignment with the later foliation. Its composition is likely to be calcite, based upon EDS analyses from domain A.

Chlorite: (~3%) anhedral, rarely subhedral pale green to colourless pleochroic grains, ~25-250 µm in *maximum* dimension, mostly occurring in as intergrowths with quartz strain fringes. Anomalous brown birefringence colours (Mg-chlorite?) are typical; an EDS analysis suggested an Fe-Mg composition (chamosite-clinochlore). Chlorite is often replaced by 'sericite', away from the strain fringes.

Biotite: (<<1%) traces of an olive pleochroic subhedral biotite (possibly of hydrothermal origin) replaced by pale green chlorite; it has a similar size range to chlorite.

Quartz: (~45%) varies from finely recrystallized polygonal grains (as per domain A), to spectacular elongated grains comprising strain fringes (up to 0.1x1 mm size) around coarse pyrite grains.

Clinozoisite (epidote): (~2%) occurs as colourless high relief subhedral fractured grains, mostly within aggregates of grains up to 0.5 mm across; this mineral is particularly concentred in aggregates on the contact with domain C. Grainsize varies from disseminated grains <20 µm, to grains ~250 µm in *maximum* dimension within aggregates. It often occurs in close association with 'sericite'.

'Sericite': (~7%) mostly occurs as diffuse masses of very fine (<15 µm size; rarely to 50 µm) grains, overprinting chlorite. Generally it is concentrated away from pyrite. It probably has phengitic compositions based on EDS analyses from domain C.

Domain C.

This domain is composed of: chlorite: (~6%) has similar grainsize and characteristics to domain B, and appears to have formed part of the earlier fabric, and has probably been subjected to later re-orientation. It is also a major part of the dominant fabric of this domain, overprinting the earlier fabric (Fig. 50D). Pale green chlorite is also particularly concentrated near the contact with domain B, where it does not display preferred orientation. Pale green chlorite also contains rare pleochroic haloes. An EDS analysis of this mineral returned a similar composition to that of domain B.

Biotite: (~2%) dark olive pleochroic subhedral to anhedral flakes of very fine biotite (characteristics as per domain B), as part of the earlier fabric, as per chlorite (Fig. 50D). It occurs mostly as grains <50 µm sizes, either as aggregates, or dispersed amongst quartz.

'Sericite': (~50%) mostly occurs as diffuse masses of very fine (<15 µm size; rarely to 200 µm) grains, overprinting chlorite. Larger (>50 µm) grains may form discernable subhedral flakes. 'Sericite' is the main mineral producing the fabric seen in hand specimen, but much of it may have been re-orientated by the later event producing the dominant fabric, as it is also seen to constitute the earlier fabric (Fig. 27d). It has phengitic compositions based on both SWIR data, and an EDS analysis (5.24 wt% FeO and 4.53 wt% MgO).

Clinozoisite-epidote: (~2%) mostly occurs as discrete colourless subhedral grains, or within grain aggregates, mostly in close proximity to the contact with domain B. Grainsize is as per domain B. Some grains may display faint yellow pleochroism.

Clinozoisite appears to replace, along with chlorite, an earlier sub-equant mineral (~1-400 µm size; possible a garnet or a pyroxene?). EDS analyses indicate up to ~11 wt% FeO, indicating that at least some of these grains are more representative of the epidote end member.

Quartz: (~40%) most quartz occurs as masses of interlobate to polygonal recrystallized quartz, cryptocrystalline to ~100 µm grainsize. Rare relicts of possible primary rounded anhedral quartz(?) to ~250 µm are also present, which show little or no strain effects.

Plagioclase: (<1%) rare strained anhedral relict anhedral grains, ~50-400 µm across, possible porphyroclasts.

Zircon: (<<1%) one rounded anhedral high relief grain, ~75x125 µm size, noted in recrystallized quartz. A single EDS analysis spot indicated a content of 1.2 wt% HfO_2.

Apatite: (<1%) disseminated anhedral to subhedral (rounded) grains, spatially associated with 'sericite' aggregates, mostly <75 µm size, rarely to 200 µm.

Pyrite: (<1%) trace of euhedral 10-100 µm sized grains in recrystallized quartz, and two subhedral grains of ~350-400 µm across.

Molybdenite: (<<1%) rare disseminated platy grains (identified by SEM imaging; Fig. 50E), no larger than 5x20 µm size, as inclusions in chlorite, typically aligned with the cleavage plane of chlorite.

Rutile: (<<1%) very fine grained (mostly <25 µm; rarely to ~40 µm) subequant grains, with marginal partial replacement by very fine (<5 µm sized) grains of titanite (confirmed by SEM imaging).

Monazite-(Ce): (<<1%) one significant subhedral (to euhedral) grain with monoclinic shape symmetry (~50x250 µm size) with a number of smaller lath-like fragments, that appear to have originated in at least in part by *in situ* fracturing of the larger grain. This larger grain is partly overgrown by clinozoisite (Fig. 27F). Its composition is confirmed by EDS analysis. Analysis of the overgrowing clinozoisite indicated ~1.2 wt% REE oxides; the veracity of this result is uncertain.

Fe oxides: (<1%) specular hematite(?) fine <25 µm grains are seen along the contact between domains B and C in transmitted light.

It is speculated that the precursor to domain C was an intermediate intrusive similar to that seen in NLD210-71, due to some similar mineralogy and textural features.

It is probable that the sulfide content has been emplaced into a shear zone, which produces the fabric seen in hand specimen. Drill core logging supports this assertion; it is also likely that the earlier (cryptic) fabric is also related to shearing, rather than being a pervasive regional fabric.

The paragenesis of this sample is difficult to interpret, due to potentially ambiguous overprinting relationships (cf., Figs. 50D and 51). A model of progressive shearing and development of fabric is favoured, with the latest foliation being that seen in hand specimen, slightly post dating the development of strain shadows, which have developed at angle to the plane of shearing (sigma 1). The latest fabric element is also associated with randomly orientated chlorite, particularly evident at the contact of domains B and C.

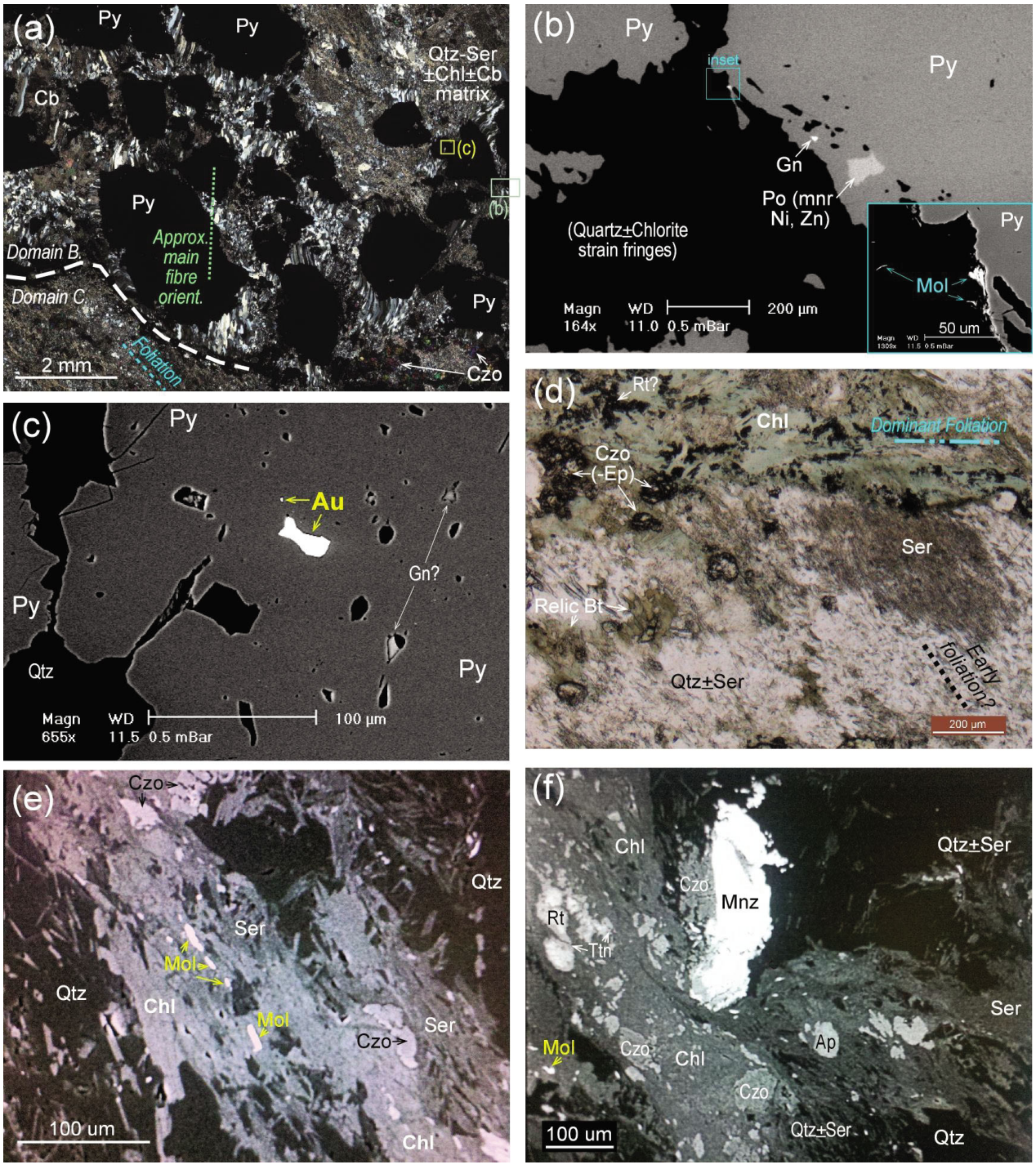

Figure 50. Photomicrographs and BSE SEM images for sample NLD210-75. (A) Contact between domains B and C, showing fabric elements, and prominent quartz strain fringes between pyrite grains in domain B. Cross polarized transmitted light mosaic image. (B) BSE image of galena, pyrrhotite and molybdenite associated with the periphery of a pyrite grain (location as per A, within domain B). (C) BSE image of Au inclusions in pyrite (location as per A, within domain B. The other inclusion species were not identified, but are likely be galena. (D) Pale green chlorite, forming part of the dominant foliation seen in domain C, overprinting an earlier fabric defined by very fine quartz-'sericite'. Plane polarized transmitted light image. (E) BSE image of very fine molybdenite dispersed in chlorite, mostly aligned with its cleavage plane. Chlorite appears to replace 'sericite' here. (F) BSE image of prominent fractured monazite grain, partly overgrown by clinozoisite; note alteration of nearby rutile to titanite, within chlorite.

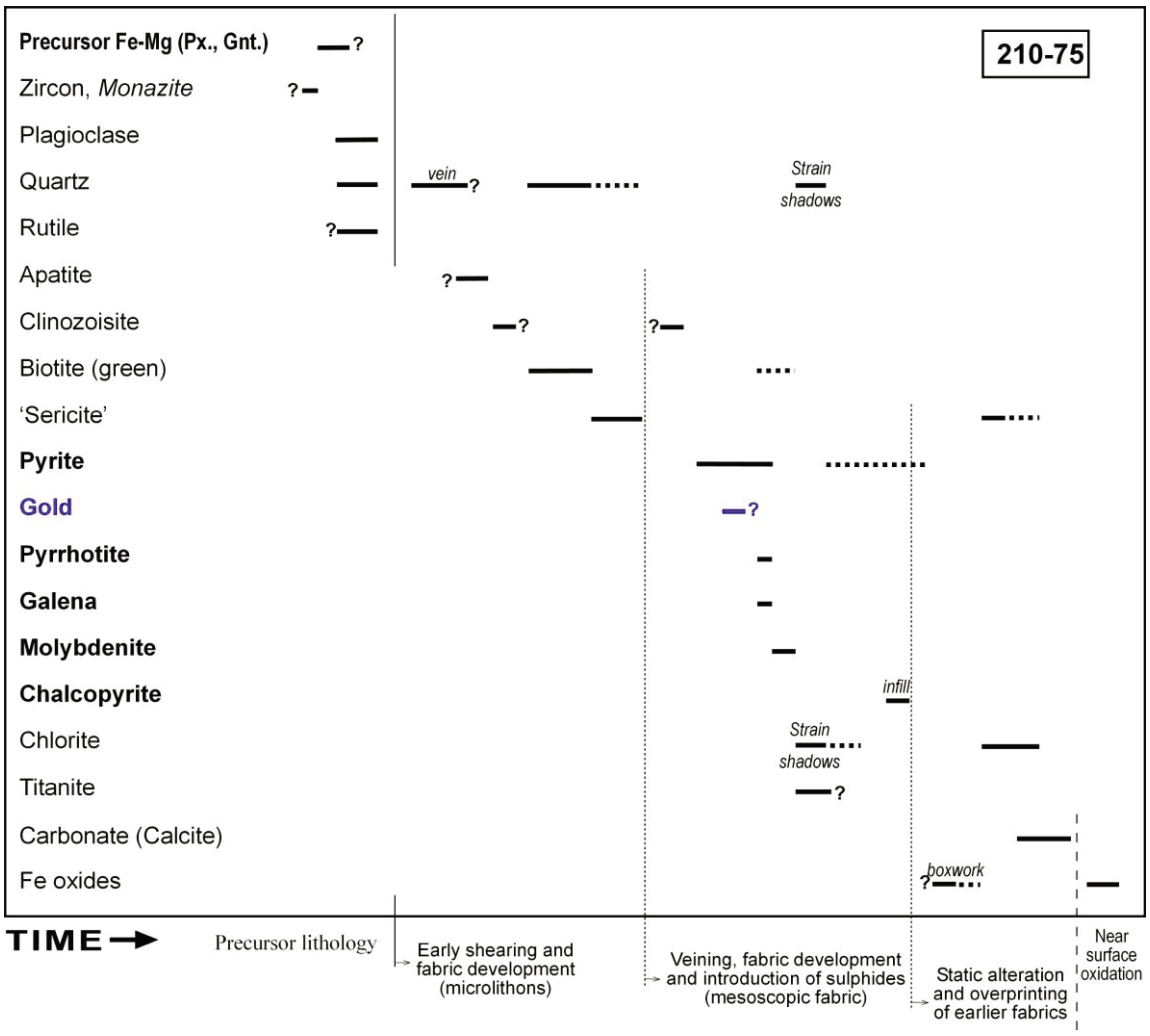

Figure 51. Interpreted paragenetic sequence for sample NLD210-75.

(2) NLD210-76 Quartz vein, with chlorite-'sericite'-carbonate segregations

Hand Specimen: milky white to grey mottled strained vein quartz with chloritic segregations and fracture fillings. Chlorite is clearly associated with fine to *medium* grained pyrite grains and aggregates.

This section is dominantly composed of recrystallized quartz, with a number of fractures or veinlets of chlorite ± 'sericite' ± carbonate (Figs. 52 and 53), mostly orientated roughly parallel in the plane of the thin section, although at a fine scale such features are randomly orientated, and may pinch out. A number of finely crystalline quartz-chlorite veinlets or fracture fillings display a preferred orientation fabric (inferred to be paragenetically early), perpendicular to the dominant fracture/veinlet orientation (Fig. 52A; tensional filling origin?).

(*Mineral percentages are provided for here the section, but are of reference value only in the context of this thin section, due to the heterogeneous nature of the sample).*

Quartz: (~91%) consists of essentially two-grain populations:

(1) Highly strained anhedral grains with consertal grain boundaries and strongly undulose extinction, ranging in size from ~0.4-2.5 mm. These grains appear to be incompletely recrystallized relicts of original vein quartz, and may have highly irregular shapes; and

(2) Recrystallized interlobate to polygonal grains mostly 50-300 µm across, forming larger (in) equigranular aggregates. Quartz associated with chlorite and fracturing tends to be ~25 µm or less in grainsize (Fig. 52A);

'Sericite': (~3%) tends to form masses of randomly orientated very fine grains <25 µm in *maximum* dimensions, often replacing chlorite. Where it is present, chlorite has been mostly replaced; rarely 'sericite' may have a pale tan colour. It may also form uncommon subhedral flakes up to ~50 µm in *maximum* dimension. It generally has a loose association with the dominant fracture/veinlet orientation of the slide. 'Sericite' has a phengitic composition, based on (Short Wave Infrared) SWIR spectra and an EDS analysis (~11 wt% FeO + MgO).

Clinozoisite: (epidote; <*1%*) has high relief, fractured colourless anhedral to subhedral grains and grain aggregates, ranging in size from ~50-250 µm across. It has a close spatial relationship to 'sericite' or 'muscovite' aggregates. Often clinozoisite aggregates within 'sericite' contain chlorite fragments, and may be associated with discolouration of neighbouring 'sericite' grains. Clinozoisite also comprises very fine (<25 µm) grains forming aggregates within a chlorite-'sericite' mass in a fracture at one end of the slide. EDS analyses indicate a significant component of FeO (~10 wt%) substitution.

Calcite: (~2%) occurs as either late stage infillings of anhedral grains, or grain aggregates, filling fractures in quartz. It may also occur as discrete disseminated grains, or as masses of polygonal textured grains replacing quartz in recrystallized veinlets in patches up to ~0.8 x 2.5 mm size. Most grains are ~35-150 µm across, with polygonal carbonate in veinlets to 250 µm. Many of the grains comprise recrystallized aggregates that appear to have at least partly pseudomorphed recrystallized quartz. An EDS analysis indicated minor Fe content (~1.36 wt%), which may relate to inclusions.

In general, calcite does not occur with 'sericite'.

Chlorite: (~2%) occurs as either unusually stubby, pale green pleochroic, subhedral flakes (~35-175 µm in max. dimension), texturally concordant with surrounding recrystallized quartz, or as masses of very fine flakes, cryptocrystalline to ~35 µm long. It commonly displays brown anomalous birefringence, suggestive of Mg enriched chlorite compositions; EDS analyses of the coarser flakes indicated a slight predominance of Mg over Fe (clinochlore compositions inferred). Most of this pale green chlorite occurs as randomly orientated fracture fillings, but it may rarely form aligned rod-like aggregates with quartz, as previously described; these chlorite grains are ~35-150 µm size in *maximum* size. It may also cut across calcite infillings (Fig. 52A, B)

Biotite: (<1%), there is a minor (relict?) component of a dark to light olive pleochroic biotite (hydrothermal origin?), intergrown with quartz, largely replaced by an associated halo of 'sericite' and chlorite associated with a fracture veinlet (≤2 mm thick) at one of the slide, of similar size and shape ranges to chlorite. This veinlet may be dilational in nature, due to locally oriented biotite and quartz within this vein. An EDS analysis indicated 0.85 wt% TiO_2 (cf., other samples).

Pyrite: (~1%). The vast bulk of pyrite in this slide is concentrated in three patches comprised of aggregates of pyrite within discontinuous chloritic segregations localized to one area of the slide. These grains are mostly anhedral, rarely subhedral, and may display a weak to moderate extent of *in situ* fracturing. They range in size from ~20 µm to ~1.4 mm in *maximum* dimension. Grains >200 µm across typically have a somewhat rounded appearance, and may have jagged grain boundaries, perhaps suggesting some later resorption or reactions. These larger grains may also contain minor quartz and/or 'sericite' inclusions.

Other pyrite occurs as disseminations, usually proximal to aluminosilicate minerals. These grains are euhedral to anhedral, not fractured, and range in size from <10 µm to ~100 µm across. These are inferred to represent a later generation (Fig. 52c).

Chalcopyrite: (<<1%) occurs as ~10 µm to 50x300 µm size anhedral bright yellow pitted anhedral grains, either as infillings (<25 µm size) within polygonal carbonate aggregates and (rarely) pyrite or as larger grains proximal to pyrite and/or 'sericite' aggregates (Fig. 52C, D).

Galena: (<<1%) occurs as rare ≤10 µm sized inclusions in pyrite (mostly <1-5 µm; Fig. 52D). It is the most common non-silicate inclusion type in pyrite.

Arsenopyrite: (<<1%) one ~10 µm (length) bladed crystal inclusion in pyrite.

Sphalerite: (<<1%) one occurrence (<5 µm wide) within a fracture in pyrite.

Gold: (<<1%) SEM imaging indicated the occurrence of traces of very fine (≤10 µm) grains as anhedral inclusions in pyrite. Gold also occurred in fractures in pyrite, adjacent to Au inclusions (Fig. 52E). This latter Au occurrence was also proximal to the occurrence of chalcopyrite and other sulfide inclusions in pyrite. It is possible that there are two separate, but related Au deposition events.

Two EDS analyses of Au indicated Ag contents of 21.7 and 31.2 wt%, for inclusion and fracture filling Au occurrence types, respectively.

A ≤3 µm sized particle of an Ag mineral was identified by SEM imaging within fine-grained 'sericite', proximal to titanite (Fig. 52F).

Tsumoite (<<1%) SEM imaging and EDS analyses indicated the presence of a few particles of stoichiometric BiTe, as very fine (≤5 µm) micron inclusions on the margins of some pyrite grains.

Titanite: (<<1%) aggregates of (relict) high relief anhedral grains of ragged appearance spatially associated with 'sericite' and pyrite (aggregates), ranging in size from <10 to 100 µm across. They invariably occur as inclusions in chlorite or 'sericite'. SEM imaging indicated that these grains may contain exceptionally fine (µm scale) inclusions of rutile (Fig. 29F); presumably primary rutile has been largely replaced by titanite. Two analyses of titanite indicated minor FeO content (~2.05 wt%).

Apatite: (<<1%) is present in races of <10 µm grains associated with the previously described biotite-rich fracture.

Hematite(?): (Fe oxides; <<*1%*) is present as minor anhedral grains <50 µm across associated with pyrite and 'sericite'.

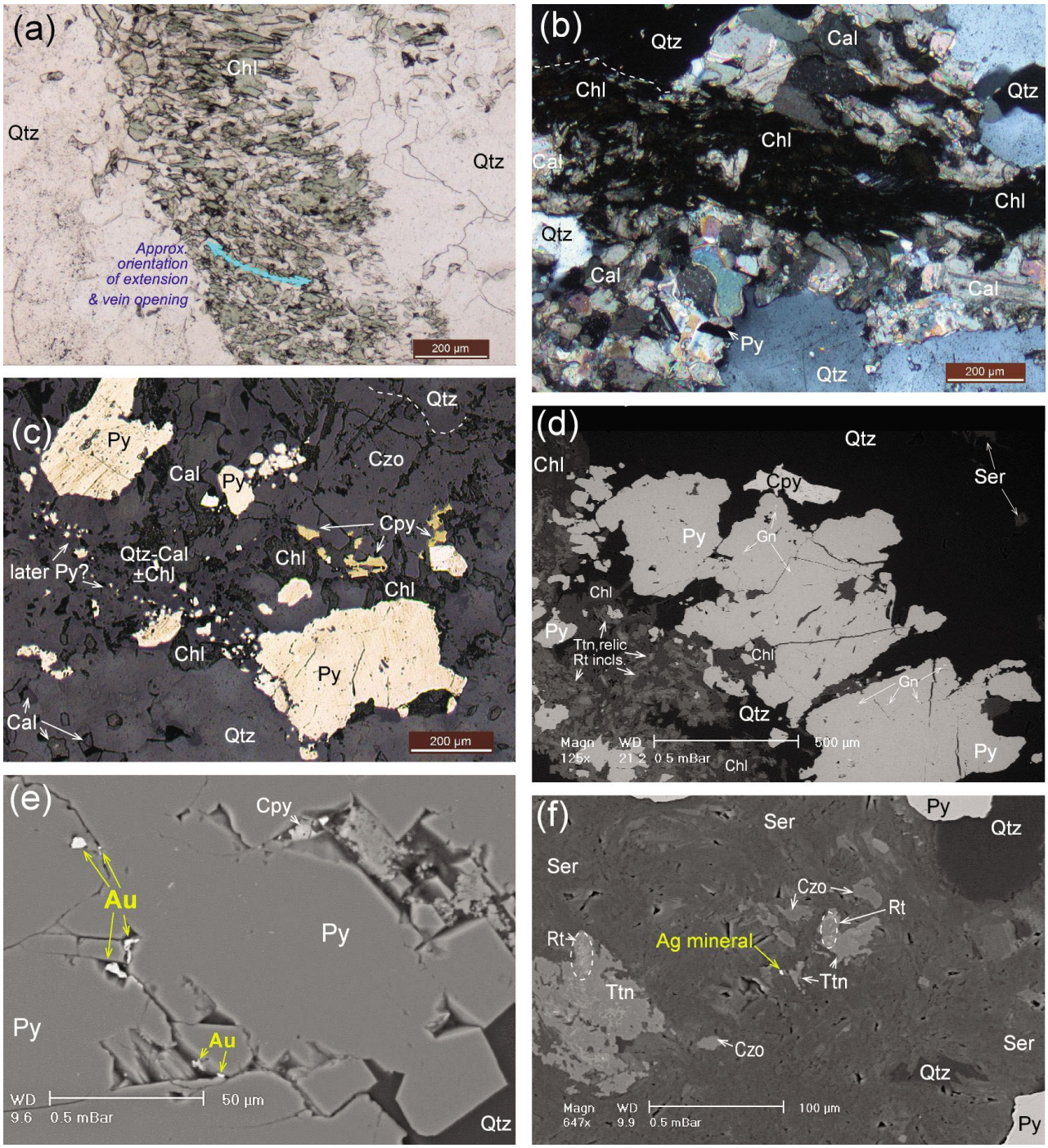

Figure 52. Photomicrographs and BSE SEM images for sample NLD210-76. (A) Detail of fabric developed in a tensional recrystallized quartz-chlorite veinlet. Transmitted plane polarized light image; (B) Chlorite infilling (at extinction) cross-cutting a calcite veinlet in quartz. Calcite may pseudomorph recrystallized quartz in places. Cross nicols light; (C) Typical cluster of pyrite grains with subordinate chalcopyrite, with associated chlorite-calcite-clinozoisite. Note trail of finer pyrite grains, interpreted to be of a slightly later generation. Reflected plane polarized light image; (D) BSE image of pyrite grains with very fine galena inclusions, adjoining a mass of intimately intergrown chlorite and titanate; (E) BSE image of detail of Au inclusions in pyrite, as both internal inclusions, and associated with fractures in the host. The latter type of Au appears to have been introduced after the pyrite crystallized; and (F) BSE image of 'sericite' with inclusions of titanite, clinozoisite and a very fine Ag mineral (type indeterminate). Titanite contains relic fragments of rutile (indicated).

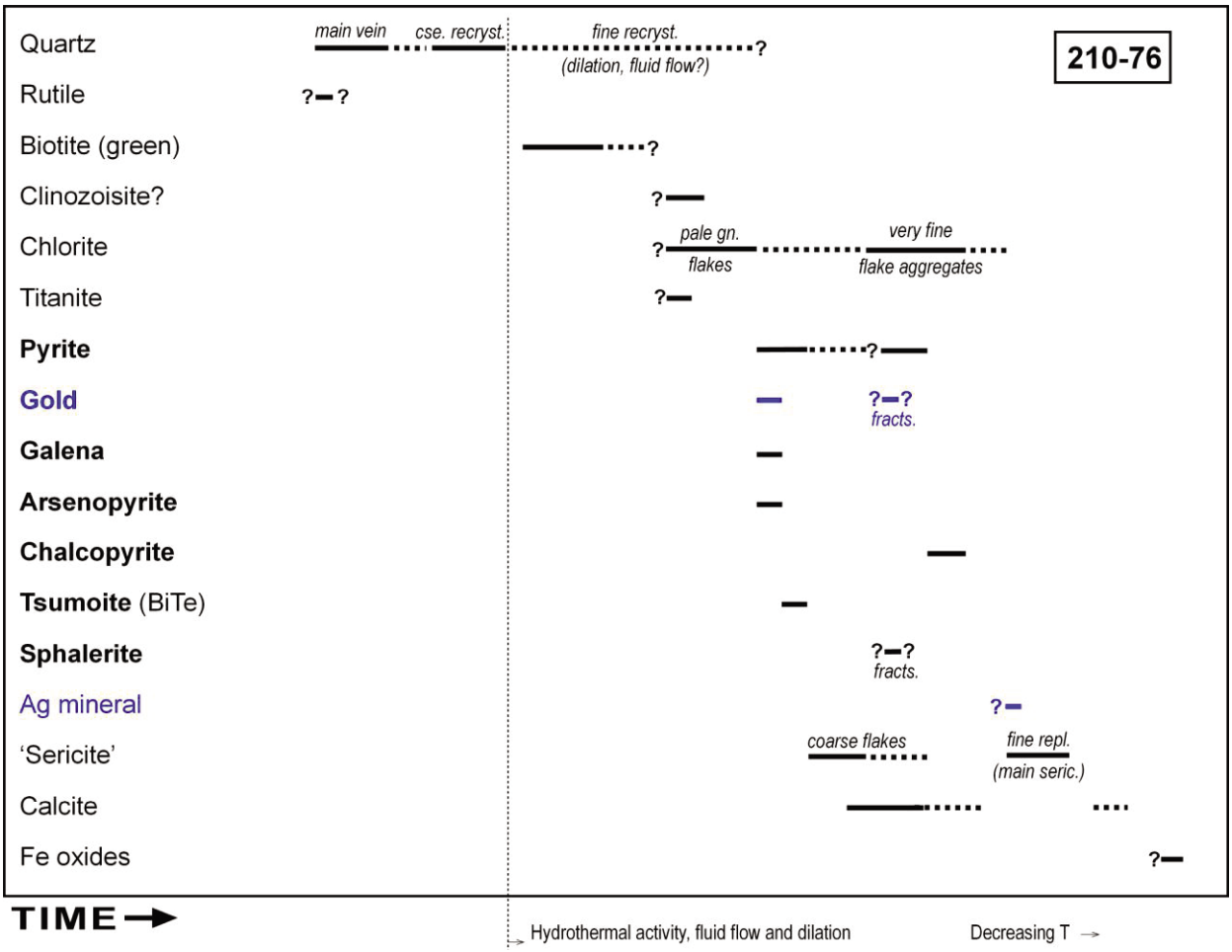

Figure 53. Interpreted paragenetic sequence for sample NLD210-76.

(3) NLD071-41 'Sericite' ± chlorite altered granitoid

Hand specimen: dark green-grey fine to *medium* grained chlorite altered lithology with pink mottling, and relict *medium* grained (1-2 mm sized) feldspars (plagioclase?). Probably a strongly altered felsic to intermediate intrusive.

Thin section: essentially this sample is comprised of an original felsic igneous intrusive that has been overprinted by 'sericite' ± chlorite alteration (Figs. 54 and 55). The extent of this alteration varies from moderate to strong. It is most probable that the original rock was a granite or monzogranite, which had undergone a variable amount of brittle deformation (up to cataclasis) and recrystallization prior to the alteration event.

A particular feature noted in this section are ~1-3 mm wide shear bands comprised of anastomosing foliated fine chlorite (replacing relict biotite) and quartz cataclasite. Some asymmetric type textures are present in these bands. Fractures filled with hematite and 'limonite' (and earlier 'sericite') run through the centre of these. Typically, the shear band foliation is oblique (crenulated?) to the orientation of the band itself, and therefore the foliation is discontinuous. These bands probably pre-dated the pervasive alteration event.

Discontinuous late hematite-'limonite' filled fractures also are oriented orthogonally to the shear bands (in the plane of the thin section, displayed in Fig. 54A).

Thus, there appear to be three fabric elements: (1) shear bands, with parallel Fe oxide filled fractures; (2) Fe oxide filled fractures orthogonal to (A); and (3) a discontinuous preferred mineral orientation preserved in micas within the shear bands, which bisects the plane between (A) and (B).

Original mineralogy *(ratios are a reconstructed estimate of the precursor rock only; these are not consistent across the section*):

Plagioclase: (~20%) occurs as weakly to moderately 'sericitized' anhedral to subhedral grains with recognizable albite twinning. These grains range from ~300-700 µm in *maximum* dimension. Scanning electron microscope EDS analyses indicate these grains have a fairly consistent composition of Ab_{96-97}.

K-feldspar: (orthoclase?; ~*45%*) has largely been replaced by 'sericite'/muscovite. Original grains appear to have had anhedral/xenoblastic shapes, ranging in size from ~0.25-1.2 mm in *maximum* dimension. Little reliable twinning (simple twinning) was observed, but some evidence was found for primary igneous zoning.

Quartz: (~30%) forms anhedral/xenoblastic irregular, highly strained (undulose extinction) grains, ranging from ~100-800 µm in *maximum* dimension, with minor subordinate (relatively) equigranular polygonal recrystallization (mostly <100 µm). Quartz also forms the majority of fine cataclastic fragments, mostly <50 µm size, rarely to ~100 µm.

It is possible that this quartz includes vein content prior to the alteration event, but no veins are extant.

Biotite: (~5%) comprised of anhedral (rarely subhedral) relict grains, partially to completely replace (chiefly) by chlorite. These grains display pleochroism from straw-brown to orange russet brown colours. Biotite relicts are usually <100 µm in *maximum* dimension, but occasionally may be up to ~0.5x1.5 mm size. Larger grains display undulose extinction. Pleochroic haloes around very fine grains (<25 µm size) are rare.

Zircon: (<<1%) occurs as traces of rounded zircon grains, <75 µm across, were noted during SEM EDS analyses.

Apatite: (<<1%) occurs as races of subhedral sub-rounded grains of apatite, <125 µm across were noted in quartz. Scanning electro microscope EDS imaging revealed <1-20 µm (max. dimension) allanite(?), (tentative identification of a LREE silicate) grains within, and proximal to these grains.

Alteration mineralogy: (ratios *where stated are estimates for the entire section "as is" for given minerals; the remaining % is derived from the primary mineralogy*)

Muscovite/'sericite': (~40% overall) typically occurs as colourless very fine (<25 µm sized) flakes, mostly replacing feldspars (locally up to 90% of grains). This mineral may also occur as a matrix to finely recrystallized or cataclastic quartz.

Chlorite: (~10%) pale green subhedral flakes, sometimes-weakly pleochroic, mostly concentrated in shear bands, or associated with fractures, as well as replacing primary biotite (Fig. 54B). Anomalous blue birefringence colours are typical. These grains range in size from cryptocrystalline up to ~150 µm in *maximum* dimensions, but often occur as hackly masses (Figs. 54B and 54D), without any preferred orientation.

Biotite: hydrothermal(?), Fe-rich chlorite(?; <<1%) Minor deep green pleochroic subhedral grains ≤125 µm in *maximum* dimension, comprised of finer (≤10 µm size) grains). It is possible that these have replaced a mineral such as an earlier amphibole.

Gedrite(?): (<<1%) traces of relicts of stubby prismatic crystals (<100 µm size), largely replaced by chlorite (Fig. 54B), have a composition corresponding to (ferro-) gedrite, from (2) EDS analyses. It is possible that this composition has resulted from the mixture of two or more minerals, but repeated analysis returned a consistent composition. The morphology of one of these grains appears to be approach the habit of a pyroxene, which could indicate two stages of replacement. In transmitted light these grains have a mottled dark green colour (Fig. 54D).

Actinolite-tremolite: (<<1%) Elongated colourless subhedral grains, up to 300 µm long and 75 µm wide. An actinolite-tremolite composition is confirmed by EDS analyses. It is typically associated with chlorite and shear bands.

Titanite: (<1%) traces of high relief subhedral crystals (<50 µm long) intergrown with actinolite-tremolite; SEM imaging also indicates titanite relicts within chlorite.

Clinozoisite/epidote: (~3%) subhedral to anhedral colourless grains or grain aggregates (<50 µm across), high relief, associated with chlorite and green chamosite(?) in shear bands, or more commonly, disseminated in altered feldspars with 'sericite'.

Accessory and opaque minerals (*% where stated are estimates for the entire section "as is"*):

Ilmenite: (<1%) anhedral to euhedral grains (isotropic in reflected light) ranging in size from ~0.2-0.8 mm (max. dimension). These grains show slight marginal oxidation/alteration to 'limonite', as well as an earlier phase of alteration to rutile.

These grains may have a primary origin, as they have undergone limited deformation (some brittle fracturing), as well as minor replacement by chlorite suggestive of a paragenesis prior to alteration.

Pyrite: (<<1%) occurs as very fine (<35 µm) subhedral to euhedral disseminated grains. It may have a primary association with quartz. In one location pyrite fills a fracture veinlet (<50 µm wide); two weakly oxidized subhedral pyrite grains up to 150 µm in *maximum* dimension occur adjacent to this vein. Is it possible that pyrite was a major constituent of the veinlets running through the shear bands prior to oxidation, which are now infilled with Fe oxides (?).

'Limonite'/hematite: late stage cryptocrystalline infill of fractures (Figs. 54A, C); they also replace earlier ilmenite and pyrite (veinlet). SEM imaging indicates the presence of micro-scale boxwork textures. Additionally, there is likely to be a component of very fine Fe oxide dispersed in primary K-feldspar, based on EDS analyses.

Gold: occurs as a single subhedral grain of truncated tetrahedral form, ~10 µm across. It occurs within K-feldspar, adjoining Fe oxide and 'sericite' altered albite (Fig. 54E). SEM EDS analyses indicate that it contains no detectable Ag content. This grain is associated with an orthogonal fracture as previously described.

Synchysite-(Ce)?: (<<1%) SEM-EDS has determined the presence of tabular subhedral-euhedral crystals of a cerium rich rare earth carbonate (most probably synchysite-(Ce): $CaCe(CO_3)_2F$) growing on the edge of a partially altered ilmenite grain (Fig. 54F). The crystal habit of these grains also corresponds to that known for synchysite.

Barite: (<<1%) trace of <5 µm sized grains spatially associated with 'sericite'.

Comment: this altered granitoid appears to have been influenced by at least two distinctly different fluids. It is probable that a metasomatic fluid, possibly related to a mafic or ultramafic source has been involved due to the presence of gedrite(?) together with the presence of traces of Ni and Cr in a number of different alteration species. The intersection of the various structural elements identified here has probably facilitated fluid flow associated with alteration and mineralization.

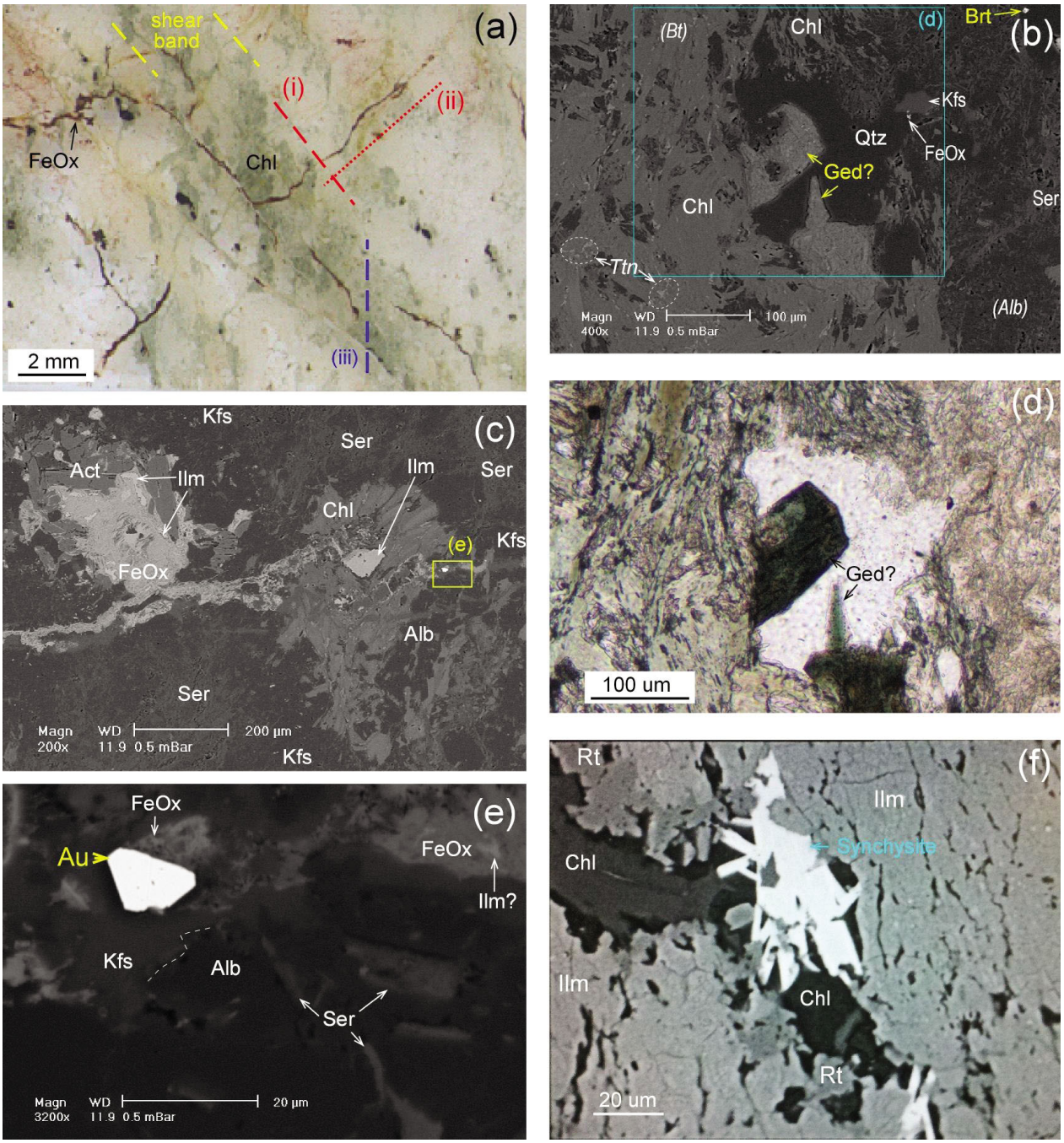

Figure 54. Photomicrographs and BSE SEM images for Sample NLD071-41. (A) Unpolarized light image displaying the three structural elements visible in the plane of the thin section. Orientation (i) contains both the shear band orientation and an earlier ('sericite') and later (Fe oxide) fractures. Orientation (ii; Fe oxide) is spatially associated with the Au grain (E). Orientation (iii) is defined by a preferred mineral orientation within the shear bands; (B) BSE image of relict gedrite(?) crystals, possibly replacing an earlier mineral (possibly a pyroxene?) occurring within quartz; (C) BSE image of an Fe oxide filled fracture (replacing ilmenite and pyrite), associated with a Au grain. Note heterogeneity of the alteration mineralogy; (D) Transmitted plane polarized image of a portion of (B), showing gedrite(?) crystals; (E) BSE image of detail from (C) showing location and morphology of Au particle (white), spatially associated with Fe oxides after ilmenite/pyrite, at the contact between altered albite and K-feldspar; and (F) BSE image of platy synchysite-(Ce) crystal clusters (white), growing on the periphery of a large (~0.2x0.8 mm) ilmenite grain, with marginal replacement by rutile.

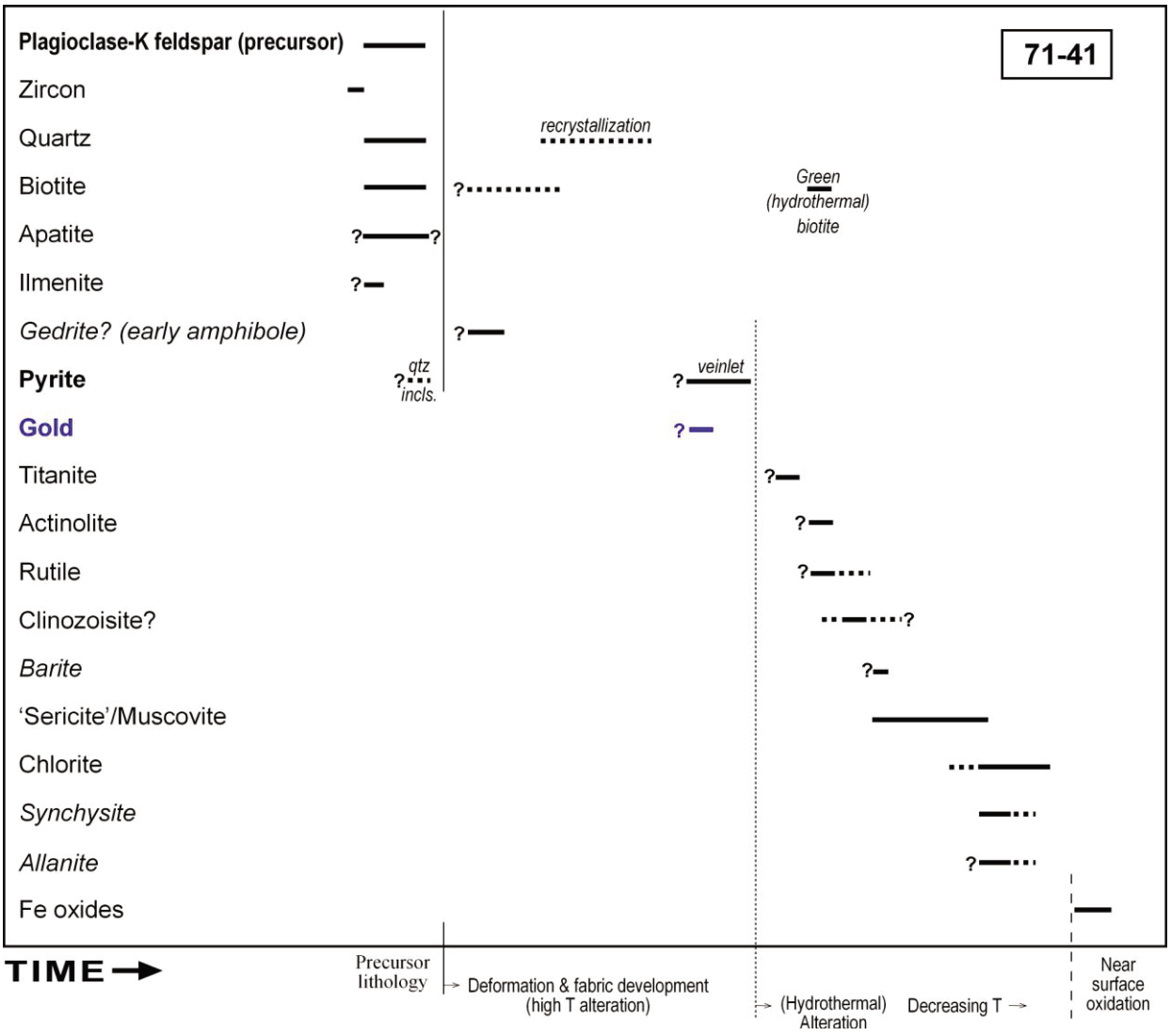

Figure 55. Interpreted paragenetic sequence for sample NLD071-41.

4.4 Discussion and conclusions

The most important conclusion from this petrographic study is that there are two distinct styles of Au mineralization between the two geographically separated sub-areas (Hercules and Atlantis) drilled at the Neale project area (Figs. 46, 47 and 48; Table 3). These styles have been deduced from the composition and associations of the Au particles observed at Hercules and Atlantis. The assertion of the presence of two generations of Au mineralization is surmised rather than a direct observation. This is partially on interpreted on the basis of geochemistry based on elemental assemblages of accessory minerals (including sulfides). The occurrence of two styles is further supported by larger scale studies of related Au prospects (Salmon Gums, Woodline and Beachcomber) in the AFO (Chapters 3 and 6).

Gold contents were identified in both prospect areas. Hercules (represented by holes NLD097 and NLD210) has Au occurring mostly as very fine (≤25 µm, mostly <10 µm) inclusions bound in pyrite, from three of eight samples. The Au of this area has a Ag content of between 12-46 wt%.

With the exception of two samples (both without Au particles), all samples studied from Hercules contained Cu minerals (typically chalcopyrite). In the highest grade Au sample (4.8 ppm Au from NLD210-77), sulfides (and consequently Au) are hosted in a chloritic (± 'sericitic') dilational jog within the quartz vein. This sample also contained traces of Cu-Pb-Zn-Bi-Te-W bearing accessory minerals. Company logging suggests that this vein may occur as later brittle fractures within a mylonitic(?) shear zone.

In the southern area, Atlantis, (in hole NLD071) Au was represented by only one particle, (~10 µm size) which displays a partly crystalline, truncated, crystal habit. This particle occurs in K-feldspar, chlorite and 'sericite', within a 'sericite'-chlorite altered granitoid. It contained no detectable Ag content.

In relation to the distribution diagram of accessory mineral based geochemical signatures (Fig. 34; Table 2), the accessory mineralogy of the two areas associated with anomalous Au may be summarized as:

Hercules: LREE-Ba-Cu-Pb-Zn-Ni-Pb-Bi-Te-As-Ag-Mo-W

Atlantis: LREE-Ba-Cu-Zn-Ni-Mo-Bi-Te; with proximal B bearing minerals (axinite, tourmaline) proximal to mineralization in some samples.

Conversely, the lack of arsenopyrite (and As bearing minerals in general) is striking. The presence of B minerals (especially axinite) suggests at least local metasomatism, due to interaction of felsic magmatic fluids with carbonates.

In general terms, from the study of these samples, an increase in Au grade is accompanied by a general increase in the number of accessory minerals bearing the above elements. In both Hercules and Atlantis, the greatest range of elements occurs in the southernmost drill holes (i.e., NLD210 and NLD070, respectively). In the case of Atlantis, most of the drill holes have few anomalous elements accompanying Au, but there is a virtual linear increase in the number of anomalous elements to the south.

The occurrence of axinite indicates at least local metasomatism in NLD69-20, where late quartz veins cross-cut an earlier near-orthogonal set of calcite tension gashes.

In terms of parageneses, sulfides (and consequently Au) have a relatively late paragenesis with respect to the rest of mineralogy of the samples in the felsic intrusive related samples. Sulfides are most commonly associated with biotite and 'sericite' (muscovite), with varying amounts of actinolite, clinozoisite/epidote, and chlorite. In the mylonitic samples, sulfides mostly post-date deformation, and may be associated with (static) biotite, chlorite and muscovite/'sericite'. Rutile may occur rarely with these minerals in both sample types. Commonly rutile has been altered to titanite. This latter reaction may have occurred at least in part due to a reaction between Ca^{2+} liberated from alteration of calcic plagioclase to albite and pre-existing rutile (and possibly ilmenite).

The primary Ti-rich nature of the suite is evident in most samples. The main opaque non-sulfide phases are rutile and ilmenite. Additionally, some granitoid samples also contained orange brown biotite, which was demonstrated to be enriched in TiO_2 (up to 5.3 wt% TiO_2). It is probable that ilmenite, and possibly rutile (in some cases) were the earliest minerals, as accessories of the intrusive suites. This observation in turn, could be used to infer an ilmenite series granitoid affiliation (cf., Ishihara, 1998), which if confirmed would indicate an affiliation with reducing type granites known to be associated with compressional tectonics, typically occurring on accreted continent margins. Although the exact type of protolith felsic intrusives commonly could not be defined due to alteration and deformation, a number of these rocks had granodiorite or intermediate affinities. The occurrence of garnet and possible primary muscovite may indicate that at least some of these granitoids could also have S-type affinities (cf., Chappell and White, 2001).

Geochemical classification of whole-rock data from Neale indicated a very diverse range of rock types and geochemistry (Chapters 2 and 6). This is reflected to some degree in the results of petrographic studies here (cf., Table 2), but is especially well reflected in core logging of the holes sampled here. The dominance of rocks with andesite/basalt or intermediate chemistries is consistent with the common occurrence of metadiorite, metasyenite and other meta-intermediate intrusive igneous rock types in many intervals of drill core. More mafic rock suites identified may relate to chlorite-rich sheared intervals and/or metagabbroic relicts identified in the McKay Creek Metasyenogranite lithologies by Spaggiari et al. (2011). The intermediate and metadioritic rocks are attributed to have an origin relating to hybridization between alkaline granitoids and metagabbro. It should be further commented that the impact of mylonitization and fabric commonly seen in many of the petrographic samples examined here has mostly likely had a significant effect on lithochemical compositions, and their diversity (cf., Chapter 3).

These combinations of the elemental signatures of these samples from accessory mineral chemistry, combined with common ilmenite-bearing granitoids with the presence of common granitoids suggest the possibility characteristic of intrusion related Au. In combination with this, the dominance of ilmenite (and related Ti minerals) in the intrusives present suggests that there may be an affinity with reduced intrusion-related Au systems (RIRGS) (e.g., Lang and Baker, 2001; alternatively named 'Au porphyries' in older literature). These Au systems are generally characterized by a Au-Bi-Te-W (-As-Mo-Sb) metal assemblage genetically linked to the emplacement of granitoids. A further key feature of this mineralization style is the development of distinct metallogenic zonation (Figs. 56 and 57). If significant carbonate or calcsilicate units are present, skarn type mineralization may also be a possibility (cf., Figs. 56 and 57). It should also be emphasized that this style of mineralization may also contain a structurally controlled component, with Lefebure and Hart (2005) documenting the presence of mineralized shear-veins in fault systems outside of the immediate plutonic environment. In the case of this area, it is probable that there would be large-scale fluid, and possibly magma emplacement, episodes associated with the major shear zones in the region of the project area.

The regional importance of these element signatures is also supported by the findings relating to other study areas (Chapter 3), where a Cu-Bi-W-(Zn) signature was documented associated with the second type of Au mineralization. Additionally, Sipa Resources (2010) reported a Bi-Te-Mo signature associated with >20 ppb Au-in-calcrete anomalies in their Woodline project area.

In any case, the presence of widespread Au and Cu mineralization together with phyllosilicate altered felsic granitoids supports the possibility of disseminated types of mineralization being present. Sample NLD097-59 contains Cu mineralization associated with a quartz-'sericite' vein in a phyllosilicate altered granitoid, of a style similar to that of porphyry Cu systems. The importance of the Au-Cu association here is further reinforced here by the aforementioned findings described in Chapter 3.

It is suggested that this mineralization could be related to later Mesoproterozoic granites of tectonic stages I (~1.3-1.2 Ga) and II (~1.2-1.4 Ga) of Spaggiari et al. (2009; and references therein), which also affected Biranup Zone lithologies. The possibility of a Mesoproterozoic age for Au mineralization is considered and discussed by Spagiarri et al. (2011). However, as the known granites of these ages are at least ~45 km away to the south-west (cf., Spaggiari and Pawley, 2012). Alternatively, such signatures could be redistributed or reworked relicts of earlier events.

The difference in fineness (Au-Ag ratio, calculated as 100 x Au/(Au+Ag)) between the two areas is striking, and needs to be followed up with a geochemical confirmation, preferably on a regional scale. The higher (and variable) Ag content of the northern area is distinctive, and also supports an intrusive or porphyry style of mineralization together with other data derived from mineral chemistry. The locating and studying more discrete Au particles *in situ* will also be most helpful in support of this objective.

As common in many other mineralized districts, it is most likely that there is more than one style of Au and/or base metal mineralization types, although more than one of these may not necessarily be of direct economic interest.

Additionally, the mylonites themselves are potential hosts for mineralization, as indicated by samples from NLD210. For example, overprinting of mylonites by remobilized Ag-Au-Cu-Pb-Zn bearing fluids at the Hongtoushan Volcanic Hosted Massive Sulfide (VHMS) deposit in China (Gu et al., 2007). In the case of lode Au mineralization, similar overprinting relationships have been documented in the Massif Centrale of France, where pre-existing mylonite zones have been subject to later fracturing, alteration and introduction of auriferous fluids (Bouchot et al., 1989); this scenario is particularly relevant here in relation to observations of mineralized samples inferred from hole NLD210. Additionally, auriferous shear zone hosted lodes are closely associated in space with mylonite zones at the late Archaean Renco deposit, Zimbabwe (Kolb et al., 2003).

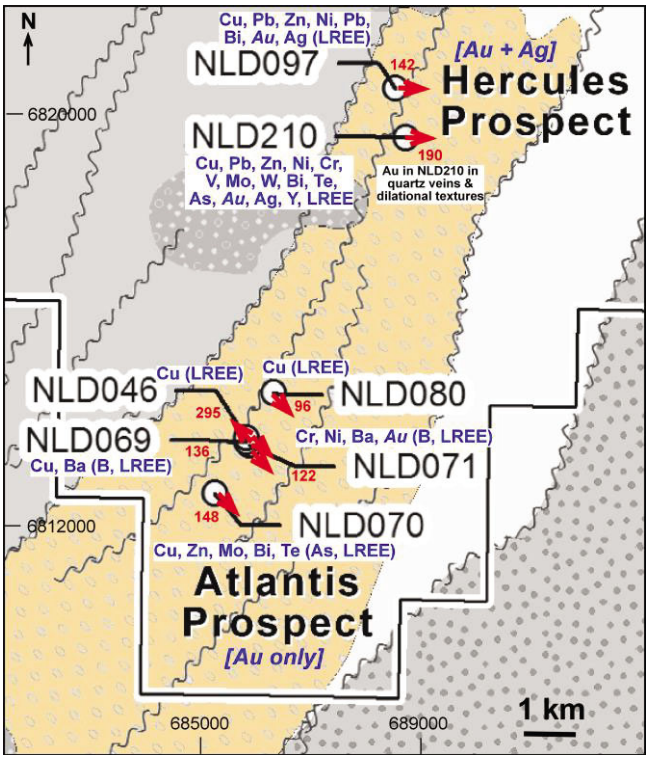

Figure 56. Schematic diagram of the spatial distribution of minor element signatures (elements in blue) of selected samples with anomalous Au values, in relation to drill hole collar locations in the Neale project area. Differences between the Atlantis and Hercules prospects are highlighted. It must be emphasized that this diagram pertains only a summarized signature derived from accessory minerals assemblages of auriferous samples. Geological units are as per Fig. 48A; only the host McKay Creek Syenogranite is highlighted in colour. Orientations of drill holes and depths (in metres) of diamond drill holes are indicated in red. All drill holes are inclined at -60° at surface, with drill hole traces oriented in the direction of the arrows.

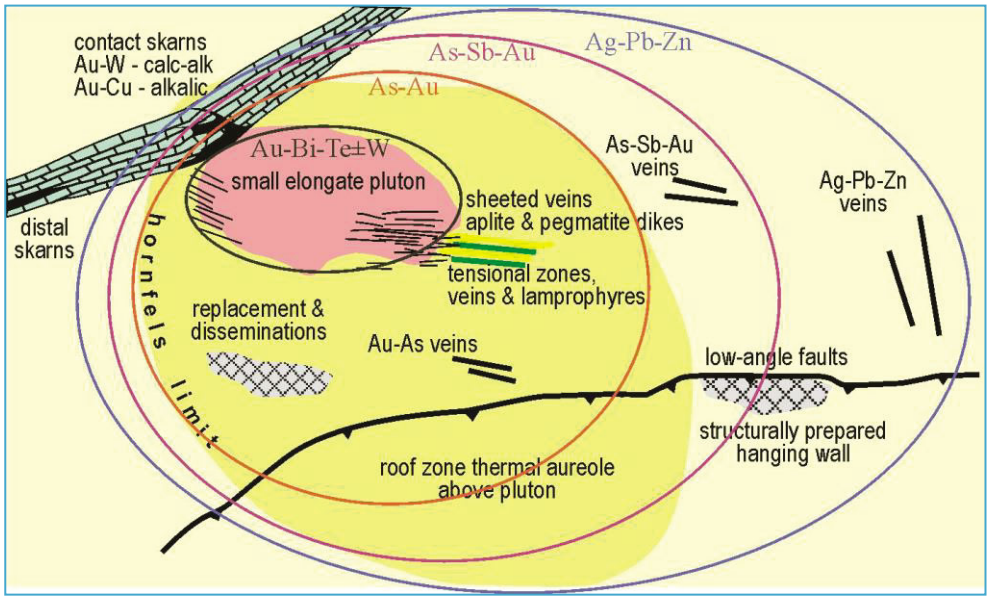

Figure 57. Conceptual model of metallogenic zonation, and varied mineralization styles, developed around a pluton associated with intrusion related Au mineralization, developed from studies of Alaskan examples of this mineralization type (Hart, 2005).

Table 3. Summary of mineralogical data by sample, for rock forming minerals containing anomalous elements, plus boron, sulfide, telluride and rare earth element mineral species. Note that it has not always been possible to assign a specific mineral type to results from EDS analysis in all cases.

Sample No.	**046_01**	**069_20**	**070_31**	**070_34**	**071_41**	**080_48**	**080_51**	**097_55**	**097_57**	**097_59**	**097_61**	**210_71**	**210_75**	**210_76**	**210_77**
from (m)	129.90	74.20	102.80	125.75	81.20	60.70	83.88	90.00	90.45	122.50	133.50	95.30	165.90	166.60	167.90
to (m)	130.10	74.40	103.00	125.95	81.40	60.85	84.05	90.15	90.65	122.70	133.70	95.50	166.05	166.80	168.00
Au (ppm)	**0.5**	**0.336**	**0.308**	**0.576**	**0.121**	**0.3**	**0.133**	**0.3**	**0.3**	**0.3**	**0.3**	**0.367**	**0.478**	**0.477**	**4.806**
Generalized host rock type	**My**	**Fs**	**Q Vn**	**My**	**Fs**	**My**	**My**	**Fs**	**Fs**	**Fs**	**Fs**	**Fs**	**Gf**	**Q Vn**	**Q Vn**
SILICATE AND OTHER MINERALS WITH ANOMALOUS ELEMENTS (AS INDICATED)															
K-feldspar		Ba													
Chlorite, 'sericite'					Ni,Cr					Ba		Cr			
Muscovite												Cu			
Biotite						Cu			Cu			Cu Cr			
Clinozoisite (epidote)												Cu Zn	REE w. mnz		
Titanite															Mo
Actinolite												Cr			
Magnetite?												V Cr			
BORON SPECIES															
Tourmaline		x									x				
Axinite		x													
SULPHIDES															
Pyrite	x	x	x	x (Zn)		x	x		x (Cu,Zn ,Ni)	x	x (Cu,Ni)	x	x (Zn)	x	x
Pyrrhotite						?					?		x (Ni,Zn)		
Chalcopyrite	x	x	x	x*					x	x	x		x	x	x
Bornite	x			x*						x					
Chalcocite				x (in Ccp)											
Galena			x (free & py)						x			x	x	x**	x**
Sphalerite									x					x**	
Arsenopyrite														x**	
Molybdenite													x		
TELLURIDES AND OTHER BASE METAL SPECIES															
Bismuth species										x					x
Mo-Bi-Te±Cu±As				x											
Tsumoite														x	x
Scheelite?[1]															x
Barite					x										
RARE EARTH MINERALS															
Allanite	x	x			x				x			x			x
Monazite				x		x		x (Th)	?		*		x		
Synchysite					x (ilmen)										
Xenotime															x
GOLD AND SILVER															
Au					**x**					**x**			**x**	**x**	**x**
Ag% of Au					**0**					**46**			**12**	**22 & 31**	**23**
Au host					**alb-Kfs-FeO**					**musc-seric**			**pyrite (Zn)**	**pyrite**	**pyrite**
Pb-Mo±Ag															x
Ag species?														x	

*Possible trace Indium in chalcopyrite and bornite (at ~ detection limit); **occur in close proximity to Au, as mutual inclusions in pyrite; [1]most probable identity of W mineral occurring as an inclusion in apatite; codes for generalized rock types: My = mylonite, Fs = felsic intrusive, Gf = granofels, Q Vn = Quartz vein.

4.5 Recommendations for further work

Further structural studies of drill core are required. Any orientations in 3D space that can be obtained from this (and other) drill holes sampled here would be most valuable for constraining basement architecture. This would also be of great value in constraining structural controls on mineralization. However, these orientations would need to be mostly derived from orientation data from the drill core. The mylonite zones in particular contain a number of potential kinematic indicators (e.g., asymmetric porphyroclasts and C/S fabric), which would be potentially invaluable for understanding the tectonic history of the basement.

Follow up petrology and mineralogy needs to be carried out on adjoining unaltered rock units, to assist in constraining changes due to deformation (e.g., mylonitization) as well as alteration.

The presence of anomalous element contents in silicate and sulfide minerals may be particularly useful to examine in other samples from these drill holes, in order to elucidate elemental zonation patterns that may serve as distal indicators of mineralization. This is particularly pertinent for intrusion related Au systems, where these systems are known to exhibit regional zonation patterns of specific metals (Fig. 35). Additionally, the mineral chemistry of species such as tourmaline may serve as useful petrogenetic indicators, due to them being able to incorporate a wide range of different elements.

The possibility of intrusion related Au system mineralization, as an exploration target, may need to take into account the likelihood that associated reduced granites will have flat magnetic signatures due to the absence of magnetic minerals in large part (Lefebure and Hart, 2005). In terms of surficial geochemical haloes, Lefebure and Hart (2005) indicate the presence of distal Sb and proximal Bi with these deposits from the Yukon. Regolith indicators of W, Au, As and Bi were documented for heavy mineral and silt samples in an Alaskan-Canadian (subarctic) context. The value of these other elements in geochemical prospecting has already been indicated by the occurrence of Bi-Te-Mo with Au in calcrete geochemical anomalies at Woodline (Sipa Resources, 2010; Chapter 2)

An extensive range of different minerals were identified in these studies that are potentially suitable for geochronological studies. These minerals include zircon, monazite, galena, pyrite and K micas of different paragenetic stages, which may be used to constrain upper and lower boundaries for Au mineralization and potential proxy mineral species (e.g., tellurides).

A range of minerals is available for thermobarometric studies. It is recommended that a range of different thermobarometers be used to provide a range of constraints for understanding conditions of formation of mineralization and alteration. The relative abundance of Ti minerals could permit the use of a number of Ti thermobarometers (e.g., Ti in quartz, Ti in zircon, Zr in rutile and Zr in titanite).

The occurrence and composition of certain early stage minerals such as gedrite should be confirmed, as these may provide useful information on the early geologic history of the lithological suite being studied here. The occurrence of gedrite itself may suggest early high T (amphibolite facies) conditions, perhaps interactions with a mafic or ultramafic suite. Regionally, amphibolite grade conditions have been inferred in lithologies hosting the Beachcomber prospect (Chapter 3) in AFO rock types to the south-west of the Neale project area, with reference to the occurrence of Ca-rich plagioclase and garnet.

Additional geochemical studies of the different granitoids present in the project area are essential to understand the likely metallogenic potential, and styles of mineralization that are present. Such work would need to be focus on unaltered lithologies, and would also ideally try to take into account additional complications such as hybridization within the primary intrusive phases. Additionally, such a study would provide further important information regarding tectonic setting.

5 Regolith stratigraphy, mineralogy and geochemistry in the Neale tenement *(Appendix E)*

Summary

Regolith profiles were characterized from rock chips collected from 32 RC drill holes from Hercules and Atlantis. Soil samples were collected from the surface sediments (0-20 cm) and separated into 5 soil size fractions (>2000, 2000-250, 250-53, 53-2 and <2 µm). Petrographic and mineralogical studies of the composition of regolith materials were undertaken by optical, scanning electron microscopy, X-ray diffraction (XRD), whereas whole-rock geochemistry was performed by using XRF, Inductively Coupled Plasma Mass Spectrometry (ICP-MS) and Neutron Activation Analysis (INAA).

The regolith at these sites commonly comprises a residual deeply weathered profile overlain by a transported blanket of ferruginous sands, gravels and lateritic pisoliths and nodules (2-25 m). The residual regolith profile consists, from base to top, of four units: (1) saprock, dominated by partially weathered granitoids, gneisses and mafic rocks (e.g., gabbros and basalts); (2) lower ferruginous saprolite (3-25 m), dominated by quartz, feldspars, kaolinite, goethite after ferromagnesian and sulfide minerals; (3) upper kaolinitic saprolite (10-40 m), dominated by quartz and kaolinite; and (4) silcrete/grit layer (4-20 m), dominated by quartz, anatase and zircon (QAZ cement). The transported cover is differentiated from the residual weathering profile by variations in sediment colour, texture and fabric. The thickness of transported cover strongly increases to the south-east in the Neale tenement area, reaching up to 75 m. It also increases towards the north-east, where it appears to be associated with the north-west/south-east palaeodrainage in the area.

The transported cover consists of sands and gravels in addition to lateritic pisoliths and nodules in the Atlantis prospect. These sediments are cemented by Fe-stained kaolinite cement, which is reflected by an increase in Si, Al, Fe and Ti oxides together with V, As, Cr and Th. The overlying soil (0-20 cm) lacks anomalies in ore-related elements such as Cu, Zn, As and Pb. A Au anomaly is recorded at the Atlantis prospect (0-3 m at NLC071). In the residual profile, a silcrete duricrust locally protects the underlying weathering profile, as it forms discontinuous lenses that laterally change into poorly cemented kaolinitic grits. The silcrete duricrust consists of quartz (>95%), anatase and zircon (QAZ cement). This is reflected by a high concentration of Si, Ti and Zr. The silcrete shows a gradational downward change to upper kaolinitic saprolite, which consists mainly of quartz and kaolinite. This change is associated with an increase in Al, Th, Ba, Sr, Pb, LREE (La-Sm)/HREE Eu-Lu) ratio and a decrease in Si concentration. These two units are highly depleted in alkali, alkaline earth elements and generally lack anomalies in Cu, Zn and As. However, in NLC071, small spikes of Au are recorded.

In drill holes NLC094 and NLC071, which were completely sampled, vertical chemical variations from the upper kaolinitic to the lower ferruginous saprolite and saprock are marked by a pronounced increase in ore- and lithology- related elements such as, Au, Cu, Zn, Pb, Cr, Ni, Co and V. The enrichment of these elements is related to hydromorphic dispersion of these elements from underlying mafic rocks. Gold is concentrated in these units and closely associated with Cu, which probably reflected the abundance of chalcopyrite in the mineralization. Therefore, the lower ferruginous saprolite and mafic saprock are the best regolith sampling *media*, both displaying enrichment in ore-related elements.

Soil analysis showed that Cr, V, As and Th are concentrated in the coarse fractions with lateritic pisoliths in the Atlantis prospect, whereas Al, Fe, Ti, alkalis, alkaline earth and transition elements are concentrated in the <50 µm soil fractions. In general, soils cannot be considered as a reliable sampling *medium* for the buried mineralization in the Neale tenement.

5.1 Regolith context

This part of the study aims to focus on: (1) the stratigraphy of the different regolith units at the Neale tenement, especially at the Hercules and Atlantis prospects (Fig. 46 in Chapter 4). The discrimination between the transported cover and the residual weathering profile is based on the various sedimentological parameters such as, colour, textures and fabrics. An improved understanding of the stratigraphic units of the regolith, and their lateral and vertical variability, has led to significantly improved descriptions of regolith architecture and landscape evolution, and therefore provides a regional context for mineral exploration and drilling strategies in the cratonic margin; and (2) the vertical and lateral mineralogical and chemical variations of the regolith units, especially along the different physical and chemical interfaces. This leads in turn to an understanding of the hydromorphic dispersion mechanism(s) that form expressions of buried mineralized targets through the regolith profile to the surface soils.

5.2 Regolith at the Neale tenement

The Neale tenement is located on a drainage divide between 400 m and 300 m elevation, with the main drainage towards the south-east to the Eucla basin (Figs. 46, 47 in Chapter 4, and 58). Native grasslands dominate this area with extensive aeolian sand dunes featuring in the landscape. By projecting the main regolith domain regions known in the Yilgarn Craton, the Neale tenement would belong to the northern region above the Menzies Line, characterized by 3,300 mm annual potential evaporation and average rainfalls of 200 mm (Fig. 58; Anand and Butt, 2010).

Relative to palaeochannels and ground water salinity, the Neale tenement experiences groundwater salinities of 3,000-1,000 mg/L (Fig. 58D). Groundwater salinity, acidity and the types of chemical ligands available are key factors that control trace element mobility, and in particular mobility of elements such as Au. Distribution of pathfinder elements and association with metals are severely affected by the acidity and salinity of the ground waters. These factors have a significant effect on the design of geochemical protocols for exploration, and the interpretation of data (e.g., Anand and Butt, 2010).

5.3 Sample strategy

Thirty-nine samples were collected from basement lithologies from 7 diamond drill (DD) holes, 206 regolith samples from 32 RC drill holes, and 92 soil samples were taken from the surface adjacent to selected drill holes within the Neale tenement (avoiding cross hole contamination), for this study (Appendix E). The Neale tenement comprises the Hercules and Atlantis prospects as displayed in Figs. 46 in Chapter 4 and 59).

Forty-three samples from “fresh” bedrock were collected from the seven available DD holes in the area (2 holes at Hercules and 5 from the Atlantis prospect). These samples were chosen to account for differences in lithology, alteration haloes and mineralization (Appendix E).

Regolith samples taken for bulk geochemistry (for fusion digestion and ICP-MS/INAA analysis for 53 elements) were collected from 32 RC drill holes in the field. The two hundred and six samples selected for analysis span the stratigraphic extent of all regolith units laterally and vertically at the Hercules and Atlantis prospects. Specifically, a complete sampling of the entire thickness of regolith profile was carried out at two metre intervals, above mineralized bedrock at NLC094/NLD210, where RC drill hole NLC094 is offset north-east several metres from diamond drill hole NLD210. Two further weakly mineralized drill holes in close proximity, with weak mineralization, NLC071 and NLD071, were sampled in the same fashion to provide a “barren/low mineralization” comparison (Fig. 59; Appendix E).

In the proximity of the 10 selected RC drill holes, soil was sampled to 20 cm depth (Fig. 59). These sample sites were distributed around NLC094 and NLC071. Five size fractions (see sections below) were taken from these soil samples to explore the associations between grainsize fraction and their geochemistry around NLD210 and NLD071. Care was taken to take soil samples away from any disturbance by drilling equipment or vehicles, as well as away from dust plumes generated by the drilling itself.

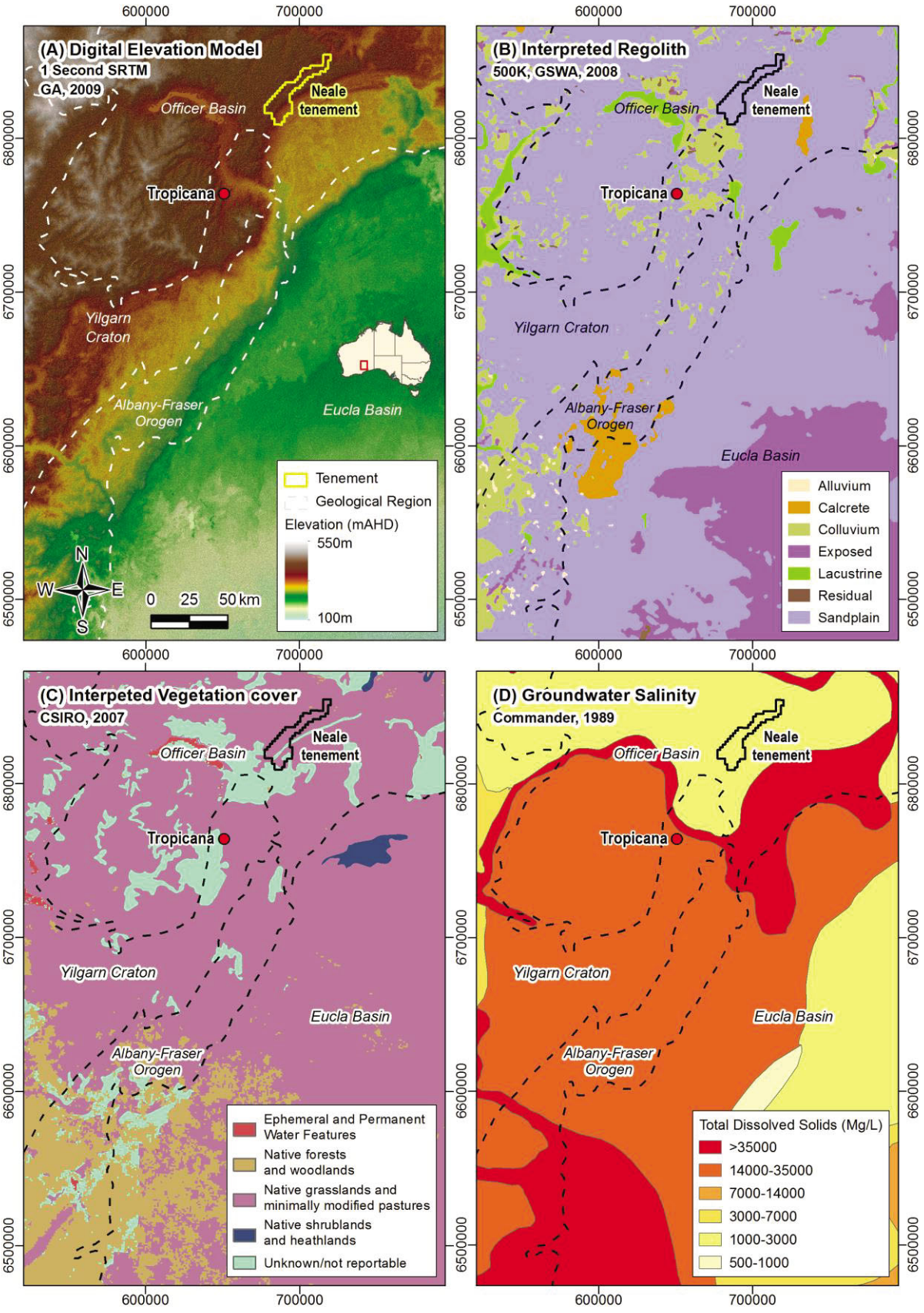

Figure 58. Maps of the regional regolith context of the Neale tenement. (A) Digital Elevation Model (DEM); (B) regolith map (500K; 2003, GSWA); (C) vegetation; and (D) salinity from Commander (1989).

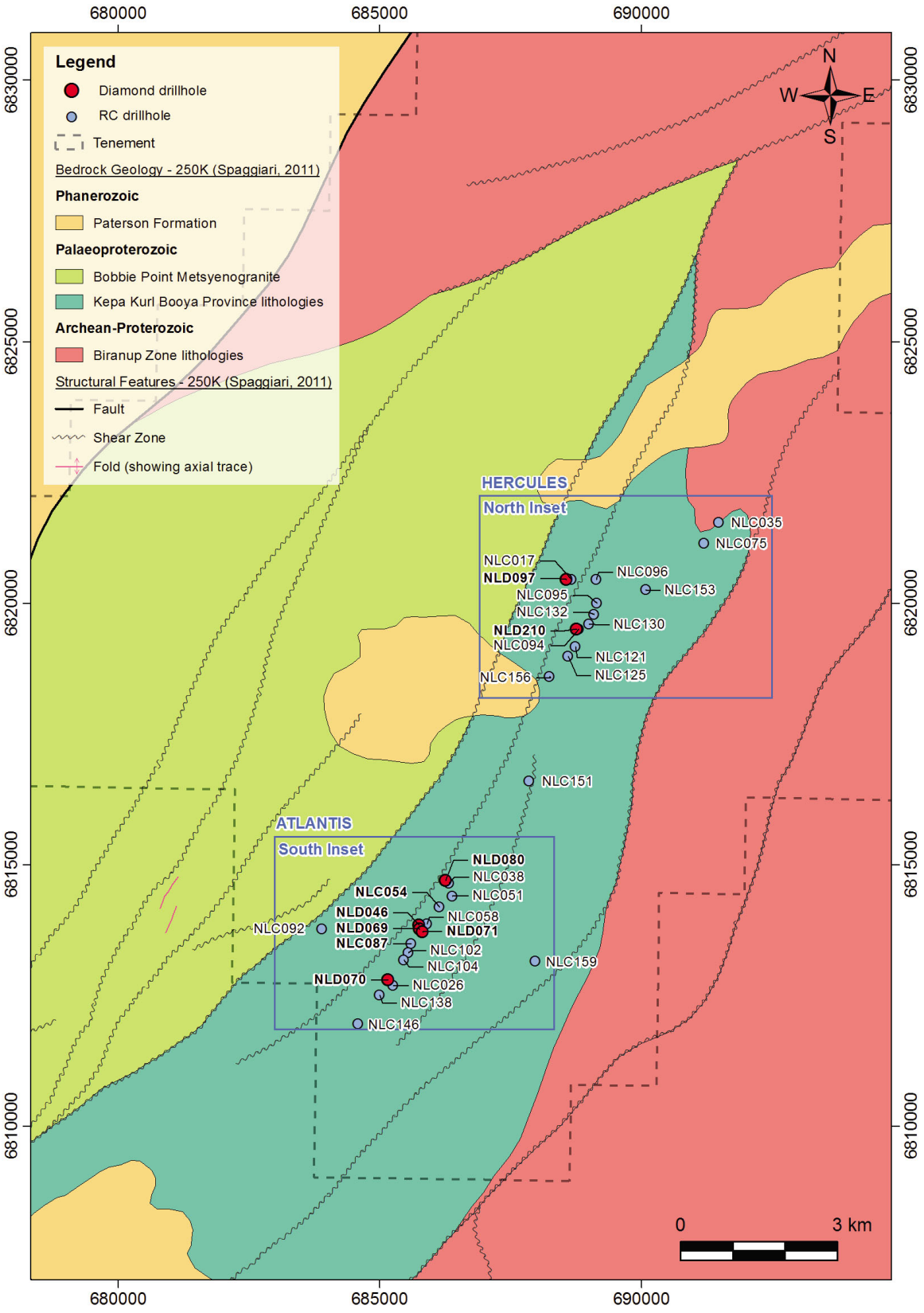

Figure 59. Location of the RC and DD holes sampled from the Hercules (north inset) and Atlantis (south inset) prospects within the Neale tenement (dashed line), with basement geological context provided.

5.4 Saprock

Saprocks are mainly composed of slightly weathered interlayered granitoids and gneisses of variable composition and texture. Mica schists are also described in some RC drill holes. These rocks invariably contain intrusions of mafic dykes and quartz veins (Spaggiari et al., 2011). Mafic dykes with crystalline interiors and thin (1-2 cm) chilled or weakly sheared margins are ascribed to the ca. 1,210 Ma intrusive suite (Wingate et al., 2000). Metagabbros and diorites were identified in some RC drill holes.

For the purpose of this section, detailed descriptions of mineralogy and rock type should be read in reference to descriptions in Chapter 4. The use of the term 'alteration' with reference to mineralogy here covers the net impact of weathering and hydrothermal alteration, as it is significantly challenging to distinguish between the effects of these processes. Where 'weathering' is discussed, it implicitly refers to the impact of surficial low temperature processes on the original mineralogy, related to regolith development.

Granitoids have variable mineralogical compositions and range from alkali granite, granodiorite and tonalite. The granitoids consist of quartz, plagioclase and alkali feldspars, micas (biotite and muscovite), and hornblende. The alkali granite consists mainly of quartz, plagioclase and alkali feldspars and muscovite (Fig. 60A). Hornblende content increases in the granodiorite and tonalite varieties. Diorite consists mainly of plagioclase and hornblende with less common quartz and apatite (Fig. 60B). The plagioclase is almost completely altered to sericite, phengitic illite and kaolinite in the saprocks. The biotite is slightly altered to chlorite, smectite and goethite, whereas muscovite is resistant to weathering. The most dominant accessory minerals in granitoids are zircon, titanite, apatite, anatase and titanite, ilmenite and pyrite.

The metamorphic rocks are represented mainly by quartzofeldspathic and pelitic (garnet-mica) gneisses and schists. Gneisses and schists consist of quartzofeldspathic gneisses, garnet-mica gneisses, mica schists and mylonitized granite. The quartzofeldspathic gneisses consist mainly of highly deformed and strained quartz set in a sericite and chlorite matrix (Fig. 60C). The mylonitized granite consists of lenses of quartz and feldspars in a matrix of foliated sericite. Plagioclase, anatase, titanite, apatite and zircon are uncommon. The garnet-mica gneiss consists of quartz, plagioclase, garnet, muscovite and biotite (Fig. 60D). Biotite and garnet are altered to chlorite. Granitic mylonite consists of lens-shaped quartz embedded in a foliated sericite matrix. Sulfide and oxide minerals are identified in both granitoids and gneisses.

The mafic rocks are represented by metagabbros and basalt and dolerite dykes (Fig. 60E). Amphibolites were also identified, and consist mainly of hornblende. They consist of weathered pyroxenes and plagioclase. Pyroxenes are almost completely altered to tremolite-actinolite, hornblende, chlorite and goethite, whereas plagioclase is altered to zoisite and calcite. Pentlandite, in addition to pyrite, chalcopyrite, and Mn-rich ilmenite, are the main opaque minerals associated with the mafic and garnet-mica gneisses (Fig. 60F).

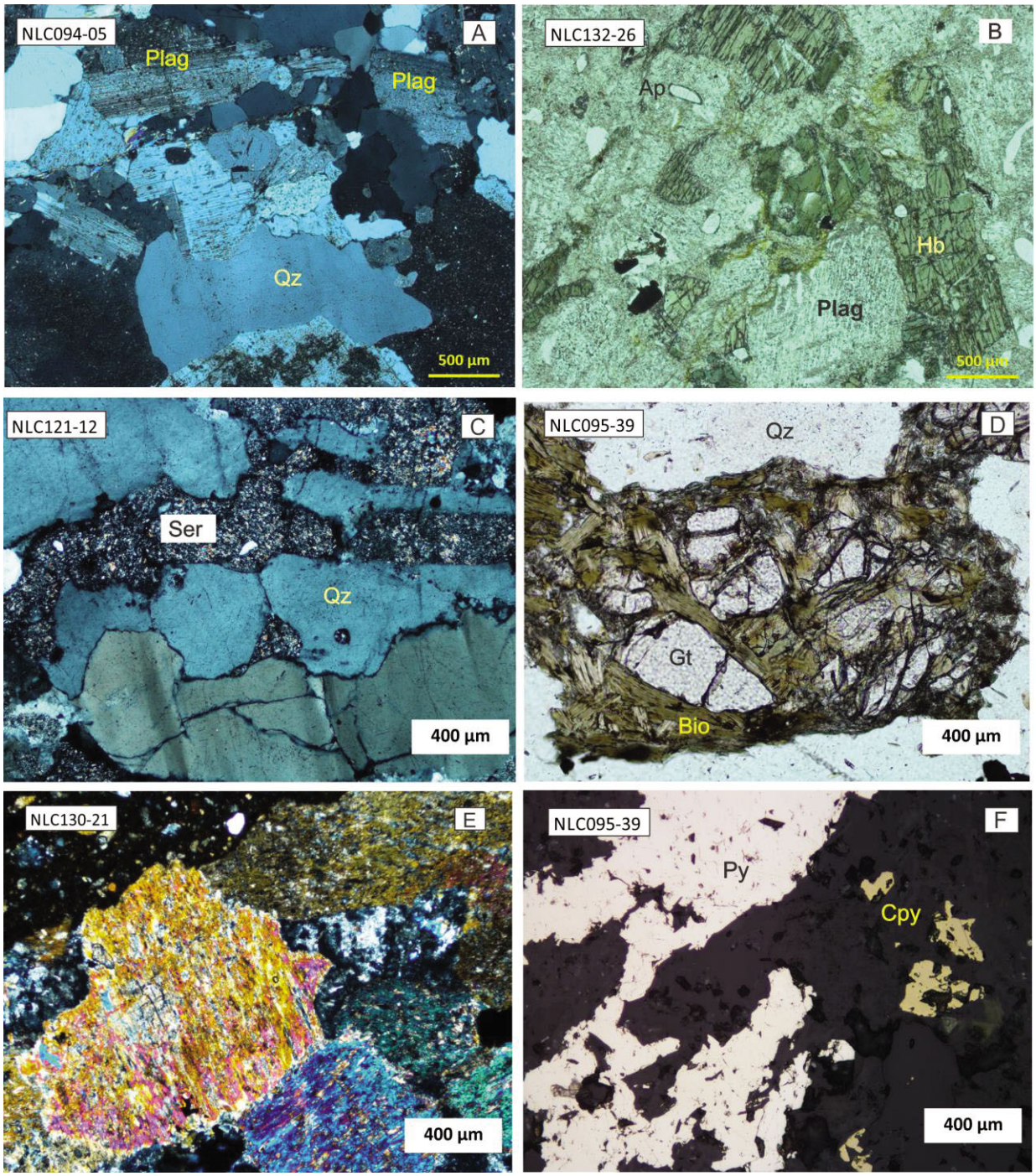

Figure 60. Photomicrographs of the granitoid and gneissic saprock. (A) Alkali granite composed of quartz and plagioclase (CN); (B) diorite composed of slightly altered plagioclase, hornblende and traces of quartz and apatite (PPL); (C) quartzofeldspathic gneiss comprised of strained quartz, and plagioclase altered to sericite (Ser; CN; cross nicols light); (D) a photomicrograph of garnet-mica gneiss comprised of quartz, garnet, biotite and chlorite (PPL); (E) metagabbro consists of pyroxene and plagioclase, with very fine alteration minerals; and (F) a reflected light plane polarized photomicrograph showing pyrite (Py) and golden brown chalcopyrite (Cpy).

5.5 Criteria used to distinguish transported from residual regolith

Table 4. Criteria used to distinguish transported cover from underlying residual regolith (Figs. 61 and 62).

Regolith type	Criteria used to distinguish the transported from the residual regolith
Transported regolith	1. The transported cover is composed of polymict sediments of sands, gravels and lateritic pisoliths and nodules. 2. The sorting of the sediments varies from poorly to well sorted. 3. The fabric is always grain-supported and the roundness varies from sub-angular to rounded. 4. The presence of a sharp contact with the underlying silcrete or saprolite, which terminates at the contact with underlying residual weathering profile. 5. The presence of poorly crystalline kaolinite, which an evidence of transportation of this sediment. 6. Variation in colour from red (ferruginous cement) in transported cover to creamy and milky white (siliceous cement) of the residual regolith
Residual regolith	1. The presence of well crystalline kaolinite in comparison with poorly crystalline kaolinite in the transported regolith. 2. The presence of similar resistant heavy minerals and relics of the rock-forming minerals in the silcrete, saprolite and underlying fresh rocks. 3. The presence of inherited polycrystalline quartz grains characteristic of the granitoid and metamorphic bedrock in the silcrete layer and saprolite.

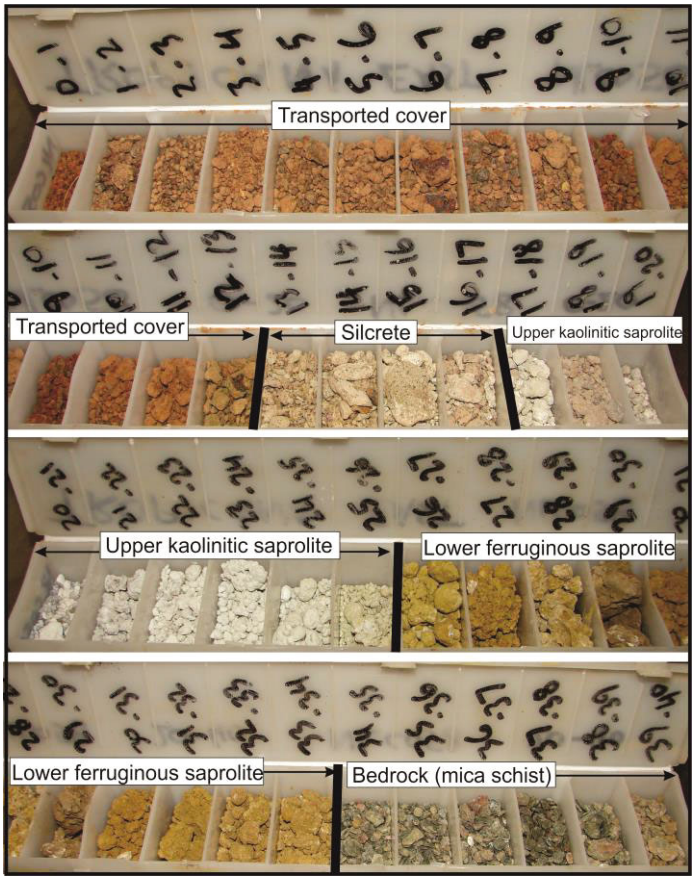

Figure 61. An example of the five main regolith units as metre intervals of drill chips in RC drill hole NLC058. The transported cover consists mainly of ferruginous lateritic pisoliths and nodules. The residual profile was developed on mica schist bedrock, overlain by lower ferruginous and upper kaolinitic saprolite units. The residual profile was terminates at the top of the silcrete duricrust.

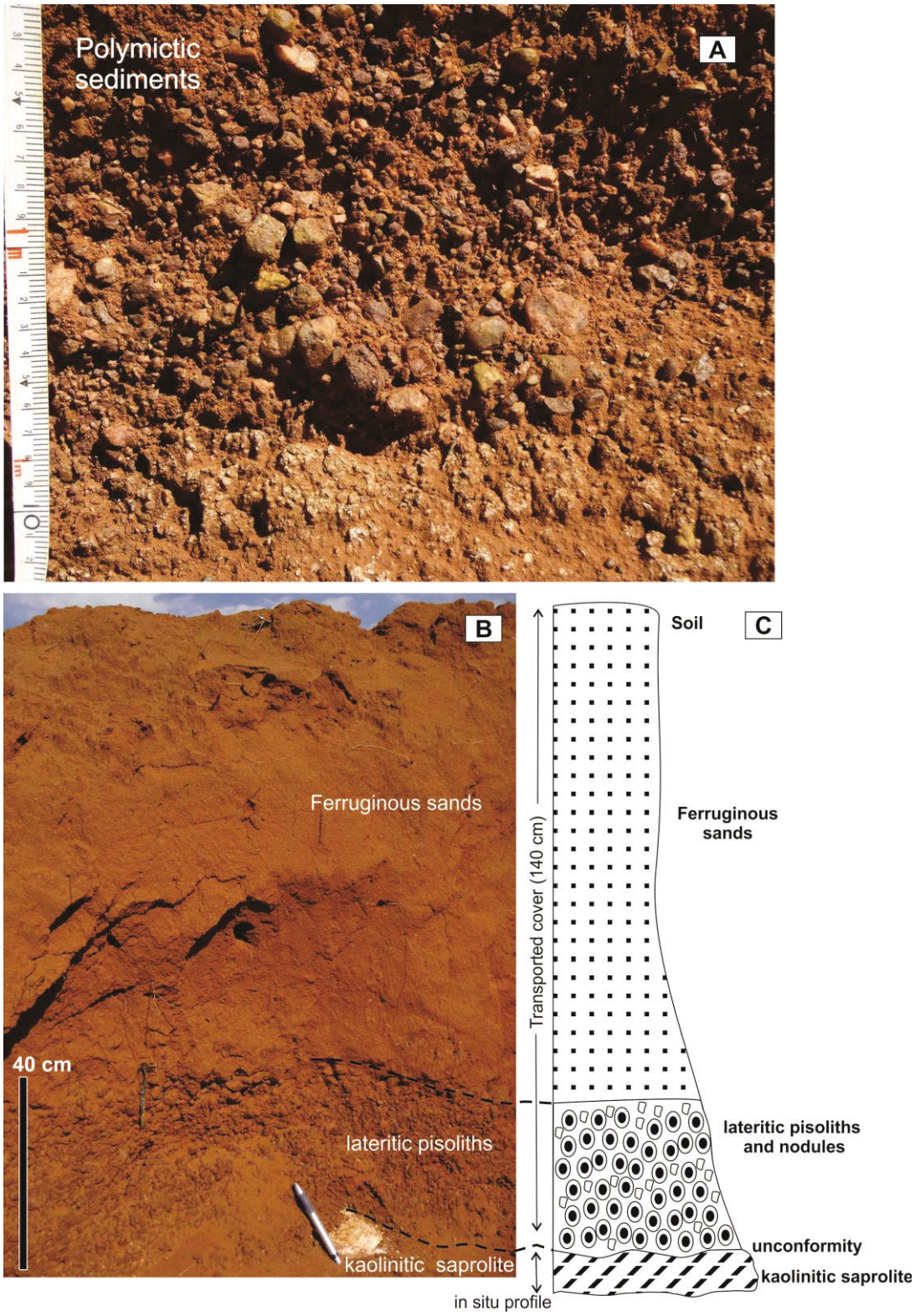

Figure 62. (A) Detail of transported cover, comprised of polymict poorly sorted ferruginous gravels in NLC097. (B) Transported cover sequence, consisting of lateritic pisoliths and nodules at the base grading upward into ferruginous sands with plant roots in the upper part (NLC159); and (C) stratigraphic profile of B showing the ferruginous pisoliths and nodules resting unconformably over the upper kaolinitic saprolite unit.

5.6 Residual regolith

5.6.1 Lower ferruginous saprolite

The lower ferruginous saprolite consists of mottled ferruginous clays and it gradually changes upward into an upper kaolinitic unit shows a gradual vertical downward change toward a lower ferruginous saprolite, consisting of mottled ferruginous clays. It consists mainly of quartz, feldspars, muscovite and ferromagnesian minerals. Quartz and muscovite are resistant to weathering, but the other mineral components are partially to completely weathered to clays and Fe and Mn oxides. The feldspars are weathered to sericite and kaolinite. Biotite, hornblende and garnet are weathered to chlorite, smectite, goethite, hematite and psilomelane (Fig. 63B). Ilmenite is oxidized to anatase and titanite, whereas pyrite is oxidized to jarosite and goethite (Fig. 63C, D). The development of the lower ferruginous saprolite depends mainly on the presence of the ferromagnesian and sulfide minerals in the bedrock. It is best developed on mica schist and gneiss, as well as Fe-rich granitoids.

There are limited lateral variations in the upper kaolinitic and lower ferruginous saprolite units. In all drill holes, the upper sandy kaolinitic saprolite is always well developed and laterally continuous. It is well developed on the granitic gneiss, whereas the existence of the lower brown ferruginous saprolite depends mainly on the presence of ferromagnesian and sulfide minerals in the bedrock. This horizon is best developed on mica, amphibole and sulfide-rich granitoids, garnet-mica schists and gneisses as well as mafic rocks (Fig. 63). It is poorly developed on alkali granites and granitic gneisses. Banding in granitoids (e.g., muscovite- and biotite-rich bands) may reflect alternating kaolinitic and ferruginous banding in the resultant saprolite.

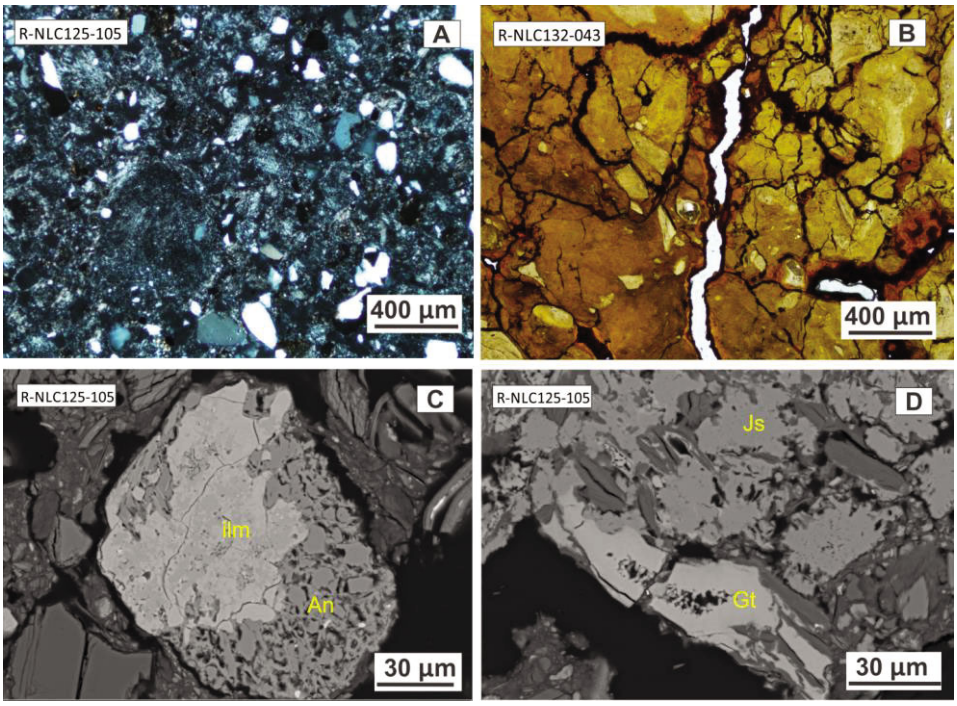

Figure 63. Images illustrating the mineralogy of the kaolinitic upper saprolite unit. (A) Transmitted light image presenting the residual kaolinite with matrix supported quartz grains (CN.); (B) transmitted light image showing secondary interconnected fractures filled with goethite cutting ferruginous clays (PPL); (C) BSE image displaying the alteration of ilmenite (ilm) to anatase (An); and (D) BSE image showing textural detail of the complete alteration of pyrite to jarosite (Js) and goethite (Gt).

5.6.2 Upper kaolinitic saprolite

The upper kaolinitic saprolite consists of quartz grain supported in a residual kaolinite and illite matrix. This unit still preserves the original textures of granitoids and gneisses, observed in drill holes NLC054, NLC058, NLC080 and NLC102. The alteration of primary minerals occurs in this zone; in addition, less stable secondary minerals such as smectite are also destroyed. Heavy minerals such as zircon, anatase, monazite and ilmenite, as well as traces of muscovite are still preserved and recognizable in the kaolinitic saprolite.

Based on Hychip^{TM} data (Appendix E), the kaolinite in the residual saprolite is well crystalline. In areas with poorly-cemented grits, the upper surface of the kaolinitic saprolite shows evidence of surficial physical disruption and dislodgment, which form mixed, locally reworked saprolite and lateritic materials. Some of these materials have been incorporated deeper into the weathering profile probably via surficial shrinkage cracks. Quartz veins are observed cutting through the kaolinitic saprolite and the overlying silcrete.

5.6.3 Silcrete duricrust/grit

Based on drilling data from the Hercules and Atlantis prospects, the silcrete layer is well-preserved as discontinuous, indurated, subsurface lenses. It is a regionally widespread marker horizon capping and protecting the underlying residual weathering profile. The silcrete lenses are indurated and have a vitreous appearance and sandy texture. The silcrete varies from matrix- to grain-supported, angular to subrounded, poorly to moderately sorted quartz grains matrix supported in fine-grained, creamy, white, siliceous, and rarely ferruginous, cement. In some RC drill holes, the silcrete has a massive appearance toward the upper part. The silcrete layer shows a gradual upward increase in the degree of silicification and decrease in clay content. The silcrete lenses are best developed where they are encountered in NLC095, NLC132, NLC130, NLC094, NLC080, NLC054, NLC038, NLC051, NLC054, NLC058, NLC102 and NLC104. These RC drill holes are located in the low relief basinal area aligned along a north-east/south-west trend.

Considerable lateral variations in thickness and degree of cementation are typical of the silcrete layer. The silcrete layer varies in thickness from 4 to 20 m (average ~7 m). The *maximum* thickness (20 m) is recorded in NLC092 on the western side of the Atlantis site. This probably matches with areas of poorly cemented grits due to intensive leaching of the kaolinitic saprolite or sand dykes, and quartz veins penetrating the underlying saprolite, similar to those described by Butt (1985). The contact between the silcrete lenses and the underlying saprolite is gradational, whereas the contact with the overlying transported cover is sharp. There are major lateral differences, with silcrete lenses varying into areas of poorly cemented kaolinitic sand and grit (Fig. 64). In these areas, the contacts between the quartz-rich grit, the underlying saprolite and the overlying transported cover are gradational and hardly discernible. Reworking and mixing of transported sediments and residual regolith materials in these areas are observed. The unconformity between the transported and residual regolith is sometimes characterized by colour variations and the presence of small rounded quartz grains. It is not obvious if these grains are the products of transportation, or are due to residual dissolution of inherited quartz from the underlying kaolinitic saprolite.

The lateral variation in the degree of silica cementation in two RC drill holes (e.g., NLC071 and NLC094) was investigated by the Hychip^{TM} system. The well-cemented silcrete does not contain clay and Fe oxide contents (e.g., NLC094). In contrast, a poorly-cemented silcrete or grit area contains well-crystalline kaolinite and hematite dust (e.g., NLC071). These data are matched with those of the field investigation and mineralogical analyses.

The microscopic investigation and XRD analyses indicate that the silcrete generally consists of more than 95% quartz, and typically displays a matrix- to grain-supported fabric with grains separated by cryptocrystalline quartz, anatase and zircon. This assemblage was previously referred as QAZ-cement in silcrete of Barr Smith Range (Butt, 1985). It is also similar to the "terrazzo" type (Smale, 1973) which composed of a framework of quartz grains embedded in a cryptocrystalline or opaline, typically Ti-rich matrix. At the base of the silcrete, quartz grains are mostly polycrystalline and dispersed in a kaolinitic saprolite. They are cemented by a mixture of brown opal, cryptocrystalline clays and small granules of hematite.

At the top of the silcrete layer, clays decrease and the quartz grains become increasingly disrupted, very angular, grain-supported and more densely packed (Fig. 64A). Secondary voids are completely, or partially, filled with secondary silica. Many void and fracture walls are coated by multiple bands of isopachous faint brown, and colourless colloform opal, fibrous chalcedony and cryptocrystalline quartz (Fig. 64B). The colloform opal generations are followed outwards by colourless fibrous chalcedony (Fig. 64B). In some cases, the remaining spaces of the cavities are left empty or filled by mosaic of cryptocrystalline and/or megacrystalline quartz. Zircon and anatase are irregularly distributed in a groundmass of quartz, and they may reach up to 50 µm in diameter (Fig. 64C, D). In addition to zircon and anatase, ilmenite is the most common accessory mineral identified in silcrete.

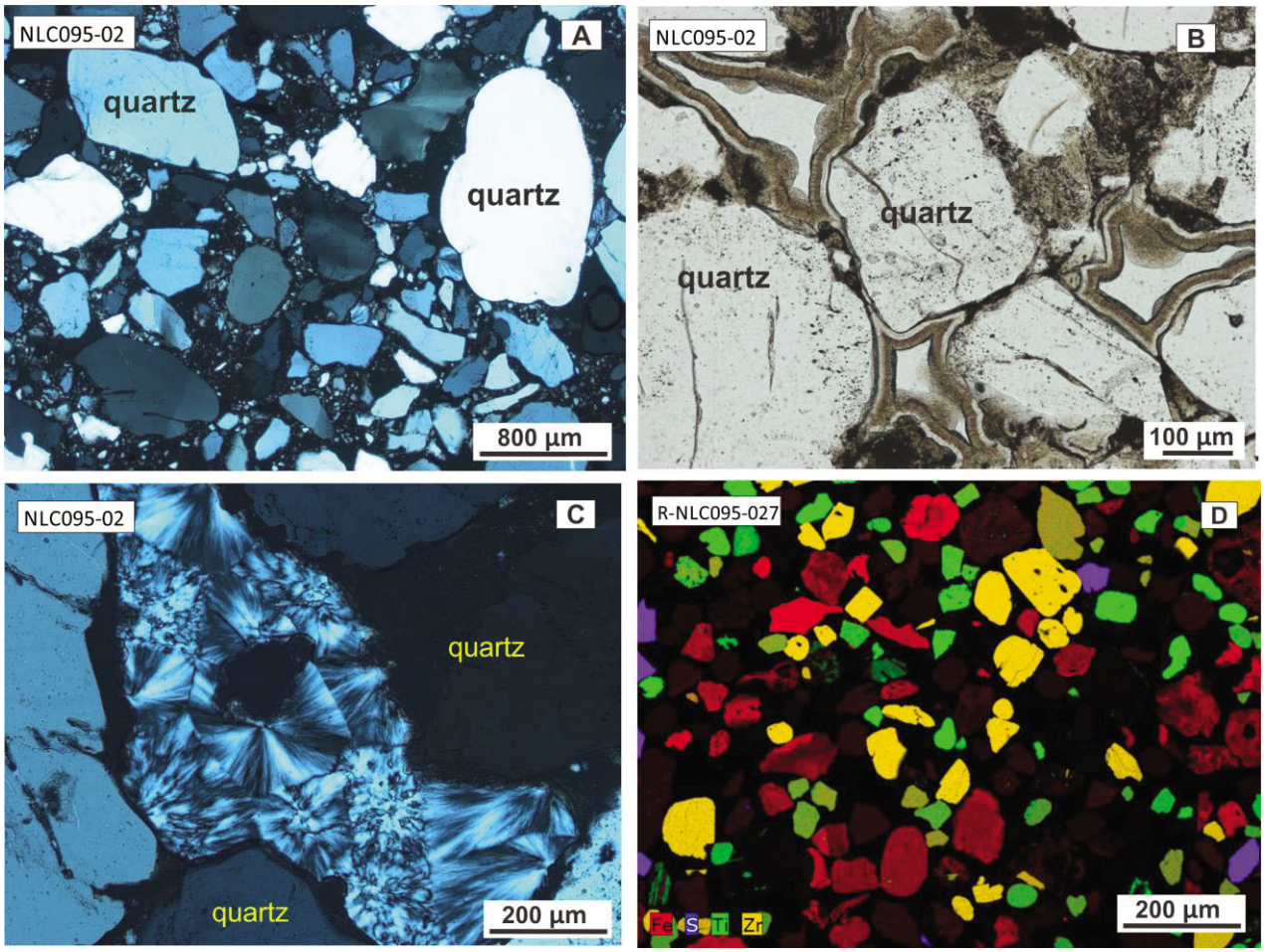

Figure 64. Images of mineralogy and texture of silcrete duricrusts and grit units. (A) Transmitted light image of silcrete consists of moderately sorted, angular to subrounded quartz cemented by cryptocrystalline quartz cement (CN); (B) transmitted light image of quartz grains cemented by clays, and later by colloform dusty and colourless opal and chalcedony; (C) transmitted light image of cavities formed between quartz grains filled by chalcedony (CN); and (D) SEM EDS false coloured element map showing the distribution of zircon (Zr-rich grains, yellow colour), anatase (Ti-rich grains, green), pyrite (purple grains), and goethite and hematite (red colour).

5.7 Transported cover

The transported cover shows a pronounced lateral variation in thickness and mineralogical composition over a short distance from east to west, and from north-west to south-east. It has a thickness of 2 m on the north-west side (e.g., NLC017, NLC092 and NLC097); whereas the other RC drill holes aligned along a north-east/south-west orientation on the south-eastern side vary in thickness of transported cover from 18 to 25 m thick at Hercules, and from 10 to 15 m at Atlantis. On the north-west side of the Hercules and Atlantis sites, the transported cover consists mainly of immature, polymict, gravel-sized, poorly sorted, angular to subrounded and matrix supported ferruginous sediments (e.g., NLC097; Figs. 65A, 66, 67 and 68).

These sediments are composed of corroded quartz grains, rock fragments of weathered granitic and mafic igneous rocks, kaolinite spheres, ferruginous sediments, silcrete, lateritic pisoliths and nodules. Toward the south-east of both sites, the ferruginous sediments are composed of mature monomictic, sand-sized, moderately to well sorted subangular to rounded and grain-supported ferruginous sediment (Fig. 64B). Lateritic pisoliths and nodules show a noticeable increase in abundance toward the south-eastern part of Atlantis area. In some drill holes (e.g., NLC159), the lateritic pisoliths and nodules rest unconformably on the underlying bleached kaolinitic saprolite and are overlain by ferruginous sands. The transported sediments show a relative downward increase in the degree of lithification and cementation by Fe-stained kaolinitic cement.

The microscopic investigation and XRD analysis indicated that quartz is the essential component forming the framework of the ferruginous sands and gravels. Ferruginous pisoliths and nodules, as well as kaolinite spheres, form the second most important framework components. They consist of goethite, hematite and kaolinite. Weathered fragments of granite, gneiss, mafic rocks, ferruginous, silcrete, quartz-veins were also identified. The quartz grains are cemented and corroded by Fe-stained kaolinite cement (Fig. 65A, B). In thin section, it is evident that the Fe-staining is due to only a small amount of Fe oxide incorporated in the kaolinitic cement. Energy-dispersive X-ray spectroscopy results are very consistent, and show high concentrations of Si and Al with significant amounts of Fe and Ti. Quartz is gradually corroded and coated with kaolinite and Fe oxides. There is a marked downward change in the shape of the cement from surface soil meniscus type (cement concentrated at grain contact; Fig. 65A) to a continuous type filling all available pore spaces (Fig. 65B). Analyses of heavy mineral concentrates indicate that zircon, ilmenite and anatase are the main accessory minerals of the transported cover (Figs. 65C, D). Pyrite was also identified; it is most probably hosted in rock fragments.

The Hychip^{TM} investigations of the ferruginous unit from NLC094 and NLC071 showed that kaolinite of the transported cover is poorly ordered, and the ferruginous cement is dominated mainly by goethite, building upon previous observations from the field and from microscopy. The ferruginous and kaolinitic cements are leached from the surficial sediments, and increase toward the base of the ferruginous unit.

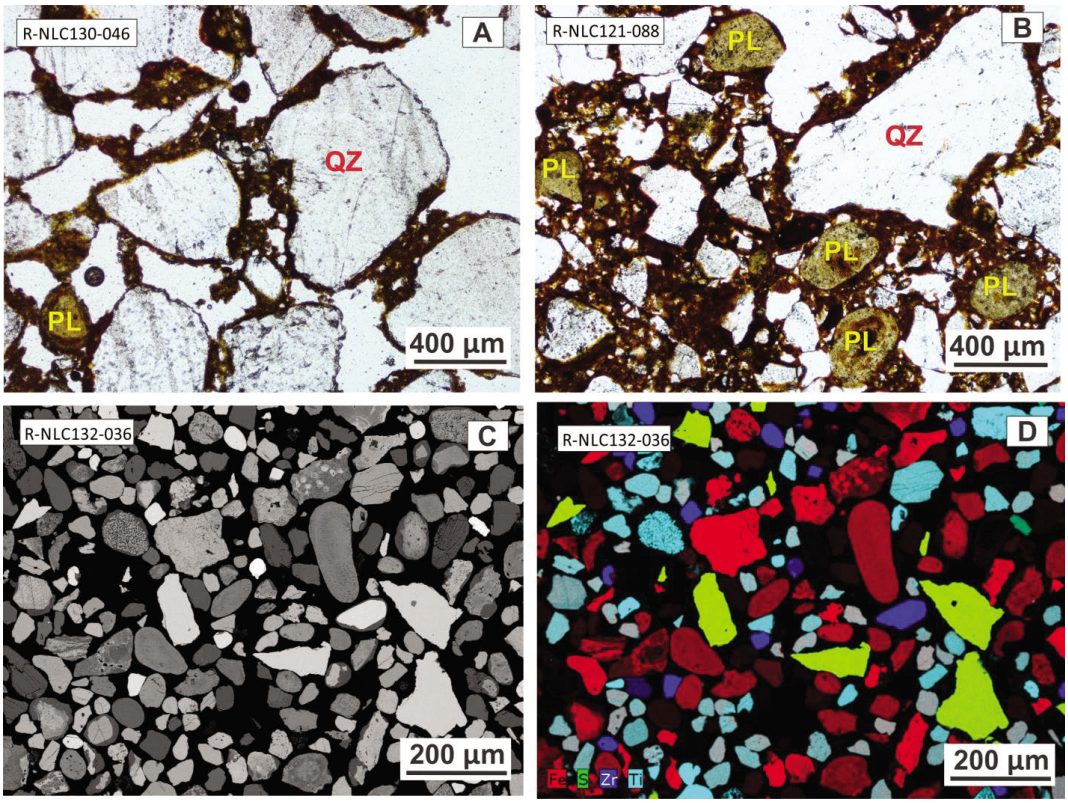

Figure 65. Images of transported cover units. (A) Polymictic ferruginous sediments at the surface; and (B, C, D) ferruginous sands from the deeper parts. (A) Transmitted light image of bridge-like (meniscus) ferruginous clay cement of the surface sediments; (B) PPL image of rounded kaolinite peloids associated with quartz, with incipient replacement by Fe oxides; (C and D) backscattered electron images of heavy mineral concentrates from the transported cover; and (D) displays a false coloured EDS element map showing that zircon (dark blue), anatase (light blue) and ilmenite (green-blue) are the main heavy minerals. Pyrite grains (green colour).

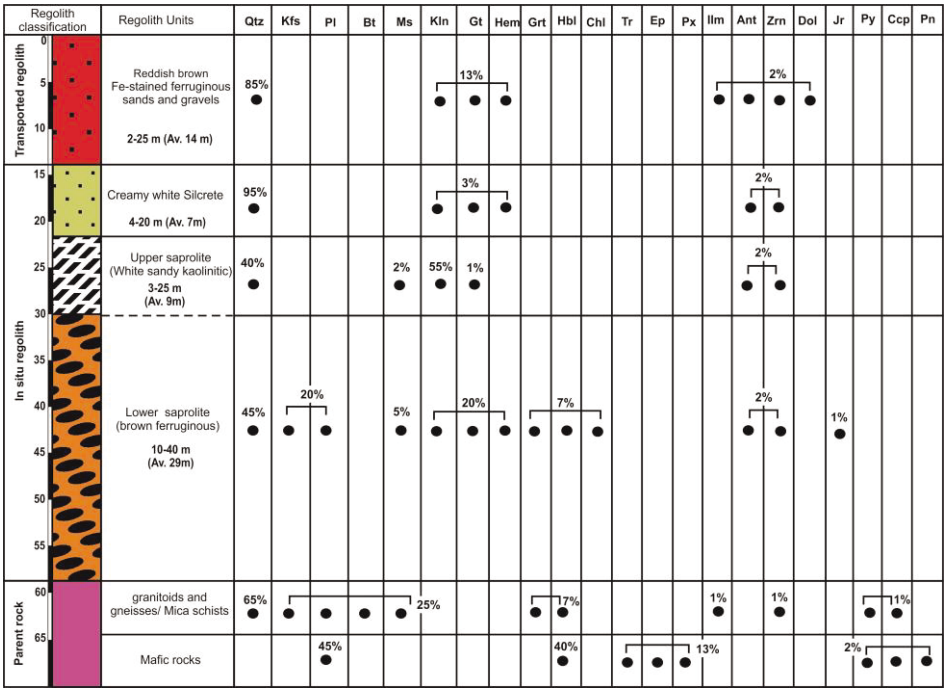

Figure 66. Idealized stratigraphic section of the study area showing the main stratigraphic regolith units and their mineralogy, with segregation of the transported cover from the residual saprolite.

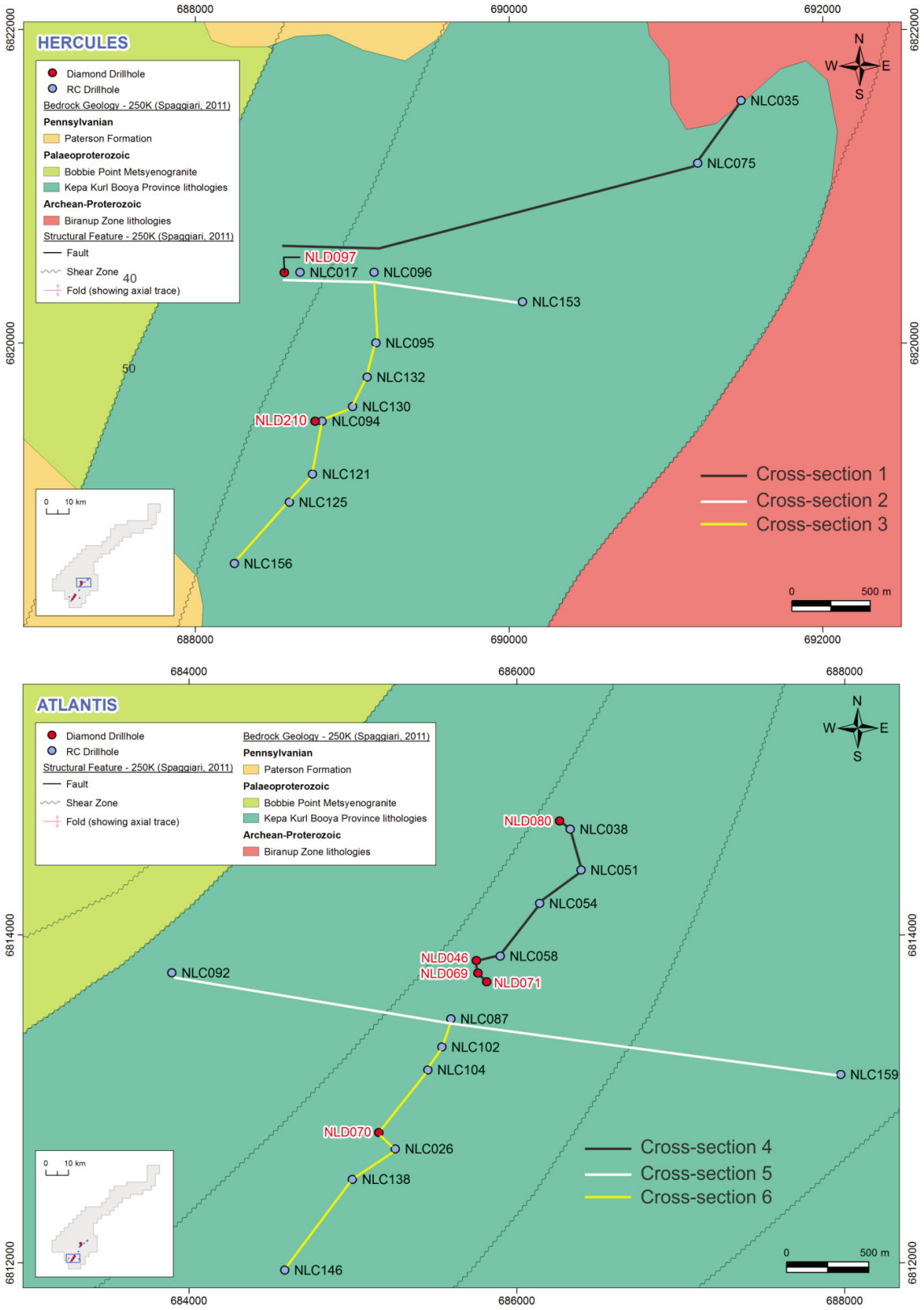

Figure 67. Detailed images of drill hole locations with basement geology (cf., Fig. 59), showing location of the regolith cross sections used to describe regolith lateral variability in these areas.

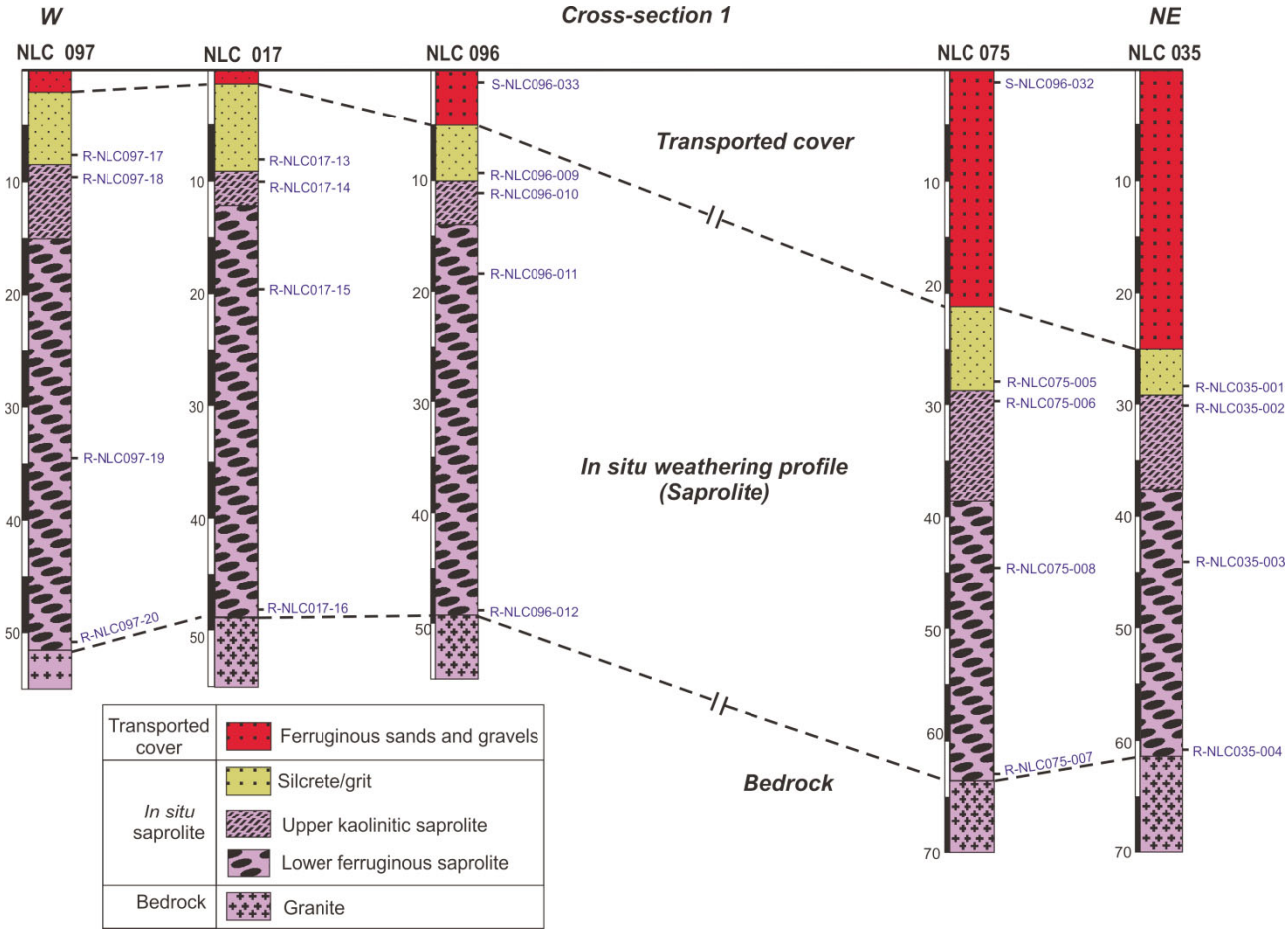

Figure 68. Stratigraphic cross-section showing lateral variations in thickness in profile 1 between drill holes. It indicates a lateral variation in thickness of the transported cover (ferruginous sediments/unit) from the western side (2 m) to the northeastern side (25 m). Selected rock samples are presented on each stratigraphic column (e.g., R-NLC097-17).

5.8 Discussion

5.8.1 Transported cover versus residual regolith

The regolith materials and landforms in the Albany-Fraser Orogen/Yilgarn Craton margin are poorly known. This is an issue, as satellite based regolith-landform mapping has revealed few areas of outcrop (3%) and extensive development of quartz-rich sand plain (70%), with approximately half the area dominated by sand dunes (McGuinness, 2010; Morris, 2013). This regolith cover obscures bedrock lithology and any associated features related to mineralization. Therefore, the nature and distribution of bedrock has been largely derived from the interpretation of aeromagnetics, supplemented by information from scattered outcrops and the results of mineral exploration drilling (Spaggiari et al., 2011).

The regolith of the study area is the product of a long and complex weathering history. An residual weathering profile is well-developed on Archaean-Proterozoic igneous and highly metamorphosed basement rocks with mafic intrusions. Based on drilling, the basement rocks are weathered to an undulating landscape, with the regolith-bedrock interface at approximately 50-70 m. The area is dissected by many parallel to sub-parallel shear zones that played a significant role in the palaeotopographic variations from north-west to south-east across the AFO. This undulating landscape of weathered basement was later covered by transported sands and gravels.

The total regolith thickness in the Neale tenement increases towards the south-east due to the increase of the transported cover toward the Eucla basin, and therefore deeper drilling is needed reach the regolith-basement interface. The regolith thickness also increases towards the north-east, which may be associated with a background complexity of palaeodrainage of the area, describing a north-west/south-east secondary palaeochannel system that drained into a main north-east/south-west palaeochannel (Chapter 6).

5.8.2 Transported cover and soils

Transported cover is composed mainly of sand plains and dunes up to 20 m thick. This thick transported cover is anticipated to prevent reliable geochemical footprints from the basement to being dispersed through the regolith. Various criteria are used to distinguish the transported cover from the underlying residual regolith profile, based on field and microscopic observations and geochemical data for each regolith unit (Appendix E). The macroscopic criteria are based mainly on colour variations, preliminary mineralogical composition and textural parameters, especially along the contact between residual and transported regolith. Microscopic criteria are based on petrographic investigations and detailed mineralogical analyses.

The transported cover sequence shows lateral variations in thickness from 2 m in the north-west to 25 m in the south-east for the investigated sites. In the northwest, the transported cover consists of polymictic and poorly sorted sediments, whereas to the south-east, it consists of monomictic and well-sorted sediments. These observations are consistent with the presence of erosional surfaces, indicating that the sediments were eroded from the north-west and transported towards the south-east. Based on thickness and lithological variations, the northwest side would represent a remnant plateau, which consists of exposed bleached saprolite, or covered by a veneer of eroded materials. As a part of the weathering profile, this plateau was probably capped by lateritic residuum, which consists mainly of ferruginous pisoliths and nodules. These regolith materials are transported south-east to the low-lying basinal or main drainage area as slope sediments, or via the secondary north-west/south-east drainage system.

At the Hercules prospect, the ferruginous sands and gravels are the main components of this transported cover. These sands are probably derived from weathered kaolinitic saprolite or sand dunes. In contrast, at Atlantis sand components are mixed with ferruginous pisolitic gravels, which are probably derived from a proximal source of lateritic materials. According to the ASTER image interpretation (Chapter 8), Hercules is flanked on the north-west side by sand dunes, whereas Atlantis is flanked on the western side by ferruginous saprolite and lateritic materials.

The relative increase of clays and Fe oxides from the soils downward through the transported cover is represented by slight increases in Al_2O_3, TiO_2 and Fe_2O_3 and a corresponding decrease in SiO_2. These chemical components appear to be leached by acidic and oxidizing meteoric water from the transported pisoliths and lateritic materials. The illuviation process is supported by variations from meniscus cement and highly porous soil sediments, to continuous and compact transported sediments downward. The increase of Zr, Nb, Ti, Th and Cr down the profile indicates a detrital source of sediments with a possible role of wind as a transporting agent. The downward increase of V and Rb is associated with the leaching and reprecipitation of Fe, K and Al, respectively.

Soil samples display different elemental associations with specific soil size fractions. The large soil size fraction (>2000 μm) is characterized by high concentrations of Fe_2O_3, SiO_2, V, Cr and As. This may indicate the abundance of detrital lateritic pisoliths and nodules, especially in the Atlantis prospect. The small soil size fractions is characterized by high concentrations of Fe_2O_3, Al_2O_3, TiO_2, Cu, Co, Ni, Cr, Pb, Ba, Rb and Sr. This may indicate the relative abundance of lateritic clays and Fe oxides.

5.8.3. Residual weathering profile

Silcrete is extensively preserved in Western Australia in low-relief landscapes (Van De Graaf, 1983). Milnes and Hutton (1974) and Hutton et al. (1978) studied high concentrations of Ti in Australian silcretes to follow the movement of Si during the silicification process. Relatively few studies have discussed silcrete associated with granitic rocks (Butt, 1985; Singh et al., 1992; Thiry et al., 2006).

5.8.4 Silcrete/grit

The silcrete unit displays a matrix- to grain-supported framework of angular to subrounded, poorly to moderately sorted, quartz grains supported by fine-grained creamy white siliceous cement. This suggests an indication of residual origin with possible very short distance of transport. Based on the geomorphology in the study area, together with the very angular grain features and the presence of polycrystalline grains, the silcrete is interpreted as the upper most unit of the residual regolith. In addition to zircon and anatase, ilmenite is the most common accessory mineral, as indicated by direct mineral observation using optical and scanning electron microscopy, and by Zr-Hf, Nb-Ta and Ti abundance. All these features can be interpreted to be the result of the residual mineralogy left after severe weathering of the bedrock. Silicon, Ti and Zr are highly concentrated with the silcrete as QAZ cement. Zircon and anatase also occur as heavy minerals in the upper kaolinitic and the lower ferruginous saprolite. As discussed below, the upper kaolinitic saprolite is geochemically similar to the silcrete, although with greater Al related to increased kaolinite content. The silcrete protects the underlying saprolite from erosion, and its indurated nature probably prevents vertical hydromorphic dispersion of ore-related elements from basement to the surface (Chapter 6).

5.8.5 Saprolite

The development of complete and intact weathering profiles suggests that the area had low to moderate relief developed under a humid climate, and subjected to a long history of weathering and tectonic stability (Nahon and Tardy, 1992).

The north-west of the study area represents a plateau remnant of an elevated palaeosurface developed mainly in the Proterozoic granitoids that has been extensively bleached and weathered (Fig. 67). The plateau remnant was eroded by pedimentation, with escarpment formation, although breakaways are rarely exposed, or it was covered by a veneer of transported ferruginous sands and gravels (Fig. 67). The deeply weathered profile has been protected from erosion by the developing silcrete duricrust. The silcrete duricrust is not well developed everywhere, but instead kaolinite-cemented grit or poorly-cemented sand is formed. This silcrete is most commonly seen at surface as a prominent duricrust protecting mesa landforms, but its lateral and subsurface extent is largely unknown (Thiry and Milnes, 1991; Anand and Paine, 2002). The major components of the upper sandy kaolinitic saprolite are quartz and kaolinite. The formation of kaolinite as a stable residue in weathering profiles requires weathering under acidic, warm and humid conditions, and removal of Na, K, Ca and Mg (e.g., Butt, 1985). The formation of the silcrete duricrust at the top was likely contemporaneous with kaolinization in the deeper horizons. This implies that kaolinite is being dissolved near the surface and forming at the base. Residual heavy minerals such quartz, zircon and rutile/anatase are concentrated higher in the weathering profile forming a sand or grit layer that was locally cemented by amorphous to cryptocrystalline silica cement. In the lower ferruginous saprolite, the ferromagnesian and sulfide minerals are partially to completely weathered to goethite and kaolinite. The development of this zone is dependant mainly on the bedrock mineralogy, where it is best developed on mafic rocks, biotite-rich schists, gneisses and granitoids. The lower ferruginous saprolite and saprock are highly enriched in Fe, Mn and Ti-oxides, and may include potentially ore-related target or pathfinder elements such as Au, Cu, Zn, Pb and As.

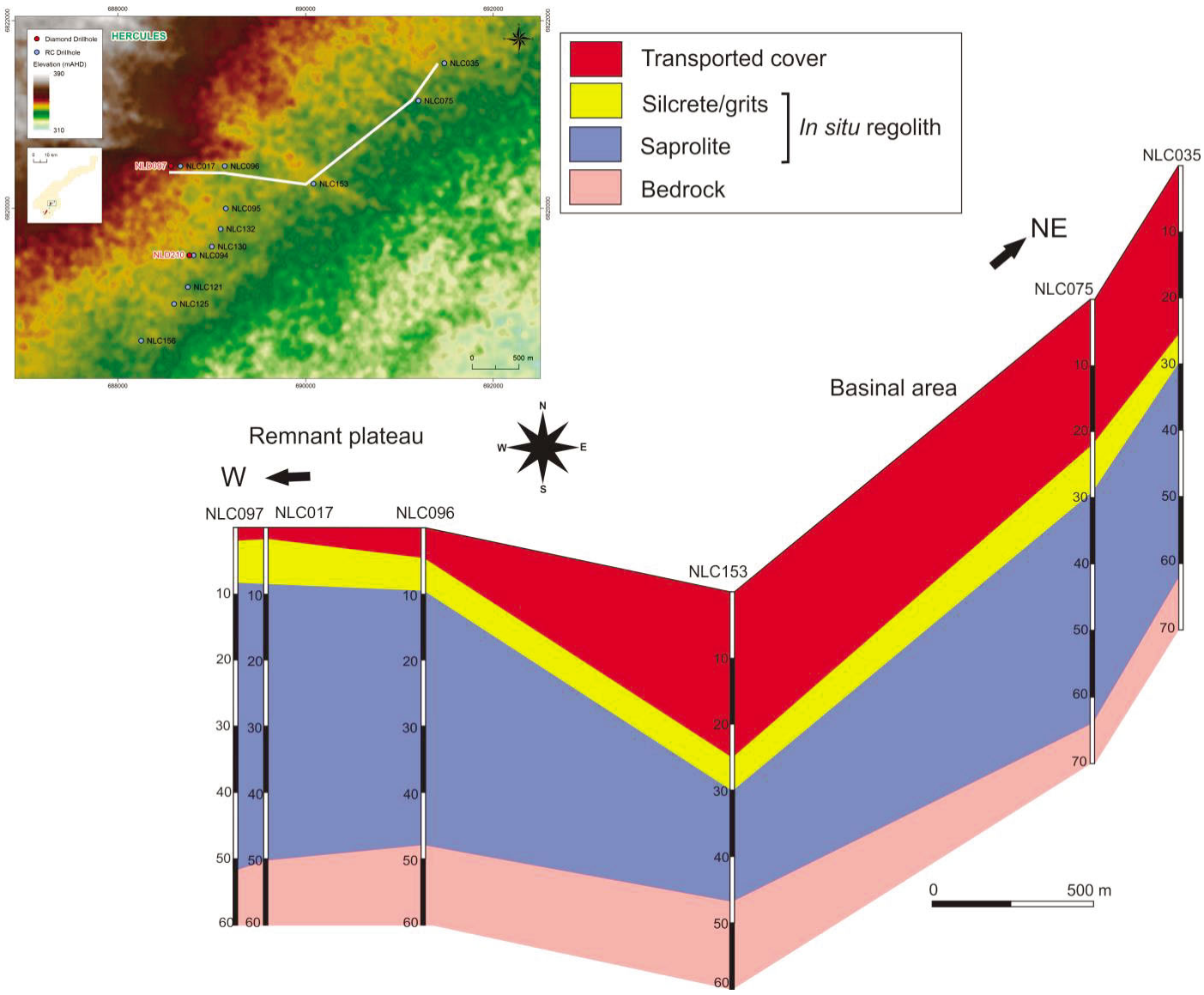

Figure 69. Top-left panel displays the digital elevation model map showing the location of the fence diagram comprised of regolith stratigraphy compiled from six RC drill holes; and lower panel illustrates a 3D fence diagram with regolith stratigraphy shown in perspective, with projections of east-west and north-east/south-west trends showing the lateral variation in different units. It illustrates that the western side of the area represents a remnant plateau dominated by saprolite with a thin transported cover. The trend of RC drill holes running in a north-east/south-west direction reveal an interpreted basinal or drainage area with thick transported cover.

5.9 Conclusions and implications for exploration

(1) Regolith thickness in the Hercules and Atlantis prospect sites varies from ~40 to ~75 m. Regolith is subdivided into two main regimes: (1) transported cover with a thickness from 2 to 25 m, and (2) residual weathered regolith varying in thickness from 20 m to 55 m (Table 5).

(2) Regolith thickness increases to the south-east due to the increase in the transported cover towards the Eucla basin. It also increases towards the north-east, which is interpreted to be associated with background complexity produced by palaeodrainage of the area, which takes the form of a north-west/south-east secondary palaeochannel system that drained into a main north-east/south-west palaeochannel.

(3) The transported cover consists mainly of ferruginous sands and gravels in the Hercules site, whereas and lateritic pisoliths and nodules are common at the Atlantis site. The transported sediments show a vertical downward increase in alumina, Fe and Ti oxide content, with a corresponding decrease in silica. Trace elements such as V, As, Pb and Cr are associated with Fe oxides and clays derived from the weathering of former lateritic materials. Heavy minerals such as zircon and anatase reflect higher concentrations of Zr, Hf, Nb, Ta and Ti (Table 5).

(4) The residual weathering profile consists mainly of four main units, arranged from base to top: (1) saprock; (2) lower ferruginous saprolite (10-40 m, better developed when ferromagnesian and sulfide minerals have greater abundances in the bedrock); (3) upper sandy kaolinitic saprolite (3-25m); and (4) silcrete duricrust (4-20 m).

(5) Gold anomalies are associated with the lower ferruginous saprolite and the underlying mafic saprock in NLC094 (*maximum* 11,700 ppb between 52-52 m depth interval) and NLC071 (*maximum* 213 ppb between 39-40 m depth interval). Increase in lithology- and ore-related elements such as Cu, Zn, Cr, Co and Ni are associated with the basaltic units and their overlying lower brown saprolite.

(6) The upper kaolinitic saprolite and the overlying silcrete cap represent the most intensive weathering within the profile. In contrast to Si, Al and immobile elements, mobile elements such as Na, K, Ca, Mg and potential indicator elements, including transition metals, are depleted in these units. Therefore, these two regolith units cannot also be considered as a reliable sampling *medium* (Table 5).

(7) The formation of local impermeable silcrete lenses, which protect the underlying saprolite from erosion, may prevent vertical hydromorphic dispersion from the underlying basement to transported sediments at surface. This effect may decrease in the laterally equivalent poorly-cemented grit areas.

(8) In NLC071, a Au anomaly (350 ppb) was detected in the uppermost 2-3 m of the transported cover. However, the anomalies in transported cover are detrital. Soil analyses from the five separated size fractions (>2000, 2000-25, 250-53, 53-2 and <2 µm) do not show any Au anomalies or hydromorphic dispersion of elements. Therefore, the surface soils cannot be considered as a reliable sampling *medium*.

Table 5. Summary of the regolith stratigraphy, mineralogy and geochemistry of the different regolith units in Beadell prospect.

Regolith Type/unit			Field and megascopic investigations	Microscopic and mineralogical investigation	Geochemical characteristics
Transported regolith	Ferruginous sediments		• They consist of iron-stained unconsolidated gravels and sand-sized sediments. • They contain ferruginous lateritic fragments, pisoliths and nodules (Atlantis site). • Sediments vary from poorly (e.g., NLC097) to well sorted (e.g., NLC159).	• Grain roundness: A. subangular to rounded corroded quartz grains. B. weathered granitic and mafic igneous rock fragments, silcrete and lateritic fragments. • Grain sorting: poorly to well sorted. • Cement: A. iron-stained poorly crystalline kaolinitic clays. B. late dolomite cement (e.g., NLC125).	• Vertical down increase in alumina, iron and TiO_2 oxides content associated with decrease in silica. • V, As, Pb and Cr are associated to iron oxides. • Zr, Hf, Nb, Ta, Th and Ti are concentrated, reflecting heavy minerals association such as zircon, anatase and monazite. • Au anomaly in NLC071 at 2-3 m depth.
Residual regolith	Silcrete/grit		• It consists of quartz grains are matrix-supported, moderately to poorly sorted, subangular to subrounded quartz grains. • Silcrete has a glassy appearance. • Silcrete has creamy-white cement. • Cement is locally stained with iron oxides.	• Grain roundness: angular to subrounded quartz. • Grain sorting: poorly to moderately sorted. • Cement: siliceous and less frequently amorphous clays. • Mineral composition: quartz, anatase and zircon (QAZ cement).	• Silica, TiO_2, Zr-Hf and Nb-Ta enrichment reflecting QAZ cement. • Depleted in alkalis, alkaline earth element, alumina and iron oxides. • Depleted in all transition metals. • Ba is locally concentrated as barite.
	Saprolite	Up. Kaolinitic	• The upper kaolinitic saprolite has milky white colour • Gradual contact with the overlying silcrete. • Porous and less dense. • Quartz grains float in a kaolinitic material. • The kaolinitic saprolite and the overlying silcrete are dissected by quartz vein (e.g., NLC159).	• The upper kaolinitic saprolite consists of quartz floating in kaolinite and less frequent illite. • Detrital reworked quartz and kaolinite clasts are also recorded. • Muscovite is still preserved. • Heavy minerals such as zircon, monazite and anatase after ilmenite are identified.	• Silica and alumina enrichment. • Zr-Hf, Nb-Ta enrichment. • LREE/HREE fractionation. • Depletion in alkali and alkaline earth elements. • Th, Zr, Ba, Sr and Pb enrichment. • Depleted in transition metals such as Ni, Co, Cr, Zn and Cu.
		L. ferruginous	• The lower ferruginous saprolite is mainly of brown colour • The original bed rock textures are still preserved.	• The lower ferruginous saprolite consists of quartz, weathered feldspars and muscovite. • Biotite, hornblende, garnet, pyroxenes and chlorite are altered to goethite. • Ilmenite and pyrite altered to titanite and jarosite. • Heavy minerals such as zircon and monazite are identified.	• Fe_2O_3, MgO, Na_2O, K_2O, Ba and Rb enrichment. • Increase in alkali and alkaline earth elements. • Enrichment in all transition metals, especially in Cr, Co, Zn, V and Ni. • Enrichment in Ba, Rb • Slight increase in Au.
Fresh rocks	Granitoids		• They show a wide range of composition staring from alkali granite, granodiorite to tonalite. • They show also colour variation from felsic to mafic-rich verities.	• They consist of quartz, plagioclase and K-feldspars, micas and hornblende. • The most dominant accessory minerals are zircon, apatite, rutile and titanite, ilmenite and pyrite.	• SiO_2, MgO, Na_2O, K_2O, Ba and Rb enrichment in granitoids and depletion in mafic rocks. • Iron and Ti-oxide decrease in granitoids and increase in mafic rocks. . • Zr-Hf and Nb/Ta increase in mafic rocks relative to granitoids which may indicate magma mixing. • Enriched in all transition metals in mafic rocks, especially in Au (11,700 ppb), Cr, Co, Cu, Zn, V and Ni.
	Gneisses and schists		• They include quartzofeldspathic and pelitic types. • Quartzofeldspathic consist of alternated white feldspar-rich bands and smoky quartz-rich bands. • Garnet-mica gneiss, schist and sheared granite.	• Quartzofeldspathic consist of alternated feldspar-rich bands that are altered to sericite and quartz-rich bands. • Garnet-mica gneiss, schist and sheared granite consist of foliated quartz, feldspars, micas and garnet together with pyrite, chalcopyrite and ilmenite.	
	Mafic rocks		• They occur as small intrusions cut through the granitic and gneissic rocks.	• Basic dolerite dykes, metagabbros consist of plagioclase weathered to zoisite, calcite and pyroxenes altered to hornblende, tremolite, chlorite and epidote.	

6. Trace element mobility in a deeply weathered regolith profile: the Hercules and Atlantis Au prospects *(Appendix F)*

Summary

This study focuses on understanding the mobility of specific trace elements from the basement rock suites, through the regolith profile to its surface expression, within the framework of a deeply weathered profile over the Hercules and Atlantis Au prospects (60 km north-east of the Tropicana-Havana Au system).

Two hundred and six samples were selected for bulk geochemistry, spanning the entire regolith stratigraphy of all units at the Hercules and Atlantis prospects. Specifically, sampling of the entire thickness of regolith was carried out at two metre intervals above mineralized bedrock in drill hole NLD210, and above weakly mineralized bedrock for drill hole NLD071, to provide a "low mineralization" contrast.

There is a wide spectrum of basement rocks at the Neale tenement, with igneous rock suites ranging from sub-alkaline and alkaline gabbro, intermingled with granites, expressed in a mixed geochemical signature. There is common metamorphism to greenschist facies, with some localized indications of amphibolite facies. As a whole, these rock suites have a typical Archaean geochemical signature of a tonalite-trondhjemite-granodiorite suite, similar to the Yilgarn Craton, resulting from slab melting in a subduction arc setting. No sedimentary packages have been identified within the basement rock suite. Due to the complexity of the basement rock suites, element ratios and metal accumulations in any stratigraphic unit of the regolith should be interpreted with caution for purposes of lithological classification of intrusive mafic-felsic-sedimentary rock units, when targeting specific rock type associations.

Results from geochemical sampling of the soil, within the uppermost first 20 cm, do not reflect any significant geochemical proxy that can address basement composition in the area. However, sampling transported cover can lead to the identification of displaced metal signatures from the basement, which can be tracked using an understanding of the associated sedimentary system. Anomalies located within the transported cover can be traced to possible near source areas at a scale of 100 m. Drill core and RC samples from the lower saprolite, preserve the main geochemical features of the basement, and therefore be used for exploration targeting strategies.

The silcrete unit (4-20 m thickness) is widely distributed in the Neale tenement, capping the kaolinitic upper saprolite. This unit varies laterally in cementation, and may present patchy permeable areas, and coincide in some cases with a more kaolinitic upper saprolite, which has resulted from more intense vertical weathering, and consequently vertical geochemical dispersion of the basement signature to the surface. Surface geochemical sampling above these permeable areas could deliver more reliable geochemical basement signatures

The weathering overprint in the environment of the Neale area developed in oxidizing acidic conditions within a low salinity groundwater environment displaying low vertical hydromorphic dispersion of REE, HFSE and transition metals within the upper saprolite and through the transported cover, with no detectable expression in the aeolian soil cover.

The most reliable soil fraction for metal and trace element content is from 53 to 2 and <2 µm fraction. Metallic elements are more concentrated in the <2 µm fraction whereas the trace elements associated with the heavy mineral fraction are concentrated in the 53-2 µm soil fraction.

6.1 Introduction

This study builds on Chapters 2, 3 and 5 where some geochemical features of the AFO basement are characterized.

More specifically, this study focuses on the understanding of trace element mobility (i.e., transition metals, REE and HFSE) from the basement rock suites, through the regolith, to its surface expression, in the framework of a deeply weathered cover profile over the Albany-Fraser Orogen/Yilgarn Craton margin, and more exclusively for the Hercules and Atlantis Au prospects (Fig. 46 in Chapter 4). Hence this study aims to contribute to the understanding of geochemical dispersion processes that affect the regolith environment, and to aid the design of more efficient mineral exploration strategies for this region.

6.2 Basement geochemistry

6.2.1 Rock classification

The sampled rock types belong to a complex lithological sequence of the Palaeoproterozoic Kepa Kurl Booya Province, which forms part of the crystalline basement of the Albany-Fraser Orogen (Spaggiari et al., 2009 and 2011).

Based on the previous section where Zr, Nb, Y and Ti are shown to behave as immobile elements in the regolith system, by application of Winchester and Floyd's (1977) classification, to the diamond drill core from the seven drill holes in the Neale tenement, at the Atlantis and Hercules prospects. These results indicate a wide spectrum and complex range of lithologies of igneous rock suites ranging from sub-alkaline and alkaline gabbro to granite (Fig. 70). Note that when samples from the basement at the Neale tenement are plotted using the Nb/Y ratio and SiO_2 (Fig. 70A), the rock classification is consistent with the results of the classification using Zr/Ti *versus* Nb/Y (Fig. 70B).

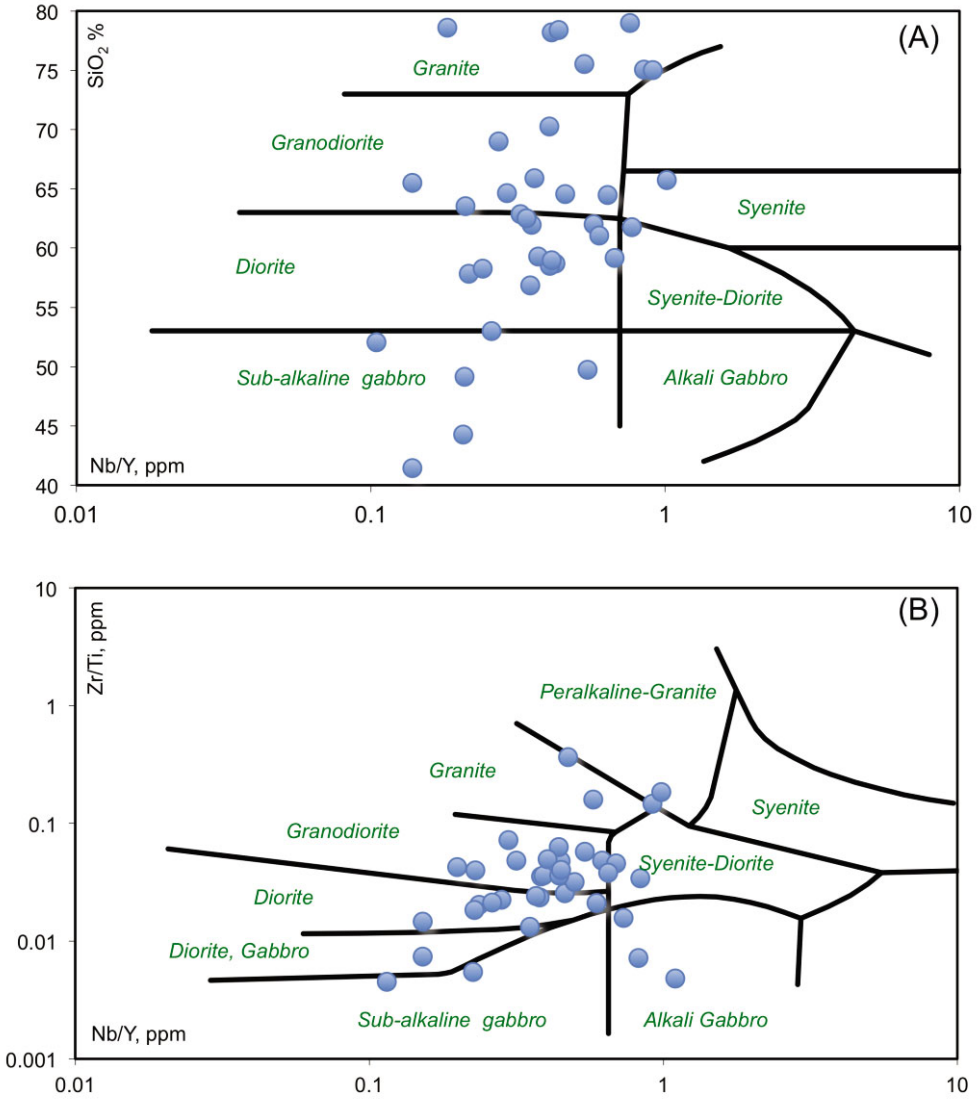

Figure 70. Geochemical classification of data from basement lithologies at the Neale tenement using the Winchester and Floyd (1977) immobile element classification scheme.

6.2.2 Element grouping

For plotting purposes, elements have been grouped in five clusters (Figs. 71 and 72): (1) major oxides together with Sr, Cs, Rb and Ba to display the principal weathering features; (2) multi-element group with a mixture of REE to display a diverse element group which show with weathering resistance; (3) transition metals; (4) REE; and (5) ore related elements such as Au, As, Sb, Ag, Mo and W.

6.2.3 Basement geochemical relationships

Most of the samples of the Neale tenement display a positive Eu/Eu* anomaly when normalized to UCC, spanning from 1.31 to 4 with most of the values between 1 and 2 (Fig. 71A, D). This indicates enrichment of Eu due to plagioclase accumulation since Eu in the divalent state is retained in the plagioclase lattice, substituting for Ca^{2+}. Positive Eu/Eu* anomalies are a widespread feature indicating the bimodal nature of Archaean crust for sedimentary packages, and are typical of mafic suites (PM; Middle Oceanic Ridge Basalts, MORB; e.g., Taylor and McLennan, 1985, 1995). These anomalies have typically been imputed to have an origin related to the timing magmatic crystallization of feldspar (particularly plagioclase), in relation to crystal-melt fractionation.

A plot of Sr/Y *versus* Eu/Eu* ratios (Fig. 71B) displays a positive correlation consistent with increasing Eu and Sr contents that can be interpreted as due to a plagioclase accumulation trend. Sr/Y ratios are mainly >10 with a few samples plotting with values >100 (Fig. 71B, D). However, a few samples display CaO alteration, and therefore, secondary enrichment of Sr that plots as outliners to the general Sr/Y trend in Fig. 71B.

In addition to the data distribution in the La/Yb *versus* Yb plot (Fig. 71E), with low Yb concentration and high $La/Yb_{n(ucc)}$, a plot of K content against Rb concentration, (K_2O from 0.8-3 wt% and Rb between 30-130), values cluster above the TTG field in relation to the Archaean andesitic-felsic rock field (Fig. 71C; after Huang et al., 2010). However, K addition by sericitic alteration could have had the effect of raising this data vertically in this plot above its original field on the Archaean andesitic-felsic rock trend. K-Rb values mostly plot as a consistent population, coherently with other immobile elements trends such as Eu/Eu* and La/Yb ratios (Fig. 71C-E).

Yttrium concentrations span mostly from 10 to 35 ppm (Fig. 71D), whereas Yb values plot principally below <2 ppm (Fig. 71E), and the La/Yb ratio ranges mainly from 10 to 50 (Fig. 71E).

Alumina content is consistent at ~15-20 wt% whereas silica concentration ranges widely which could be a feature related to geodynamic settings, as well as the impact of silica increases related to deformation and fabric development (especially mylonitization) for some of the samples (Fig. 71F). This is coupled with REE patterns enriched in LREE relative to HREE (Fig. 72D), a systematic significant depletion of Nb-Ta, and a variable negative Zr-Hf anomaly (Fig. 72B). The metal budget is variable, showing a positive Cr anomaly (Fig. 72C).

The Kepa Kurl Booya Province, where the samples of this study were taken, is described as Palaeoproterozoic rock suite described as metasyenogranite interlayered with mingled metagranodiorite and metagabbro, and including a component of Archaean rocks (Spaggiari et al., 2011). This generalized description does not preclude the development of TTG rock suites, although it suggests a regional dominance of alkali feldspar rich rocks. Certainly, observations of drill core from the Neale and Hercules prospects indicate a local dominance of a plagioclase rich intrusive suite.

The TTG suite formed a major component of the Archaean crust. These rock suites are interpreted to form by partial melting of hydrated oceanic crust in a subduction dominated geodynamic setting (e.g., Condie, 2005). This suite features high silica contents of ~60-70 wt%, alumina values above ~15%, high La/Yb (>30), and low Yb (<2 ppm) for the most immobile elements (e.g., Smithies, 2000; Huang et al., 2010).

Based on the previous, and taking the geochemistry of the suite as a whole, the data is consistent describing a main Archaean geochemical signature of TTG similar to Yilgarn granitic-greenstone belts.

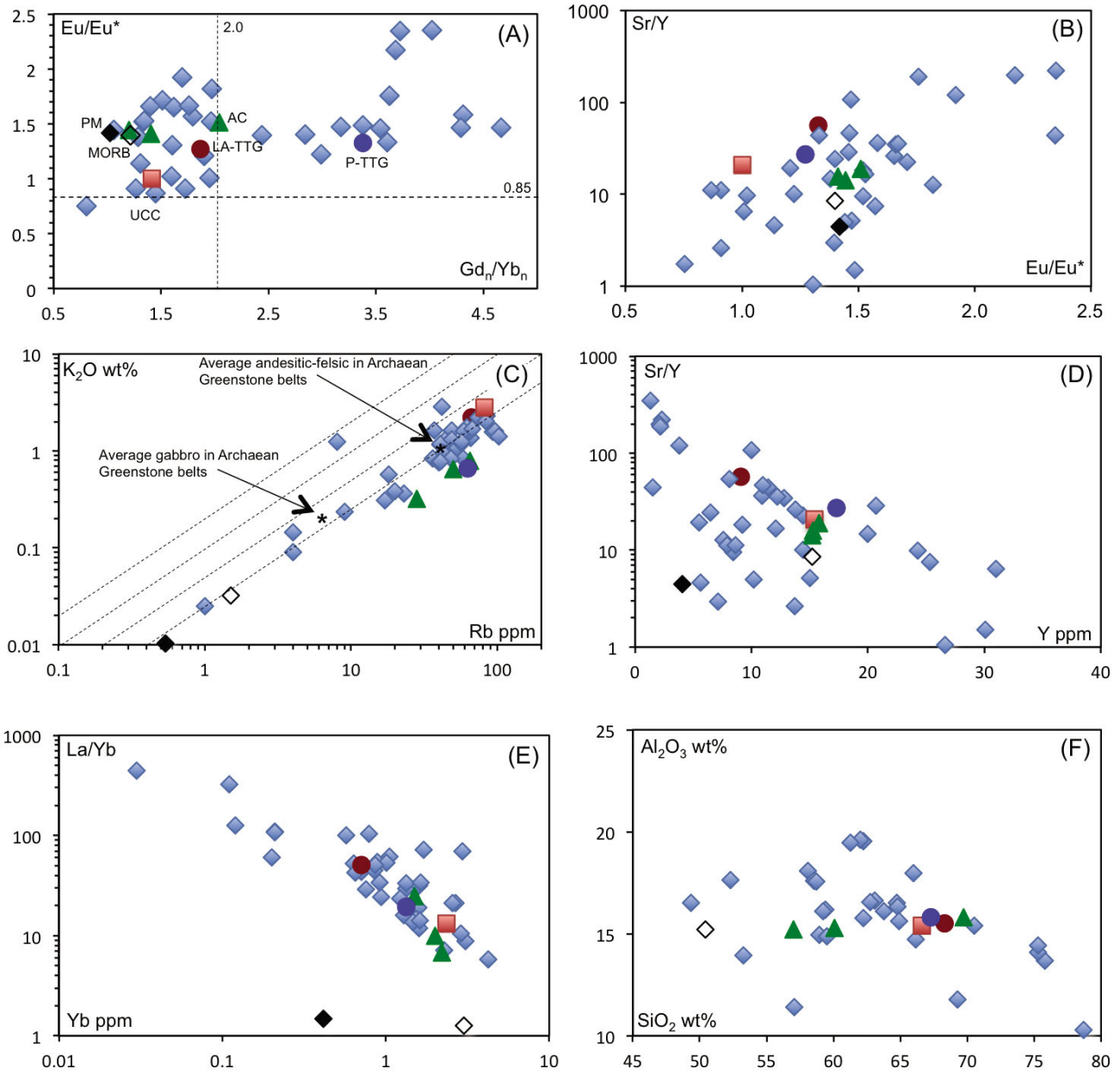

Figure 71. Selected plots of element ratios for basement lithologies of the Neale area, showing characteristic Archaean geochemical signatures, such as a systematic high positive Eu/Eu anomaly, $(Eu/Eun)/[(Smn)(Gdn)]^{1/2}$, (Taylor and McLennan, 1985). Tonalite-trondhjemite-granodiorite features in (A), (B), (C), (D), (E) and (F). Green triangles are Archaean Crust (AC) average values from Taylor and McLennan (1985; general composition for felsic crust, upper crust and total crust values); Red dot is Late Archaean-TTG average composition (LA-TTG) and the blue dot is Proterozoic TTG average composition (P-TTG; Condie, 2005); red square is Upper Continental Crust average values from Rudnick and Gao (2003); black diamond is PM from Zindler and Hart (1986); and open diamond is MORB (Arevalo and McDonough, 2010), as indicated in (A).*

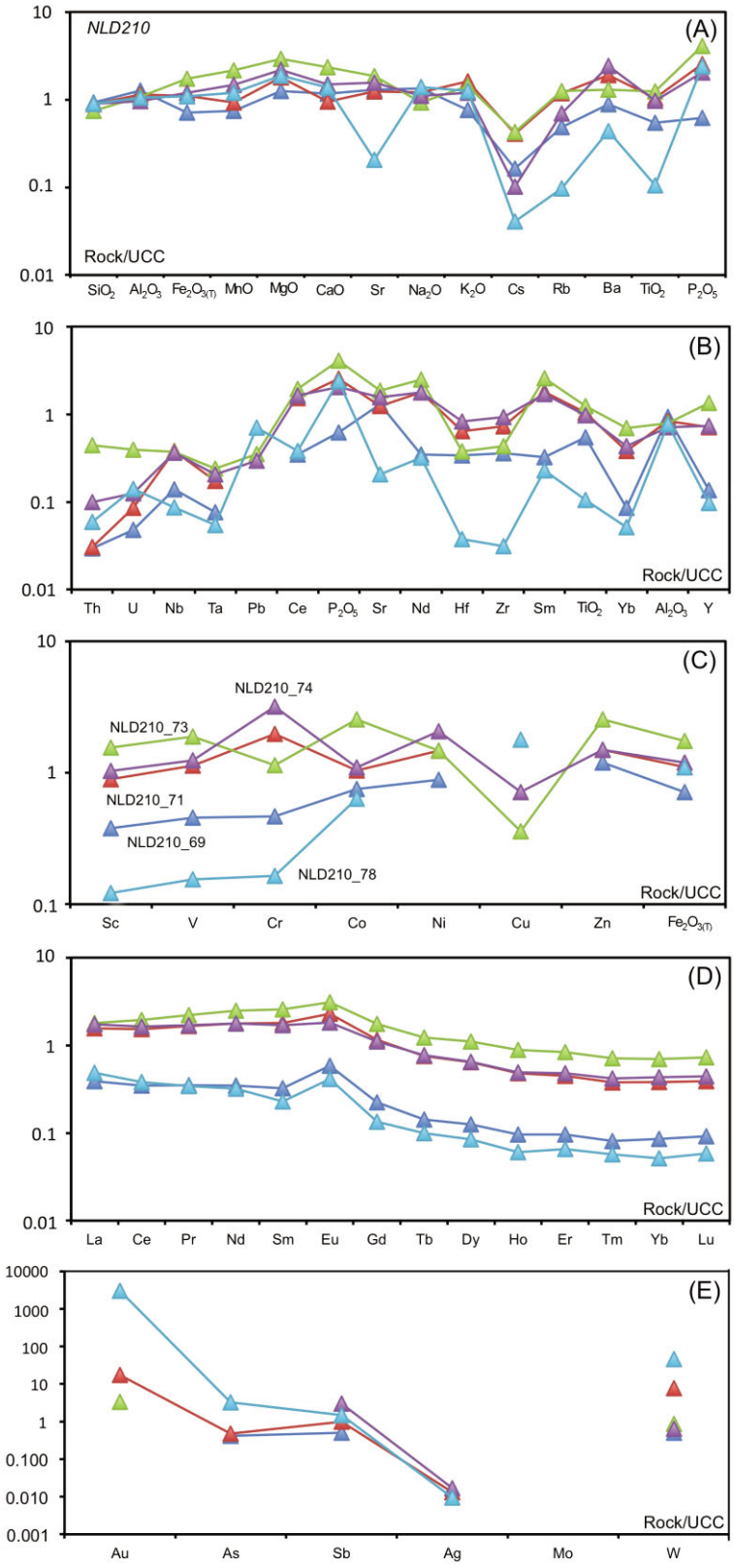

Figure 72. Geochemical multi-element spider plots of a representative basement sample set for geochemical characterization normalized to UCC. (A) Major oxides; (B) multi-element spider plot; (C) transition metals; (D) REE; and (E) Au and selected elements sensitive to hydrothermal mobilization (Appendix B).

6.2.4 Are there any deformed and metamorphosed sedimentary units within the "Neale" package?

The host rocks of ore deposits may play an essential role in localizing their formation. Therefore, the discrimination between sedimentary packages and igneous rock suites can have great significance for mineral exploration in areas where metamorphism and deformation may have overprinted the original lithological or deposit features. In this section, this issue is addressed using geochemistry of immobile elements.

Most TiO_2 values vary from 0.2 to 0.8 wt% (Appendix F; Fig. 73A), similar to the Upper Continental Crust (UCC) reference values, but with a trend towards a more felsic component (Fig. 13A), with higher concentrations and lower silica contents than average Archaean TTG rock suites.

Zirconium does not follow a consistent trend toward more abundant silica contents, plotting at <200 ppm. Most Zr values are lower than the 152 ppm value of average Archaean TTG. However, Zr values displayed a wide variety of values at <100 ppm, lower than total Archaean average crustal values of 100 ppm. When Hf is plotted against Zr, most of the Zr-Hf values lie between MORB and PM reference values (Appendix F), with practically no values plotting close to UCC or felsic Archaean crust values. The same trend is shown for Nb and Ta values, with most values plotting between MORB and PM values, or in close proximity to MORB values (Appendix F).

For the transition metal budget, Ni, Co and Cr values are 20-100 ppm for Ni, ~10-50 ppm for Co and <200 ppm for Cr, compared to UCC average values of 34, 17 and 73 respectively, Archaean Upper Crust has average values of 105, 25 and 180 ppm, and Archaean Total Crust values of 130, 30 and 230 ppm, respectively (e.g., Fig. 73E for Ni). Therefore, the Neale geochemical values are consistent with a bimodal mafic-felsic crustal composition and plot close to UCC average values.

Scandium values, indicative of a mafic component, cluster between 10-30 ppm for 55 to ~70 wt% silica values, averaging as UCC values of ~15 ppm at lower silica contents (Fig. 73F), whereas Th content ranges from 0.5 to 4 ppm, regardless of silica content in the field of Archaean Total Crust, averaging of 2.9 ppm (Fig. 73C). Rubidium values scatter independently from silica content, and vary mainly between 30 and 90 ppm, spanning from the 28 ppm average value for Archaean Total Crust to slightly more than the 82 ppm value of the UCC (Fig. 71C).

Total LREE content varies mostly between 50 and 200 ppm, clustering mainly around the average Archaean Upper Crustal value of 90 ppm. However, outliers of total LREE values from 200-300 ppm have low silica values of ~45-60 SiO_2 wt% (Fig. 73D). The LREE/HREE ratio increases with silica value, and varies mainly between 10 and 100, with most values clustering between felsic (igneous) Archaean and Archaean Upper Crust values (Appendix F).

All of the above observations from data presented here do not provide any evidence for the geochemical profile of a sedimentary package. Key sedimentary indicator elements that are typically significantly enriched in sedimentary rock suites, such as Zr and Th, are here depleted towards MORB-PM values of 90 and 10 for Zr, and lower than average values for total Archaean crust. In addition, petrographic and hand-specimen observations from core/chips report igneous or meta-igneous textures (Chapter 4).

This geochemical signature is interpreted to be the result of the absence of a sedimentary package in the basement rocks of the Neale area; may at least in part be the result of mixing and mingling of magmas of different compositions.

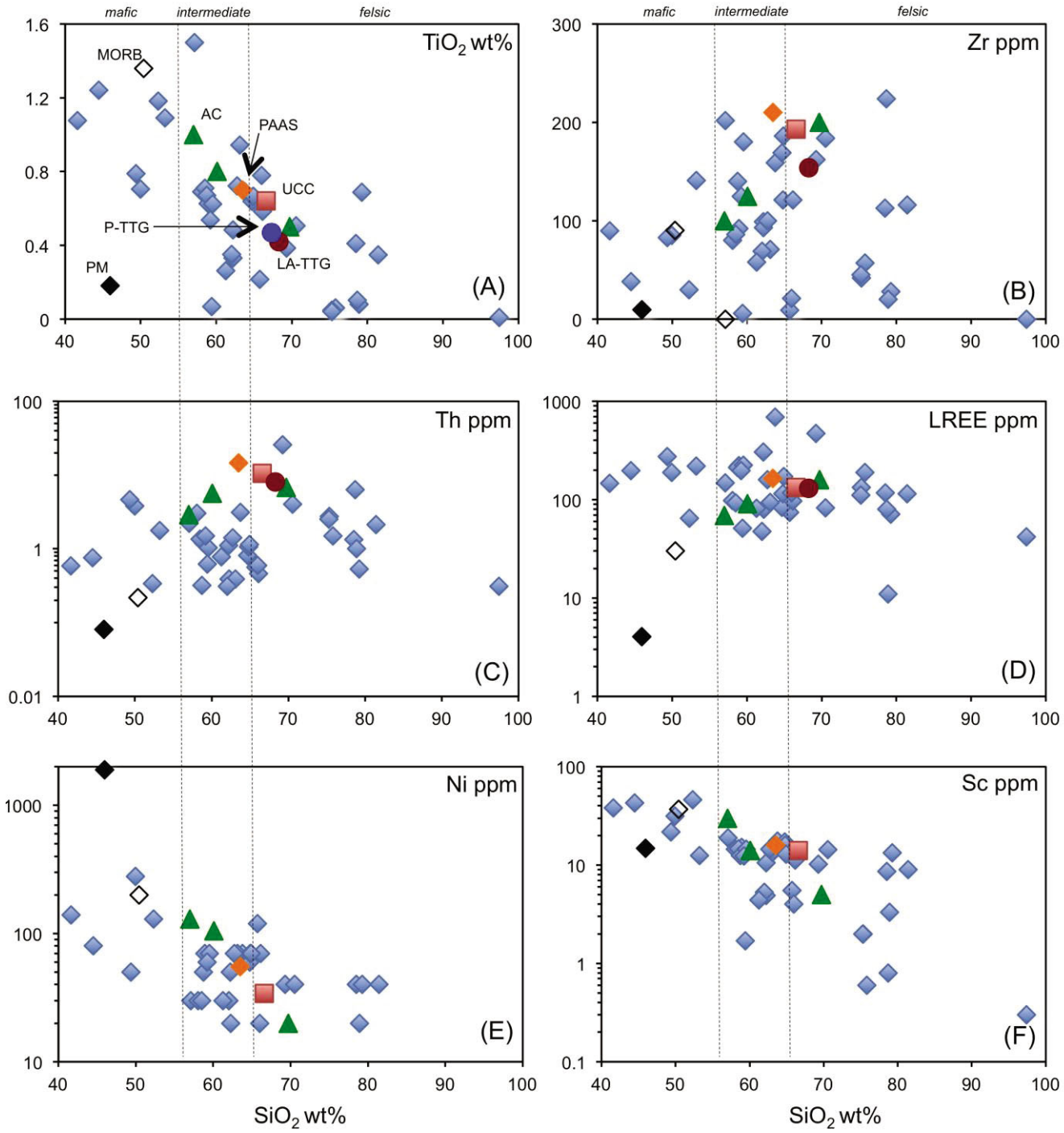

Figure 73. Geochemical plots for basement lithologies from the Neale area, for selected key elements against silica content, for sedimentary rocks normalized to UCC. These plots typically display complex elemental signatures, spanning from mainly Post Archaean Australian Shale (PAAS; Taylor and McLennan, 1985 and references therein), sedimentary LREE and Sc concentrations (D and F) to low Zr and Th concentrations below typical PAAS values of <210 ppm, and 14.6 ppm, respectively. Data displays a wide range of silica content, and mainly less than 65 wt% SiO2.

6.2.5 Regolith and soil geochemistry

Logging of 32 RC and diamond drilling holes in the Neale tenement has indicated the presence of a variable thickness of transported cover between 2 and 25 m. The transported cover is characterized by Fe-stained ferruginous clast-supported sand and gravels, which display variable sorting and polymict clasts (Fig. 74; Chapter 5).

The residual regolith is divided into three units: (A) a lower saprolite mainly expressed as ferruginized parental rock (granites, gneisses, schists and mafic rock suites; 10-40 m thickness); (B) a sandy kaolinitic upper saprolite (3-25 m thickness); and (C) a laterally continuous silcrete unit (4-20 m thickness) with variable content of silica cement; The saprolite, including the silcrete unit, has a total thickness from 17 to 85 m (Fig. 74; Chapter 5). For further detail on regolith mineralogy and petrography see Chapter 5.

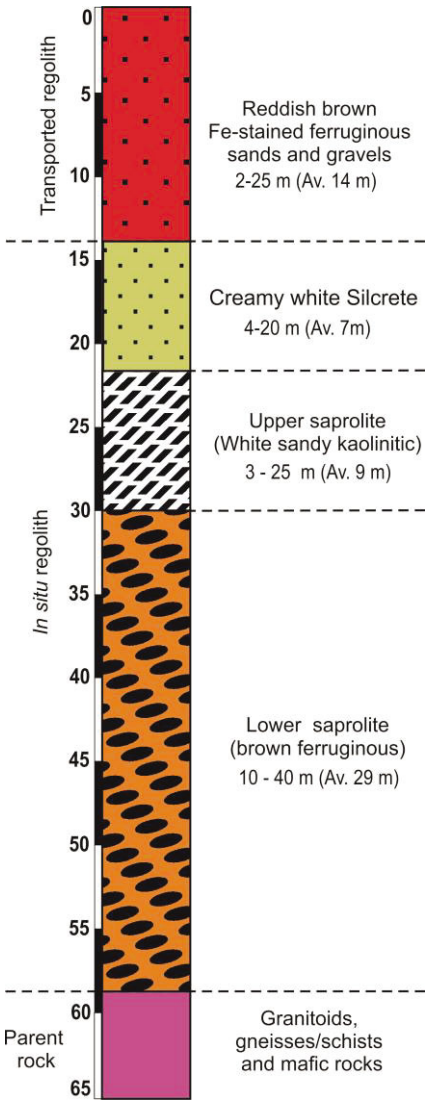

Figure 74. Idealized stratigraphic sequence of the regolith profile in the Neale area. This Fig. has been compiled from summarized drill hole data (Appendix E).

From the bottom saprolite to the top-soil unit, the main geochemical features presented in Figs. 75 and 76, are summarized as follows (Table 5):

(1) The lower ferruginous saprolite mimics the same geochemical features as the saprock for major oxides, REE, HFSE and transition metals (Sc, V, Cu, Cr, Co, Ni, Zn), and Au when present, but at higher absolute values (Figs. 75 and 76). This is due to a relative increase in trace element concentration due to leaching of major oxides during incipient mineral weathering. Uranium is fractionated from Th increasing its concentration relative to Th (Fig. 75B).

Rare earth element patterns display the same positive Eu anomaly for the lower ferruginous saprolite as for the saprock (Fig. 75D).

The lower saprolitic package has a gradational contact with the saprock, displaying common geochemical features, consistent with the geochemical characteristics of the basement rock described in the previous section (Figs. 75 and 76J-O).

(2) The kaolinitic unit displays intense weathering, with leaching of the main mobile major oxides, and an increase in LREE concentration (due to Ti oxides content and kaolinite) relative to HREE, which have been mobilized.

The Eu/Eu* anomaly is obliterated, and there is an increase in the relative concentration of HFSE (Nb-Ta, Zr-Hf, Th-U), with a drop in the metal budget, except for Sc, V and Cr, that retain concentrations close to UCC values. Absolute element concentrations are reduced due to silica-kaolinite dilution (Fig. 75A-D).

Vanadium is strongly linked with both Cr and Ti as oxides, and phosphate is correlated with LREE. Titanium oxide minerals, zircon and monazite carry the main REE signature of this unit (Fig. 76G-I).

Scandium, V and Cr can thus be used as conservative metal proxies for the basement rocks within the upper saprolite. Gold signature from the basement is not shown for this unit (Figs. 75C and 76I).

(3) The silcrete has geochemical features similar to those of the upper saprolite, with the main difference in silica content, due to an increase in silica cement. Rare earth element patterns in the silcrete and the kaolinitic units, are similar although total REE abundances have been diluted by silica in the silcrete (Fig. 75D). Zirconium is highly concentrated with the silcrete as quartz cement is found together with anatase (Fig. 76D-F).

(4) Geochemically, the soils and the upper ferruginous saprolite have similar REE and HFSE patterns. Rare earth elements plot parallel to UCC values with lower abundances, due to dilution of silica and iron oxides (Fig. 75A-C).

The transported cover has similar geochemical patterns as for the upper saprolite and silcrete units, but with negative La/Yb slopes. However, multi-element plots, major oxides and transition metals follow similar patterns to those displayed in the saprolite described previously. However, field observations coupled with mineralogical observations allow distinction of this unit as being transported (Chapter 5).

The samples collected from NLC071 at Atlantis potentially show a more complex pattern that could have a significant residual component (Figs. 75D and 76A-C).

Geochemically, soil samples display a positive Zr-Hf anomaly (Fig. 75B) that is interpreted as the result of selective aeolian sorting, resulting in the accumulation of a fine grain-sized fraction of zircon.

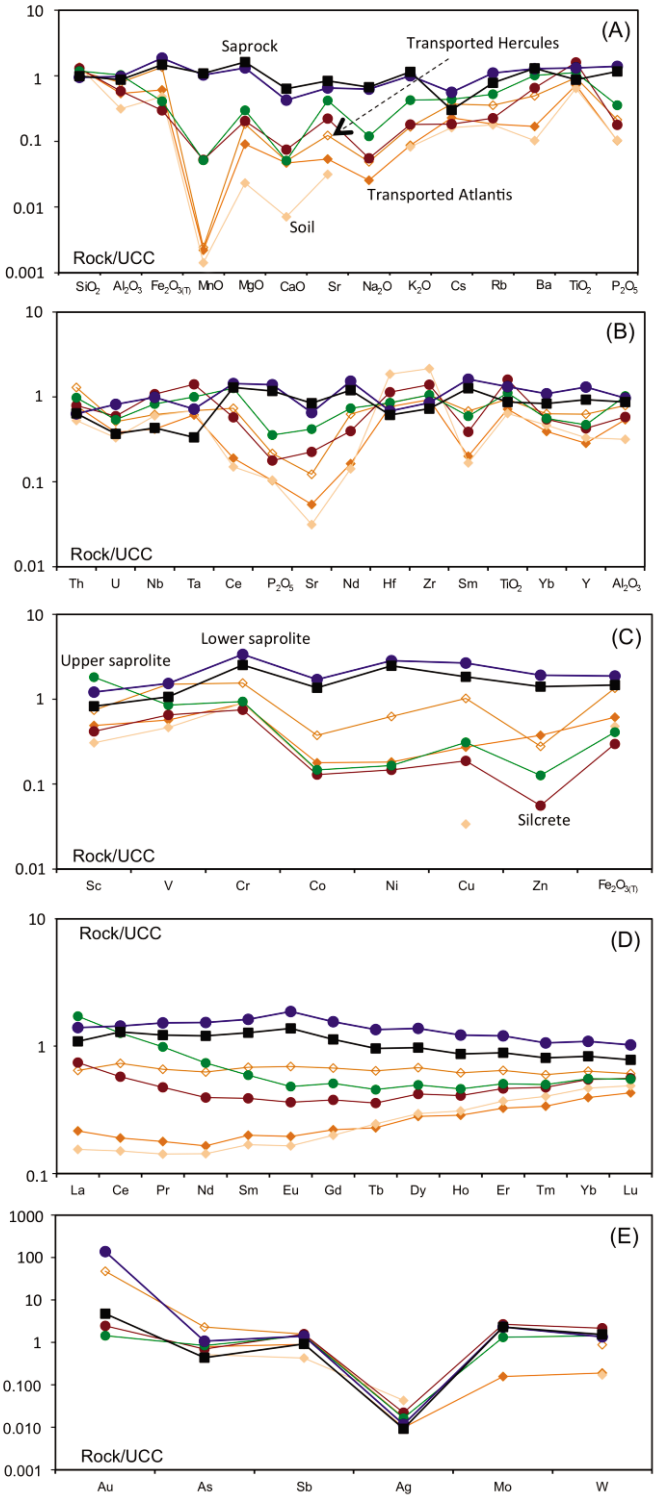

Figure 75. Bulk geochemical plots for average geochemical analysis of the different regolith units identified, with elemental values normalized to UCC values (Rudnick and Gao, 2003). Plot (A) displays parallel major oxide concentrations between saprock and the lower saprolite units; (B) shows a dominant leaching of phosphates and Sr from the saprock to the transported cover, together with an increase in relative concentration of Zr-Hf and Nb-Ta from the saprock to the transported cover; plot (C) illustrates coherent behaviour of Co-Ni and Cu from the saprock to the upper saprolite; (D) REE plot with a positive Eu anomaly and positive slope from La to Lu; and (E) transition metals exhibit positive Au anomalies with a systematic depletion in Ag content.

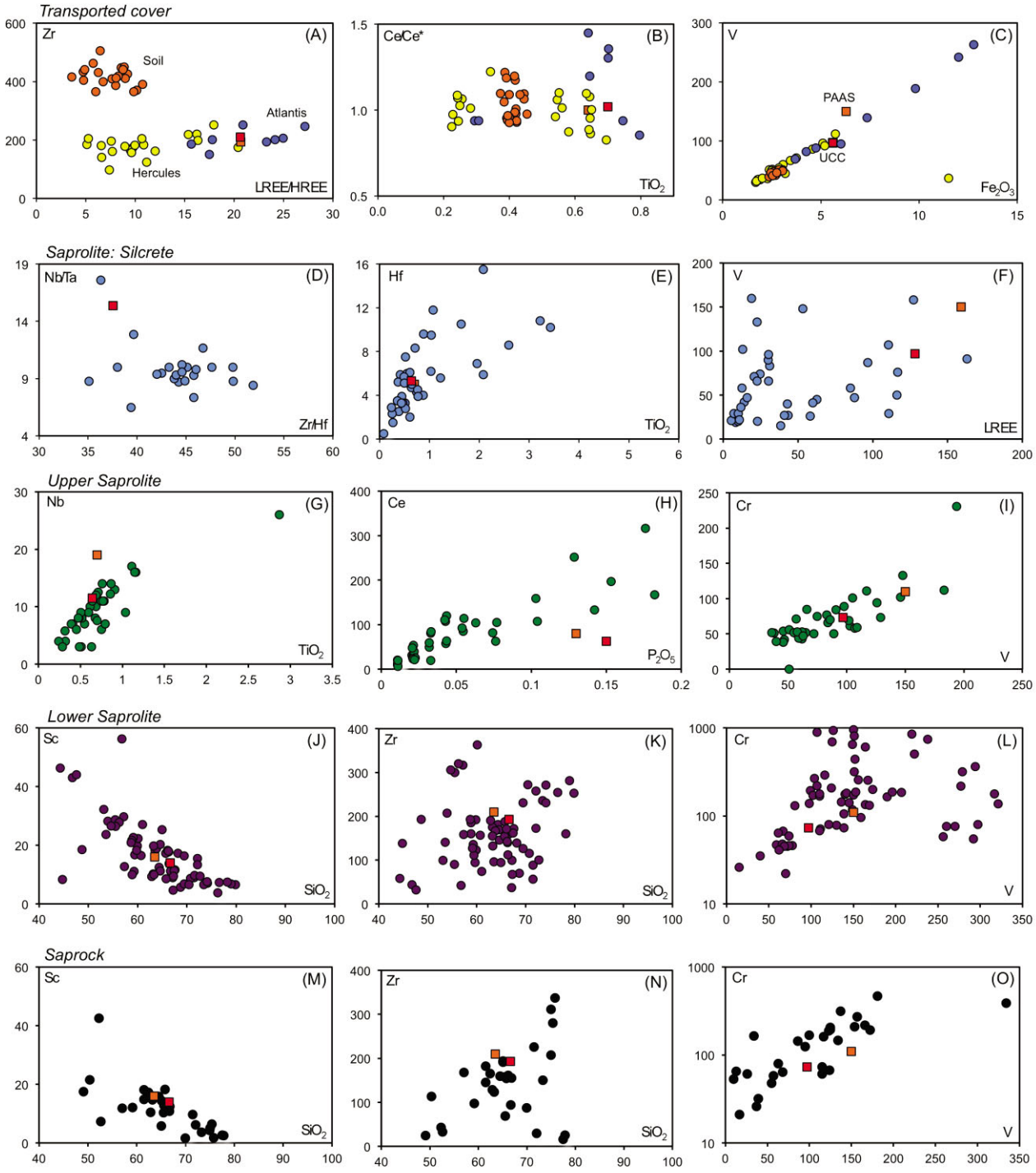

Figure 76. Selected geochemical plots for average regolith units, with elemental values normalized to UCC values (Rudnick and Gao, 2003). (A), (B) Ce/Ce = $\{[(Ce/Ce_n)/[La_n)(Pr_n)]^{1/2}\}$ from Taylor and McLennan (1985), and (C) display geochemical features for the transported cover; (D), (E) and (F) for silcrete; (G), (H) and (I) for the upper saprolite; (J), (K) and (L) for the lower saprolite: and (M), (N) and (O) for the saprock. Vanadium is linked consistently throughout the complete regolith profile with Cr, LREE and Fe (C), (F), (L) and (O). Oxides in wt% and elements in ppm.*

Table 6. General geochemical vertical features of the saprolite at the Neale area (Figs. 75 and 76).

	Major oxides			***REE +Y***	***HFSE***	***Transition metals***	***Ore related/pathfinder elements***	
	MnO, MgO, CaO, Na_2O, K_2O	***Al_2O_3; SiO_2***	***TiO_2***	***La-Yb-Y, Eu/Eu*, La/Yb***	***Nb/Ta, Zr/Hf, Th/U***	***Sc, V, Cr, Co, Ni, Cu, Zn***	***Au***	***As, Ag, Sb, Mo, W***
silcrete	intensely leached	SiO_2 cement enrichment	conserved	LREE enrichment	reseting of the Nb/Ta and Zr/Hf ratios	Sc concentration; V-Cr conserved; Co--Ni-Cu-Zn leached out	leached	conserved
Upper saprolite	intensely leached	conserved	conserved	Eu/Eu* anomaly removal; partial removal of HREE-MREE and LREE with increasing La/Yb slope	conserved original ratios	Sc-V-Cr conserved; Co--Ni-Cu-Zn leached out	leached	conserved
Lower saprolite	conserved	conserved	conserved	conserved concentration with same Eu/Eu* anomaly and La/Yb ratios	ratios conserved; increased of U concentration	conserved	anomaly increased	conserved
Bedrock				original concentration with positive Eu/Eu* anomaly, and positive La/Yb				

6.3 Geochemical features of NLD210 and NLD071: element dispersion from basement to the soil

Diamond drill hole NLD210 intersected granitoid-syenite-dolerite basement rock suites (Fig. 77), whereas drill hole NLD071 intersected a basement rock suites of granitoid-dolerite. Both drill cores display a positive La/Yb slope and systematic positive anomalies of Eu/Eu*, as well as Nb-Ta and Zr-Hf depletion, consistent with the signatures of Archaean TTG lithologies.

In the regolith profile, from basement to soil, the silica content increases, due to resistance of quartz to weathering and sedimentary sorting effects, up to 95 SiO_2 wt%. Major oxides are leached from the profile (i.e., MnO, K_2O, MgO, CaO and Na_2O; Appendix F), decreasing in concentration in the upper regolith profile where kaolinite is the main residual clay component.

Rare earth elements are locked mainly in heavy mineral fractions, in species such as anatase and zircon, which accumulate in the silcrete unit. Zr-Hf concentration increases from ~60-320 ppm in the basement and lower saprolite, up to 130-700 ppm in the upper units (Appendix F). However, the Zr/Hf ratio in the basement rocks varies between 30 and 55, whereas in the regolith it spans 40 to 65. Ilmenite is altered to anatase. Niobium changes in the lower saprolite, expressed as Nb/Ta ratio values from ~15 and ~65, although for the upper regolith levels this ratio varies from ~7 to ~15 with two outliners at 26 and 20.

Zirconium/Hf and Nb/Ta may be influenced by parent lithology. However, these ratios change in value at the same depth as the seasonal water table oscillations, and remain constant within the upper saprolite and the overlying transported cover, suggesting that the HFSE ratio change is due to weathering processes, which remain enigmatic. This implies that heavy mineral species within these fractions have been altered and do not reflect the original geochemical element ratios of the basement (Appendix F). Yttrium, Middle REE (MREE) and LREE were leached, and their concentrations vary due leaching of major components, with silica increasing proportionally in the regolith units (Figs. 74, 75 and 76). This is displayed as a relative concentration increase in the lower saprolite compared to the saprock and basement, with the dilution effect of silica in the soil and silcrete units (Appendix F). The Eu anomaly is no longer present in the basement rocks (Appendix F).

Titanium shows a distribution characterized by higher concentrations in basement rocks and the lower saprolite than in transported cover and soils, concentrating in the form of anatase in silcrete with values up to ~0.52 wt%. This is much lower than the concentration 3.5 wt% of TiO_2 in silcrete from NLD210, probably due to a weaker cementation.

Chromium increases in concentration in the lower saprolite, retaining UCC values of ~50-160 ppm throughout the profile. Cobalt is leached out and Ni mostly is within the same range as Cr and Co, staying at background values of 80 ppm, with many samples having Ni concentrations below detection limit (Appendix F).

Gold concentration from the intersection in the basement is reflected in the lower saprolite, but not in the upper saprolite. However, the silcrete unit and the transported cover have some anomalous Au values not detected in soil sampling (Appendix F). These anomalous values are interpreted as lateral sedimentary dispersion, and are not produced by vertical movement of Au, since the anomaly is lacking in the upper saprolite.

The geochemical composition of the basement is mimicked in the lower saprolite (Appendix F). There is a geochemical fingerprint overlapping across the upper saprolite, silcrete and the transported cover (Appendix F).

Soil samples do not reflect REE, HFSE and transition metal anomalies from the basement other than the Zr-Hf anomaly associated with loess deposits (Appendix F).

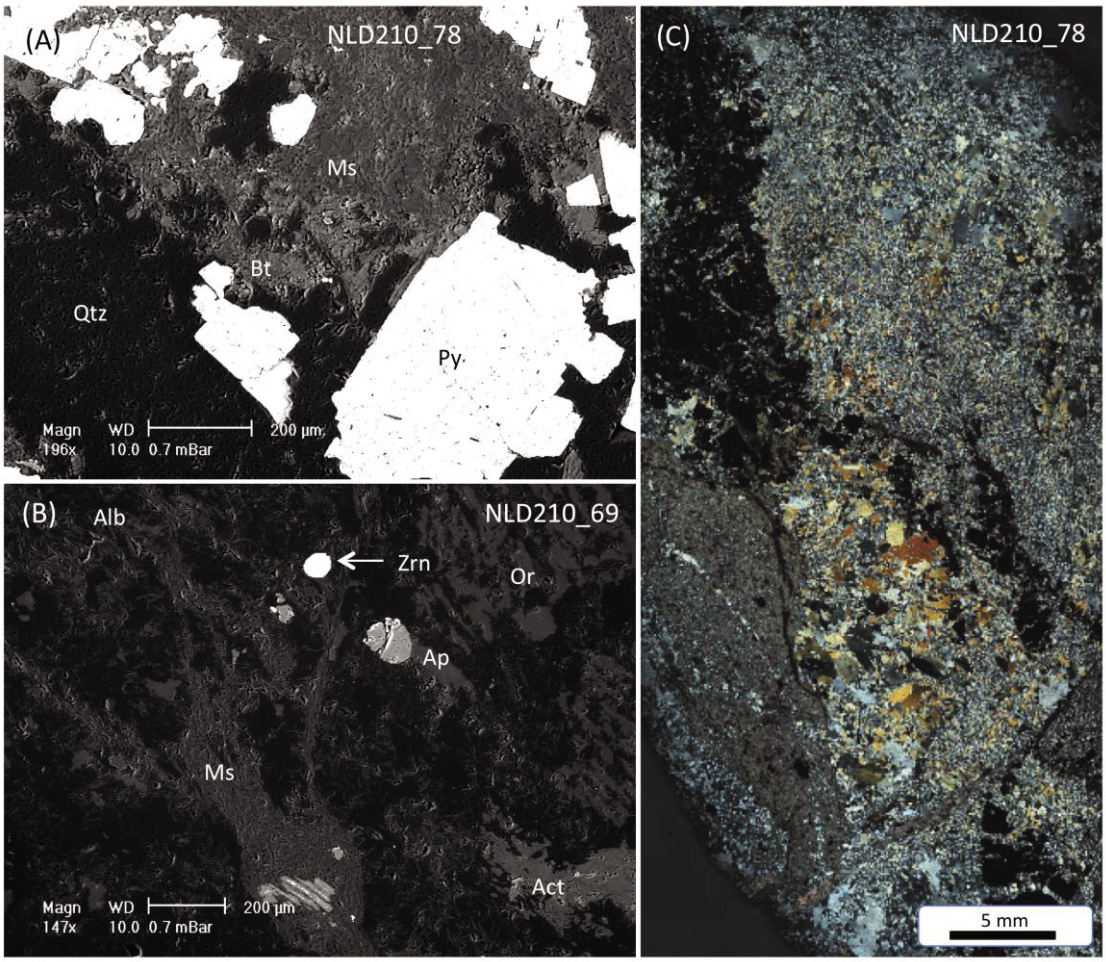

DD hole	Interval (m)		Lithology	Texture	Mineralogy	Alteration	Sulphides
NLD210_68	57.9	61.85	Leucogranite	massive	weakly oxid, alkali fsp-quartz, primary musc/biot?	weak pervasive seric±chl alt; 57.85-58 & 60.15-60.4 clotted patchy fg chl-seric masses, locally more intense alt	
NLD210_69	72.25	82.95	Alkali feldspar granite	massive to banded	alkali fsp-quartz±musc±biot±plag; epidote indicated from hylogg ~65-79	weak pervasive seric-chl±hem, mostly selective alt of plag & mafic mins; rarely more intense - see comments. Musc from hylogg	
NLD210_71	94.75	101.1	Altered intermediate intrusive (meta-syenite?)	weak banding/foliation	ksp-plag-qtz-chl-act-hbl	Selective alt of hbl to act-chl	traces of f-mg py
NLD210_73	122.24	123	Dolerite	Massive equigranular	chl-amph-biot-fsp		
NLD210_74	141.7	144.4	Altered/meta-intermediate intrusive (meta-syenite?)	weak-mod banding, align of spaced amph grains	ksp-plag-qtz-chl±biot±act±hbl	tr sericite; apparent hematitic oxid haloes	<1% f-cg dissem and veinlet py; cser grains display in situ bxation
NLD210_76	163.92	166.8	Altered intermed intrusive to granofels	massive to foliated	chl±biot±seric±CO3±qtz; ± primary Kspar±act±hbl	strong overprint chl±seric±biot±silica	tr vf-fg dissem py
NLD210_77 NLD210_78	166.75	168.4	Quartz vein	massive mottled	qtz; tr chl-seric infill		fg py assoc with chl fracs/shears
NLD210_81	187.6	189.7	Alt sheared metasyenite	weakly to moderately foliated	ksp-plag-qtz-chl-hbl±biot±seric±act±px?±hem	weak silica±seric, patchy; weak hem alt of Kspar	

Figure 77. (A), (B) and (C) selected petrographic images from NLD210 drill core, showing lithotextures and mineralogy, coupled with a table presenting with the main petrographic features of the samples taken from the core. Mineral abbreviation key in Appendix F.

6.4 Contextualization of the data

6.4.1 Variations in regolith thickness, salinity and digital elevation: complexities in tracking anomalies

The oldest geomorphological feature preserved in the regolith of the Yilgarn Craton/Albany-Fraser Orogen margin is the palaeochannel pattern. Between the late Tertiary and Quaternary, semi-arid to arid climatic conditions were widespread in the Yilgarn (Anand and Butt, 2010). This resulted in the failure of major river systems, which turned into a sequence of lakes. At the same time, surface and ground water became increasingly saline.

Saline water is concentrated in areas with higher porosity within the riverine sedimentary sequences, and therefore can be used as a tracer in defining potential palaeochannels from ground water salinity maps (Chapter 5 see Fig. 58D). This salinity feature has significant effects on trace element mobility within the regolith and its expression at surface, since element dispersion is driven mainly by fluid conditions: salinity, acidity (pH) and oxidation-reduction potential (Eh), and salinity enhances the mobility of many trace elements (González-Álvarez and Kerrich, 2010). However, the Neale tenement is located in an area of low ground water salinity <1,000-3,000 mg/l (Fig. 58). This groundwater salinity value does not significantly enhance trace element and metal mobility, as much as hypersaline values from other areas with values >30,000 mg/l (Fig. 58D).

Valley elevation expressed as gradient is presented in Fig. 78. This was derived using the Gallant and Dowling (2003) algorithm. This algorithm describes the landscape by enhancing the basal features of valleys, which discriminates between uplands (dark grey colours) and lowlands (pale shades).

The multi-resolution index of valley bottom flatness (MrVBF) identifies areas that are low and flat relative to their surroundings, and may be expected to have accumulated more sediment. Larger values of the MrVBF index indicate broader and flatter valley bottoms, and hence thicker deposits of sediment. The relationship between MrVBF and the depth of deposits has not been investigated in detail to date, but there are suggestions that a relationship does exist.

Accordingly, this depiction has the potential to map the main depositional areas and describe geomorphologic domains in relation to palaeovalleys and palaeochannels in the Neale area. It indicates how the dynamics of the sedimentary system worked in the area, and therefore where the thickest sedimentary packages could be expected, by following the drainage geometry of the area. Figures 78 and 80 can be applied to better interpret geochemical anomalies in the area, by linking them to transported cover features and local sedimentary dynamics.

From a previous study based on AEM, González-Álvarez et al. (2013) showed that the regolith thickness in the Neale tenement, increases to a *maximum* of ~75 m. This thickening has two trends: one towards the south-east due to the increase of the transported cover of the Eucla basin; therefore deeper drilling to sample the basement is required here.

Such thicknesses of transported cover would prevent reliable geochemical signatures derived from the basement from reaching the surface. The second thickening trend is towards the north-east, which may be associated with a background complexity of palaeodrainage in the area, describing a south-east-north-west secondary palaeochannel system that drained into a main north-east/south-west palaeochannel (Fig. 78).

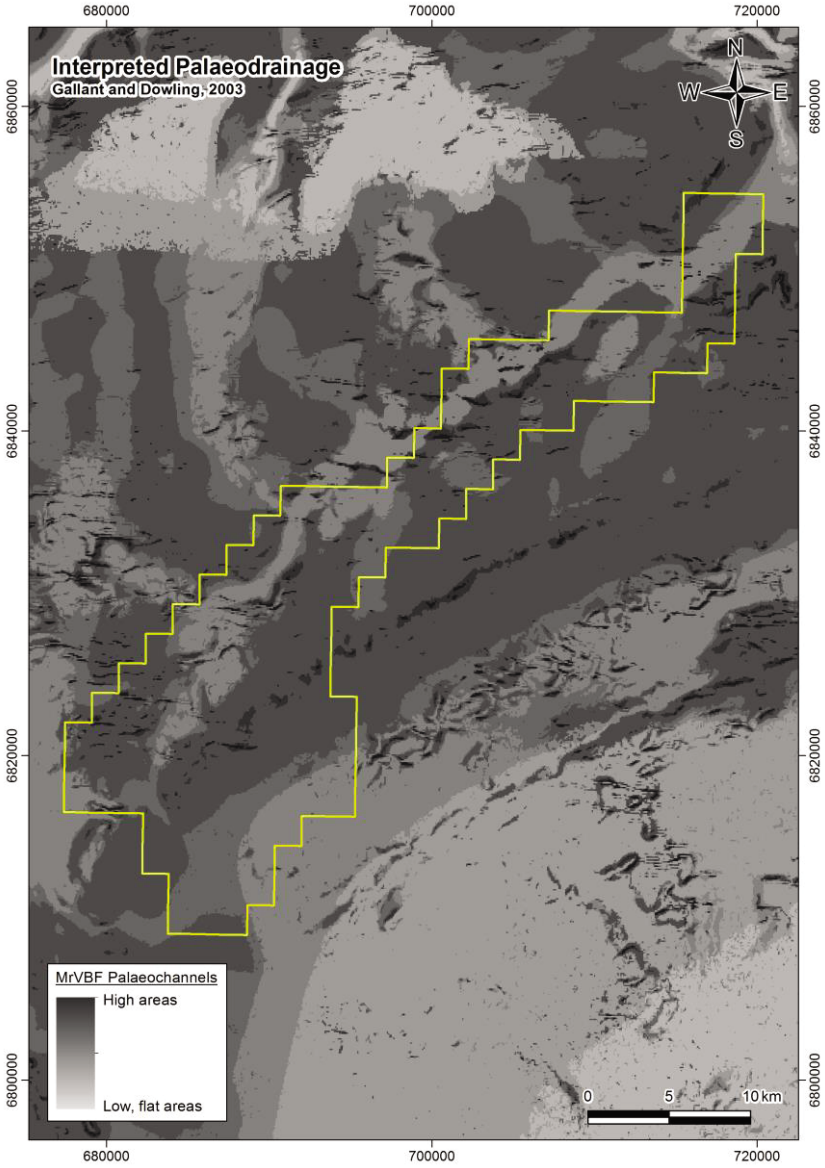

Figure 78. Digital elevation model data presented after filtration applying the Gallant and Dowling (2003) algorithm. It describes the landscape and enhances the valley features. Dark greys represent steeper areas. The flattest areas are represented by light grey colours that may indicate the presence of a palaeochannel. The slope gradients visualized in this Fig. may be used to interpret the sedimentary evolution of the area. The dominant drainage direction in the south-east may indicate a greater thickness of transported cover. Legend: MrVBF = comparative multiresolution index of valley bottom flatness used for mapping depositional areas.

Bulk chemical analyses of the transported cover shows that the SiO_2, Al_2O_3, TiO_2 and Fe_2O_3 contents represent >99 wt% of total oxides (Fig. 75A). SiO_2 decreases downwards from the surface soil (within 0-3 m), and is accompanied by a relative increase in Al_2O_3, TiO_2 and Fe_2O_3 contents. These oxides are the main chemical components of the Fe-stained kaolinite cement, as well as ferruginous pisoliths and nodules.

Alkali and alkaline elements are strongly depleted when normalized to UCC average values (Rudnick and Gao, 2003; Fig. 75). Samples from the Hercules prospect at NLC071 display higher average Fe contents than samples collected from soil, similar to the Atlantis prospect (Fig. 75A and C). This can be related to differential weathering intensity, due to its geomorphological position.

Geochemically, the soil sample set is different from the deeper regolith units, featuring a Zr-Hf average content twice that of the UCC (Fig. 76B). The transported cover displays a strongly depleted Sr concentration with reference to UCC values. Rare earth elements display a slight slope with minor HREE enrichment, plotting almost parallel to UCC values. Samples from this ferruginous unit at Hercules plot parallel to REE UCC values with no HREE enrichment (Fig. 76D). Vanadium and Cr are enriched for Hercules samples corresponding to a higher Fe content, whereas Cu plots close to 1 UCC average values.

Atlantis samples present the same V-Cr-Fe association, but at lower UCC values (Fig. 76C). These trends are continuous in the upper saprolite unit (Fig. 17A-I). Therefore, there is a geochemical overlap between the transported cover and the upper saprolite-silcrete. However, field observations of preserved textures of granitoids and gneisses, recorded in drill holes NLC054, NLC058, NLC080 and NLC102 strongly supports an residual development of the upper saprolite unit as described in Chapter 5.

Other geochemical features that were noted in the saprolite are related to the positive Au anomaly of 1.17 ppm at 52-53 m depth in NLC094 (Appendix F), which coincides with a weathered basaltic intrusion. Chromium, Co and Ni are associated with a mafic intrusion in the lower ferruginous saprolite and saprock. Nickel and S are the main constituents of pentlandite, which may also contain significant amounts of Co hosted in a mafic unit (51-60 m depth, NLC094; Appendix F).

In the drilled area of the Neale tenement, there is a low relief landscape. Within this geomorphological framework, the overlapping geochemical features of the transported cover-silcrete-upper saprolite sequence are interpreted to be the result of erosion (lateral mechanical dispersion), mixture and deposition of local basement rock suites and/or their weathering profiles associated with close breakaways, and therefore, the elements of these features appear to have been only transported short distances.

Metal anomalies, such as the Au anomaly in transported cover under soil, spatially associated with drill hole NLD210, would be displaced from its original source, but originating nearby, only ~100 m away in some cases, can be tracked down by defining the associated transporting sedimentary system. Displaced Au anomalies located in the transported package of the south-west part of the Neale tenement could have originated from the north-east along the main geomorphological “palaeostructure” (Fig. 78). Care should be taken regarding possible contamination during drilling processes.

6.4.2 Surface expression of basement geochemical signature

Out of the five size fractions selected for study of the soil (>2000, 2000-250, 250-53, 53-2, <2 µm) the most reliable size-fractions for geochemical sampling are 53-2 and <2 µm. All five grain fractions of the soil samples are completely leached of Ni, Cu and Zn. Scandium content is also depleted to half of UCC values for the sample set (Fig. 75C).

Gold content as an average value normalized to UCC plots, is higher than the UCC value, although it has a large standard deviation, produced by a Au anomaly in samples from Hercules. Arsenic and Sb values plot close to 1 UCC average value whereas Ag is strongly depleted, and Mo and W plot close to 0.1 UCC average values (Fig. 76E).

The Neale area is dominated by a thin cover of thin aeolian deposits. Geochemically, soil samples display a significant Zr-Hf positive anomaly (doubling UCC average values; Fig. 16B). This is attributed to selective sorting by wind, resulting in the accumulation of a fine grain-sized fraction of zircons in the surface soil (20 cm; Taylor and McLennan, 1985, 1995).

This geochemical feature is not present in the deeper lower saprolite ferruginous unit, indicating that the aeolian component within this sedimentary package was not significant (Fig. 16B), and that the actual aeolian soil is a very thin layer and was deposited very recently, and therefore, might have not been exposed to vertical element dispersion processes for sufficient time to be influenced by the geochemical signature of the basement (Figs. 76, 77 and 78; Appendix F).

Surface soil (20 cm) is not a reliable *medium* for geochemical sampling in the Neale tenement area for mineral exploration, and in particular for Au.

Metallic elements are more concentrated in the <2 micrometre fraction, whereas other trace elements associated with the heavy mineral fraction are concentrated in the 53-2 micrometre soil fraction (Fig. 79).

Next page:

Figure 79. Soil Plots of major and trace element data from soils for the five-grain fractions at the surface of NLC071 and NLD094 (Appendix F). These plots display the main geochemical features for selected elements and ratios, with MORB and UCC reference values.

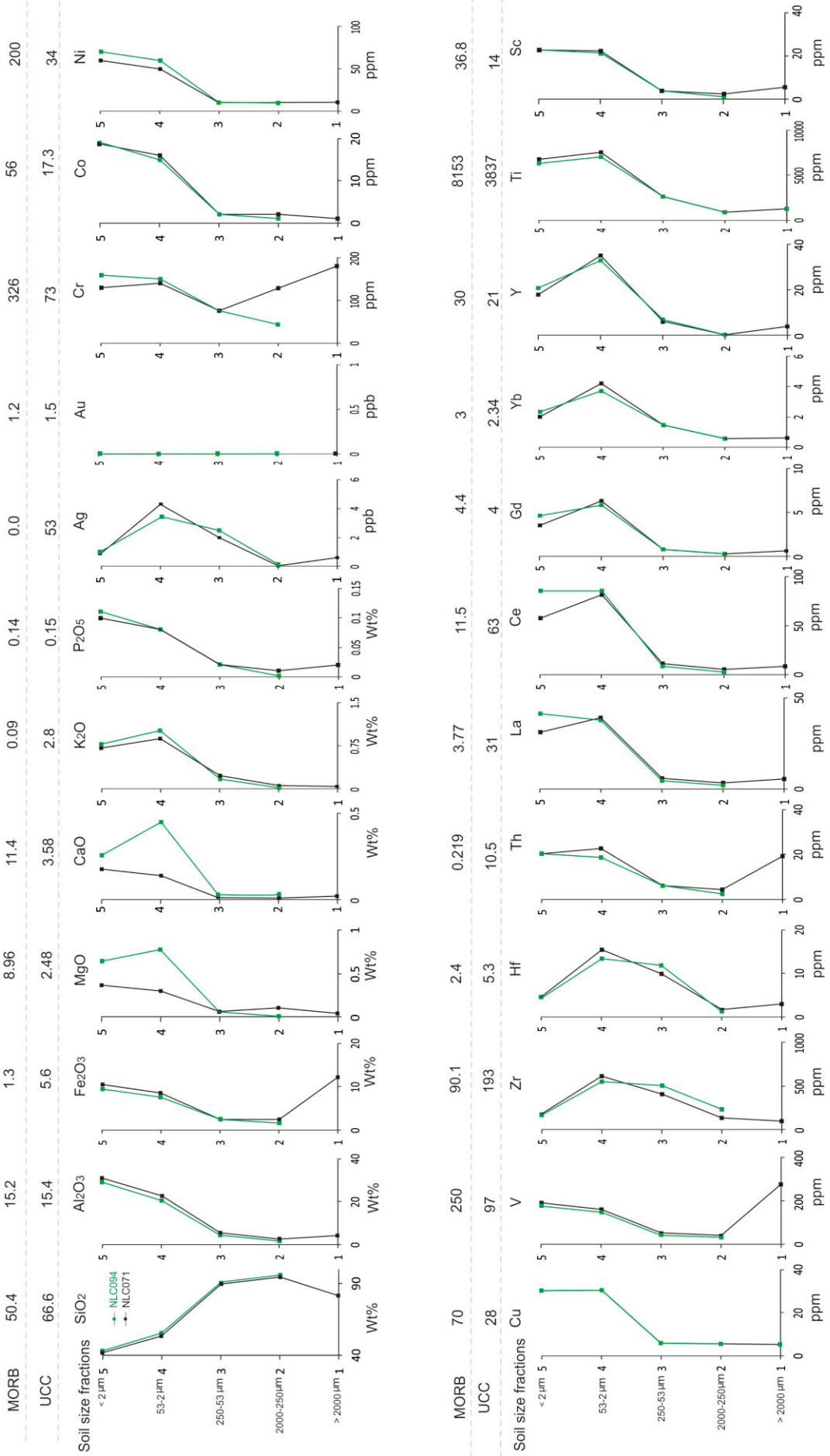
MORB 50.4 15.2 1.3 8.96 11.4 0.09 0.14 0.0 1.2 326 56 200
UCC 66.6 15.4 5.6 2.48 3.58 2.8 0.15 53 1.5 73 17.3 34
Soil size fractions
SiO2 Al2O3 Fe2O3 MgO CaO K2O P2O5 Ag Au Cr Co Ni
Wt% Wt% Wt% Wt% Wt% Wt% Wt% ppb ppb ppm ppm ppm
NLC094
NLC071
< 2 µm 5
53-2 µm 4
250-53 µm 3
2000-250µm 2
> 2000 µm 1
MORB 70 250 90.1 2.4 0.219 3.77 11.5 4.4 3 8153 3837 36.8
UCC 28 97 193 5.3 10.5 31 63 4 2.34 30 21 14
Soil size fractions
Cu V Zr Hf Th La Ce Gd Yb Y Ti Sc
ppm ppm ppm ppm ppm ppm ppm ppm ppm ppm ppm ppm

Figure 79.

6.4.3 Regolith architecture and silcrete "windows"

Three profiles 1, 2 and 3 were selected to investigate variability of the regolith architecture at Neale (Figs. 80 and 81). These were based on the study of AEM by González-Álvarez et al. (2013).

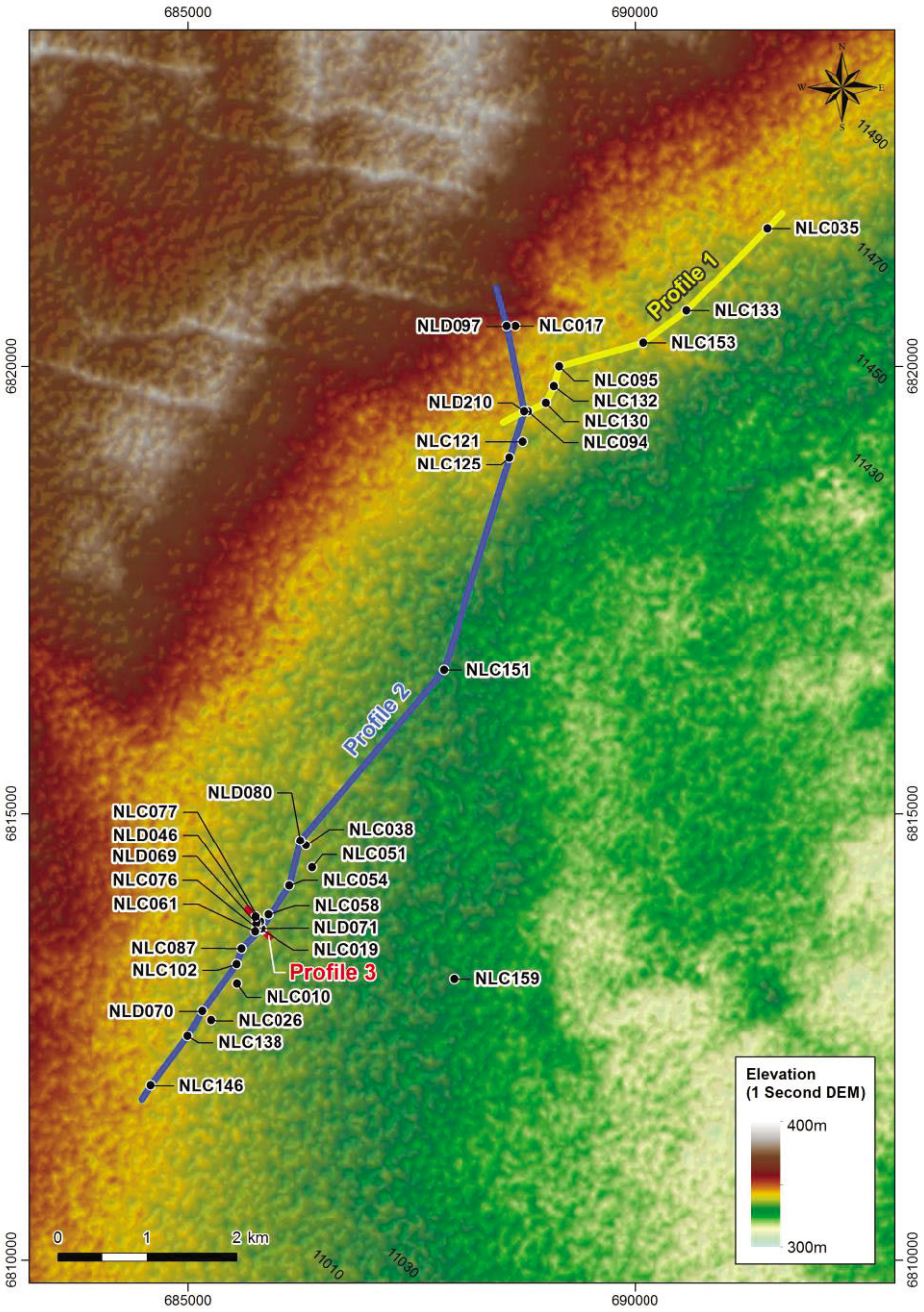

Figure 80. Location of AEM profiles in the Neale tenement. AEM Profiles 1 and 2 were designed to describe north-east/south-west electrical conductivity of the area (excerpted from González-Álvarez et al., 2013).

Next page:

Figure 81. Transported cover (A) and the silcrete unit (B) appear as low conductors with blue colours, as well as a rare dolomitic horizon (C), whereas the upper saprolite (D) is mostly more conductive than the adjacent units. Unit (D) shows lateral variability in clay content. Lower saprolite (E) appears light blue as a transitional layer, with fresh rock (FR) at depth. Numbers in brackets by the drill hole labels represent the distances from the drill hole to the AEM flight line (excerpted from González-Álvarez et al., 2013).

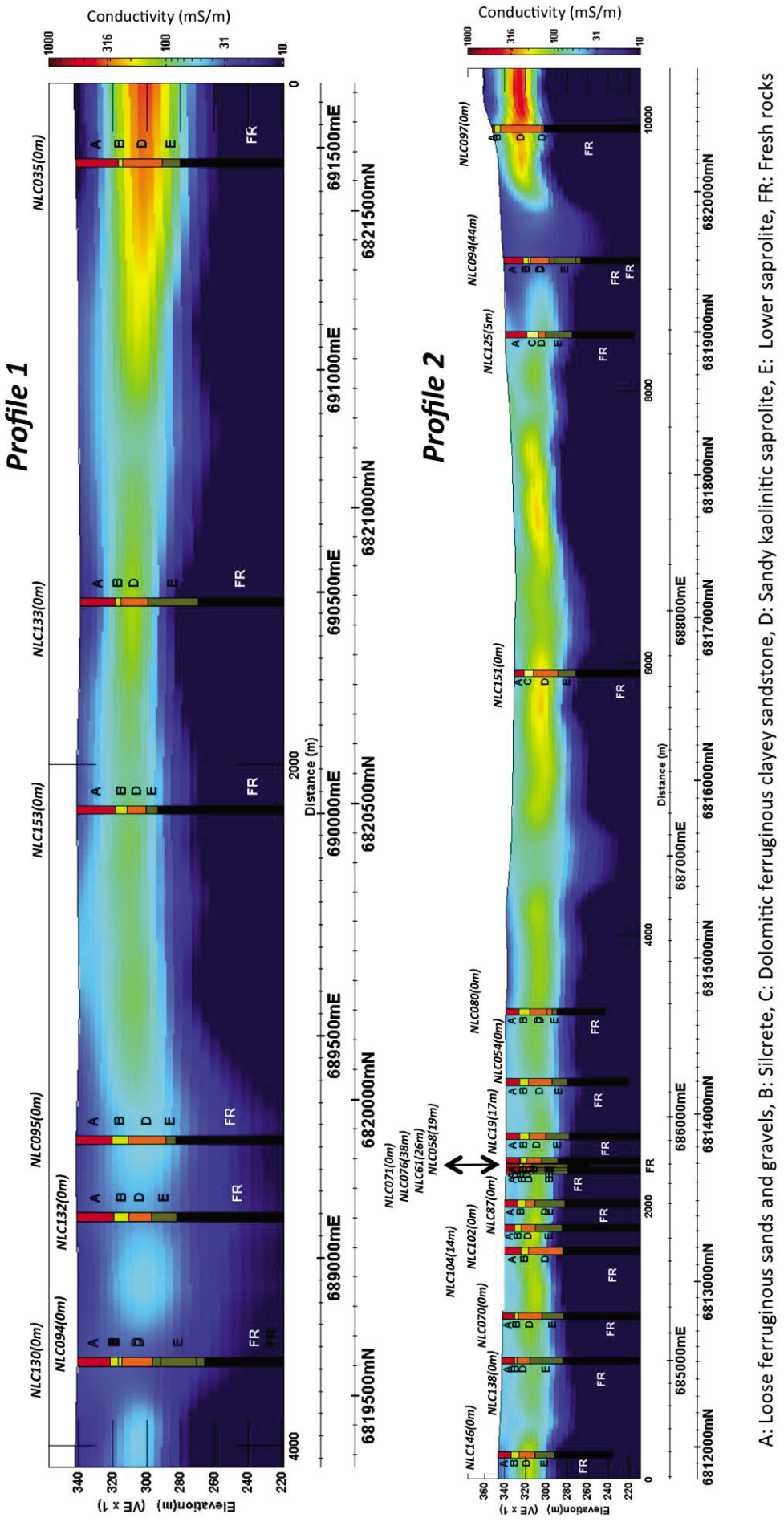
Profile 1
Profile 2
Conductivity (mS/m)
1000
316
100
31
10
Elevation(m) (VE x 1)
Distance (m)
NLC130(0m)
NLC094(0m)
NLC095(0m)
NLC132(0m)
NLC153(0m)
NLC133(0m)
NLC035(0m)
NLC146(0m)
NLC138(0m)
NLC070(0m)
NLC102(0m)
NLC104(14m)
NLC087(0m)
NLC071(0m)
NLC076(38m)
NLC061(26m)
NLC058(19m)
NLC19(17m)
NLC080(0m)
NLC054(0m)
NLC151(0m)
NLC125(5m)
NLC094(44m)
NLC097(0m)
A
B
D
E
FR
A: Loose ferruginous sands and gravels, B: Silcrete, C: Dolomitic ferruginous clayey sandstone, D: Sandy kaolinitic saprolite, E: Lower saprolite, FR: Fresh rocks
Loose Fe-stained ferruginous sands and gravels: A
Sandy kaolinitic saprolite: D
Siliceous sandstone or silcrete: B
Lower saprolite: E
Dolomitic ferruginous clayey sandstone: C
Fresh rocks: FR

Figure 81.

The location and interpretation of key AEM profiles, combined with drilling information and field observations of regolith stratigraphy are shown in Fig. 80. The thickness of the transported cover unit corresponds mainly with unconsolidated sand dunes at the surface, and cemented ferruginous sands and gravels at depth. These materials are poor electrical conductors, and are plot in blue in the interpreted AEM profiles (e.g., Fig. 81).

The residual regolith is divided into three units (following the key colour-letter legend from Fig. 81): (B) a laterally continuous silcrete unit; (D) sandy kaolinitic upper saprolite; and (E) lower saprolite (ferruginous parental rock). Unit (B) has a very low conductivity, and therefore mimics the AEM response of the transported cover in the AEM profiles.

The upper saprolite (D) is interpreted from the AEM profiles due to its high kaolinite content, which makes the unit highly conductive (Fig. 81), whereas the lower saprolite (E) is sandy and less kaolinitic, and therefore more resistive than the upper saprolite (Fig. 81), reducing its EM response and differentiating it from units A and B. The basement rock suites (FR) are fresh granites, gneisses, schists and mafic units, and have low conductivities, and appear as a deep blue colour in the AEM interpretation maps and profiles.

The regolith units in the study area show little variation across the landscape, and most are laterally continuous.

However, the silcrete duricrust is not well developed everywhere, and a kaolinite-cemented grit or poorly-cemented sand is formed instead (Chapter 5). This type of silcrete is similar to the pedogenic silcrete capping weathered granitic rocks. This silcrete is most commonly seen as prominent duricrust protecting mesa landforms, but its lateral and subsurface extent is largely unknown (e.g., Anand and Paine, 2002).

Unit D (kaolinitic upper saprolitic unit) as visibly defined in the drill logging, whereas in the AEM profile signature, it shows a weak conductive response, fading laterally, and both below and above. This is interpreted as a response to unit's patchy solidification of the sands resulting in "windows" of weak cementation in the silcrete. These are probably due to permeable to fluid flow, and appear to be associated with more intense vertical weathering. This can have the result of producing a more kaolinite rich upper saprolite unit, which is displayed in the AEM profiles as being more conductive (Fig. 81). However, the more cemented the silcrete unit becomes, the more sheltered the units below will be from weathering. This results in a less kaolinitic, more resistive unit, with a lower AEM response. This can have significant implications for exploration dataset interpretation.

These "windows" in the silcrete are potentially the most reliable areas to obtain near-surface geochemical information derived from efficient vertical dispersion from the basement. More strongly cemented may be a barrier to prevent dispersion reaching the surface. These "windows" may possibly be linked to the basement topography (Figs. 81 and 82).

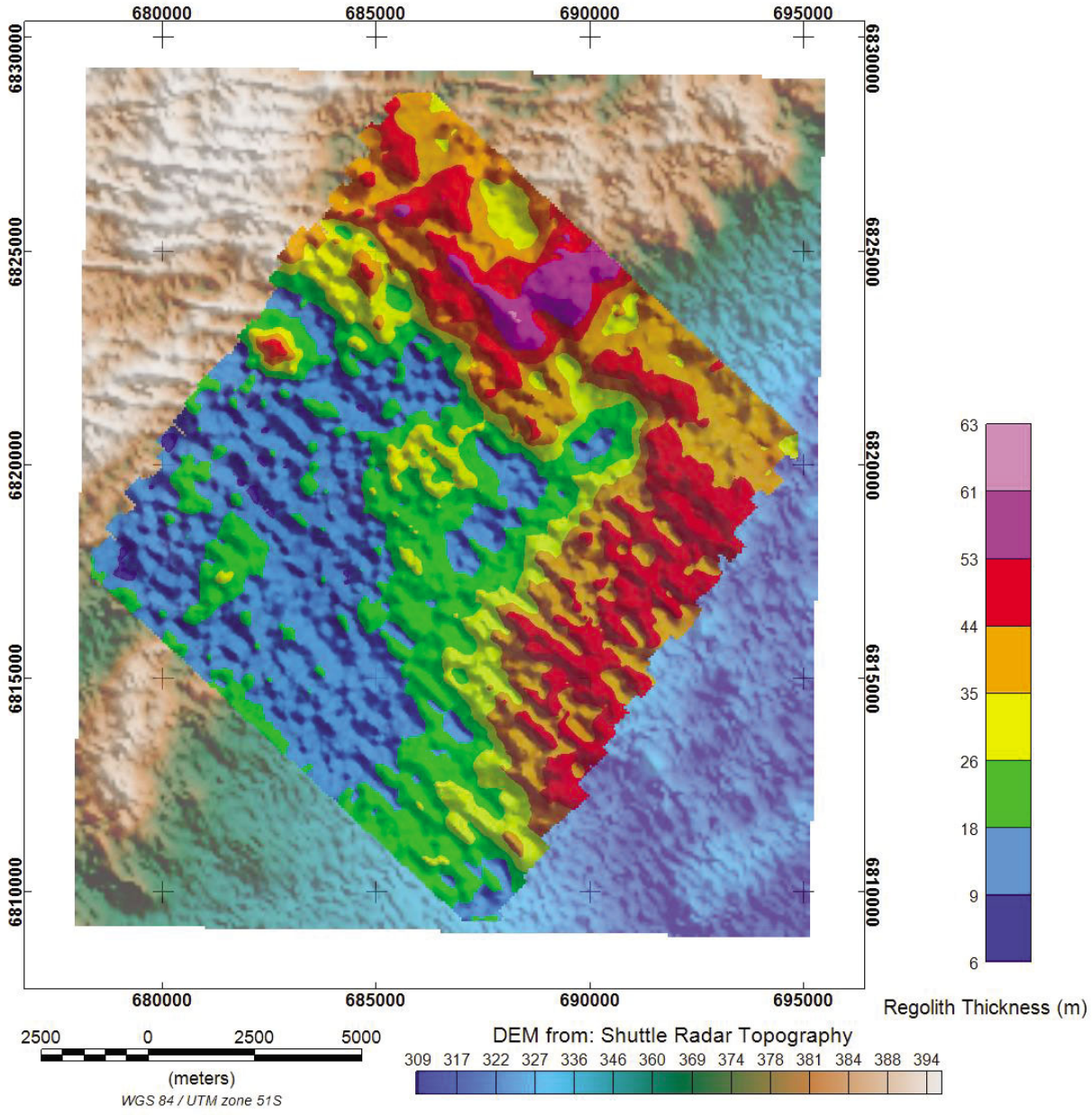

Figure 82. Airborne electromagnetics interpreted displaying total regolith thickness for the Neale tenement area (flown by Spectrem Air Ltd. combined with the DEM). The image shows that regolith thickness does not correlate with the DEM and describes a more complex pattern, where the deepest regolith/cover sequence is located in the north where there is higher relief (excerpted from González-Álvarez et al., 2013).

6.5 Mineralogical transformations and geochemical dispersion processes

Local geochemical differences in lithology average out in the transported cover, resulting in homogenization for elements conserved in the weathering-erosion-transport-deposition cycle (e.g., Th, REE, Sc and Cr), producing compositions resembling those of the upper continental crust.

However, intense weathering conditions and overprinting by diverse weathering cycles can change the geochemical signature of the weathering profiles, and produce varying degrees of element mobilization, to the extent that, otherwise immobile elements can be fractionated and dispersed from their "twin" elements (e.g., Zr-Hf, Nb-Ta, Y-Yb). This differential mobility of otherwise highly immobile elements can be used to track element dispersion processes that may not be recognizable using other more mobile elements.

The north-west of the study is a remnant plateau of an elevated palaeosurface developed mainly on extensively bleached and weathered Proterozoic granitoids. The remnant plateau has been eroded by pedimentation; but exposed or covered by a veneer of transported ferruginous sands and gravels. The deeply weathered profile has been protected from erosion by the development of a silcrete duricrust (Chapter 5).

Granitoids, gabbros and gneisses are the dominant rock types in the basement of the Neale area. During weathering, feldspars, biotite and amphiboles ultimately transform into goethite and kaolinite, retaining alumina and Fe. The more mobile elements such as P, Mn, Mg, Na, K and Ca are leached with more intense weathering. Feldspars and ferromagnesian minerals are transformed into kaolinite under acidic conditions, which is the major component of the upper kaolinitic saprolite. Alumina was partially removed from the weathering profile. This implies pH <4 (Panahi et al., 2000 and references therein).

Heavy minerals such as zircon and rutile/anatase are concentrated higher in the weathering profile within a sand or grit layer (silcrete), which is locally cemented by quartz-cement forming a lenticular or discontinuous silcrete layer (described further in Chapter 5).

The concentration of anatase and colloform opal or chalcedony within silcrete indicates periodic and localized mobility of TiO_2 and silica at a low pH (3.5-4) in a poorly drained environment (Summerfield, 1983; Butt, 1985). This implies that the profile was acidic, with kaolinite forming at the base and being dissolved near the surface.

Weathering under oxidizing acidic conditions in a low saline groundwater environment forms profiles that have low vertical hydromorphic dispersion of REE, HFSE and transition metals within the upper saprolite, and no detectable expression in the overlying transported and aeolian soil cover. Zr/Hf and Nb/Ta may be influenced by parent lithology. However, these ratios change in value at the same depth as the water table seasonal oscillations, and remain constant within the upper saprolite and the overlying transported cover, suggesting that the HFSE ratio change is due to a weathering process, which remains enigmatic. Further study is needed to decouple these observations from vertical changes in regolith stratigraphy.

Transition metals were flushed out, with the exception of V and Cr that could be linked to the Ti oxides. However, Sc, Ni and Co were extracted and depleted in the system. Gold anomalies located in the basement and lower saprolite are not present in the upper saprolite and/or silcrete. This implies that the vertical dispersion of key pathfinders is not present. The vertical oscillation of the water table was not an efficient vertical dispersion agent, probably due to the lack of sufficient salinity (Fig. 83). On the other hand, it might be possible that rising fluctuations of the palaeowatertable under changing climatic conditions, with a higher rainfall average, could have removed the Au anomalies from the upper saprolite. This last scenario is not favoured in this Chapter by the authors for the Neale regolith framework.

As a whole, the geochemical weathering overprint developed in oxidizing acidic conditions within an environment of variable low salinity ground-water, displaying low vertical hydromorphic dispersion of REE, HFSE and transition metals within the upper saprolite and through the transported cover.

It is remarkable to see how this low temperature setting distorted the geochemical fingerprint of the basement rocks quite significantly; whereas deformation, metamorphism and hydrothermal fluid flow circulation did not produce such a change.

González-Álvarez et al. (2014)

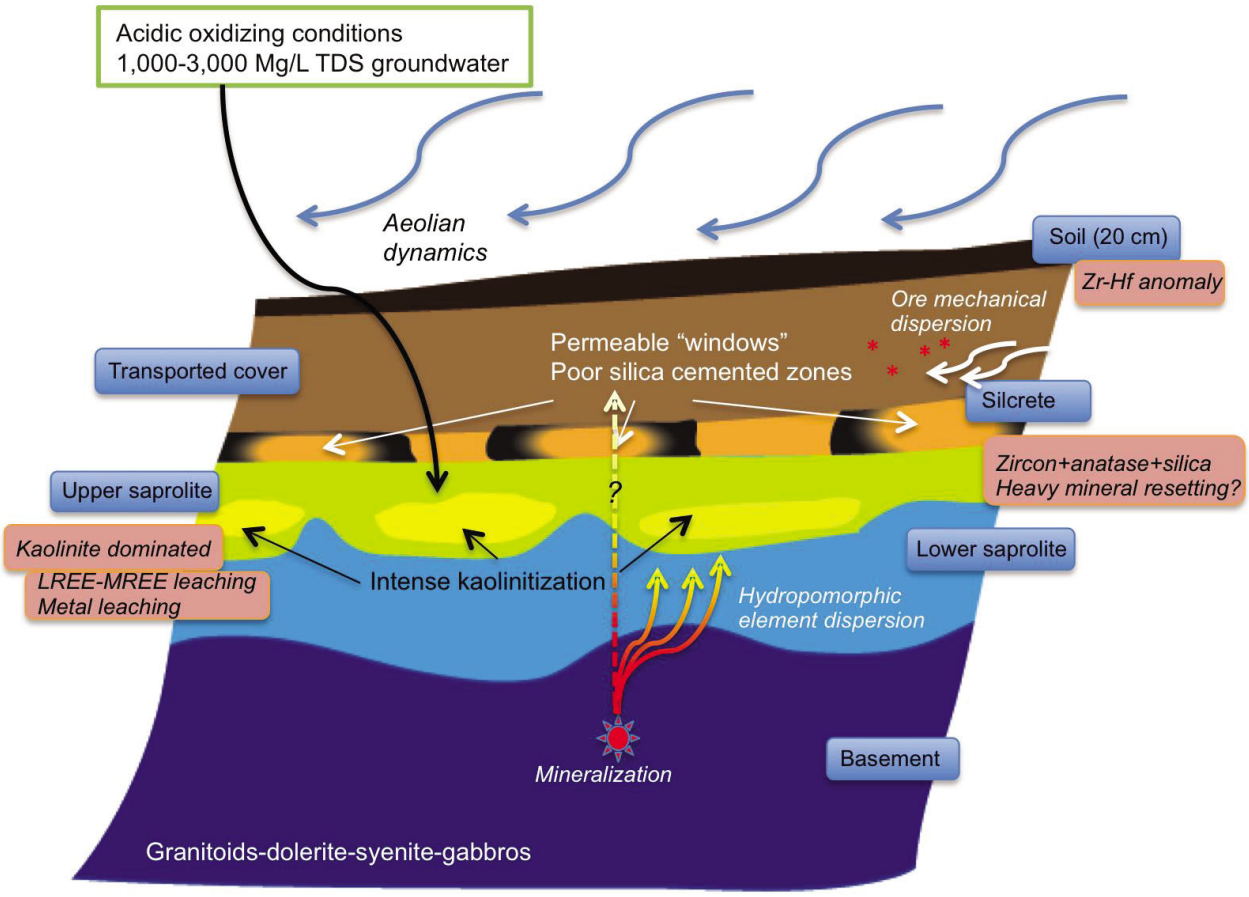

Figure 83. Geochemical dispersion model, of pathfinder and ore elements from basement to cover, for the Neale area.

6.6 Conclusions

Combining field observations from Chapter 5 and airborne electromagnetic survey results from González-Álvarez et al. (2013), the Neale area has a total thickness of ~75 m, with a variable transported cover of between 2 and 25 m in thickness. The residual regolith is divided into three units: (1) silcrete unit (4-20 m thick); (2) sandy kaolinitic upper saprolite (3-25 m thick); and (3) lower saprolite mainly expressed as ferruginized parent rock.

Based on this study, several deductions can be drawn about the geochemical features of the basement, regolith and soil in the Neale tenement.

(1) The rocks recovered by diamond drilling from seven holes at the Hercules and Atlantis Au prospects display a wide spectrum and complex lithology of igneous rock suites, ranging from sub-alkaline and alkaline gabbros to granites. The basement rocks have a mixed geochemical signature and display mineral assemblages consistent with of greenschist metamorphic facies, with local indications of amphibolite facies.

(2) As a whole, these rock suites have a geochemical signature consistent with an Archaean TTG suite similar to Yilgarn granite-greenstone terranes. No sedimentary package has been identified by geochemical or other methods within the basement rock suite.

(3) The lower saprolite unit has similar geochemical features as the saprock and the underlying basement rocks. The geochemical signature of the basement is distorted and partially obliterated in the upper saprolite.

(4) The authors favour the interpretation that the upper saprolite and units above have undergone internal chemical resetting, in element pairs such as Zr-Hf and Nb-Ta. Rare earth element metal budget are leached from the profile so that only Cr, at UCC values. The geochemical signature from the original basement lithologies is reset, with no apparent vertical dispersion further up than the lower saprolite. However, further study is needed to decouple these observations from vertical lithological changes.

(5) The silcrete unit is weakly to strongly silica cemented. The weakly cemented silcrete “windows” have greater permeability to fluid flow, and greater kaolinite development in the upper saprolite unit. Geochemical sampling above these silcrete “windows” may potentially detect leakage anomalous derived from bedrock.

(6) The transported overburden, with a variable thickness spanning 2-25 m, is the result of proximal erosion and transport of nearby outcropping regolith units. This is consistent with the finding that geochemical features mostly mimic the dominant geochemical signature of the upper saprolite. However, this is in turn overprinted by variable extents of weathering, and fluctuations in the water table level.

(7) The previous may explain displaced metal anomalies observed in the first metre of transported cover. These anomalies may be sources from proximal “*in situ*” anomalies (distances in hundreds of metres), or in the north-east direction following the main geomorphological palaeostructure.

(8) Soils in the top 20 cm do not have any geochemically recognizable features from the metal budget of the underlying basement. This is interpreted to be due to recent and dynamic Aeolian deposition in the area studied.

In summary, the chemical weathering overprint developed in oxidizing, acidic conditions with a variable low salinity groundwater environment displays low vertical hydromorphic dispersion of REE, HFSE and transition metals within the upper saprolite, and through to transported cover, with no detectable expression in the Aeolian soil cover.

6.7 Implications for exploration

This study has led to an improved understanding of the geochemical relationship between basement rocks, residual regolith and transported cover. At least five significant implications for exploration can be drawn, which may contribute to a more effective understanding of geochemical results obtained from drilling in this region, and therefore towards more efficient regional exploration targeting.

(1) Geochemical sampling of the soil (first 20 cm) does not reflect any geochemically significant proxy for basement composition in the area. However, sampling beneath the transported cover can lead to the identification of displaced metal anomalies from the basement that can be tracked through an understanding of the associated sedimentary system.

(2) The most reliable soil fractions for determining metal and trace element content are the <2 and 53-2 micrometre fractions. Metallic elements are more concentrated in the <2 µm fraction, whereas the trace elements associated with the heavy mineral fraction are concentrated in the 53-2 µm soil fraction.

(3) Anomalies located within the transported package could be traced from possible near source areas at scales of 100 m.

(4) Drill samples from the lower saprolite, between ~10 and ~75 m depth, preserve the principal geochemical features of the basement, and therefore can be used for mineral exploration and identification of basement lithologies.

(5) The silcrete unit is widely distributed in the Neale area, and caps the kaolinitic upper saprolite, as well as effectively confining the geochemical signature of the basement. However, the silcrete unit varies laterally in cementation, and may have some more permeable areas. These areas coincide in some of the cases studied with a more conductive upper saprolite unit. Permeable poorly cemented silcrete units may allow vertical geochemical dispersion of the basement signature to the surface. Near surface geochemical sampling above these areas may detect geochemical release anomalies derived from the basement.

(6) Due to the complexity of the basement rock suites, metal ratios and indices in any stratigraphic unit of the regolith should be interpreted with caution for the purposes of lithological classification of basement units, such as intrusive mafic, felsic-and sedimentary packages, when targeting specific rock type associations.

7. Airborne EM geophysics in the Albany-Fraser Orogen/Yilgarn Craton margin *(Appendix G)*

Summary

The inductive method of airborne EM (AEM) is non-intrusive and can cover large extensions of ground over a short period of time. It is a technology well suited to exploration and mapping; and can assist in unravelling complex weathered geology in remote areas with difficult access, which may have had limited exploration drilling as well as scarce outcrop.

Basement lithologies such as those which host the Tropicana (~5 Moz) Au deposit are not exposed at surface. The complex depositional and weathering geological regolith sequence present overlies these host rocks with layers of saprolite and other regolith materials of variable thicknesses. Therefore alternative ways of exploring undercover are sought.

This Chapter shows how a publically available dataset of fixed wing airborne time domain EM system (TEMPEST) airborne electrometric data was examined, by re-inverting each sounding with a sample-by-sample (SBS) full-layered earth inversion in order to derive models of the underlying geology. The modelled conductivity depth profiles match the reported deposition of recent aeolian sands over a Permian sequence of siltstone, sandstone and pebble conglomerate. Results illustrate the potential of the method in assisting exploration of the weathered cover in this region. Proposed re-inverted conductivity depth models were cross-validated against publicly available lithological data from known drill holes.

The fully inverted dataset permits a distinction to be made between areas where the underlying ground can or cannot be accurately represented with a horizontal layered earth model. A better understanding of the electrical response generated by differently layered rock forming materials in this region allows inferences to be made about their composition, as well as to delineate basement topography, and to describe the architecture of saprolite-transported regolith sequences. This added layer of information has direct implications for mineral exploration, especially in establishing target locations for future drilling campaigns and to identify regions where sub-surface geochemical sampling might be effective.

7.1 Introduction

7.1.1 AEM and other geophysical methods

Australia has national geophysical potential field gravity and magnetic datasets available, which cover the whole country. These datasets are commonly used for regional geological and structural mapping, among other uses. In some areas in Western Australia, existing registered "historical" AEM surveys acquired by exploration companies are uploaded and are available, through Geological Survey of Western Australia's web page http://www.dmp.wa.gov.au/.

This study considers the application of a full-layered earth inversion on a TEMPEST (Lane et al., 2000) AEM dataset. We have compared products from a sample-by-sample inversion and results from the approximate transform derived using EM-Flow, both of which have been used for interpretation. In this study we sought to add value to existing AEM products by considering their use in describing the regolith architecture across the area in the vicinity of the Tropicana deposit.

The Tropicana Au deposit is located in the north-east of the Albany-Fraser Orogen (Fig. 84A). Tropicana is the first major deposit discovered in the orogen, defining the region as a new greenfields Au province, and thus triggering a new mineral exploration interest in the area.

This Chapter illustrates the advantages of performing full-layered inversions on AEM data, when attempting to assess conductivity models. Vallee et al. (2011) reported that full AEM inversions are seldom utilized by the mining industry today. The limited use of inversion on AEM data is probably due to its used as an anomaly detector, instead of as a quantitative high-density geological mapping technique.

The physically diffusive nature of EM fields implies that we can obtain information of how the signal propagates and changes through the induced ground as a function of time and associated electrical properties. Potential field methods measure an overall response of all the influencing sources at the measuring sounding point without the ability to distinguish which sources are relatively closer or further from the point of measurement. Therefore, potential field methods are not optimal for modelling variations with depth. Vertical propagation with time permits depth estimates to be extracted from EM measurements; the ability to make such measurements makes EM a powerful tool in these applications.

AEM has proved to yield the most valuable information when analyzed in a geographical framework and interpreted in conjunction with other information (e.g., Fig. 84). Underlying structure can be extracted from magnetic data, contrasting densities from the gravity surveys, and surface material composition from radiometric data.

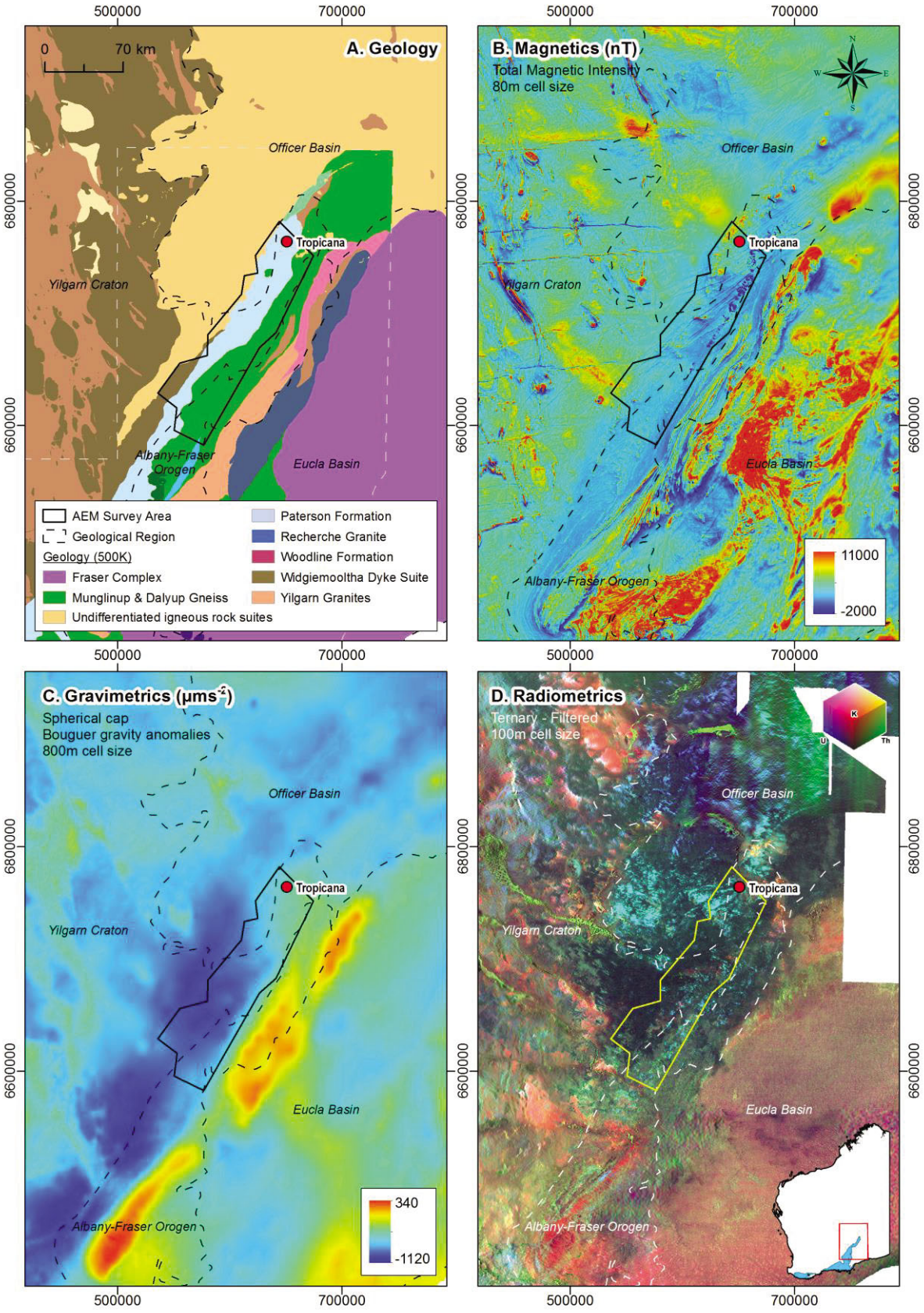

Figure 84. Geological and geophysical datasets for the northeastern part of the Albany-Fraser Orogen, in the vicinity of the Tropicana Au deposit. (A) Interpreted basement geology (Spaggiari et al., 2011); (B) magnetics; (C) gravity; and (D) radiometric geophysical data. These datasets provide a framework for interpretation and analysis of the AEM datasets for this area.

7.2 Methods: data acquisition, processing and inversion

7.2.1 Data acquisition

Over 1000 line kilometres of fixed-wing Tempest AEM data was acquired, with readings taken every 0.2 s (~12.5m) along 24 survey flight lines. The resulting dataset covered a total area of $20{,}000\ \mathrm{km}^2$; it is high density and spatially continuous along flight paths, and is the equivalent of acquiring more than 80,000 individual soundings. A schematic diagram of the Tempest system and its relative transmitter-receiver positions is given in Fig. 85. A thorough description of the system can be found in Lane et al. (2000).

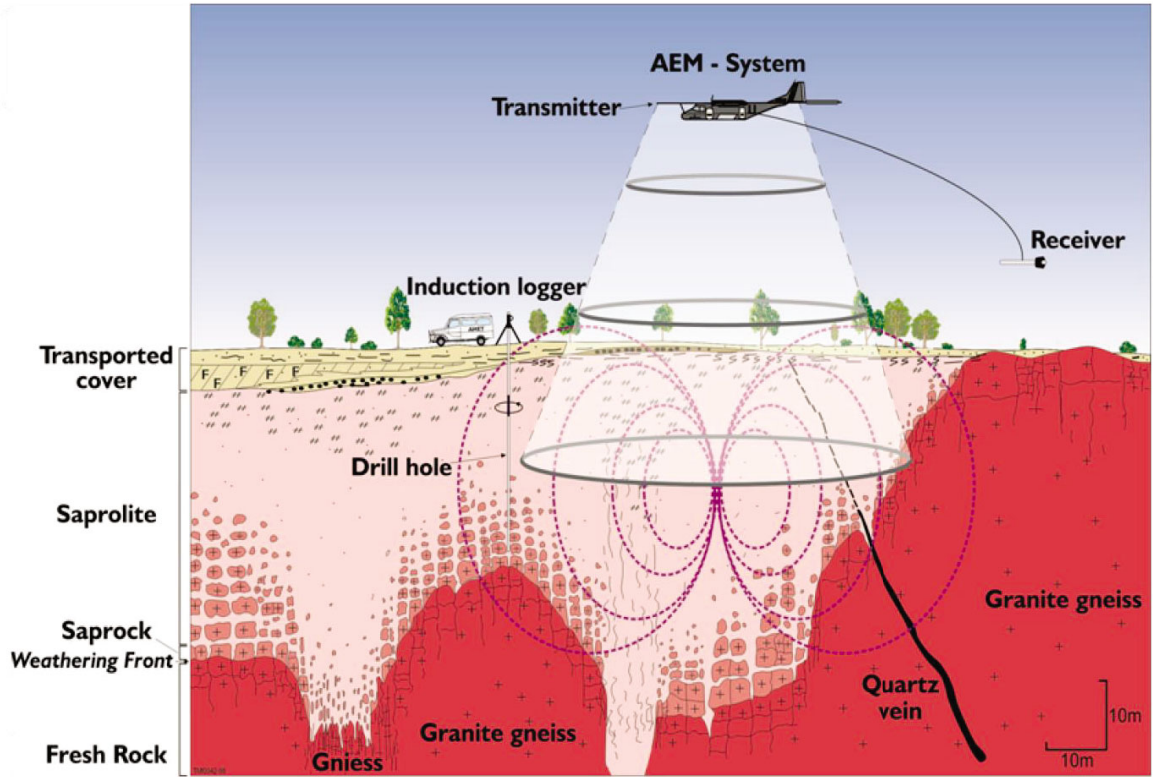

Figure 85. Schematic diagram of the Tempest AEM system and its relative transmitter – receiver positions, and the interaction of EM field with basement geology and regolith. *The primary EM field from a fixed wing system polarizes the underlying ground. The different materials in the ground produce a secondary field, which is measured. The particular electrical properties of these materials guide geoelectrical interpretations.*

The survey was flown for regional lithological recognition purposes, hence the broad spacing between flight lines. These vary from ~5 km on the northern most part of the survey, to more than 13 km between some lines on the southern part (Fig. 86). This particular survey design indicates detailed interpretation should preferentially be done on profiles following the survey's flight paths. Horizontal lateral resolution between the lines relies heavily on the algorithm used to interpolate results and assumes broad lateral isotropy, which we found not to be the case. This issue is further discussed later in this text.

To emphasize the point regarding lateral resolution of AEM systems, Reid et al. (2006) defined the system's footprint as: "the side of a square at surface, directly centred below the transmitter coil, that contains the induced currents which account for 90% of the observed secondary magnetic field". The

system's footprint is determined by the height, separation and orientations of the transmitter loop and receiver coils, and depends also on the conductance of the ground.

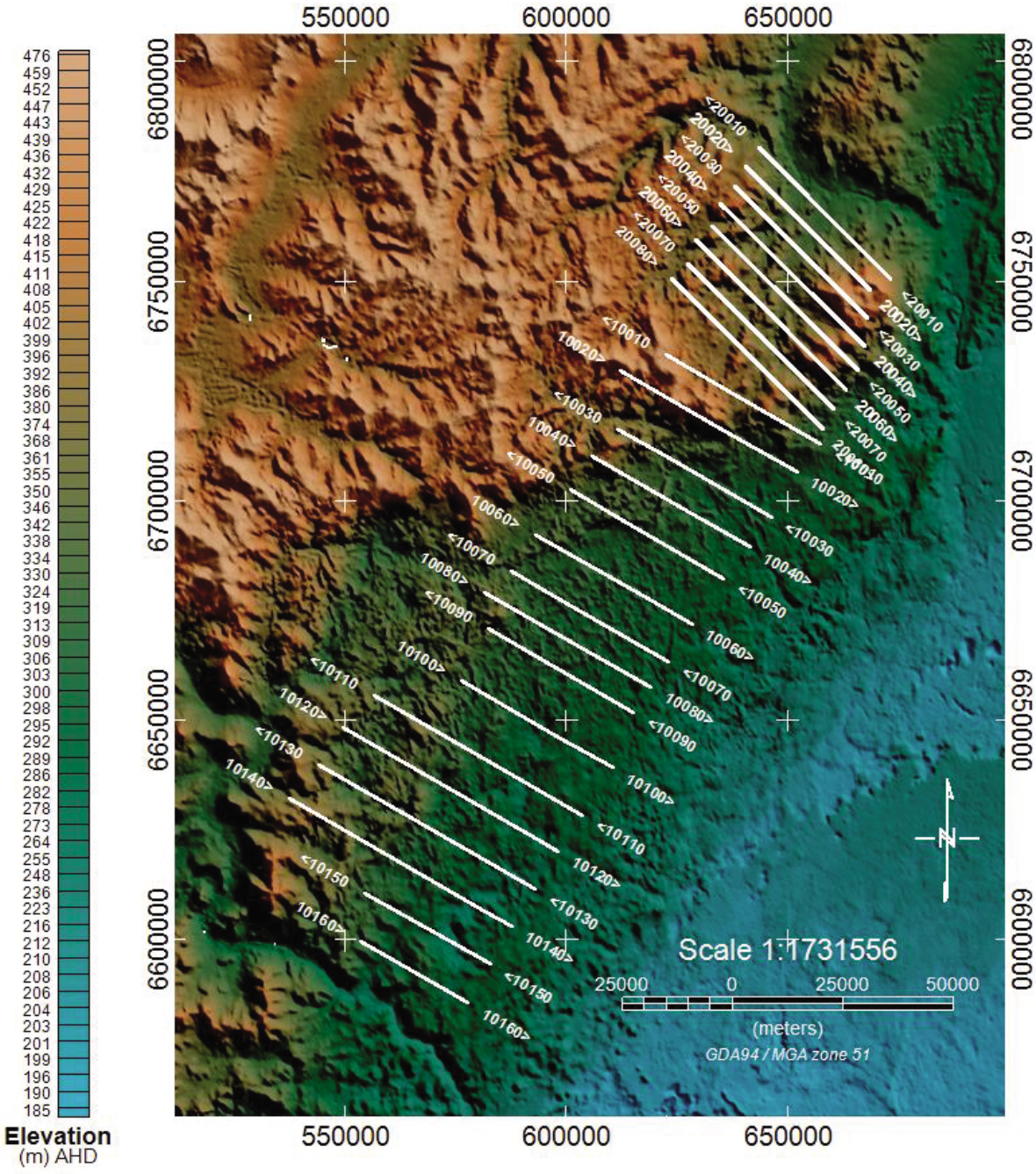

Figure 86. Digital elevation model of the regional airborne survey flown with a TEMPEST AEM system. Flight paths are shown in white.

7.2.2 Processing and inversion

The AEM dataset was processed and inverted by applying two algorithms that transform raw AEM data into layer models of conductivity and depth. (1) Conductivity depth images (CDI's) were obtained using EM-Flow (Macnae et al., 1998), and (2) inversion models produced using a 1D layered earth sample by a sample inversion algorithm developed by Brodie (2010), and described in Costello et al. (2011). By stitching the inverted 1D samples together a conceptual 3D conductivity structure can be built, which can then be coupled with geological information for interpretation (Appendix G).

7.3 Applying Geoscience Australia's layered-earth inversion algorithm Tropicana dataset

The Tropicana dataset was processed using both the receding image conductivity transform algorithm EM-Flow that is an industry standard; and a full sample-by-sample (SBS) inversion developed by Geoscience Australia (GA-LEI).

The Geosciences Australia-LEI SBS inversion, the data inputs to the inversion of each sample are: the observed X and Z components of EM data and the transmitter-receiver relative position, the measurement of the sensors rotation, and distance from the ground (the geometrical parameters). The starting model parameters that describe the thicknesses of layers can be optionally fixed or allowed to vary, as can the initial values of ground conductivity. Parameters are permitted to vary within a specified range of tolerance. The inversion then proposes a one dimensional conductivity model that will fit the collected data. In this case we inverted for conductivities of 80 and 30 fixed-thickness layered models. We have also inverted for both conductivities and thicknesses of 3 and 5 layer models.

The inversion algorithm we used to invert the TEMPEST data, was conceptualized by Lane et al. (2004) and has continuously been developed since by Brodie (2012). It was designed to solve the non-linear problem of obtaining subsurface values of conductivity from a measured AEM response while accounting for geometric unknowns. It inverts for layer conductivities, unmeasured values of the system's geometry and can resolve layer thicknesses. It is based on an idealized layered-earth model calculation for each sounding, assuming every individual layer is laterally homogenous over an area as wide is the 'system's footprint'.

The input data at each station are the recorded X- and Z-component data, and additional measured or assumed elements of geometry.

The mathematical result obtained by assuming a parameter distribution, the forward task or the forward model solution, is derived by either using analytical formulae and numerical integration, or numerical schemes deploying finite difference or finite element techniques. The GA-LEI algorithm requires the partial derivatives of the primary field Green's tensor and the reflection coefficient for individual layers (Wait, 1982), which have been analytically calculated in Brodie (2010).

The theoretical total field response of an AEM system flying above a layered earth is calculated given a set of unknown parameters (conductivity, elements of geometry and layer thicknesses) and some measured known such as transmitter height, system, waveform and window positions.

The algorithm's forward model is a based on Wait's (1982) formulation frequency-domain field expressions for vertical and horizontal magnetic dipole sources, above a horizontal layered earth environment. The formulation assumes contributions from the dielectric permittivity and magnetic susceptibility to be that of free space, $\varepsilon_k = \varepsilon_0$ and $\mu_k = \mu_0$ respectively.

The system's current waveform is then transformed to the frequency domain via fast Fourier transform (FFT). The secondary B-field is calculated using 6 logarithmically equivalently spaced frequencies per decade (in the range between 25 Hz and 37,500 Hz), using Wait's (1982) expressions. The in-phase and out-of-phase or quadrature components are then splined to obtain linearly spaced values at the same frequencies as the nodes of the FFT transformed current waveform. The B-field transient response for each sounding is the product of the convolved multiplication of the splined secondary B-field with the FFT transformed current waveform, followed by its inverse FFT.

Each decay is then sampled and averaged into the 15 time windows. The computed primary and secondary fields are then added to produce the X- and Z-direction windowed total field. Finally these windows are rotated and aligned with the X- and Z-component receiver coil's axis in accordance to the receiver pitch model parameter.

The inversion scheme then minimises a composite objective function of the form,

$$\phi = \phi_d + \lambda(\alpha_c\phi_c + \alpha_g\phi_g + \alpha_{cv}\phi_v) \quad (1)$$

where ϕ_d is a data misfit term, λ is a regularisation factor, ϕ_c is a layer conductivity reference model misfit term, ϕ_g is a system geometry reference model misfit term, and ϕ_v is a vertical roughness of conductivity term, and the α values are relative weights. The details of the inversion algorithm is beyond the scope of this study; Brodie's (2010) thesis contains a description with the intrinsic details.

7.4 Data misfit parameter ϕ_d

An important calculated parameter is ϕ_d *;* which is an indicator of how well the proposed layered earth models represent the measured survey data at each sounding point. It is a quantitative measure of agreement between the observed data $d^{obs}$and the forward model, produced by the model parameters described in f(m), which normalized by the expected error and the number of data as defined in:

$$\phi_d = \frac{1}{N_D}\sum_{k=1}^{N_D}\left(\frac{d_k^{obs} - f(m)}{d_k{}^{err}}\right)^2 = [d^{obs} - f(m)]^T W_d [d^{obs} - f(m)] \quad (2)$$

where N_D is the number of data and W_d is diagonal normalization matrix with the level of error for each of data.

The spatial distribution of parameter ϕ_d is depicted in green in Fig. 87. This is a measure of how well the ground's EM response can be modelled by the inversion process to resemble a stacked horizontally layered earth. This 1D earth model assumes the conductivity properties are constant and vertically bounded by the layer thickness, and remain isotropic at each layer horizontally constrained by the system's foot print, which in the case of TEMPEST has been calculated to be of ~450m at surface.

The white to green colour bar in Fig. 87 has been set to a threshold of 1.5 ϕ_d. The intention of this map is to show how well the data have been interpreted to represent a horizontally layered-earth.

Each individual sounding of AEM data has been inverted using an 80, 30 and 5 layer model. The level of agreement between the data and the proposed model parameter is quantified in parameter ϕ_d, which assesses how well the measured data can be represented by the proposed layered- earth models. The parameter is a good proxy to have for the results when interpreting the data.

Analysis of the parameter ϕ_d has helped us conclude that the data in this survey area cannot always be interpreted as extensive slowly varying horizontal layers. The high values of ϕ_d (>1) can be associated with abrupt breaks in the lithologies as a result of different historical events of erosion, mixing and other depositional processes such as braided palaeochannels; resulting in structures of more ribbon-like (2 and 3 dimensional) forms. The effects of these breaks in the rock types can lead to erroneous interpretation as has been discussed in Ley-Cooper et al. (2010).

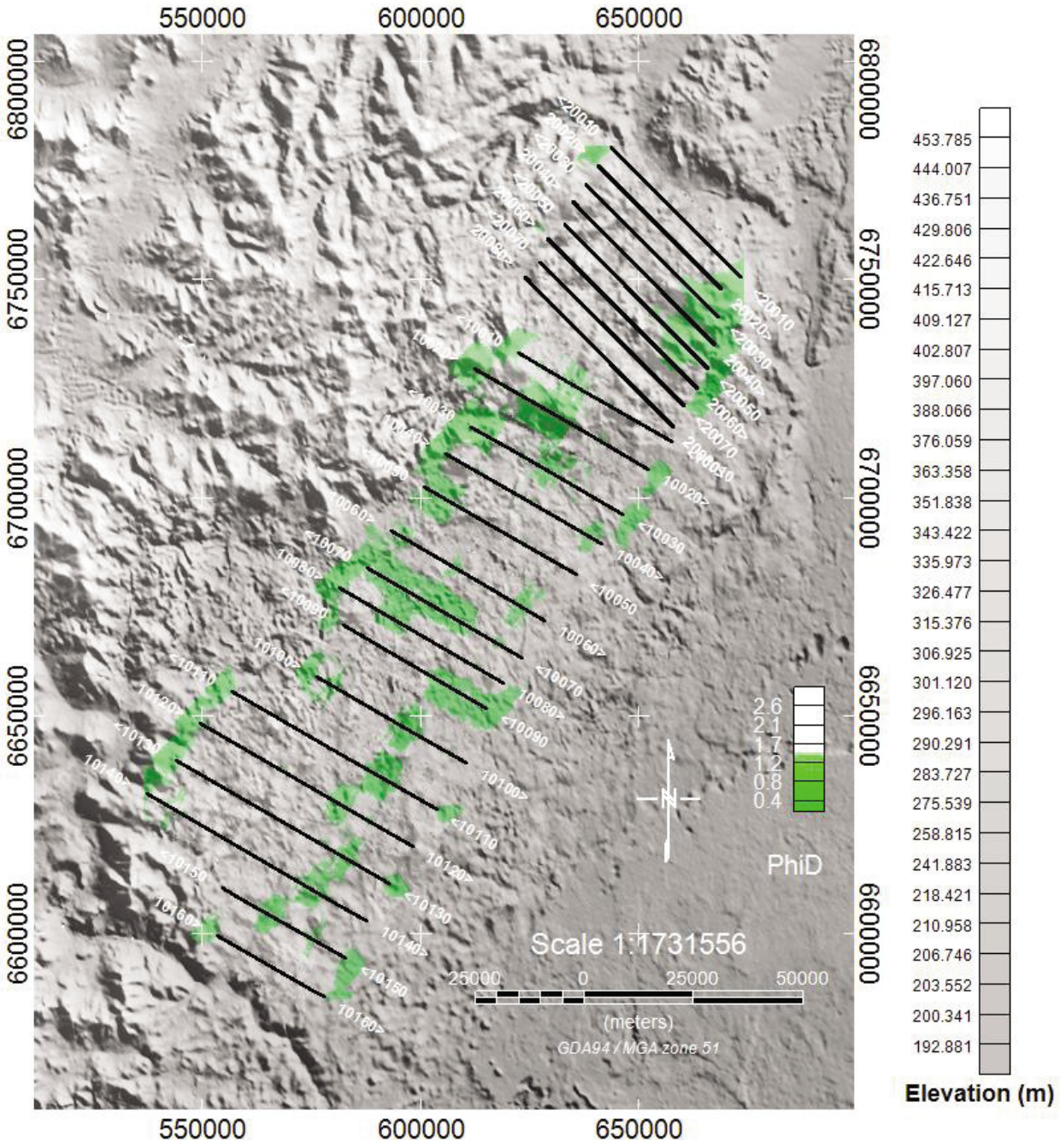

Figure 87. Gridded interpolation of the parameter Φ_d with a threshold set at a value of 1.5 (green shade). The spatial distribution of Φ_d is an indicator of how well the response from the ground can be represented by a 1D horizontally layered isotropic earth.

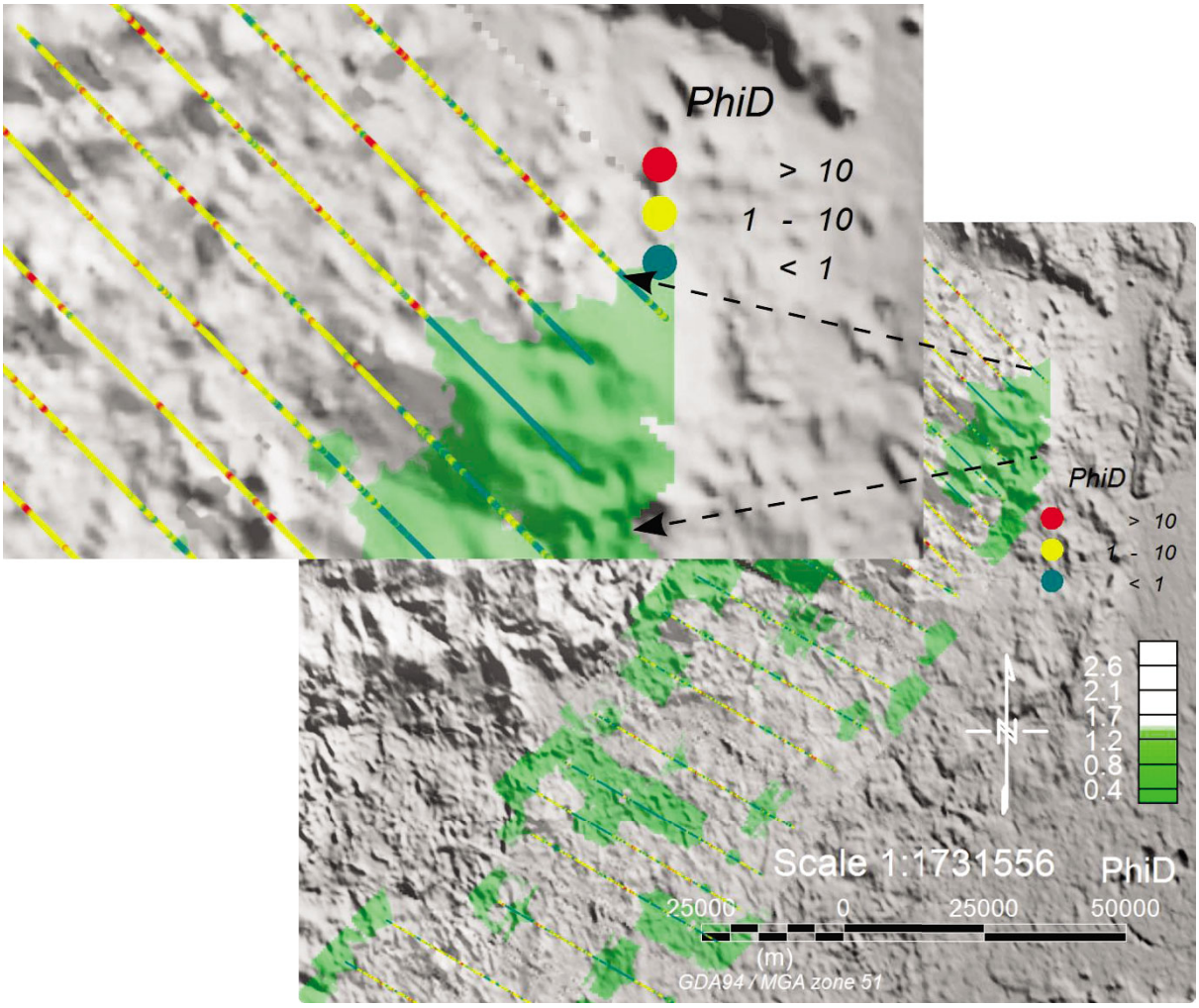

Figure 88. Graphical display of Φ_d binned into three groups. Green circles are soundings where inversion has yielded good fits between the observed data and the models (values 0 1or less). Soundings with Φ_d values in the range of [1-10] are represented in yellow. Red is assigned for Φ_d values above 10.

The map in Fig. 88 shows two important aspects of the nature of AEM data. In Fig. 88 small coloured dots on the survey lines are scaled to reflect the true surface footprint of the system, and to show their small dimension in relation to the extension of the survey and the distance between survey lines. The second aspect of interest arises from the areas colour coded with yellow and red dots; these areas seem to reflect zones of high variable lateral discontinuity, most probably related to several overprinting events of deposition and erosion.

7.5 Gridding algorithms

The image in Fig. 89B was produced using a Kriging algorithm, which is a geostatistical gridding technique well suited to grid data that are variable between sample locations, known to be statistical in nature, in this case collected in non-parallel lines with variable spacing as displayed in Fig. 86. The algorithm is known to have better control in anomalous sampled patterns.

A *minimum* curvature gridding method to interpolate between white lines on the map in Fig. 89 was applied. The algorithm searches for the smoothest possible surface that will fit the data. The *minimum* curvature gridding method is also reportedly adequate for randomly distributed data, or data sampled along arbitrary orientation lines, as is the case of our survey.

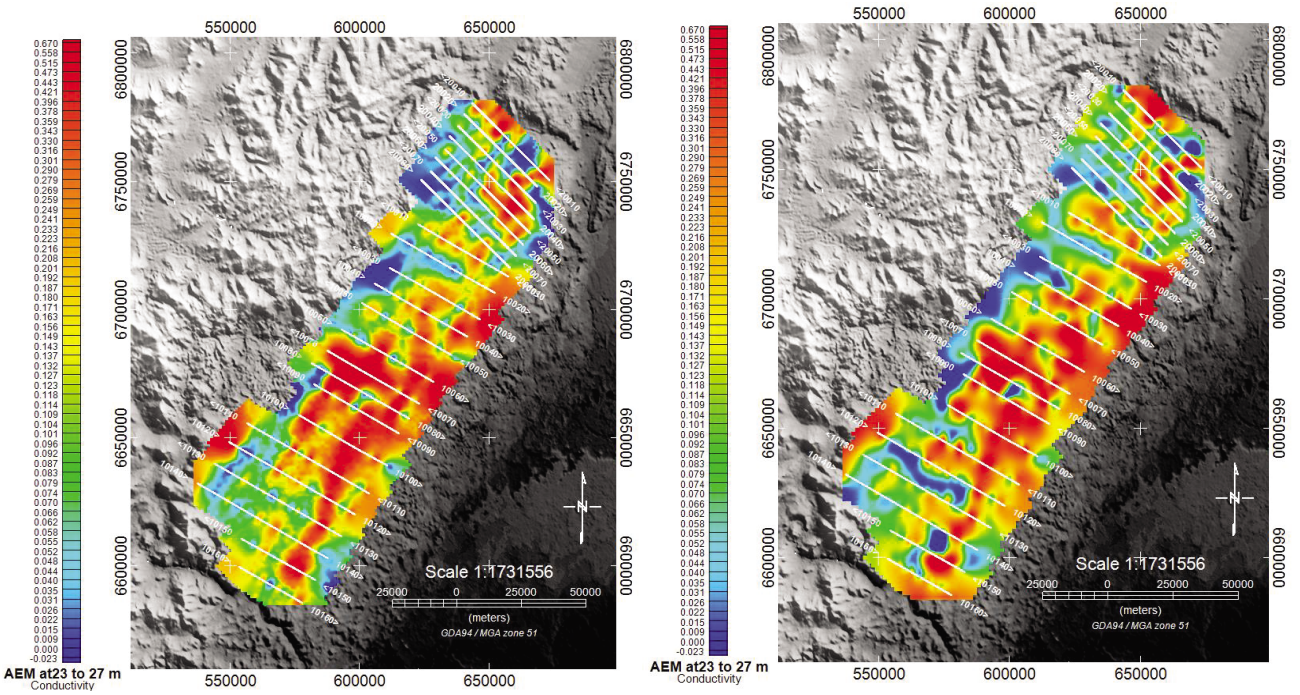

Figure 89. Images of conductivity interval depth slice from 25 to 27 m, draped on elevation. The difference between images (A) left image and (B) right image, is the interpolation algorithm used for interpolation between the flight lines. Image (A) has used Kriging and the image (B) is a minimum curvature.

As can be seen from both images in Fig. 86, the selection of the interpolation (gridding algorithm) will have a big influence on how the data are rendered, particularly in the case where flight lines are several kilometres apart. Good examples of the differences can be seen towards the south-west, between survey lines 10120 and 10130, and between 10140 and 10150.

Swain (1976) presented geostatistical analysis, Kriging and *minimum* curvature. From analysis of the resulting grids, we consider the Kriging grids to provide a better representation of the lateral distribution of our data.

7.6 Interpretation

Stacked images such as that in Fig. 90 shows the spatial distribution and variations with depth of all the profiles simultaneously (Appendix G). Three major geoelectrical provinces can be defined through the analysis of these spatially distributed sections.

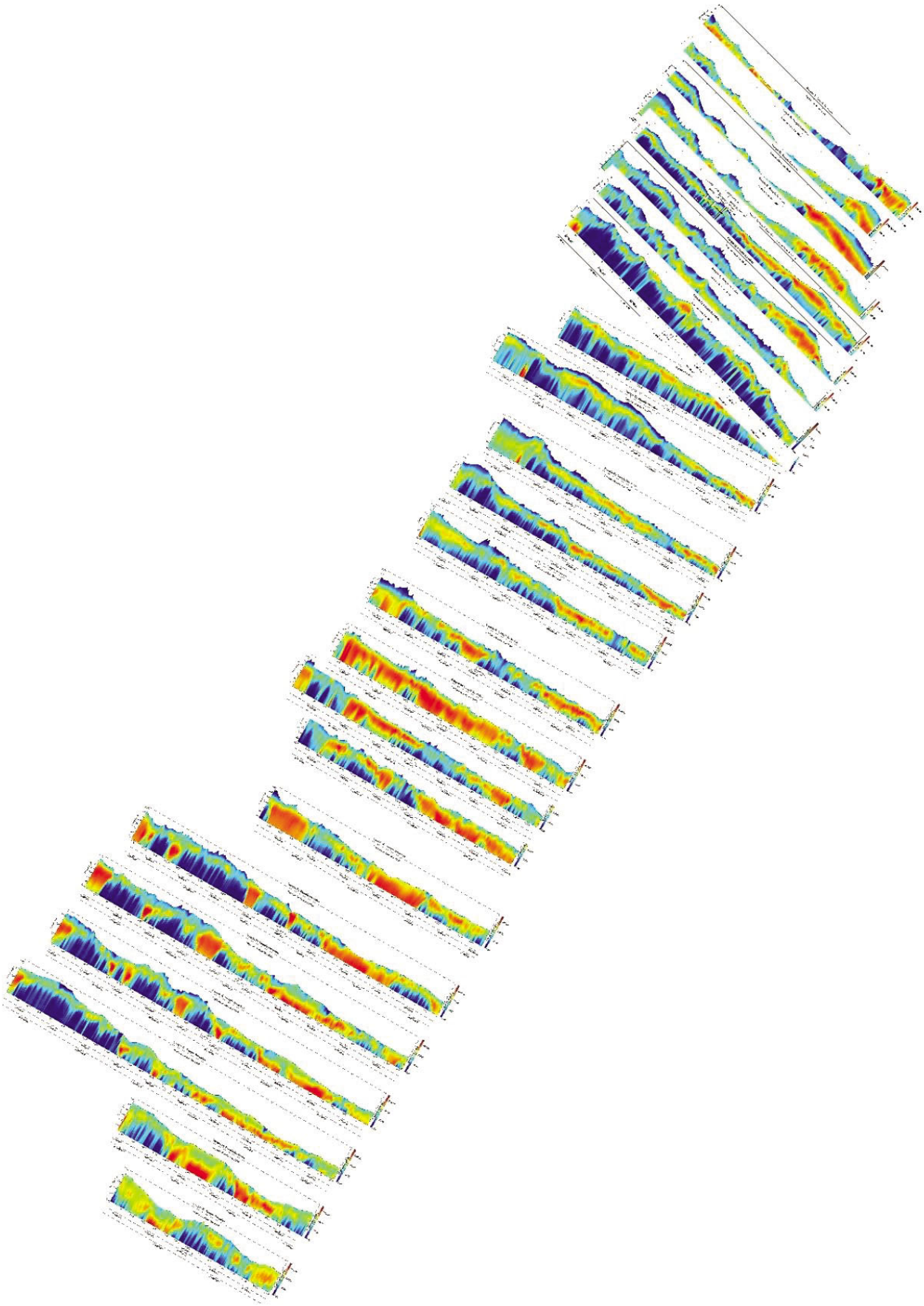

Figure 90. Airborne EM section profiles, with geographically referenced to Figs. 84, 87, 89 and 90, showing both spatial distribution and variations with depth up to 250 m from surface. See Appendix G for full profile details.

(1) A conductive block to the north-east composed of a thick sequence of conductive sediments at surface.

(2) A low lying area that extends from the centre of the study area towards the southernmost easterly side of the profiles, comprised of what appears to be thick layers within the regolith. Incised sand-rich channels filled with shallow conductive saline saturated ground water.

(3) The north and south-west AEM profiles in the area to the west show a distinctly high elevation, where conductive features are incised into what appears to be fresher less altered rocks.

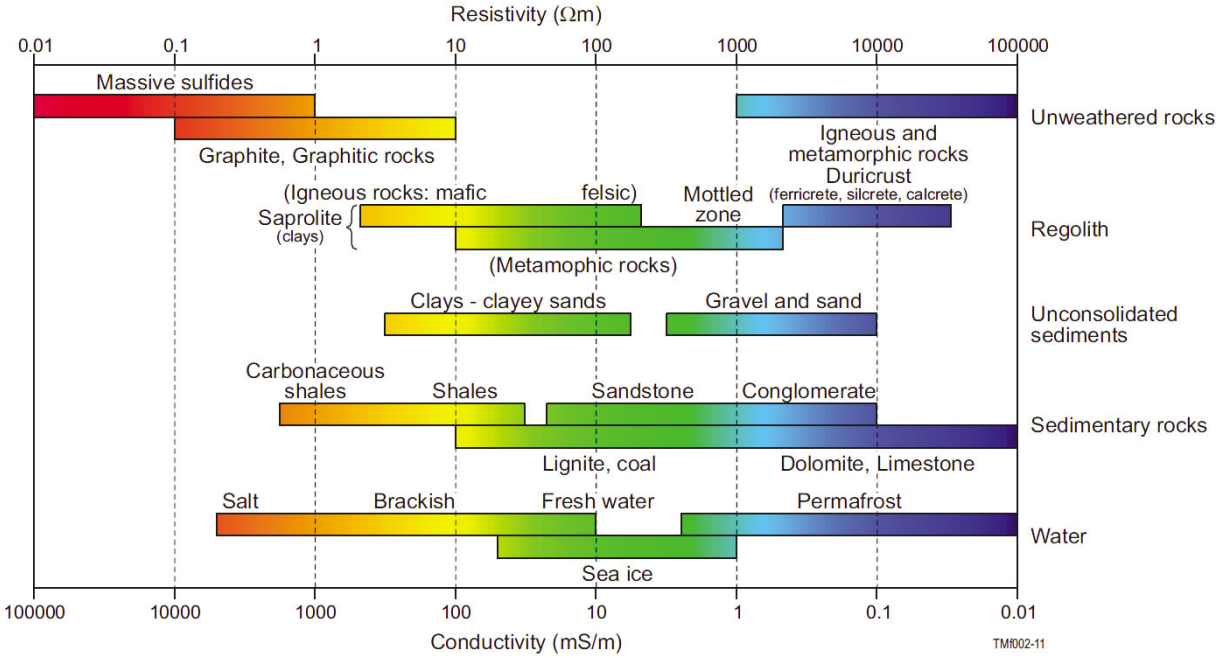

Figure 91. Conductivity-resistivity values of various rock-forming materials, adapted from Palacky (1987). Factors such as porosity, fractures and fluid saturation influence conductivity measurements; therefore, a wide spread of values for the same material are available in the literature. Some materials have a range of conductivities of several orders of magnitude.

7.6.1 AEM and available drilling

Open file report A6865 Vol 3 from 1976 has diamond and reverse circulation core drill data, which we have grouped in what has been interpreted as reasonable lithologies for the area (Figs. 91, 92 and 93).

The location of some of these drill holes in relation to the flight lines is shown in Fig. 92. Diamond drill holes over the AEM sections were overlain, previously establishing a search radius of 200 m from the flight path and projecting logs of holes only within that region.

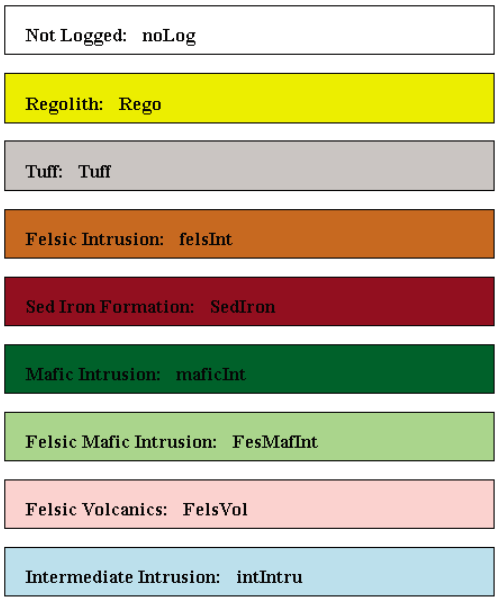

Figure 92. Lithologies derived from compilation of logs in open file report A6865 Vol 3.

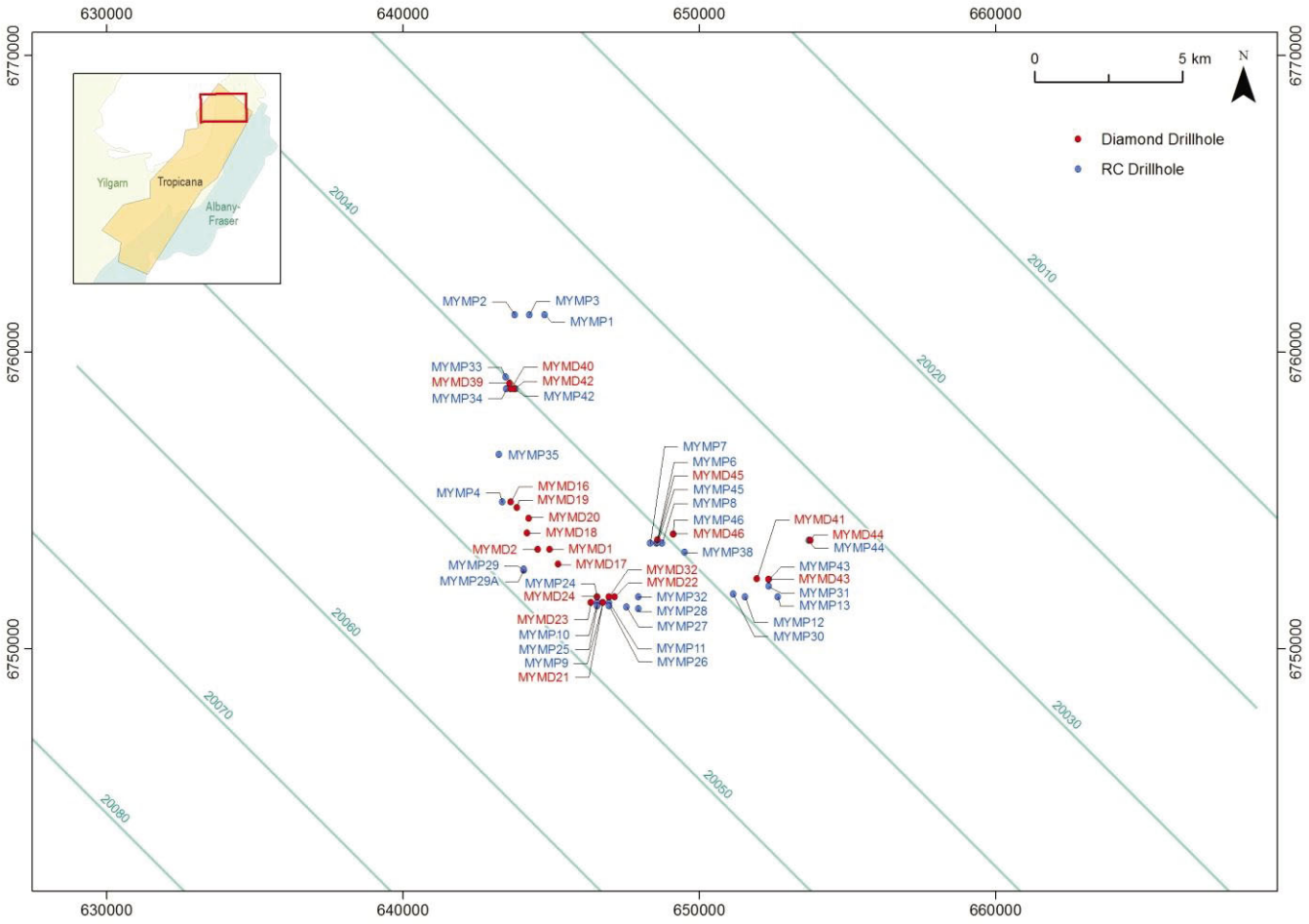

Figure 93. Surface plan with coordinates showing drill hole collar locations in the vicinity of the AEM flight lines, with location plan inset.

Each individual sounding of AEM data has been acquired at a distance of approximately 12 m apart, which in the context of lines 10 Km long means that the visualization and analysis of data should be done at different scales as in Fig. 94. The longer more regional sections help us visualize the broad structures as shown in the top panel in Fig. 94, whilst a different level of detail can be seen in the consecutively increasing zoomed-in details of the section shown in the middle and bottom panels.

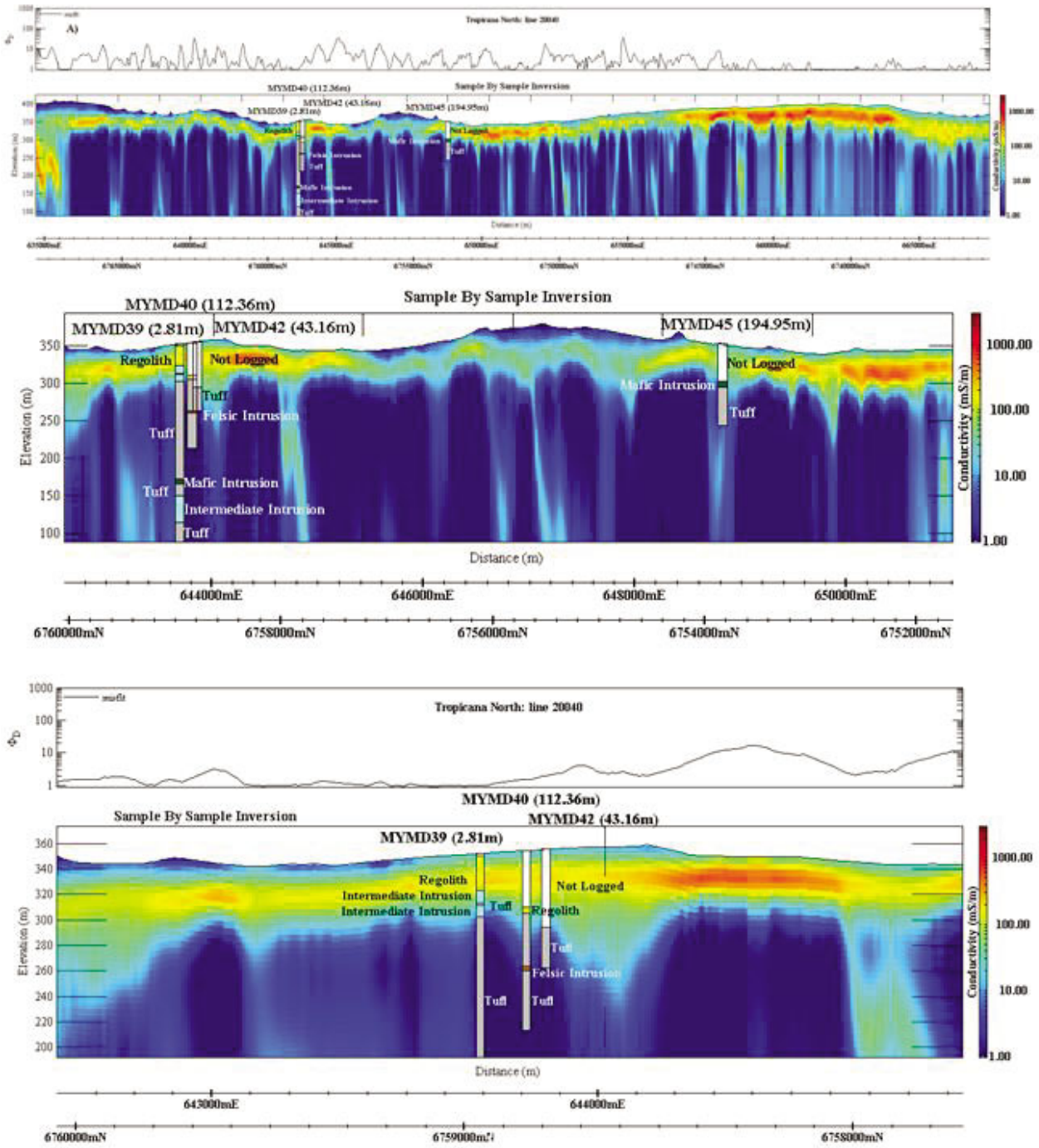

Figure 94. Airborne EM section of line 20040 overlaid with lithologies from diamond drill holes. The three panels showing this line section display increasing zoom-ins in order to demonstrate the different levels of detail at these scales. A search radius of 200 m from each sounding of the AEM lines was established, the final distance from the flight path is shown in brackets next to each drill hole label. These sounding points provide the basis for projecting of the lithologies from these drill holes (Appendix G).

Agreement between the interpretations from available boreholes and the AEM seems reasonable, particularly at delineating the basement. Lithologies reported as regolith or not logged seem to match areas where the AEM is mapping more conductive structures, which we have associated with saprolite units. The quality of the logging is unknown, and from experience in other areas we have noticed that it can be of variable quality.

Lines such as 20040 in Fig. 94 (lower panel) are representative of the area flown to the north, where two distinct EM responses are present: a flat thick homogenous layer to the north east extending for ~14 km, indicating a structure that fits well with a 1D earth model (Fig. 94 panel A, ϕ_d <1); and a mixing of discontinuous layers to the north west of the profiles, where the 1D assumption cannot easily describe the structure, at least at a regional scale. When zoomed-in profiles are taken into account, reasonable levels of agreement are still achieved between derived models and the data reflected on the top panel ϕ_d.

7.7 Conclusions

A fixed wing airborne electromagnetic dataset acquired at the Albany-Fraser Orogen/Yilgarn Craton margin exhibits numerous local conductivity responses, which can be attributed to regolith materials, rather than the isolated conductive mineralization targets.

The new inversions of AEM provide a clearer picture of regolith thickness and potential basement depth. Inversions profiles of each survey flight line show areas of thickening and thinning of the overburden.

The remote location of this survey implies that large ϕ_d values, calculated during the data inversion, are unlikely to be a product of anthropogenic noise like roads and power lines which have been seen in surveys flown over built-up areas. In this case, large misfits are probably the response of disrupted lithologies, due to weathering and erosion, dipping layers or other sharp boundaries, which have been inadequately modelled with a 1D layered earth.

At this stage we have used AEM data to derive maps and sections, which can further be interpreted using other constraints (e.g., drilling, magnetics, radiometrics). We have integrated AEM sections with historical diamond drill logs, but the same could be done with information from reverse circulation and other drilling. It is possible to attribute an appropriate model from the above set to most of the local anomalies of regolith origin observed in the survey. In areas where poor level of agreement was derived, the slow process of plate modelling and interpreting individual responses could be attempted. This methodology would be of particular value for the purpose of distinguishing between bedrock mineralization responses from those due to regolith structure.

For regional surveys flown with long separations between flight lines, the selected interpolation (gridding algorithm) chosen will have a big influence on how the data are rendered. Therefore the more detailed analysis such as regolith thickness, drill-hole assessments, and any other type of comparison with the AEM data should be done by zooming in and out at different scales within the profiles. After analysis of the results, gridded kriging is preferred over the *minimum* curvature in this case.

Interpretation of the AEM sections suggests that in the central region of the study area, the presence of conductive material can be interpreted as thick layers of regolith. Other factors driving the high conductivity response could be incised sand-rich palaeovalleys filled with shallow saline groundwater that extend to the south and north of the study area. The lines flown to the north show two distinct EM

responses that could be associated with regional thick homogenous layers that extend to the north-east for several tens of kilometres. Incised sand-rich palaeovalleys filled with shallow saline ground water seem to be prevalent throughout the survey area and could also be responsible for the conductive response. The mixing of disrupted discontinuous structures in some of the profiles suggest the 1D assumption used in the inversion can fail to resolve the structure, so in these areas caution must be taken during interpretation.

Inversion of AEM data does not provide a unique solution, the derived model is only the result of the search for the simplest explanation of the surface observations, and be sensibly integrated with other data for interpretation.

Results from inverting the AEM data have yielded valuable information in areas adjacent to the Tropicana Au deposit where no publicly available drilling data are available. The AEM has unveiled a much clearer picture of the spatial distribution of different materials. The method is able to map areas of weathered overburden, the variation in thickness of transported sediments and where the basement is closer to surface.

8. Spectral sensing technologies in the Albany-Fraser Orogen: ASTER and HyLogging™ *(Appendices H1, H2, H3 and H4)*

Summary

Spectral remote (Advanced Spaceborne Thermal and Reflection Radiometer, ASTER) and proximal (HyLogging™) sensing technologies were evaluated for mapping regolith and bedrock lithologies and alteration mineral assemblages in the Albany-Fraser Orogen. An orogen to regional scale evaluation of the Western Australia ASTER Geoscience products. A suite of precompetitive maps showing the relative abundance and composition of key mineral groups, does not show any consistent distribution of major mineral groups in the AFO at different scales that can be detected in neighbouring geological provinces (i.e., Yilgarn Craton, Eucla basin). The main impediments are: dense vegetation cover, fire scars, clouds and scene boundaries.

The accuracy of ASTER data increases when focusing on the district to camp scale. At these scales, fire scars and scene boundaries can be more readily distinguished from geological features. At a district scale for example, patterns in single regolith units enable a more detailed classification and enhance differences between different regolith domains. The ferric oxide and AlOH group Geoscience products can provide important information about erosional *versus* depositional environments, as well as the identification of possible outcrop.

The geology at the Hercules area comprises Proterozoic metagranites and metagabbros as well as remnants of Archaean rocks, partly covered by Mesozoic sediments. The bedrocks are extensively covered by Cenozoic sandplains, silcrete, colluvium and dunes. The new regolith map differs from the available surface geological map by suggesting that larger areas can be attributed to saprolite developed over Proterozoic basement. The basement of the Salmon Gums area is dominated by the Munglinup Gneiss, and is covered by Eocene sedimentary rocks of the Bremer Basin, which also occur in palaeochannels incised in the basement. The palaeochannels can possibly be mapped by using the ASTER Geoscience products, by mapping variations in the kaolin and ferric oxide abundance when compared to shallow cover material on top of the Munglinup Gneiss.

Spatially dense HyLogging™ data (1 cm steps) were acquired from drill holes of the Hercules and Atlantis sites (Neale tenement) located in the northeastern AFO as well as the Salmon Gums in the central AFO, and were interpreted for their primary, alteration and regolith mineralogy. At Atlantis, the cm-spaced VNIR, SWIR and TIR data show detailed variations within the major lithologies, enabling, for example, mapping of thin carbonate-altered and chert layers. One example is given by a 5 to 10 m thick horizon containing thin intense carbonate alteration, allowing a correlation across several drill holes. Due to their variations in thickness and occurrence, it is uncertain at this point how far the chertified units can be used for correlating lithologies across the drill holes. Gradual mineralogical changes can be examined in various segments of the analyzed data, such as gradually increasing sericitization of the deformed granitoids, which is accompanied by increasing carbonate alteration, and may point to fluid-rock interaction processes during development of the mineral system.

The HyLogging™ data can be used to determine the thickness of the regolith as well as single layers in the regolith. At Salmon Gums, the regolith thickness varied from 33 m, to at least 58.5 m, within three major zones that can be identified. Furthermore, transported material can be distinguished from residual material, using the abundance and composition of kaolin group minerals and Fe oxides, and the occurrence of primary minerals. Other studies have shown that this can also be achieved by hyperspectral scanning of rock chips.

Integration of ASTER with Hylogging™ data shows that mineral maps derived from multispectral remote sensing data can be used to infer mineral assemblages of heavily weathered or concealed bedrock and can distinguish transported from residual areas. Detailed regolith maps can be developed in a short time frame, prior to field campaigns, aiding geological mapping and mineral exploration. Hyperspectral drill core data can be used as ground control points, providing detailed information about the basement and the regolith architecture, and assisting in the logging of the drill core. These two dimensional datasets can then be extrapolated over larger areas, using the Western Australia ASTER Geoscience products, and can be integrated in a 3D model, that helps to infer the distribution, thickness and relationships between the regolith landforms.

8.1 Introduction

Multispectral remote sensing technologies have been increasingly applied over recent years for mapping lithologies and hydrothermal alteration footprints (e.g., Ninomiya et al., 2005; Hewson et al., 2006; Hewson and Cudahy, 2010; Duuring et al., 2012). ASTER is a multispectral sensor that captures radiation reflected and emitted from the Earth's surface, that records 14 spectral bands, covering parts of the visible-near (VNIR: 350-1,000 nm), shortwave (SWIR: 1,000-2,500 nm) and thermal infrared (TIR: 8,000-12,000 nm) wavelength ranges. The locations of the single ASTER bands in the electromagnetic spectrum were designed to cover absorption features that are diagnostic for mineral groups of major rock and regolith forming minerals. This makes ASTER the first "geoscience-tuned" satellite to date.

CSIRO's Western Australian Centre of Excellence for 3D Mineral Mapping (C3DMM) was granted access to all ASTER scenes that were collected over Western Australia since the launch of ASTER in 1999. From these scenes C3DMM created 14 Geoscience products, which were publically released together with the Geological Survey of Western Australia in November 2011. These Geoscience products comprise a suite of mineral group content and composition maps, as well as a false colour composite, a green vegetation content map and a regolith ratio, the latter comparable to the Landsat TM regolith ratio. The ASTER Geoscience products of WA and the other Australian states and territory are publically available via http://c3dmm.csiro.au/. An Australian continent scale ASTER map was released at the 34th International Geological Congress in Brisbane in August 2012. This is the first continental scale mineral map of the Earth's surface derived from Spaceborne data to date.

The aim of this project was to evaluate the publically released Western Australia ASTER Geoscience products for geological mapping from orogen (>100km) to district (<100km) and camp/deposit (<10km) scale in the Albany-Fraser Orogen (Fig. 95). A number of Geoscience products are evaluated for the first time in this Chapter, as well as the multiscale approach had rarely been applied before. The Geoscience products were primarily tested for their applicability for characterizing the regolith, and mapping of bedrock rock types. Furthermore, the factors that conflict with mineralogical information embedded in the ASTER data are addressed.

In addition to the above, the VIRS HyLogging™ data of diamond drill core from salmon Gums and Neale tenements were queried for contact of regolith and basement and development of saprolite, mineral characterization, trends in mineral abundance and composition that could point to mineralization related alteration, or to provide stratigraphic correlations between different drill holes. Neale Hylogging™ data was integrated with ASTER to produce a regolith model for the tenement based on spectral technologies.

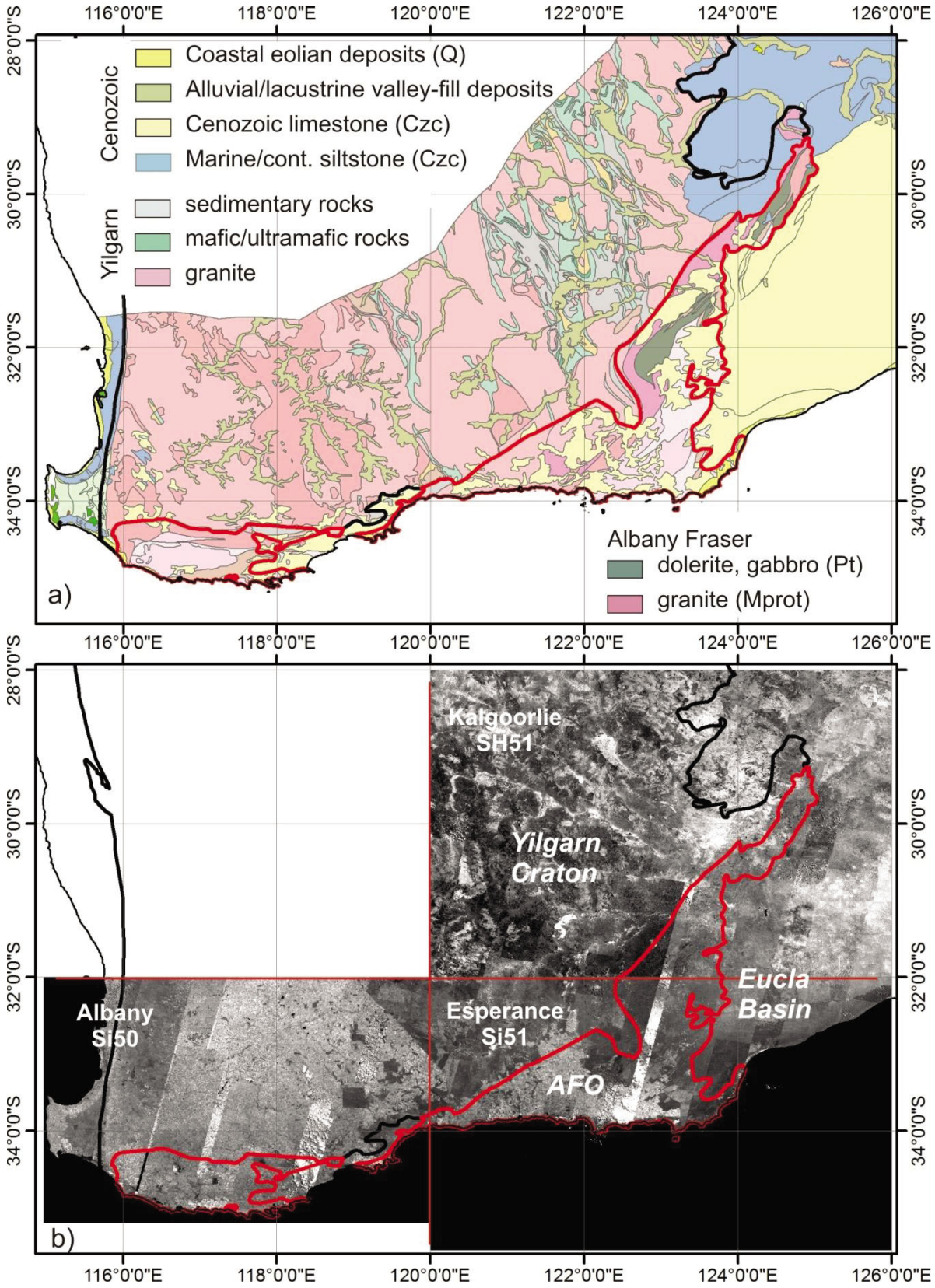

Figure 95. Upper panel, geological map (Geology 2.5M; GSWA, 2001); and lower panel, 1:1M map sheet indices of ASTER Geoscience products covering the Albany-Fraser Orogen (greyscale applied to false colour RGB). Red line shows the extent of AFO, black line shows the extent of the Yilgarn Craton.

8.2 ASTER regolith mapping *(Appendix H1)*

8.2.1 Regional scale (>100km)

The various ASTER Geoscience products can be used at different scales to interpret geological features. However, a number of non-geological features compromise the application of the ASTER derived products, such as high vegetation abundance in the central/south-west and fire scars in the northeastern Albany-Fraser Orogen. Together with the Australian Geological Surveys, CSIRO is currently working towards a revised version of the continental ASTER Geoscience products compensated for vegetation. This should improve the applicability of the ASTER, derived mineral maps for exploration in the AFO considerably.

At a regional scale, large geological provinces are highlighted by a number of Geoscience products. For example, Fig. 96 shows a geological map and the ASTER derived ferric oxide content map, for the Eastern Goldfields of the Yilgarn Craton, the central and northeastern AFO and the western Eucla basin. In the Yilgarn Craton, high ferric oxide contents match with mafic rocks, intermediate to high contents with alluvial and lacustrine valley-fill deposits and low to very low values with granites and plateaus in the dissected landsurface. In the northeastern AFO intermediate to high Fe oxide contents maps a variety of erosional features, such as weathering profiles containing ferric oxide rich saprolite and ferricrete, as well as depositional features, such as transported alluvial sediments, sourced from ferric oxide rich saprolite, but also granites. However, at the regional scale, the AFO shows a low ferric oxide content, when compared to the Yilgarn Craton and the Eucla basin. The Eucla basin is characterized by an intermediate to high ferric oxide content (Fig. 96B). Major differences observed in the ferric oxide content in the Eucla basin occur along the north/north-east trending swath boundaries and along west/north-west trending scene boundaries, highlighting processing issues that were not resolvable during the development of the 1st pass ASTER Geoscience products of western Australia.

In addition to scene boundary issues, Fig. 96C exemplifies the influence of green vegetation especially on the continent to regional scale data. In this Fig., areas of high vegetation abundance in yellow to red colours cover vast areas of the central Albany-Fraser Orogen. Most of the pixels in the same area of the ferric oxide content map are masked out, as it is not possible to estimate the relative abundance and composition of minerals when the amount of green vegetation is too high (ca., above 60%). Similarly, the AlOH group content and MgOH group content maps do not show any response over large areas of the Albany-Fraser Orogen (Fig. 96D). However, a major mineralogical difference is observed between the Eucla basin (high content of ferric oxides ± MgOH bearing hydrated silicates and/or carbonates) on one side and the Albany-Fraser Orogen/Yilgarn Craton (generally high abundance of Al-clays with locally enhanced ferric oxide abundance) on the other side. The difference is due to the contrasting bedrock and cover lithologies, with carbonate and siliciclastic rock types in the Eucla basin compared to the granite/gneiss dominated basement of the AFO/Yilgarn Craton margin, and their respective regolith domains.

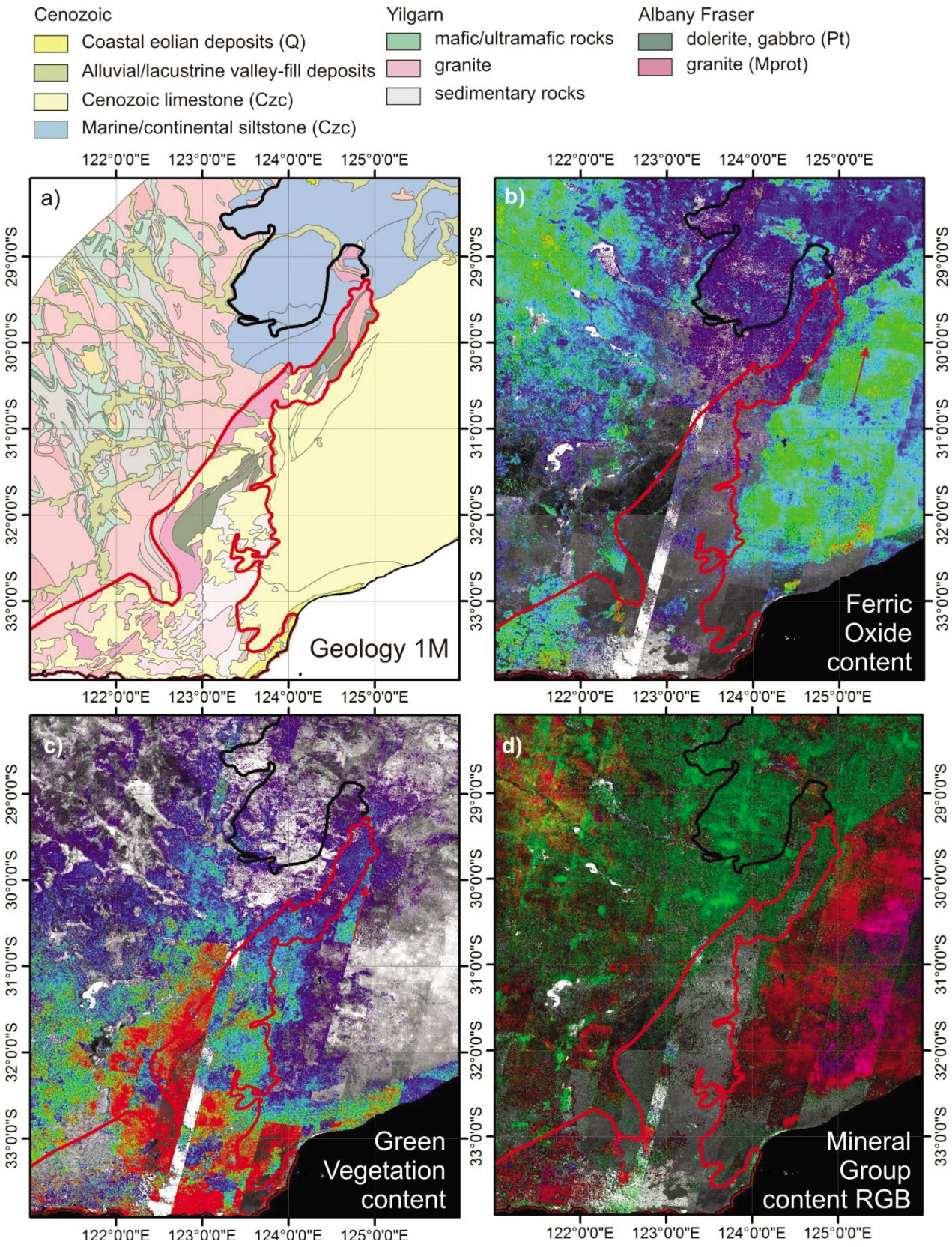

Figure 96. Geological base map and hyperspectral mineral maps of the eastern Albany-Fraser Orogen. (A) Geological map (Geology 2.5M; GSWA, 2001) of the central and eastern Albany-Fraser Orogen; (B) ferric oxide content, and (C) green vegetation content (blue colours-low content, yellow/red-high content); and (D) mineral group content RGB with ferric oxide content in red, AlOH group content in green and MgOH group content in blue. The red arrow in images (B) and (C) indicates changes in mineral group content by scene boundary effects. The red line shows the extent of the AFO, and the black line shows the eastern extent of the Yilgarn Craton.

Although the Albany-Fraser Orogen can be visually distinguished using a number of ASTER Geoscience products from other geological provinces, such as the Yilgarn Craton and the Eucla basin, it is difficult to separate different basement domains in the Albany-Fraser Orogen on a larger regional scale.

Reasons for this include processing issues due to high vegetation abundance or low coverage of available ASTER raw scenes. Regional compositional differences of the regolith can be interpreted from the ferric oxide content, ferric oxide composition, ferrous Fe index, AlOH group content and AlOH group composition maps.

Regolith in the northeastern Albany-Fraser Orogen is characterized by low ferric oxide contents in most areas, cross-cut by lacustrine and colluvial environments showing intermediate to high ferric oxide abundances. In contrast, the central and south-western Albany-Fraser Orogen shows, in general, an intermediate to high ferric oxide abundance. The ferric oxide composition shows an interesting pattern in the northeastern Albany-Fraser Orogen, where hematite is developed as the major ferric oxide mineral along the north-east trending orogen (Fig. 97). The hematite-rich domain is surrounded by goethitic materials of the Eucla basin in the east, and by a narrow zone of hematitic surface material located between the Albany-Fraser Orogen and the Yilgarn Craton to the west (Fig. 97). Towards the north, in the Tropicana-Hercules area, the hematite rich surface material occurs throughout the area with no clear separation from the neighbouring geological provinces discernable.

Ten to 20 km diameter spots of very hematite rich surface materials are developed in the Fraser Zone between Tropicana in the north and the Eyre Highway in the south. This pattern is common in the Albany-Fraser Orogen and the Yilgarn Craton and is due to mineralogical differences between the domains of a dissected landsurface typical of the two geological provinces. This becomes clearer at a smaller scale, where the elevated areas show a low content of ferric oxides (Fig. 97A, B) dominated by hematite (Fig. 97C, D), and higher content of Al-clays (Fig. 97E, F). In contrast to this, the drainage areas show a high ferric oxide content, dominated by goethite, and low Al-clay contents. Differences are observable in the composition of the alluvium and to a lesser degree in the colluvium. The alluvium in the Yilgarn example shows a low ferric oxide content, but high Al-clay content, whereas in the Albany-Fraser example Fe oxides together with MgOH bearing hydrated silicates and/or carbonates dominate the alluvium.

In the AlOH group content and composition maps (Fig. 97E, F), the Eucla basin shows in general, a low content of Al-clays that are dominated by montmorillonite or white micas. Low to intermediate abundance of Al-clays is evident in the Yilgarn Craton. Areas with elevated Al-clay contents feature mineral assemblages dominated by kaolin and Al-rich mica or smectite, whereas areas of low Al-clay content most likely contain montmorillonites or white micas, similar to the Eucla basin. The northeastern Albany-Fraser Orogen shows a pattern similar to the Yilgarn Craton, but with overall lower Al-clay contents. However, in both the Yilgarn Craton and Albany-Fraser Orogen, the AlOH group content and composition maps are heavily influenced by fire scars. The extent of distinct kaolin and Al-rich mica or smectite dominated zones in the south-western part of Fig. 97F matches the distribution of fire scars, visible in the False Colour RGB and Green Vegetation content maps. At a regional scale, a visual distinction between fire scars and geological features is difficult to recognize and might lead to incorrect conclusions. Furthermore, the evident correlation between the AlOH group content and composition maps in the Eucla basin and Yilgarn Craton indicates a processing issue that has to be taken into account when interpreting the AlOH group composition map (Cudahy, 2011).

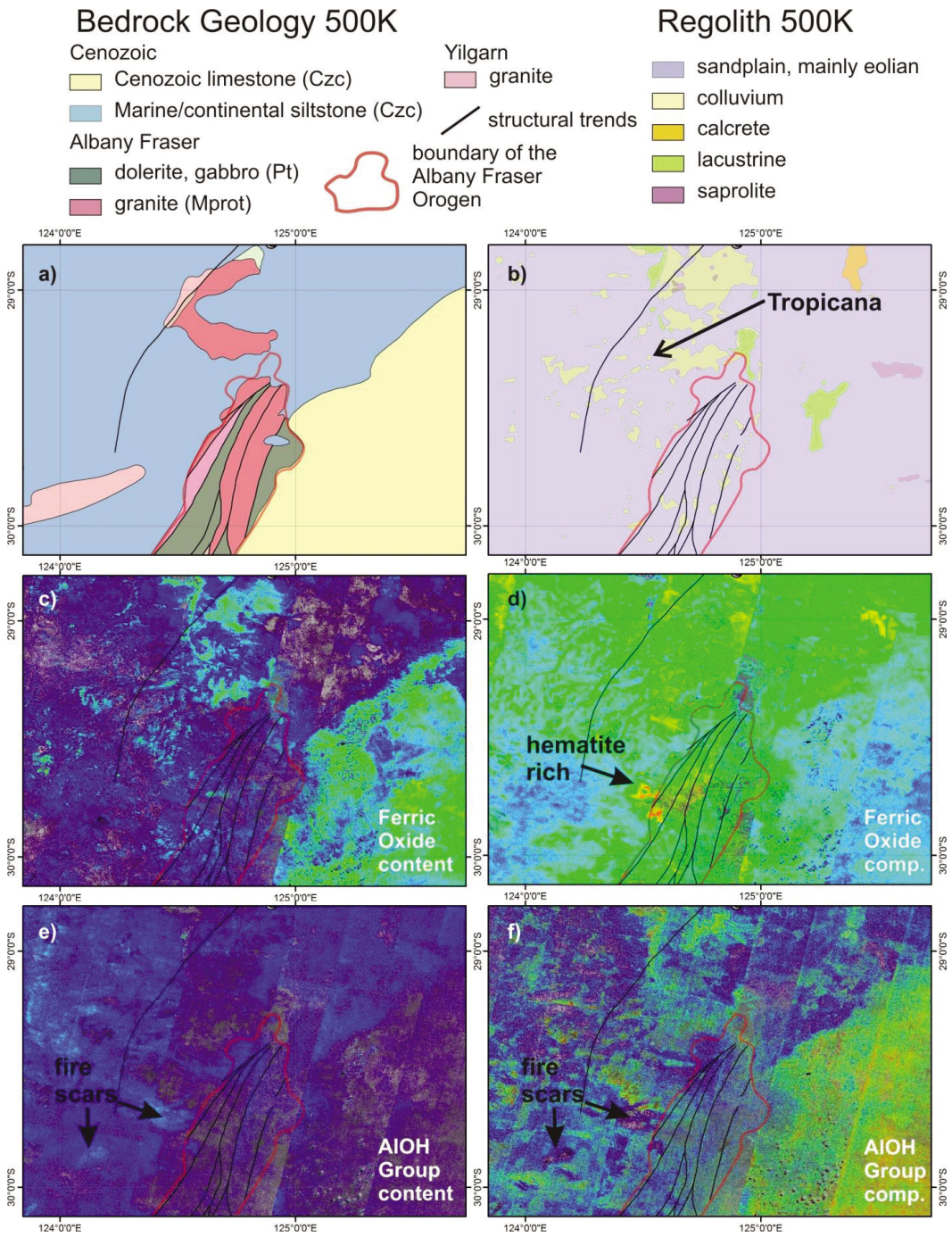

Figure 97. Interpreted geological plans and hyperspectral mineral maps of the eastern Albany-Fraser Orogen. (A) Bedrock geology 500K (Department of Mines and Petroleum, 2010a); (B) regolith 500k (Department of Mines and Petroleum, 2010b); (C) ferric oxide content (blue colours show low content and yellow/red colours show high content); (D) ferric oxide composition (blue: goethite, yellow/red: hematite); (E) AlOH group content (blue: low content, yellow/red: high content); and (F) AlOH group composition (blue: kaolinite, Al-rich white mica (muscovite, paragonite) or smectite (beidellite), pyrophyllite; yellow/red colours: Al-rich white mica (phengite) or smectite (montmorillonite).

Next page:

Figure 98. ASTER Geoscience products of drainage areas in the Albany-Fraser Orogen (A, C, E) and Yilgarn Craton (B, D, F). Images (A) and (B): ferric oxide content (blue colours-low content, yellow/red – high content). Images (C) and (D): ferric oxide composition (blue-goethite rich, yellow/red-hematite riche). Images (E) and (F): mineral group content RGB with ferric oxide content in red, AlOH group content in green and MgOH group content in blue.

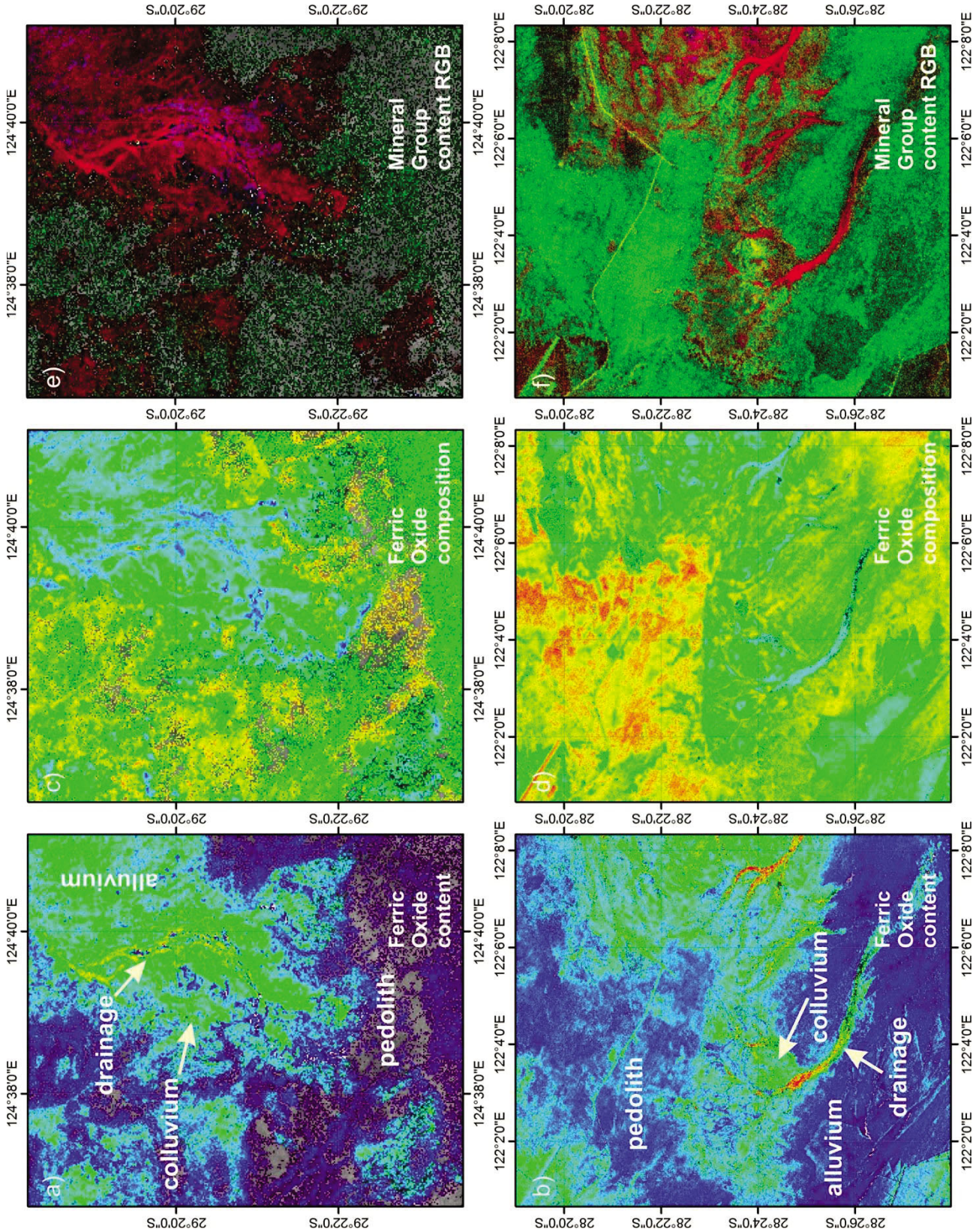
a)
alluvium
drainage
colluvium
pedolith
Ferric Oxide content
b)
pedolith
colluvium
drainage
alluvium
Ferric Oxide content
c)
Ferric Oxide composition
d)
Ferric Oxide composition
e)
Mineral Group content RGB
f)
Mineral Group content RGB
124°38'0"E
124°40'0"E
122°2'0"E
122°4'0"E
122°6'0"E
122°8'0"E
29°22'0"S
29°20'0"S
28°26'0"S
28°24'0"S
28°22'0"S
28°20'0"S

Figure 98.

8.2.2 District scale (10 to 100km)

At a district scale, the influence of vegetation and other complicating factors are easier to distinguish from geological features. This increases the usefulness of the ASTER Geoscience products significantly. The geological map in Fig. 99A shows the area around the Hercules prospect (Neale tenement) and represents an outcrop and regolith environment typical for the northeastern AFO. Mesoproterozoic granites and metasedimentary/volcanic rocks are covered by the Carboniferous Paterson Formation or the Cretaceous Madura/Loongana formations. It should be noted that rocks mapped as Paterson Formation where reclassified by studies presented in Chapter 5 (Appendix E).

HyLogging™ data show a distinct weathering horizon beneath the Paterson Formation, which is characterized by poorly crystalline kaolin group minerals, high Fe oxide contents and a downward increasing abundance of primary minerals, such as chlorite and amphibole. Cenozoic sandplains and silcrete as well as quaternary alluvial and lacustrine valley-fill deposits and dunes cover the Proterozoic and Mesozoic successions. The lacustrine environment is clearly visible in the western part of the false colour image (Fig. 99B) in blue tones. In the same false colour image, occurrences of the Paterson Formation (orange in Fig. 99A) are shown in dark-bluish colours in the west and brighter colours in the centre, showcasing difficulties when interpreting lithologies from visible and near infrared bands only, for example based on Landsat TM.

The ferric oxide content image (Fig. 99C) highlights areas of shallow regolith and outcropping Proterozoic and Mesoproterozoic successions with intermediate to high ferric oxide abundances, respectively, at this scale. Dunes show a low to very low ferric oxide content. The AlOH group content map (Fig. 99D) shows an overall low abundance of Al-bearing clays in areas of Cenozoic deposits. Fire scars are clearly visible in the false colour RGB of the same area (Fig. 99B) and heavily influence the AlOH content and composition maps. The mineral group content RGB image (Fig. 99E) shows the distribution of ferric oxides in red, Al-clays in green and Mg-bearing hydrated silicates and carbonates in blue. Areas containing mixtures of any of the three mineral groups are shown in their respective hues. Large parts of this scene are dominated by Al-clays, with small scale variations due to local compositional changes of the respective regolith environment and large scale abrupt changes due to scene boundaries and fire scars as seen in the false colour RGB and the AlOH group related mineral maps. Of particular interest are compositional changes of the colluvium, whose appearance is enhanced in the mineral group content RGB image.

The colluvium around outcrops of Mesoproterozoic granites in the centre of the image can be separated in areas dominated by ferric oxides (red) on one side and Al-clays (green) on the other side. In contrast, colluvium surrounding outcrops of the Paterson Formation are highlighted by red to pink and purple colours, suggesting a high abundance of ferric oxides, mixed with MgOH bearing hydrated silicates or carbonates in the pink to purple areas. The latter observation could point to an increased abundance of primary minerals (e.g., chlorite, amphiboles), which can be found in the saprolite beneath the Paterson Formation as indicated by preliminary HyLogging™ data. Silcretes covering both granites and Paterson Formation are highlighted by yellow colours in Fig. 99A, suggesting ferric oxides and Al-bearing hydrated silicates (i.e., kaolin, smectite and white mica) being intimately connected in these hardcap units.

Next page:

Figure 99. Geology map and hyperspectral mineral maps for the area around the southern end of the Neale tenement. (A) Geological map from Geology 1:1M, Stewart et al. (2008) and ASTER Geoscience products; (B) false colour RGB; (C) ferric oxide content; (D) AlOH group content; blue/cool colours-low content, yellow/red-high content) of the Hercules area in the northeastern Albany-Fraser Orogen; and (E) mineral group content RGB with ferric oxide content in red, AlOH group content in green and MgOH group content in blue.

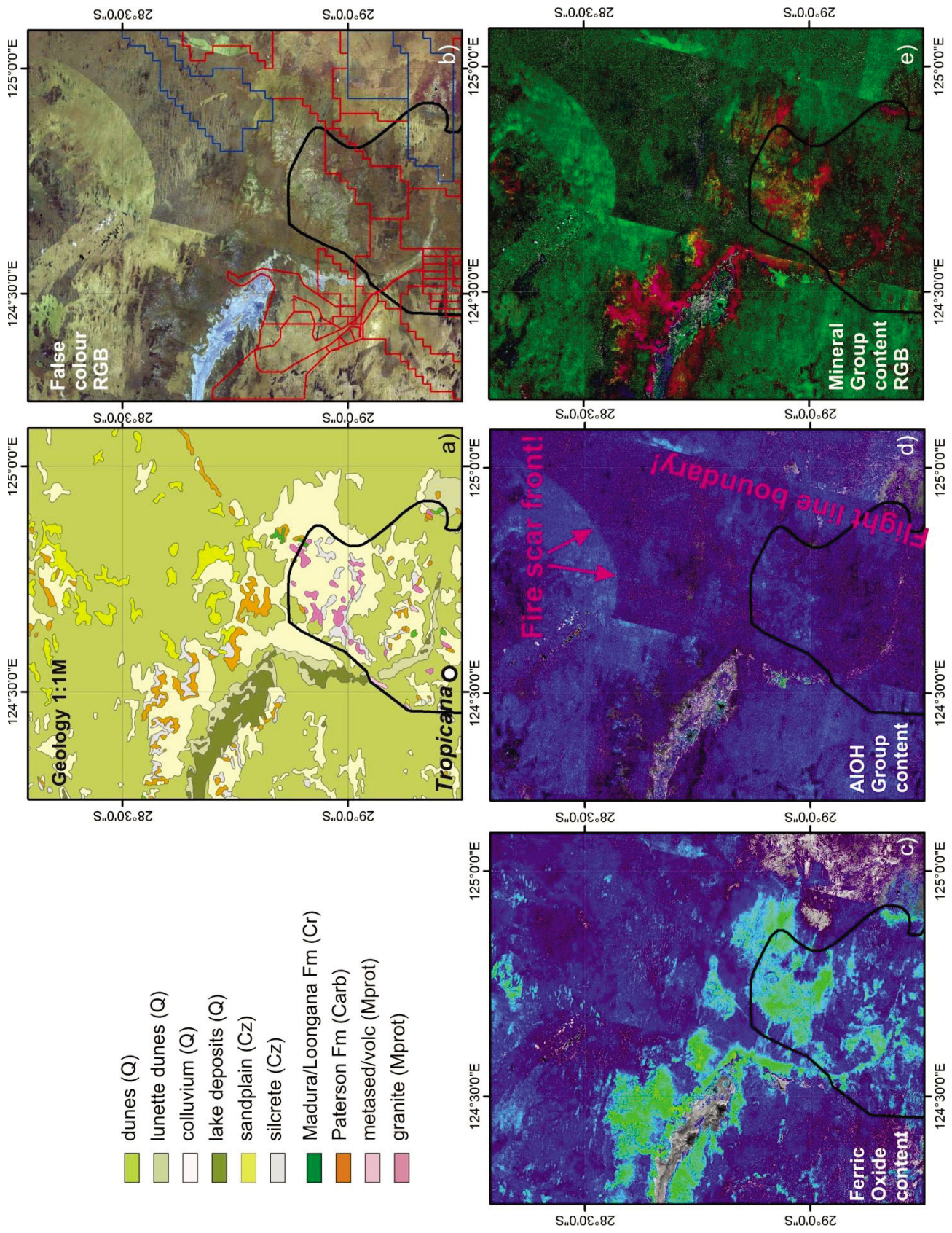
Geology 1:1M
Tropicana
a)
False colour RGB
b)
Ferric Oxide content
c)
Fire scar front!
Flight line boundary!
AlOH Group content
d)
Mineral Group content RGB
e)
dunes (Q)
lunette dunes (Q)
colluvium (Q)
lake deposits (Q)
sandplain (Cz)
silcrete (Cz)
Madura/Loongana Fm (Cr)
Paterson Fm (Carb)
metased/volc (Mprot)
granite (Mprot)
125°0'0"E
124°30'0"E
28°30'0"S
29°0'0"S

Figure 99.

8.2.3 Camp scale (<10km)

On a camp scale, the ASTER Geoscience products allow a better distinction between geological and non-geological (e.g., scene boundaries, fire scars) features. As a first example, mesas north-west of the Hercules prospect were chosen (Fig. 100). The ferric oxide content map (Fig. 100A) indicates saprolite and mottled zones below the Paterson Formation, the latter one building the upper layers of the mesas. A ring like distribution of high ferric oxide contents can be observed in Fig. 100B, which coincides with the flanks of a mesa shown in Fig. 100D, where a distinct weathering horizon lies beneath the Paterson Formation.

HyLogging™ data from the Hercules site confirm a high Fe oxide abundance (mottled zone or saprolite) below an almost Fe oxide devoid Paterson Formation. The mineral group content RGB (Fig. 100C) shows the distribution of ferric oxides (red) in direct comparison with Al-bearing clays (green) and Mg-bearing hydrated silicates (e.g., amphibole) and carbonates (blue). The high Fe oxide abundance on the flanks of the mesa is shown in pink to purple colours indicating a ferruginous saprolite material comprising an intimate mix of either carbonates or Mg-bearing silicates with abundant Fe oxides. Green colours on the top of the mesa reflect the high Al-clay abundance of the Paterson Formation, which is also recorded in the HyLogging™ data. More clearly visible than in the pure Fe oxide content image (Fig. 100B) is a neighbouring mesa to the north-east, showing the same characteristic pattern. Also of interest are the three different depositional environments surrounding the central mesa. To the east, high ferric oxide content is evident (colluvium according to the geological map) changing into an Al-clay dominated area in the south and south-west (dunes according to the geological map). These two areas are clearly separated from a carbonate and/or hydrated Mg-silicate rich surface material. This could possibly point to additional saprolite exposures to the north-west of the mesa.

The second example of the improved possibilities for geological mapping in the Albany-Fraser Orogen is given by the base of the alluvial deposits, and their source areas south-west of the Hercules prospect (Fig. 101). Basement rocks in this area comprise Mesoproterozoic granites and metasedimentary/metavolcanic rocks.

Sedimentary material is shed to the north-west and dispersed in a flat area of colluvium (Fig. 101A). Erosional areas (bright colours), transported material along creeks (dark brown) and depositional environments (dark brown to red) are clearly visible in the false colour RGB (Fig. 101B). The quality of the ASTER derived ferric oxide content map is very good in this area, showing a high abundance of ferric oxides in the creeks, where erosional material of the basement rocks is collected and transported further into larger creeks. The two larger channels (1 and 3 in Fig. 101C) show an intermediate ferric oxide content, whereas the smaller channel in between (2 in Fig. 101B) shows a lower ferric oxide content. This could be due to the smaller area from which this channel is sourced, with source material deriving from a distinct bedrock lithology or regolith layer. On the other hand, Fig. 101D (AlOH group content) and Fig. 101E (ferrous Fe associated with MgOH and carbonates) show differences in the source regions of channel 1 and 3 compared to channel 2.

The Al-clay content is elevated in the source area of channel 2, whereas high contents of Mg-bearing hydrated silicates and/or carbonates are only evident from the source areas of channels 1 and 3. This supports the hypothesis that mineral assemblages of erosional and depositional environment are intimately linked with one another.

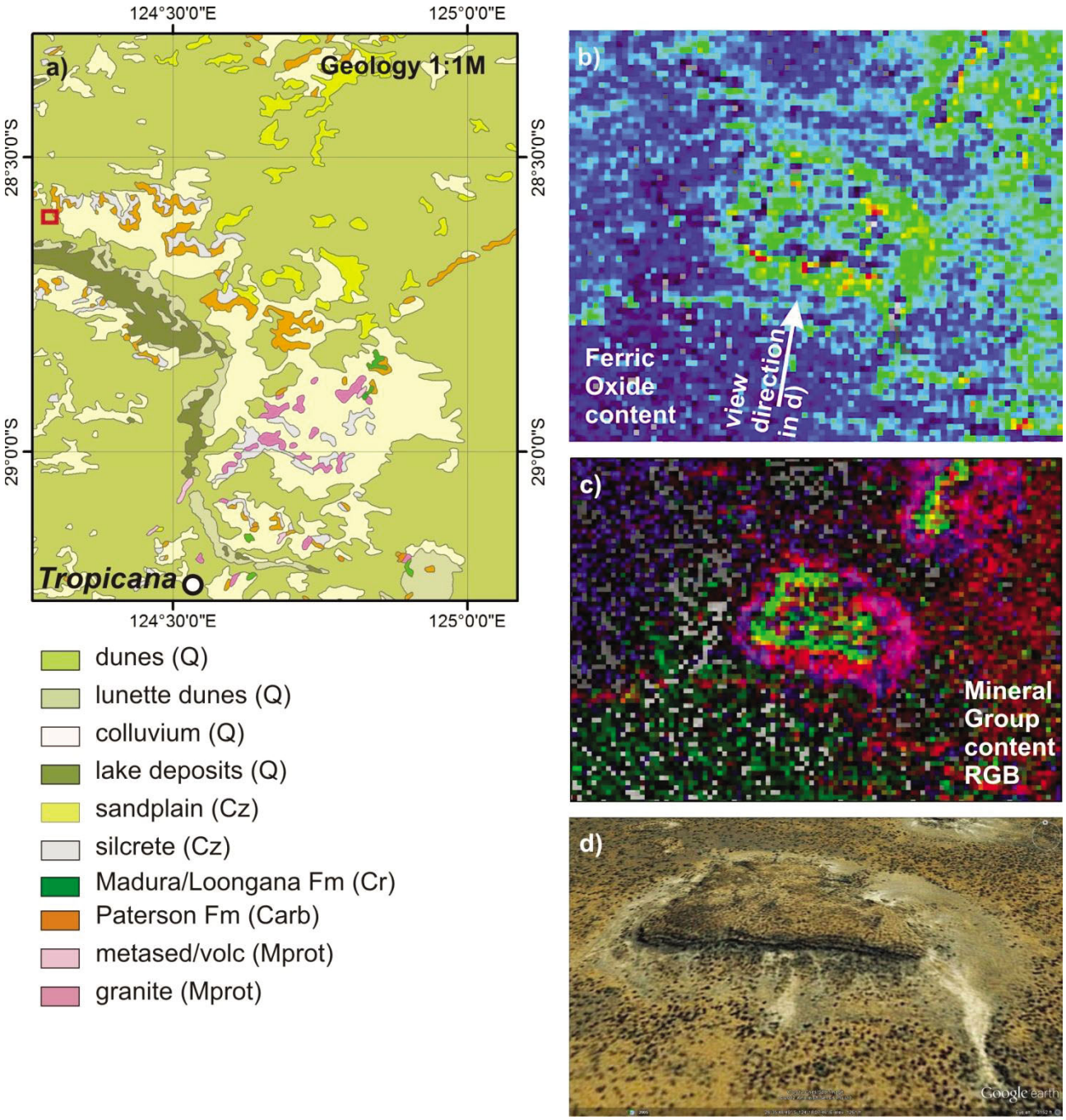

Figure 100. Geological, geographical and hyperspectral mineral maps of a Paterson Formation mesa, north/north-west of the Tropicana Au deposit. (A) Map of geological setting from (Geology 1M), Stewart et al. (2008) of the Hercules prospect, red frame marks location of (B); (B) relative ferric oxide content (blue/cool colours-low content, yellow/red-high content); (C) RGB image of the of the mesa, with detail showing distribution of major mineral groups (red-ferric oxide content, green -AlOH bearing clays, blue- Mg bearing hydrated silicates and carbonates); and (D) Google Earth image of the mesa in perspective, with view direction from the south as indicated with white arrow in (B).

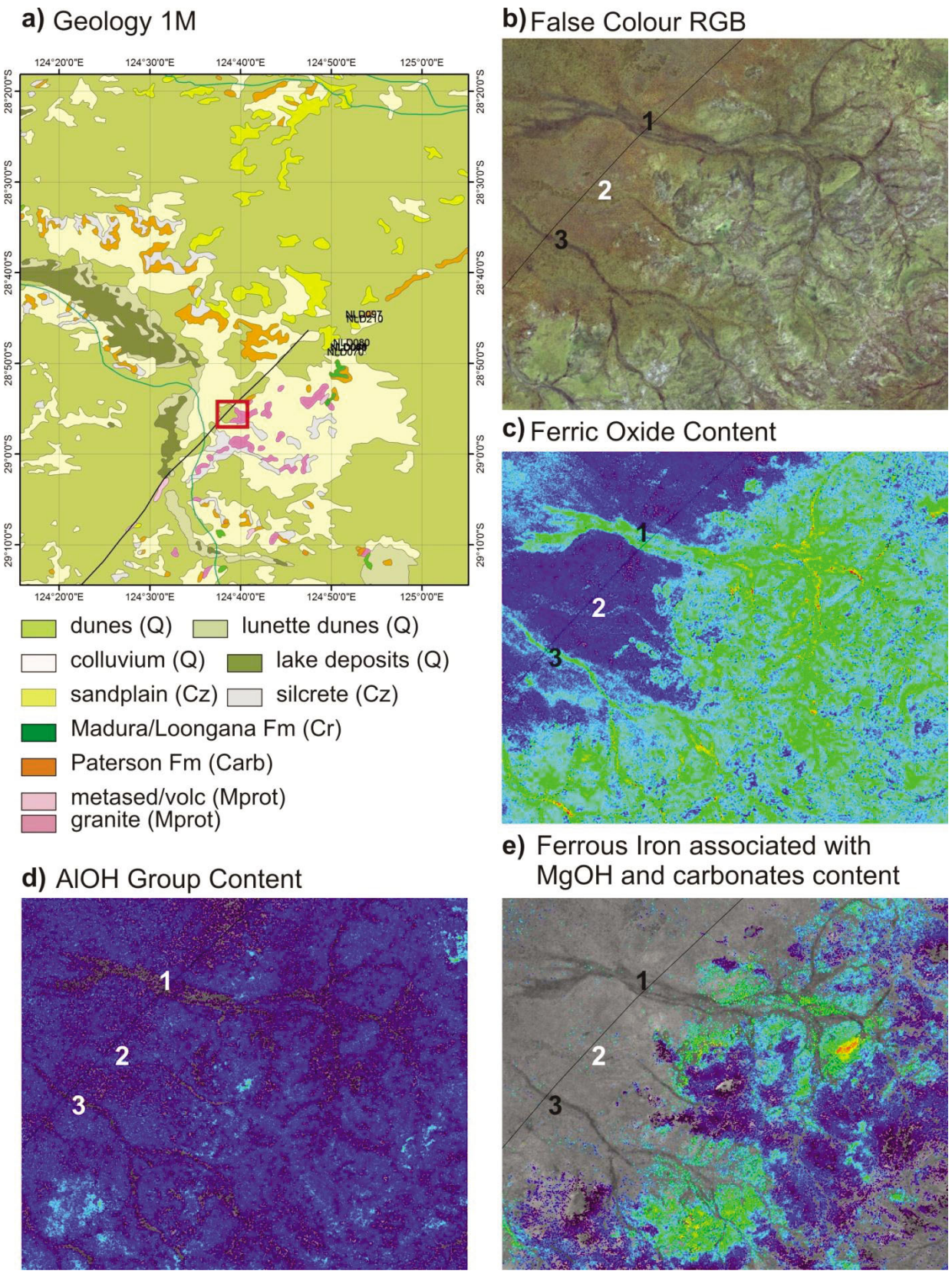

Figure 101. Geological, geographical and hyperspectral mineral maps of alluvial fans south of the Hercules prospect. (A) Geological map (Geology 1M, Stewart et al., 2008) of the Hercules area, red frame marks location of (B) to (E); (B) false colour RGB; (C) ferric oxide content; (D) AlOH group content; and (E) ferrous Fe associated with MgOH and carbonates; in all mineral group content maps blue/cool colours show a low and yellow/red colours indicate a high content of the respective mineral group. Numbers 1, 2 and 3 indicate the three channels described in the text, with channels 1 and 3 showing similar mineral assemblages and are sourced from similar rocks, whereas channel 2 has a different mineral assemblage, possibly derived from a different rock type.

8.2.4 Conclusions

The Western Australia ASTER Geoscience products were evaluated for their applicability for geological mapping from orogen to camp scales. A number of precompetitive datasets, such as geological and regolith maps, were used for the evaluation of the products, to enable a distinction of geological from non-geological features and patterns. At the orogen to regional scale, the Geoscience products show no consistent distributions of the major mineral groups that can be detected in neighbouring geological provinces (i.e., Yilgarn Craton and Eucla basin), such as the generally high abundances of ferric oxides in the Eucla basin, visible in the ferric oxide content map. The main impediments are dense vegetation cover, fire scars, clouds and scene boundaries.

Separation and characterization of the various geological domains of the Albany-Fraser Orogen was successful in a few cases. Most of the Geoscience products show variations in the Munglinup Gneiss area, which probably reflect the distribution of basement rocks *versus* Cenozoic sediments. In the Eastern Biranup Zone, an improvement of the regolith characterization (e.g., calcrete *versus* slope deposits *versus* sandplain) and mapping is possible by reviewing and referencing the ferric oxide content, ferrous Fe index and AlOH group content maps.

Unrelated to, major geological domains, the accuracy or level of interpretation possible from the ASTER data increases when focusing on the district or camp-scale. At these scales fire scars and scene boundaries can be more readily distinguished from geological features. At a district scale, for example, patterns in single regolith units enable a more detailed classification and enhance differences between different regolith domains. The ferric oxide and AlOH group Geoscience products can provide important information about erosional *versus* depositional environments. In addition, in the Hercules area, for example, a combination of three different mineral group content maps separates Al-clay rich domains from ferric oxide rich domains in colluvium around granite outcrops (Figs. 100 and 101), which are not shown on precompetitive datasets. This implies possibilities for an advanced characterization of regolith material in this area that is highly prospective for Tropicana style mineralization. At camp scale the ASTER Geoscience products allow, in some cases, a detailed interpretation of regolith profiles and compositional changes of colluvium and alluvium and their relation to source areas, as well as the identification of possibly new outcrop. This again can have important implications for exploration.

In summary, each of the Geoscience products show their strength at different scales, though almost all of them provide additional information about the geology at a smaller scale. However, this can vary from area to area, depending largely on the quality of the ASTER scenes available as well as the environmental conditions of the acquisition area (e.g., vegetation *versus* no vegetation). The key lies in separating geological from non-geological features based on a sound understanding of the geology.

8.3 HyLogging™ data from Neale and Salmon Gums diamond core *(Appendices H2 and H3)*

HyLoggingTM data were acquired from seven drill holes from the Neale tenement (Atlantis and Hercules prospects) and five drill holes from the Salmon Gums site at GSWA's core library in Carlisle (WA). The rationale of this project was to evaluate visible-near (VNIR), short wave (SWIR) and thermal infrared (TIR) reflectance spectroscopic data for mapping regolith and bedrock lithologies, and hydrothermal alteration patterns in the northeastern Albany-Fraser Orogen. Visible and infrared reflectance spectroscopy (VIRS) can be used to map the abundance and composition of major rock forming minerals, and can be applied to map hydrothermal alteration associated with various mineral deposit types and country rocks.

8.3.1 Visualisation of HyLogging™ interpretation

The relative abundances and composition of mineral species derived from HyLogging™ data was interpreted using the Multiple Feature Extraction Method (MFEM), which targets absorption features in the reflectance spectra that are characteristic for the respective mineral groups and species. Results are displayed in this Chapter as downhole plots with Fig. 102.

The strategy behind this visualization. Figure 102A shows the abundance of white mica (x-axis) in drill hole NLD071 (Neale tenement) from 105 to 120 m depth (y-axis). Every black point represents one measurement. Figure 102B shows the composition of white mica (x-axis and colour scale) in the same drill hole interval, with the values representing the wavelength position of the 2,200 nm feature diagnostic for white mica. Low values indicate Al-rich white micas (e.g., paragonite and muscovite), whereas high values represent Al-poor white micas (e.g., phengite). Figure 102C is the combination of plots (A) and (B), with the white mica abundance displayed on the x-axis and the white mica composition represented by the colour scale. Due to the high sample spacing (1 cm steps) several measurements appear to be from the same sample point. Figure 102D displays a detail of the interval between 109.5 and 110.5m, showing representatively that every sample point is essentially separated.

The remaining MFEM scripts are displayed in the same way with the relative abundance values on the x-axis and compositional parameters in the colour scale. An exception is the quartz abundance. This is coloured by the "Restrahlen feature position", which provides an estimate of accuracy of the quartz abundance script as well as of the degree of mixture with other silicates.

The VNIR, SWIR and TIR derived mineral abundance and composition information of the drill holes are stored in TSG-files in folder ("hyperlink"). A free TSG viewer to query the data in detail can be downloaded from: http://www.thespectralgeologist.com/tsg_viewer.htm.

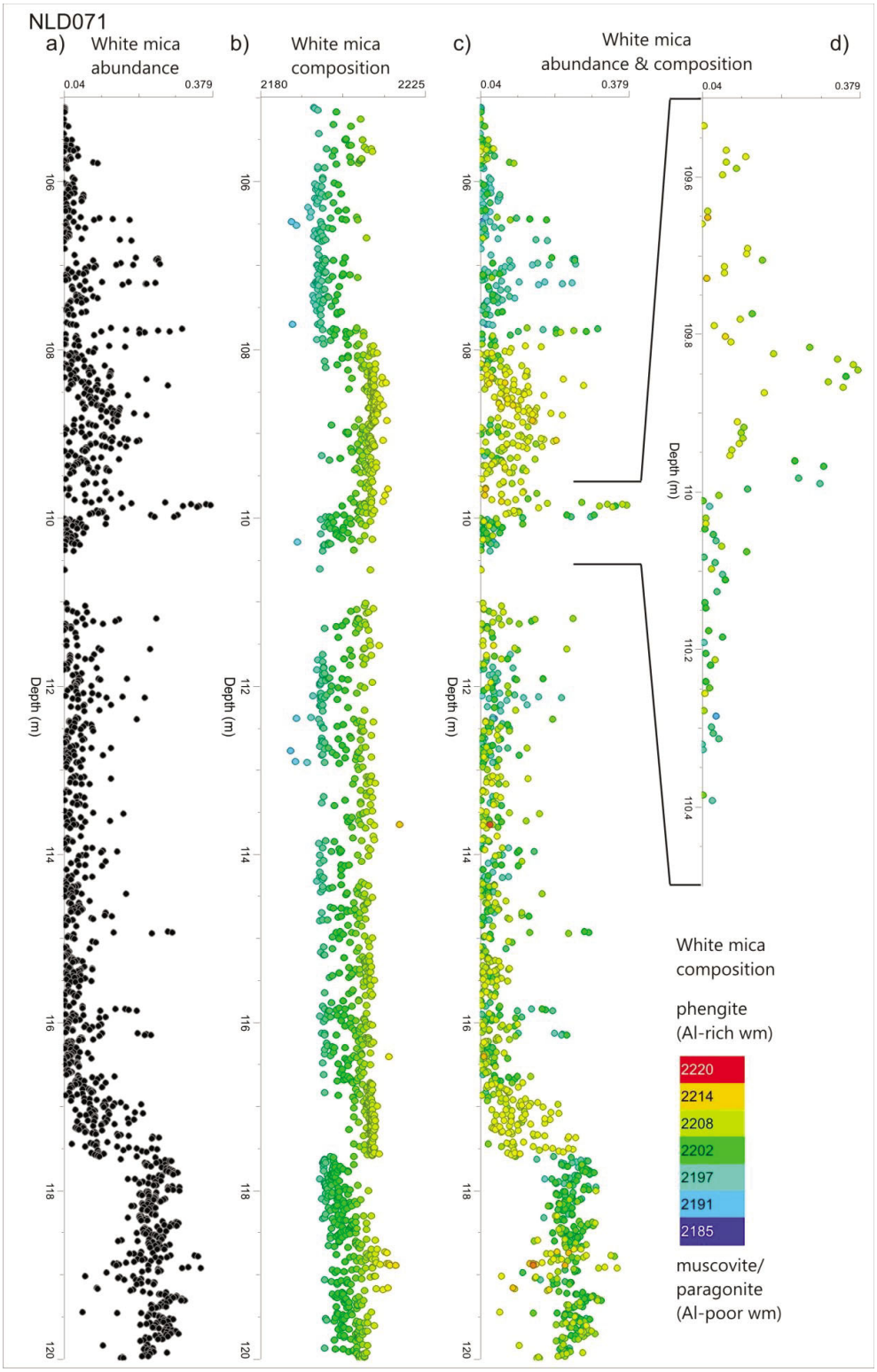

Figure 102. White mica parameters of drill hole NLD071, 105-120 m depth. (A) Relative white mica abundance; (B) white mica composition: low values – Al-rich white mica (e.g., paragonite, muscovite), high values – Al-poor white mica (e.g., phengite); (C) relative white mica abundance coloured up by white mica composition; (D) detail of 109.5 to 110.5m of plot (C). Colour scale for (B), (C) and (D) bottom right.

8.3.2 Lithological data interpretation using HyLogging™ data - an example from the Neale tenement

At the Neale tenement the VIRS HyLogging™ data (drill hole locations shown in Fig. 103) were queried for:

(1) Weathering front/base of weathering and development of saprolite (clay mineralogy from VNIR and SWIR);

(2) Contact between eastern garnet gneiss and western granite gneiss (garnet, feldspar and quartz abundance and composition from TIR);

(3) Localization of a metachert layer (quartz abundance from TIR); and

(4) Any hitherto unknown trends in mineral abundance and composition that could point to mineralization related alteration, or provide stratigraphic correlations between different drill holes.

An example of lithological description based on HyLogging™ data is shown in Fig. 104. Data from the lower part of drill hole NLD097 shows the detail of information that can be inferred from the hyperspectral data. The base of NLD097 (142.75-~135 m) consists of a highly deformed igneous rock with moderately consistent contents of white mica, chlorite/biotite and quartz. Chlorite/biotite and amphibole are enriched at around 139.8 m depth, coinciding with a substantial decrease in white micas. Rocks are increasingly deformed to the top, transitioning into a mylonitized interval between 135 and 129.3 m. An increase in phyllosilicates can be associated with a decrease of quartz (130.2 m).

Amphiboles and carbonates are less abundant in this interval, disappearing in a chertified hanging wall layer that separates lower and upper deformed units. The chert layer is described in more detail in Appendix H. An amphibole-free transition zone at the upper contact between the chert and the granitoids features a distinct shift of the white mica composition to more phengitic micas, whereas the white mica-rich chert level contains more Al-rich white micas.

Between 115.8 to 108 m, quartz and phyllosilicate levels are similar to the lowermost domain. But in contrast to the lower units, the grain size increases considerably, and the fabric is less well developed (Fig. 104), possibly due to a weakly developed crenulation cleavage. A 30 cm thick zone with high amphibole (Mg-rich) contents appears at ca. 114.5 m.

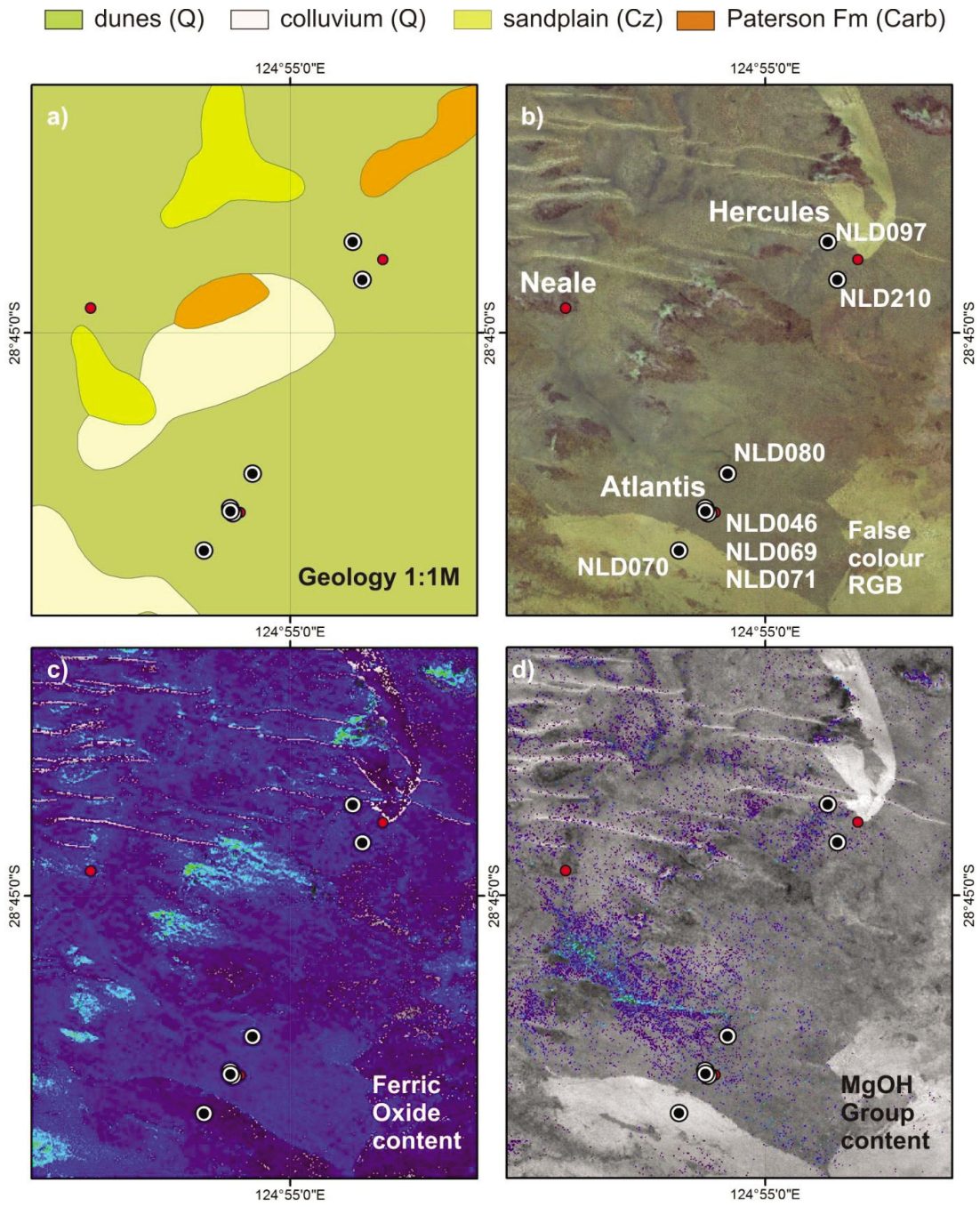

Figure 103. Location of drill holes from the Hercules and Atlantis sites scanned with the HyLogging™ systems, with geological, geographical and hyperspectral mineral context. (A) Geological map, extracted from Stewart et al. (2008); (B) false colour RGB image of the Landsat; (C) ferric oxide content; (D) MgOH group content. Blue/cool colours in mineral group content maps show low content of the given mineral group and yellow/red colours show high content, respectively. Red circles are RC drill holes, whereas black circles are diamond drill holes.

Next page:

Figure 104. Down hole mineral abundance plots for drill hole NLD097 at 98-116 m depth showing variations in mineralogy for a variety of granofels and granitoids: (A) white mica abundance and composition; (B) chlorite/biotite abundance and composition; (C) amphibole abundance and composition; (D) carbonate abundance and composition; and (E) quartz abundance. Images and TIR spectra on the right present detailed examples from two typical granofels at 100.75 and 112.45 m, respectively.

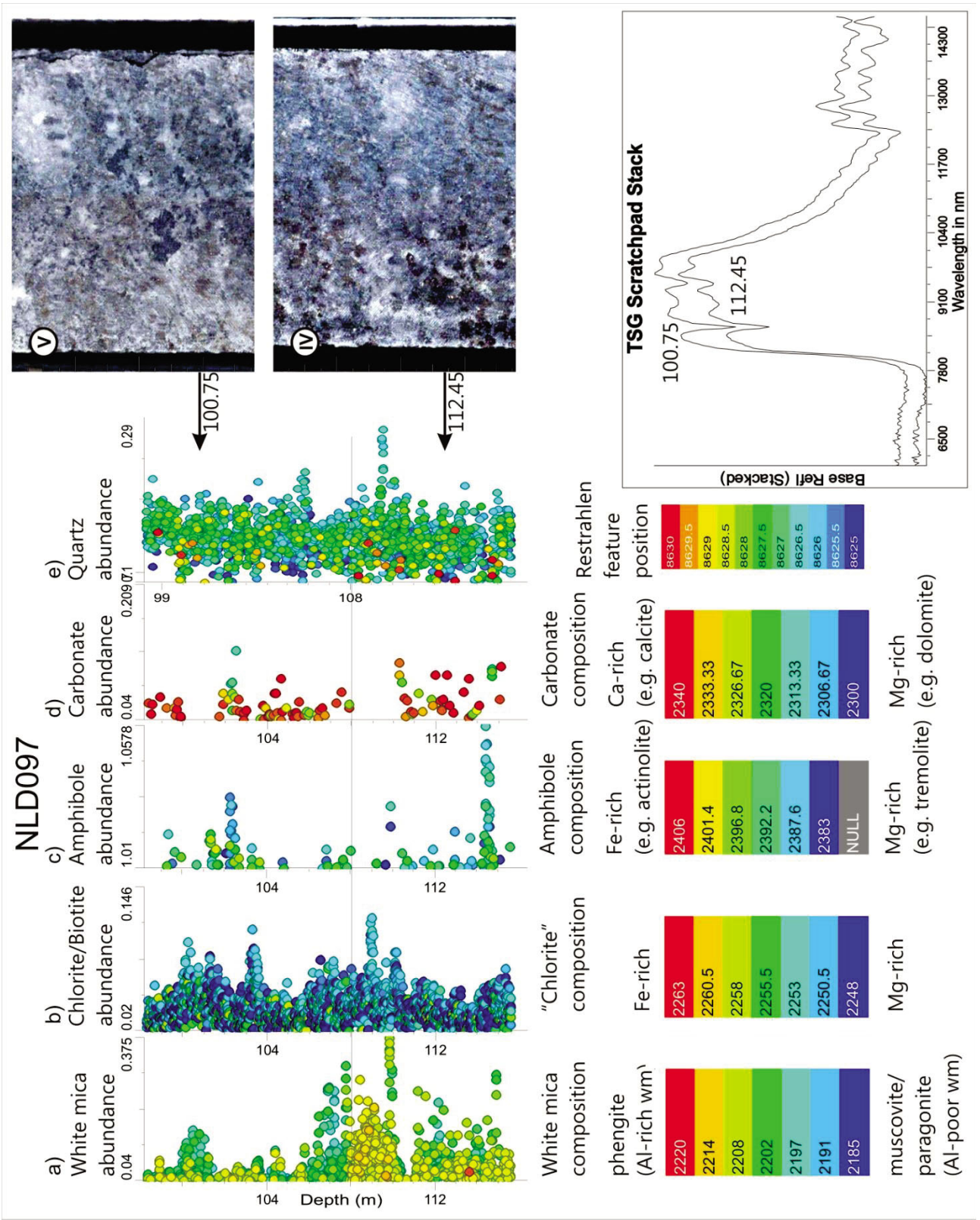
NLD097
a) White mica abundance
b) Chlorite/Biotite abundance
c) Amphibole abundance
d) Carbonate abundance
e) Quartz abundance
Depth (m)
100.75
112.45
TSG Scratchpad Stack
Base Refl (Stacked)
Wavelength in nm
White mica composition
phengite (Al-rich wm)
muscovite/ paragonite (Al-poor wm)
"Chlorite" composition
Fe-rich
Mg-rich
Amphibole composition
Fe-rich (e.g. actinolite)
Mg-rich (e.g. tremolite)
Carbonate composition
Ca-rich (e.g. calcite)
Mg-rich (e.g. dolomite)
Restrahlen feature position

Figure 104.

8.3.3 Lithological data interpretation using HyLogging™ data - an example from the Salmon Gums

Five drill holes from the Salmon Gums site were scanned using the HyLogging™ data. Based on these data, rocks from drill hole SGD005 can be subdivided into (1) mica-rich gneiss (white mica, chlorite, quartz ± amphibole, plagioclase and carbonate); and (2) chlorite-rich mafic gneiss (chlorite, amphibole, quartz ± white mica and minor carbonate) and mafic gneiss (amphibole, quartz ± white mica and chlorite).

The mafic gneiss in drill hole SGD005 has three zones with distinct amphibole ± chlorite alteration. A direct lithological correlation between the drill holes based on this type of mafic gneiss is questionable, as high chlorite contents only overlaps to a varying degree with the amphibole-rich intervals. But the strikingly similar spatial distribution of similar mineralogical horizons in both drill holes might point towards a genetically related overprint, possibly in the form of hydrothermal alteration along shear zones. In SGD005, the amphibole ± chlorite rich mafic gneiss can host significant amounts of Au associated with quartz veining at around 155 m depth.

Quartz veining, indicated by single spikes in the quartz abundance in the down holes figures and plots, is at first sight randomly distributed in Salmon Gums north. However, coarse-grained quartz veins were definitely spatially associated with the amphibole ± chlorite altered mafic gneiss. Iron oxides occur mainly in the chlorite-rich mafic gneiss. A distinct increase of Fe oxides in the upper part of SGD005 (red points in ferric oxide abundance plot in Fig. 105) probably does not reflect the true mineral assemblage, but rather dust/stain on the drill core as observed in the line-scan images collected during VIRS scanning.

Next page:

Figure 105. Down hole mineral abundance plots for drill hole SGD005 over the interval around 210-250 m depth, with images of representative examples of rock types, i.e. (I) pegmatite(?), (II) amphibole-rich gneiss and (III) chlorite-mica altered gneiss. (A) White mica abundance and composition; (B) chlorite/biotite abundance and composition; (C) amphibole abundance and composition; (D) carbonate abundance and composition; (E) quartz abundance. At 219.4m: intermediate felsic (bt, chl, pl, alb, K-fsp, qz, cal). At 244.3m: pegmatite (bt, chl, alb, Kfsp, qz, epi, cal, brt, py).

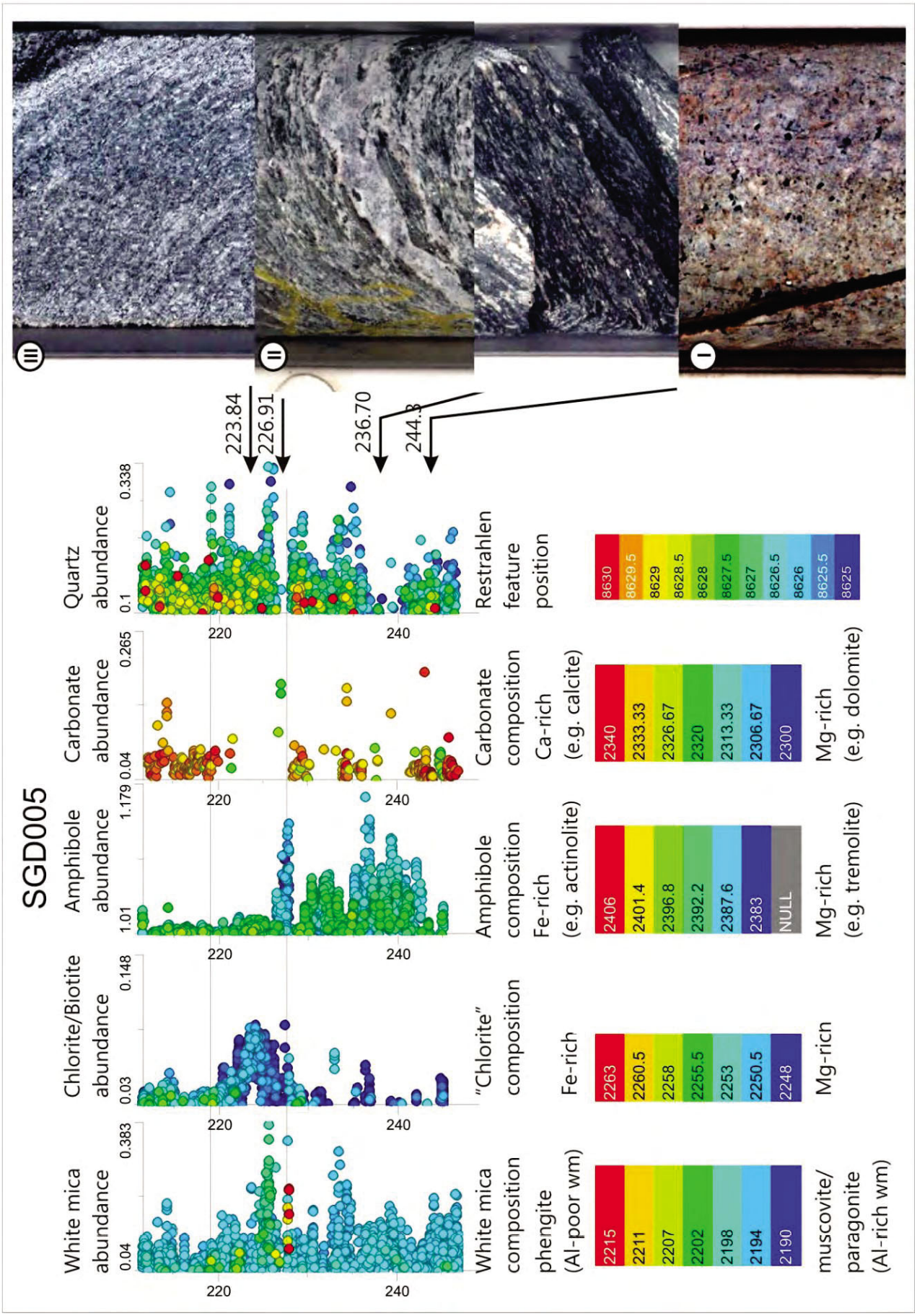
SGD005
White mica abundance
0.383
0.04
White mica composition
phengite (Al-poor wm)
muscovite/ paragonite (Al-rich wm)
2215
2211
2207
2202
2198
2194
2190
Chlorite/Biotite abundance
0.148
0.03
"Chlorite" composition
Fe-rich
Mg-rich
2263
2260.5
2258
2255.5
2253
2250.5
2248
Amphibole abundance
1.179
1.01
Amphibole composition
Fe-rich (e.g. actinolite)
Mg-rich (e.g. tremolite)
2406
2401.4
2396.8
2392.2
2387.6
2383
NULL
Carbonate abundance
0.265
0.04
Carbonate composition
Ca-rich (e.g. calcite)
Mg-rich (e.g. dolomite)
2340
2333.33
2326.67
2320
2313.33
2306.67
2300
Quartz abundance
0.338
0.1
Restrahlen feature position
8630
8629.5
8629
8628.5
8628
8627.5
8627
8626.5
8626
8625.5
8625
220
240
223.84
226.91
236.70
244.3
III
II
I

Figure 105.

8.3.4 Regolith characterization using spectral sensing data: mapping transported versus residual regolith

Drill hole NLD210 from the Neale tenement shows a transect through a considerable part of the regolith. For comparison, drill holes NLD071 and NLD080 feature intensely weathered bedrock in the upper meters of the VIRS scanned intervals. The kaolinite abundance and composition (Fig. 106), the Fe oxide abundance and composition (Fig. 106C), the abundance of white mica and Al-smectites (e.g., montmorillonite; Fig. 106D) and the quartz abundance (Fig. 106E) show distinct changes, which can be interpreted as various stratigraphic layers in the regolith recorded in drill hole NLD210.

Seven distinct horizons on top of the bedrock can be inferred from the VIRS data. From bottom to top these horizons are: (1) saprock; (2) saprolite I (containing all primary minerals such as chlorite); (3) saprolite II (containing only certain primary minerals); (4) mottled zone; (5) Paterson Formation (?; kaolin and quartz-rich, pale grey-fine grained rock); (6) lateritic duricrust; and (7) lateritic gravels.

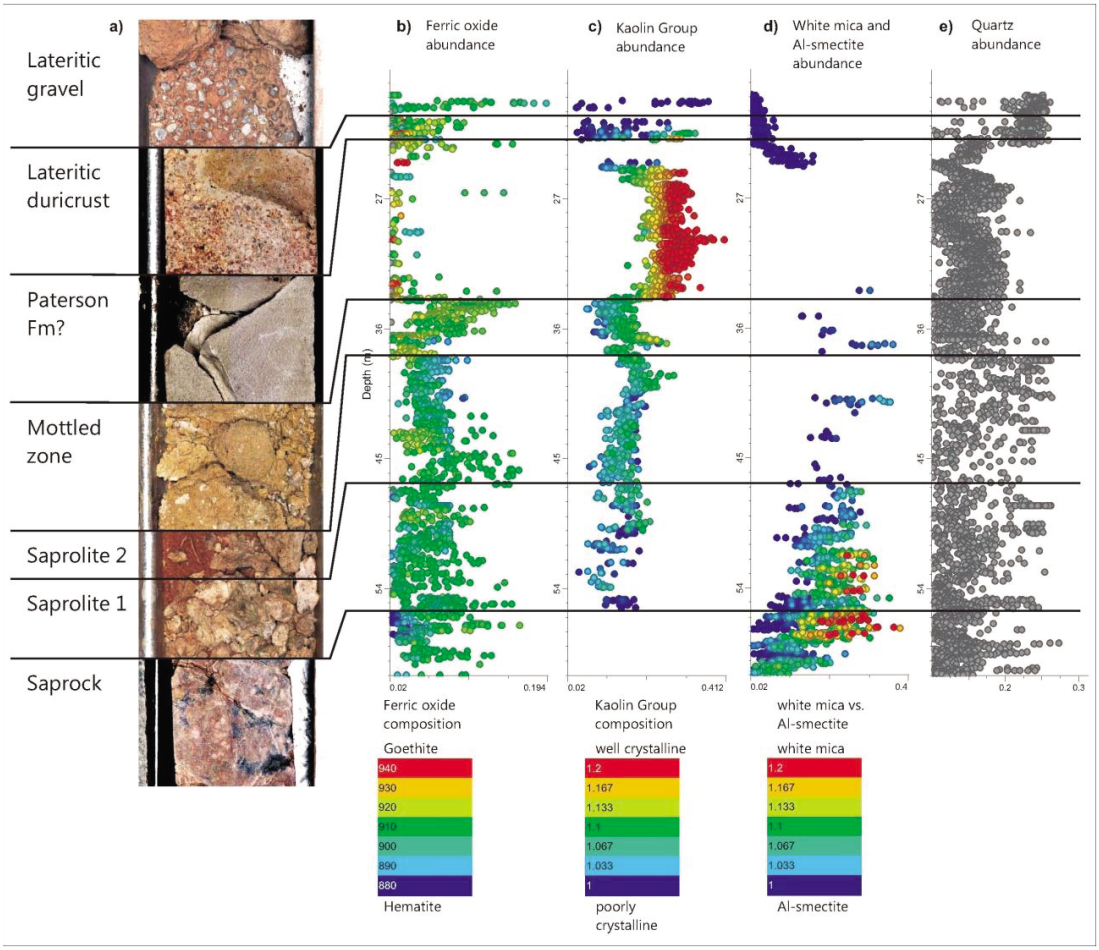

Figure 106. Regolith profile inferred from VIRS data of drill core NLD210, with representative images of drill core of each of the defined regolith units.

The lower four zones possibly represent a weathering profile that developed below the Paterson Formation, and are characterized by abundant intermediate crystalline kaolinite and varying amounts of quartz and Fe oxides. A downward increase of white mica is recognizable, which is accompanied by the occurrence of further primary minerals such as chlorite and amphibole.

Zone 5 contains well crystalline kaolinite, abundant quartz and only minor amounts of ferric oxides. The quartz content is partly correlated with the kaolin group abundance, but, to the top, Al-smectites are the

dominant clay phase. The lateritic duricrust and gravel mainly consist of goethite and quartz, and varying amounts of kaolin group minerals.

8.3.5 Conclusions

Spatially dense HyLogging™ data (1 cm steps) from twelve drill holes were acquired from the Salmon Gums, Hercules and Atlantis prospects and interpreted for their primary, alteration and regolith mineralogy. Drill holes were successfully characterized for major lithologies cross-referenced to direct logging of the core.

The cm-spaced VNIR, SWIR and TIR data show detailed variations within the major rock suites, allowing mapping of thin carbonate-altered or chert layers. One example is given by a 5 to 10 m thick horizon containing thin intense carbonate alteration that can be found in most of the drill holes at the Atlantis site, again allowing a correlation across several drill holes.

Gradual mineralogical changes can be examined in various segments of the analyzed data. At NLD097 for example, a gradually increasing sericitization of the deformed granitoids is accompanied by increasing carbonate alteration. The same pattern, but with additional epidote and chlorite/biotite alteration in the central part, is reported from drill holes NLD201 and NLD046.

Another result of this study of diamond drill core from Atlantis and Hercules is the rectification of falsely interpreted mineralogy. Garnet bearing gneiss was described in information provided by Beadell Resources to be one of the major basement rock types. The contact of this lithology with a granite gneiss hosts mineralized cherts of the Hercules trend. HyLogging™ (and petrographic) data, however, show that the garnet abundance is negligible. The abundance of visually discernable garnets might have been over interpreted in the former Beadell drill core logging. Because of its spatial discontinuity and rather random occurrence, it is not recommended to use garnet as an indicator to delineate certain rock types. The same comment is valid for talc, which was reported in previous company work, but could neither be found in the HyLogging™ data nor in detailed petrography and relogging of drill core.

The thickness of the respective regolith units can be determined down to cm scale and the kaolin crystallinity provides, for example, important information about which regolith units are developed residual and which are transported.

Two issues, which can be traced to the scanning process, complicated the interpretation of the hyperspectral data: firstly, in the high resolution line scan images, red and blue markers can be seen, which were probably used during core logging. These marker pens have their own characteristic absorption features in the VNIR and SWIR wavelength bands, which can overlap with diagnostic mineral absorption features. Therefore, it is critical that during the scanning process the core is physically turned over, so that no marker pen is visible to the spectroradiometer. However, in the current dataset, the number of sample points influenced by the markers was limited. Secondly, the core trays are made of white plastic, which has its own characteristic spectral signature. In the Salmon Gums dataset the HyLogging™ data were evaluated for the influence of the white plastic-related absorption features on the interpretation of mineral abundance and composition.

By using the MFEM scripts, which are focused on the mineral specific absorption features, the influence of the white plastic on the interpretation was kept to a *minimum*. Regarding the mineral interpretation, good results were achieved by applying the VNIR and SWIR MFEM scripts. However, it should be noted that chlorite and biotite could not be reliably distinguished from the VNIR and SWIR with any existing interpretation method (including MFEM, TSA, end member classification). The abundance of prehnite was estimated from a single diagnostic absorption feature, without any masking effect from other overlapping minerals and, therefore, has to be viewed with caution. The abundance and composition of anhydrated silicates can only be derived from the thermal infrared. However, the respective algorithms used for the interpretation are still at a preliminary stage, leading to reliability issues regarding the determination of garnets and certain feldspar species.

8.4 Integration of ASTER and HyLogging™ data at Salmon Gums and Neale tenements *(Appendix H4)*

Precompetitive, multispectral remote sensing data and hyperspectral drill core data were evaluated for mineral mapping at two case study sites in the regolith-dominated Albany-Fraser Orogen. The evaluated remote sensing data comprise mineral abundance and composition maps that were processed from ASTER data, and are publically available in the form of 14 ASTER Geoscience products from GSWA. Hyperspectral drill core data were acquired using the HyLogging™ system at GSWA's core library in Carlisle. The two case study sites are (1) the Hercules area in the northeastern Albany-Fraser Orogen, and (2) the Salmon Gums area in the central Albany-Fraser Orogen. Appendix H4 describes in detail the work presented in this chapter. In the following sections the Hercules regolith map model is presented as the key result that shows the potential of the spectral techniques for regolith mapping.

Mineral group maps, derived from ASTER and HyLogging™ were acquired from two case study sites in the Albany-Fraser Orogen. The aim of this Chapter is to evaluate whether the detailed mineralogy obtained from the HyLogging™ data can be extrapolated to mineralogical expressions at the surface using the ASTER data. The main focus is the regolith characterization using spectroscopic techniques in this regolith-dominated terrain. For this reason, the mineralogy of regolith systems is briefly reviewed prior to the results chapter. Results from two case study sites are presented.

8.4.1 Regolith landforms in the Neale tenement

Results from previous studies on ASTER and HyLogging™ data from the Hercules area were compared and reviewed with consideration of recent regolith landform modelling of the neighbouring Yilgarn Craton (Anand and Paine, 2002). A false colour RGB image of the Hercules area (Appendix H) provides some basic information about some of the regolith landforms in this area, without details about the respective mineralogies. The false colour RGB is similar to a Google™-style image, but the three RGB channels are derived from different positions in the electromagnetic spectrum. Vegetation appears in these images in red. In order to improve the interpretation of the remote sensing data, the false colour RGB image was also draped over a DEM of the Neale, Hercules (NLD210) and Atlantis (NLD046) sites and the surrounding area (Fig. 107A). Three distinct domains can be inferred from the false colour RGB: (1) an erosional regime with drainage systems (example location indicated by red arrow); (2) a flat depositional regime (black arrow, NLD046, NLD210); and (3) dune fields north-west of a north-east trending barrier.

When comparing the false colour RGB image with the surface geological map, a major difference in the distribution of the dune fields appears. In the surface geological map large parts of the Hercules area are mapped as Quaternary dune fields, whereas the false colour RGB suggests that the dune fields are restricted to the area north of the Neale and Hercules sites. The DEM of the Hercules area indicates that this area, is elevated compared to the lower lying area, to the south-west of a north-east trending morphological boundary. When comparing the whole range of available ASTER Geoscience products with the surface geological map, differences in terms of geological interpretation become clear.

For regolith characterization, mineralogical factors, such as changes in the abundance and composition of clay minerals and Fe oxides, are of major importance and the respective WA ASTER Geoscience products (Cudahy, 2011) show distinct differences in the three major regolith landforms. In the following text, mineralogical changes interpreted from the WA ASTER Geoscience products are discussed in comparison with the existent regolith landform model for the Yilgarn Craton (Anand and Paine, 2002). The three

major regolith landforms are: (1) saprolite and bedrock-dominated terrains (i.e., erosional landforms), and (2) sediment-dominated terrains (i.e., depositional landforms), and 3) sands, ferruginous gravels and duricrust-dominated terrains (i.e., relict landforms).

Three of the ASTER Geoscience products proved to be the most valuable mineral maps for mapping the regolith landforms in the Hercules area, and are focused on in the following text. These are the AlOH group composition image (Fig. 107B; Appendix H), and the ferric oxide content image (Fig. 107C; Appendix H). However, all of the WA ASTER Geoscience products provide valuable information for mineral identification and regolith mapping in the Hercules area. It should also be noted that in the AlOH Group Composition image (Fig. 107B), blue areas north-east to the black arrow indicate fire scars, complicating the interpretation of the remote sensing data. A schematic regolith map (Fig. 107D) was developed, based on the interpretation of the ASTER Geoscience products in relationship with a newly proposed regolith landform model (see Table 3 in Appendix H4).

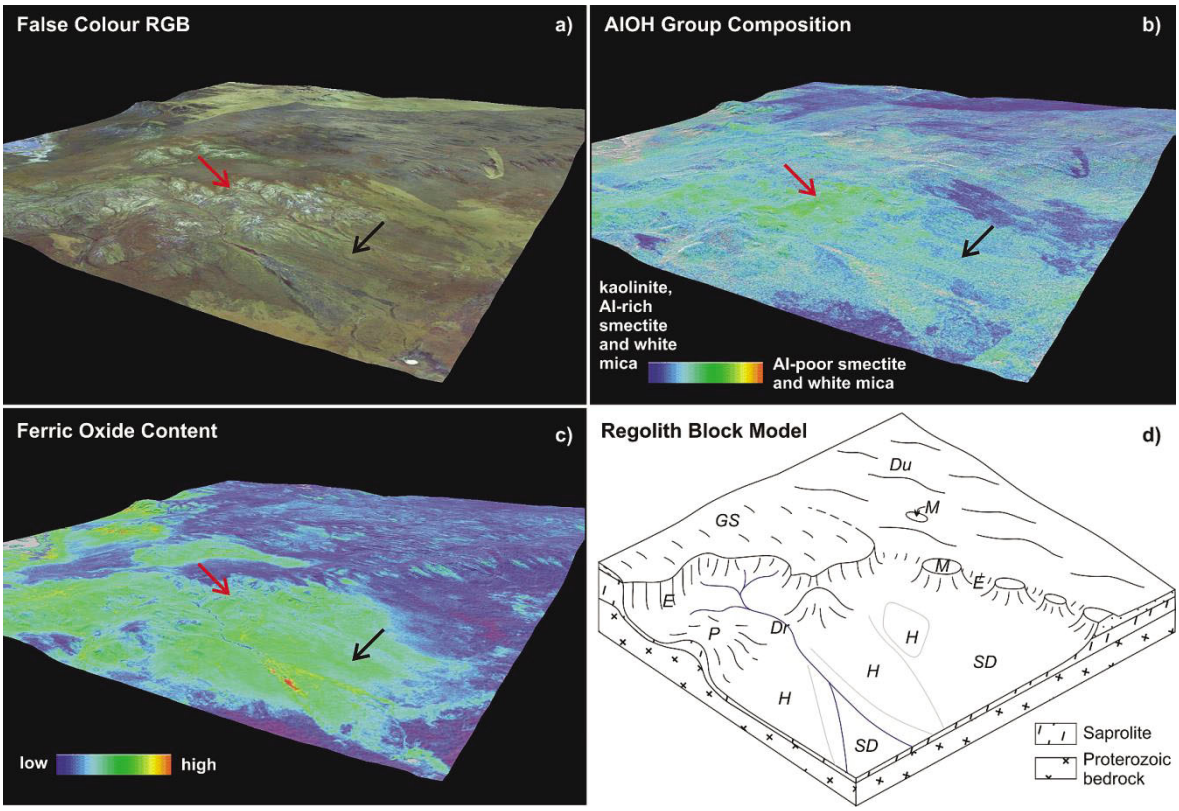

Figure 107. ASTER Geoscience products (Cudahy, 2011) draped over DEM (20x vertical exaggeration; A, B, C) using Geoscience Australia's World Wind 3D Data Viewer and schematic regolith block model (d) of the study area in the northeastern Albany-Fraser Orogen (Western Australia). Sediment-dominated (SD) terrains: Du-dunes, H-hardpans; Saprolite and bedrock-dominated (SP): M-"Mesozoic", P-Proterozoic, E-erosional; Levelled plateaus (GS). Red arrows in ASTER Geoscience products point to an erosional regime, black arrows point to a flat, depositional area. North is parallel to the right and left borders of the 3D maps.

8.4.1.1 Erosional regime

The erosional regime is represented by the "saprolite and bedrock-dominated terrains" (SP). The AlOH group composition image highlights mainly Al-poor smectites (e.g., montmorillonite) and/or white micas without kaolinite (red arrow, Fig. 107B), in weathered Proterozoic bedrock (SP_P) or silicified sandstone (SP_M) together with their transition into lower saprolite.

However, upper ferruginous saprolite (SP_F/FG) can contain kaolinite, shown as a halo surrounding the bedrock or lower saprolite (white arrow, Fig. 107B). The abundance of Fe oxides can vary considerably in this erosional regime. Bedrock has an intermediate to high Fe oxide abundance, with silicified sandstone in the north-east of this area showing the highest contents, especially where they form mesas. Goethite is the dominant Fe oxide type in the bedrock, as indicated by the blue colours in the ferric oxide composition image (red arrow, Fig. 107C).

The ferruginous saprolite can be subdivided in a goethite-rich (SP_FG) and a hematite-rich (SP_F) end member, with the latter end member having, in general, a lower Fe oxide content. Although the surface geological map shows both Mesozoic and Proterozoic bedrocks in the south-west, the ASTER Geoscience products imply a distinctly different mineralogical signature between the bedrock in the south-west (around the Voodoo Child and Purple Haze sites) and those in the north-east (between the Neale and Hercules sites). Therefore, all outcrops and related saprolites are tentatively assigned to Proterozoic bedrock.

8.4.1.2 Depositional regime

In contrast to the erosional regimes, the depositional regimes (i.e., dune fields and flat depositional environment) can contain all major Al-clay phases. The relative abundance of clay minerals can vary significantly between the different depositional environments (Fig. 107C). Low Al-clay abundances, dominated by Al-smectite and white mica, were observed in drainage systems (SP_Dr) and colluvium (SP_C), whereas alluvium (SP_A) and hardpans (SP_H) are both characterized by an intermediate to high abundance of kaolinite and Al-smectite. The reason for the low Al-clay abundance in the drainage systems and the colluvium could relate to the erosional component of this regime. The differences between these two groups were also reflected in the abundance of Fe oxides (Fig. 107C), with purely depositional regimes (SP_A, SP_H) containing less Fe oxides than the depositional/erosional regimes (SP_Dr, SP_C). Hematite is the main Fe oxide mineral in hardpans, compared to goethite dominating in drainage channels. The two regolith environments can be mapped in great detail when occurring in the same area (Fig. 108). Four drill holes at the Atlantis site are located in one of these hardpans. Only two of the drill holes from Atlantis (NLD070, NLD080) record HyLogging™ data from the lowermost regolith, represented by saprock, but all four drill holes show an increased Fe oxide abundance towards the top of the core, which might be related to the formation of the hardpan. High abundance of low crystalline kaolinite in the upper metres of drill hole NLD080 (ca., 51 m depth) suggests input of material of a transported origin.

Dune fields (SD_Du) show low to intermediate Al-clay contents, mainly comprised of kaolinite and, possibly, smectite, according to the AlOH Composition image. This is in contrast to erosional features, which dissect this otherwise depositional environment, and are characterized by high white mica and/or Al-smectite abundance and low kaolinite abundance. This enhances the possibility of mapping bedrock or saprolite (i.e., erosional features) in the dune fields. The resulting bedrock or saprolite domains are shown in Fig. 108. The dune fields north of the Neale and Hercules sites also show a low abundance of Fe oxides (Fig. 107C; Appendix H4), dominated by goethite (Fig. 107C; Appendix H4), whereas other depositional areas south-east of the north-east trending morphological boundary contain relatively more Fe oxides, often dominated by hematite (e.g., in hardpans, SP_H).

The surface geological map divides the depositional area to the east of the north-east trending morphological boundary into dune fields in the north and colluvium in the south. The ASTER Geoscience products support this subdivision, but, with a different position of the boundary (Fig. 108). Based on the ASTER Geoscience products, a more uniformly sediment-dominated terrain in the north can be distinguished from the sediment-dominated terrain in the south, as described above. A comparison of the mineralogies in the two sediment-dominated terrains, with possible source areas in the north-west, imply that the transported material in the east was sourced from the northwestern dune fields, whereas the transported material in the south-east derived from the Proterozoic basement to the west.

8.4.1.3 Relict landforms

The third major regolith environment is represented by the relict landform, which comprises leveled plateaus that feature in the Yilgarn Craton regolith model, typically sands, ferruginous gravels and duricrusts (Tables 2 and 3 in Appendix H4). In the Yilgarn Craton, an intermediate abundance of kaolinite and smectite, as well as a low characterize this relict landform to high abundance of Fe oxides, with hematite being the dominant Fe oxide mineral. In relict landforms at Hercules however, the abundance of clay minerals is in general low (Fig. 107B) and Fe oxides are mainly goethitic (Fig. 107). These observations set the relict landform apart from the surrounding erosional landforms (i.e., saprolite and bedrock dominated terrains). The transition of the newly mapped relict landform to the northern dune fields is very well defined in the Fe oxide content and opaques index images (not shown here), with increased abundance of opaque material at erosional features dissecting the depositional landform of the dune fields. This is in contrast to the surface geological map, where the same area is described as dunes and sandplains, stretching from west of the Purple Haze site to the north of the Neale and Hercules sites. However, the ASTER Geoscience products clearly show mineralogical differences between these two areas.

8.4.1.4 Summary of regolith landforms in the Neale area

The ASTER Geoscience products provide detailed information about the mineralogy of the three major regolith environments and allow even further distinctions (Fig. 108). VIRS active mineralogical factors were used to classify the three major regolith landforms of the model after Anand and Paine (2002), introduced in Chapter 3, and were further subdivided into regolith domains typical for the area studied (Table 4 in Chapter 5). In summary, the Hercules area can be subdivided into four major sectors:

(1) Dune fields intersected by saprolite occurrences north of Neale and Hercules;

(2) A leveled plateau surrounded to the east, south and west by saprolite and bedrock-dominated (Proterozoic) terrains in the south-west (around Purple Haze and Voodoo Child);

(3) Sediment-dominated terrain in the south-east with transported material sourced from the Proterozoic basement to the west; and

(4) Uniform sediment-dominated terrains in the east with transported material sourced from the northern dune fields and underlying saprolite.

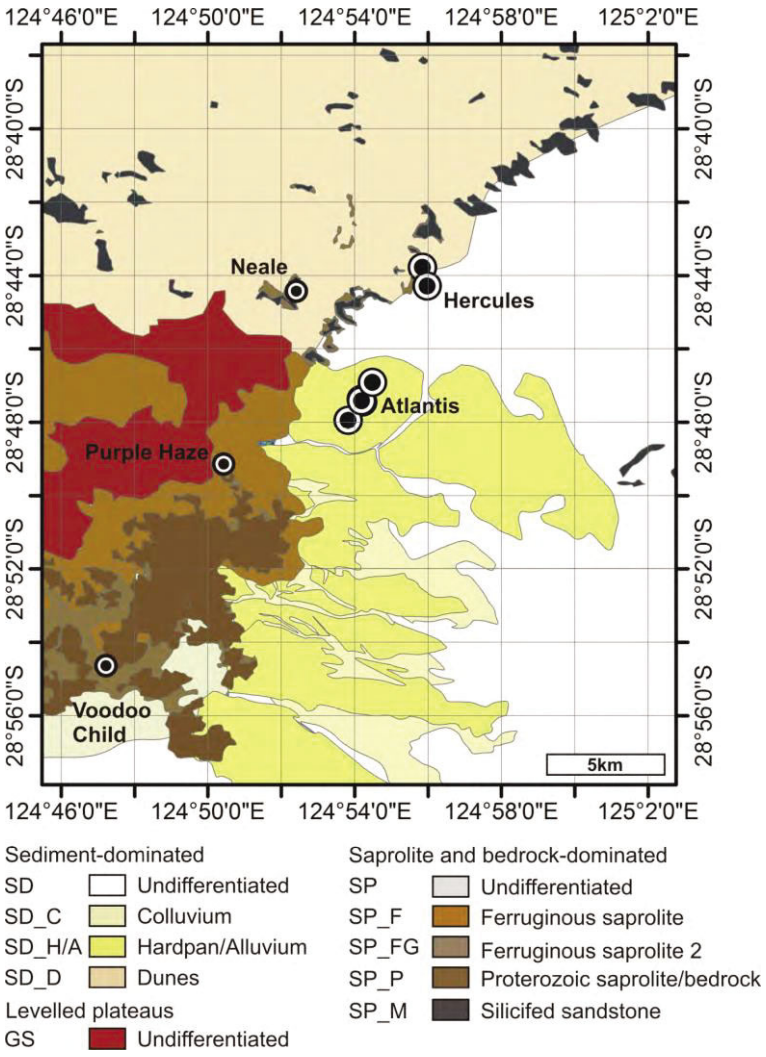

Figure 108. Regolith landform map in the Neale tenement, Albany-Fraser Orogen (Western Australia), inferred from HyLogging™ and ASTER data. The map includes the prospect locations for Purple Haze and Voodoo Child (AngloGold Ashanti) and the diamond drill hole collar locations (large black circles; Chapters 5 and 6 for further information).

8.4.2 Bedrock and alteration patterns at Hercules

Gold mineralization in the Tropicana area is hosted by Proterozoic and/or Archaean rocks (Doyle et al., 2009; Spaggiari et al., 2011). In the Hercules area, Au is hosted by Proterozoic metagranitic rocks (Spaggiari et al., 2011) and is spatially associated with chertified horizons, but also other alteration patterns, such as potassic (e.g., sericite) or epidote and/or chlorite/biotite alteration, which were all detected by HyLogging™ data. However, no distinct correlation between Au mineralization and any of these alteration mineral assemblages could be found (this Chapter). Furthermore, gradual changes in the alteration minerals, in terms of both abundance and composition, happen on a small scale (typically less than 5 m; e.g. changes in white mica abundance and composition in NLD097).

This matter is further complicated by the substantial sedimentary cover over the area of interest and the high abundance of Al-clays, which overlap any spectral signatures related to sericite alteration. The sedimentary cover also includes a layer of silicified sandstones, which were assigned to the Paterson Formation of the Mesozoic Gunbarrel Basin in the surface geological map (Stewart et al., 2008) and this Chapter. Independent from their classification, these silicified sandstones in the northern Hercules area (i.e., around Neale and north of Hercules; Fig. 108) cover any patterns that would otherwise be possibly recognizable at the current land surface. Up to now, no alteration related to the primary mineralization in the area was recognized in these sediments. However, a few important observations can be made by comparing ASTER Geoscience products with radiometric datasets. A high K index (Fig. 109A) reveals the occurrence of the Proterozoic granitoids, which coincides with the southern erosional domain (Fig. 108). The Mesozoic bedrocks are not detected by this index. In the Hercules area, the regolith landforms over Proterozoic and Mesozoic bedrock show some distinct differences. Erosional regimes over Proterozoic bedrock are well developed, with extensive breakaways showing a high Al-clay and Fe oxide abundance that can be related to ferruginous saprolite. Erosional features over Mesozoic rocks are much smaller in size. Furthermore, erosional material derived from Proterozoic rocks is deposited in large Fe oxide rich fans and often cemented in hardpans (as intersected by drill holes at the Atlantis site). The Proterozic bedrocks, as well as the respective saprolite and the sediment dominated terranes show a low silica abundance when compared to the sediment dominated terranes around the Mesozoic bedrock and related saprolite. The high silica index in this area is due to the silica rich dune-fields in the north-west, shedding off to the lower plains in the south-east. The silica index image was released as part of the continental scale ASTER Geoscience products (Cudahy, 2012) and was not part of the original Western Australia ASTER Geoscience products (Cudahy, 2011).

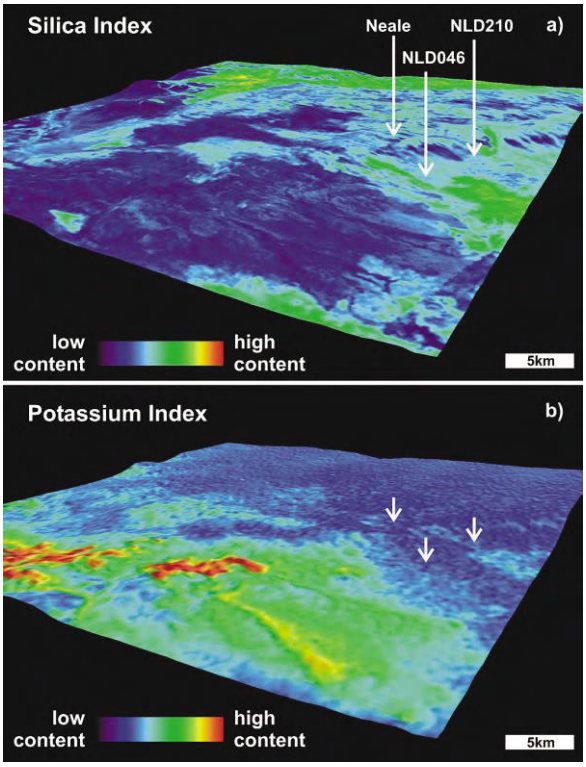

Figure 109. Detail of the Neale area as shown in an image from the ASTER Geoscience product (Cudahy, 2012) in (A), and K index derived from radiometric data in (B), draped over DEM (20x exaggeration) in Geoscience Australia's World Wind 3D Data Viewer (Version 2.1). Exploration drilling program locations are indicated by arrows. The Neale prospect and drill holes NLD046 (Atlantis) and NLD210 (Hercules). North is parallel to right and left borders of 3D maps.

8.4.3 Conclusions

The separation of transported from residual domains was achieved for the northeastern Albany-Fraser Orogen by applying regolith models of similar landform types, such as has been done for the Yilgarn Craton (e.g., Anand and Butt, 2010). Regolith landforms can be sometimes distinguished in great detail using ASTER and HyLogging™ drill core data. This enables us to not only distinguish transported from erosional regimes, but also to relate depositional material to its source rocks and to identify the type of bedrock, by characterising the mineralogy of its equivalent saprock.

The main mineralogical factors for detailed regolith characterization comprise the abundance and type of Al-clays and Fe oxides. Multi- and hyperspectral technologies are ideal to determine these critical factors. The classical example is the crystallinity of kaolinite, where transported sediments are typically characterized by poorly crystalline kaolinite, whereas residual materials are dominated by well crystalline kaolinite.

The Hercules area features two types of sediment dominated terrains, namely (1) dune fields to the north-west and (2) *alluvium/colluvium* plains to the east, with the latter having characteristic hematite-rich hardpans in the south of the study area, where erosional material derived from the Proterozoic bedrock is deposited. The Atlantis site is located at the transition of these two domains, although being on the lower plains to the east of a north-east trending morphological step, the regolith is probably thinner than at Neale, for example, when assuming a rather levelled Mesozoic landsurface. The regolith material at Atlantis displays a distinct increase in Fe oxide abundance, which might be related to the formation of hardpans at the surface, which were mapped using the ASTER data.

The resulting regolith map shows significant differences to the published surface geological map and provides a much more detailed picture of regolith landforms in the Hercules area. The results of this regolith mapping study were summarized in a block model, and the regolith landforms. However, the derived regolith landform model requires further comparison with detailed regolith analysis from drill holes and validation based on field sampling (Chapters 5 and 6). The regolith map developed can be used to design transects through different regolith landforms.

This study shows that time consuming field-mapping could effectively be complemented by using mineral maps derived from multispectral remote sensing data in combination with a few ground control points (i.e., HyLogging™ data). This would help to target fieldwork, to efficiently design exploration-drilling programs, based on the information about the inferred composition and thickness of the overburden, and support the drill logging on site by geologists. Mineralogical characterization of the regolith can be used to identify the respective depositional/erosional environment and provide insights to the type of concealed stratigraphy.

References

Anand, R.R., 2005. Weathering history, landscape evolution and implications for exploration. In: Regolith landscape evolution across Australia: a compilation of regolith landscape case studies with regolith landscape evolution models. Anand, R.R. and De Broekert, P.P. (Eds.), CRC LEME Monograph, pp. 2-40.

Anand, R.R., Butt, C.R.M., 2010. A guide for mineral exploration through the regolith in the Yilgarn Craton, Western Australia, Aust. J. Earth Sci. 57, 1015-1114.

Anand, R.R., De Broekert, P.P., 2005. Regolith landscape evolution across Australia: Aacompilation of regolith landscape case studies with regolith landscape evolution models. CRC LEME Monograph, 354 pp.

Anand, R.R., Paine, M., 2002. Regolith geology of the Yilgarn Craton, Western Australia: implications for exploration. Aust. J. Earth Sci. 49, 3-162.

Arevalo, R., McDonough, R.F., 2010. Chemical variations and regional diversity observed in MORB. Chem. Geol. 271, 70-85.

Blenkinsop, T.G., Doyle, M., 2013. Structural controls on gold mineralization on the margin of the Yilgarn craton, Albany Fraser orogeny: the Tropicana deposit, Western Australia. FUTORES, Townsville-Australia, June2013, Minerals System/GIS based Prospectivity Mapping Symposium, 37.

Blenkinsop, T.G., Doyle, M.G., 2014. Structural controls on gold mineralization on the margin of the Yilgarn craton, Albany-Fraser orogen: the Tropicana deposit, Western Australia. J. Struct. Geol., doi: 10.1016/j.jsg.2014.01.013.

Bouchot, V., Gros, Y., Bonnemaison, M., 1989. Structural controls on the auriferous shear zones of the Saint Yrieix District, Massif Central, France; evidence from the Le Bourneix and Laurieras gold deposits. Econ. Geol. 84, 1315-1327.

Boynton, W.V., 1983. Cosmochemistry of the rare earth elements: meteorite studies. In: Rare Earth Element Geochemistry. Henderson, P. (Ed.), Elsevier, pp. 63-114.

Brodie, R.C., 2010. Holistic Inversion of Airborne Electromagnetic Data, PhD thesis. The Australian National University, 305 pp.

Broidie, R.C., 2012. Appendix 3: GA-LEI Inversion of TEMPEST data, in the frome airborne electromagnetic survey, South Australia: implications for energy, minerals and regional geology. Geoscience Australia Record 2012/40-DMITRE, Report Book 2012/00003, pp. 278-287.

Butt, C.R.M., 1985. Granite weathering and silcrete formation on the Yilgarn Block, Western Australia. Aust. J. Earth Sci. 32, 415-432.

Butt, C.R.M., Robertson, I.D.M., Scott, K. M., Cornellius, M., 2005. Regolith expression of Australian ore systems: a compilation of exploration case histories with conceptual dispersion, process and exploration models. CRC LEME Monograph.

Cassidy, K.F., Champion, D.C., Krapež, B., Barley, M.E., Brown, S.J.A., Blewett, R.S., Groenewald, P.B., Tyler, I.M., 2006. A revised geological framework for the Yilgarn Craton, Western Australia. Western Australia Geological Survey, Record 2006/8.

Chappell, B.W., White, A.J.R., 2001. Two contrasting granite types: 25 years later. Aust. J. Earth Sci. 48, 489-499.

Clarke, J.D., Bone, Y., James, N.P., 1996. Cool-water carbonates in an Eocene pleoestuary, Norsman Formation, Western Australia. Sed. Geol. 101, 213-226.

Commander, D.P., 1989. Western Australia groundwater salinity map, SCALE (1:10,000,000). Geological Survey of Western Australia.

Condie, K.C., 2005. TTGs and adakites: are they both slabs melts? Lithos, 80, 33-44.

Condie, K.C., Mayers, J.S., 1999. Mesoproterozoic Fraser Complex: geochemical evidence for multiple subduction related sources of lower crustal rocks in the Albany-Fraser Orogen, Western Australia. Aust. J. Earth Sci., 46, 875-882.

Costello, M.T., Brodie, R., D.K., A.H., 2011. AEM Geophysics, in Geological and energy implications of the Pine Creek region airborne electromagnetic (AEM) survey, North Territory, Australia. Geoscience Australia Record 2011/18, 110-138.

Cudahy, T., 2011. Satellite ASTER Geoscience product notes Western Australia.- http://c3dmm.csiro.au/WA_ASTER/stage_1_geoscienceproductnotes.html , 23 pp.

Cudahy, T., 2012. Satellite ASTER Geoscience product notes Australia.- http://c3dmm.csiro.au/Australia_ASTER/stage_1_geoscienceproductnotes.html, 23 pp.

Doyle, M., Gibbs, D., Savage, J., Blenkinsop, T., 2007. Geology of the Tropicana Gold project, Western Australia. In: Smart Science for Exploration and Mining. Williams P.J. et al. (Eds.), Proceedings Volume, 50-52.

Doyle, M.G., Gibbs, D., Savage, J., Blenkinsop, T.G., 2009. Geology of the Tropicana Gold project, Western Australia. In: Smart Science for Exploration and Mining. Economic Geology Research Unit, James Cook University; 10th Biennial SGA Meeting of The Society for Geology Applied to Mineral Deposits, Townsville, Queensland; Proceedings Volume 1, 50–52.

Duuring, P., Hagemann, S., Novikova, Y., Cudahy, T., Laukamp, C., 2012. Targeting iron ore in banded iron formation using ASTER data: Weld Range greenstone belt, Yilgarn Craton, Western Australia. Econ. Geol. 107, 585-597.

Finkl, C.W., 1979. Stripped (etched) landsurfaces in southern Western Australia. Australian Geographical Studies 17, 33-52.

Gallant, J.C., Dowling, T.I., 2003. A multiresolution index of valley bottom flatness for mapping depositional areas. Water Resour. Res., 39, 1347.

González-Álvarez, I., Ley-Cooper, Y., Salama, W., Abdat, T., Anand, R., 2013. Regolith architecture in the SE Yilgarn Craton-Albany Fraser Orogen margin: an AEM based study to assist exploration strategies for the Neale and Zanthus tenements. Internal CSIRO Technical report for Beadell Resources Ltd., EP132645, 47 pp.

González-Álvarez, I., Kerrich, R., 2010. REE and HFSE mobility due to protracted flow of basinal brines in the Mesoproterozoic Belt-Purcell Supergroup, Laurentia. Precambrian Res. 177, 291-307

Gu, L., Zheng, Y., Tang, X., Zaw, K., Della-Pasque, F., Wu, C., Tian, Z., Lu, J., Pei, N., Li, X., Yang, F., Wang, X., 2007. Copper, gold and silver enrichment in ore mylonites within massive sulfide orebodies at Hongtoushan VHMS deposit, NE China. Ore Geol. Rev. 30, 1-29.

Hart, C., 2005. Classifying, distinguishing and exploring for intrusion-related gold systems. The Gangue 85, 7 pp.

Heine, C., Müller, R.D., Steinberger, B., DiCaprio, L., 2010. Integrating deep earth dynamics in palaeogeographic reconstructions of Australia. Tectonophysics 483, 135-150.

Hewson, R.D., Cudahy, T.J., 2010. Geological mapping accuracy issues using ASTER in Australia. In: Applications in ASTER, Land Remote Sensing and Global Environmental Change: NASA's Earth Observing System and the Science of ASTER and MODIS. Ramachandran, B., Justice, C., and Abrams, M. (Eds), Springer, New York.

Hewson, R.D., Cudahy, T.C., Drake-Brockman, J., Meyers, J., Hashemi, A., 2006. Mapping geology associated with manganese using spectral sensing techniques at Woodie Woodie, East Pilbara. Expl. Geophys. 37, 389-400.

Hou, B., Frakes, L.A., Sandiford, M., Worrall, L., Keeling, J., Alley, N.F., 2008. Cenozoic Eucla Basin and associated palaeovalleys, southern Australia-Climatic and tectonic influences on landscape evolution, sedimentation and heavy mineral accumulation. Sed. Geol. 203, 112-130.

HuangX-L., Niu, Y., Xu, Y-G., Yang, Q-J., Zhong, J-W., 2010. Geochemistry of TTG and TTG-like gneisses from Lushan-Taihua complex in the southern North China Craton: implications for late Archean crustal accretion. Precambrian Res. 182, 43-56.

Hutton, J.T., Twidale, C.R., Milnes, A.R., 1978. Characteristics and origin of some Australian silcretes. In: Silcrete in Australia. Langford-Smith, T. (Ed.), Department of Geography, University of New England, Armidale, 19-39.

Ishihara, S., 1998. Granitoid Series and Mineralization in the Circum-Pacific Phanerozoic granitic belts. Res. Geol. 48, 219-224.

Jones, S.A., 2006. Mesoproterozoic Albany-Fraser Orogen-related deformation along the southeastern margin of the Yilgarn Craton. Aust. J. Earth Sci. 53, 213-234.

Kirkland, C.L., Spaggiari, C., Wingate, M. T. D., Smithies, R. H., Pawley, M., 2010. New geochronology from the Albany-Fraser Orogen: implications for Mesoproterozoic magmatism and reworking. 2008-09 Annual Review article, Geological Survey of Western Australia, 8 pp.

Kirkland, C.L., Spaggiari, C., Pawley, M. J., Wingate, M. T. D., Smithies, R. H., Howard, H. M., Tyler, I. M., Belousova, E. A., Poujol, M., 2011. On the edge: U–Pb, Lu–Hf, and Sm–Nd data suggests reworking of the Yilgarn craton margin during formation of the Albany–Fraser Orogen. Precambrian Res. 187, 223–247.

Kolb., J., Kisters, A.F, Meyer, F.M., Siemes, H., 2003. Polyphase deformation of mylonites from the Renco gold mine (Zimbabwe): identified by crystallographic preferred orientation of quartz. J. Struct. Geol., 25, 253-262.

Lane, R., Green, A., Golding, C., Owers, M., Pik, P., Plunkett, C., Sattel, D., Thorn, B., 2000. An example of 3D conductivity mapping using the TEMPEST airborne electromagnetic system. Explor. Geophys. 31, 162-172.

Lang, J.R., Baker, T., 2001. Intrusion-related gold systems: the present level of understanding. Mineralium Deposita 36, 477-489.

Lefebure, D.V., Hart, C., 2005. Plutonic-related Au quartz veins and veinlets. BC Mineral Deposit Profile L02, Yukon-British Columbia Geological Surveys, 8 pp.

Ley-Cooper, A. Y., Macnae, J., Viezzoli, A., 2010. Breaks in lithology: interpretation problems when handling 2D structures with a 1D approximation. Geophys. 75, W179-W188.

Lintern, M.J., Craig, M.A., Walsh, D.M., Sheridan, N.C., 2001. The distribution of gold and other elements in surficial materials from the Higginsville palaeochannel gold deposits, Norseman, Western Australia. CRC LEME 28R, Exploration and Mining Report 275R.

Lintern, M.J., Sheard, M.J., Chivas, A.R., 2006. The source of pedogenic carbonate associated with goldcalcrete anomalies in the western Gawler Craton, South Australia. Chem. Geol., 235, 299-324.

Lintern, M.J., Hough, R.M., Ryan, C.G., 2011. Experimental studies on the gold-in-calcrete anomaly at Edoldeh Tank gold prospect, Gawler Craton, South Australia. J. Geochem. Explor. 112, 189-205

Myers, J.S., 1995. Geology of the Albany 1:1,000,000 sheet. Geological Series Explanatory Notes, Geological Survey of Western Australia, 10 pp.

Nahon, D., Tardy, Y., 1992. The ferruginous laterites. In: Regolith exploration geochemistry in tropical and sub-tropical terrains. Butt, C.R.M. Zeegers, H. (Eds.), Handbook Explor. Geochem. 4, Elsevier, 41-55.

Ninomiya, Y., Fu, B., Cudahy, T.J., 2005. Detecting lithology with advanced spaceborne thermal emission and reflection radiometer (ASTER) multispectral thermal infrared “radiance-at-sensor” data. Remote Sensing Envir. 99, 127-139.

McGuinness, S.J., 2010. Regolith-landform mapping of the east Wongatha area. East Albany-Fraser and southeast Yilgarn Geological Exploration Package. Geological Survey of Western Australia.

Macnae, J.C., King, A., Stolz, N., Osmakoff, A., Blaha, A., 1998. Fast AEM data processing and inversion. Explor. Geophys. 29, 163-169.

Milnes, A.R., Hutton, J.T., 1974. The nature of microcryptocrystalline titania in 'silcrete' skins from the Beda Hill area of South Australia. Search, 5, 153-154.

Morris, P.A., 2013. Fine fraction regolith chemistry from the east Wongatha area, Western Australia: tracing bedrock and mineralization through thick cover. Geochem. Explor. Environ. Anal., 13, 21-40.

Palacky, G., 1988. Resistivity Characteristics of Geologic Targets. Electromagnetic Methods in Applied Geophysics, pp. 52-129.

Panahi, A., Young, G.M., Rainbird, R.H., 2000. Behavior of major and trace elemnts (including REE) during Palaeoproterozoic pedogenesis and diagenetic alteration of an Archean granite near Ville Marie, Quebec, Canada. Geochim. Cosmochim. Acta 64, 2199-2220.

Pillans, B., 2005. Geochronology of the Australian regolith. In: Regolith landscape evolution across Australia. Anand, R.R. and De Broekert, P.P. (Eds), CRC LEME.

Pillans, B., 2007. Pre-Quaternary landscape inheritance in Australia. J. Quatern. Sci. 22, 439-447.

Reid, J.E., Pfaffling, A., Vrbancich, J., 2006. Airborne electromagnetic footprints in 1D earths. Geophysics 71, G63-G72.

Rudnick, R.L., Gao, S., 2003. The composition of the continental crust. In: The crust. Rudnick, R.L. (Ed.), Treatise on Geochimistry, vol. 3, edited by H. D. Holland, and K. K. Turekian, Elsevier, Oxford, New York, pp. 1-64.

Smithies, R.H., 2000. The Archaean tonalite–trondhjemite–granodiorite (TTG) series is not an analogue of Cenozoic adakite. Earth Planet. Sci. Lett. 182, 115-125.

Smithies, R.H., Howard, H.M., Evins, P.M., Kirkland, C.L., Kelsey, D.E., Hand, M., Wingate, M.T.D., Collins, A.S., Belousova, E., 2011. High-temperature granite magmatism, crust–mantle interaction and the Mesoproterozoic intracontinental evolution of the Musgrave Province, Central Australia. J. Petrol. 52, 931-958.

Smale, D., 1973. Silcretes and associated silica diagenesis in Southern Africa and Australia. J. Sed. Petrol. 43, 1077-1089.

Singh, B., Gilkes, R.J., Butt, C.R.M., 1992. An electron optical investigation of aluminosilicate cements in silcretes. Clays Clay Mineral. 40, 707-721.

Spaggiari, C.V., Pawley, M.J., 2012. Interpreted pre-Mesozoic bedrock geology of the Tropicana region of the east Albany–Fraser Orogen (1:250 000). In: The geology of the east Albany-Fraser Orogen — a field guide compiled by C.V. Spaggiari, C.L. Kirkland, M.J. Pawley, R.H. Smithies, M.T.D. Wingate, M.G. Doyle, T.G. Blenkinsop, C. Clark, C.W. Oorschot, L.J. Fox, and J. Savage, Geological Survey of Western Australia, Record 2011/23.

Spaggiari, C.V., Bodorkos, S., Barquero-Molina, M., Tyler, I.M., Wingate, M.T.D., 2009. Interpreted bedrock geology of the South Yilgarn and central Albany-Fraser Orogen, Western Australia, Geological Survey of Western Australia, Record 2009/10.

Spaggiari, C.V., Kirkland, C.L., Pawley, M.J., Smithies, R.H., Wingate, M.T.D., Doyle, M.G., Blenkinsop, T.G., Clark, C., Oorschot, C. W., Fox, L.J., Savage, J., 2011. The geology of the east Albany-Fraser Orogen — a field guide, Geological Survey of Western Australia, Record 2011/23.

Summerfield, M.A., 1983. Petrography and genesis of silcrete from the Kalahari Basin and Cape Coastal Zone, Southern Africa. J. Sed. Petrol. 53, 895-909.

Stewart, A.J., Sweet, I.P., Needham, R.S., Raymond, O.L., Whitaker, A.J., Liu, S.F., Phillips, D., Retter, A.J., Connolly, D.P., Stewart, G., 2008. Surface geology of Australia 1:1,000,000 scale, Western Australia [Digital Dataset].

Swain, C.J., 1976. A fortran IV program for interpolatin irregularly spaced data using the difference equations for minimum Curvature. Comput. Geosci. 1, 231-240.

Tardy, Y., Roquin, C., 1998. Derive des continents palaeoclimates et alterations tropicales. BRGM Editions Orleans, France.

Taylor, S.R., McLennan, S.M., 1985. The continental crust: its composition and evolution. Blackwell, Oxford, U.K.

Taylor, S.R., McLennan, S.M., 1995. The geochemical evolution of the continental crust. Rev. Geophys. 33, 241-265.

Thiry, M., Milnes, A.R., 1991. Pedogenic and groundwater silcretes at Stuart Creek Opal Fields, South Australia. J Sed. Petrol. 61, 111-127.

Thiry, M., Milnes, A.R., Rayot, V., Simon-Coinçon, R., 2006. Interpretation of palaeoweathering features and successive silicifications in the Tertiary regolith of inland Australia. J. Geol. Soc. London 163, 723-736.

Vallee, M.A., Smith, R.S., Keating, P., 2011. Metalliferous mining geophysics, State of the art after a decade in the new millennium. Geophys. 76, W31-W50.

Van Der Graaff, W.G.E., 1983. Silcrete in Western Australia: geomorphological settings, textures, structures, and their genetic implications. In: Residual Deposits: Surface Related Weathering Processes and Materials. Wilson, R.C.L. (Ed.), pp. 159-166.

Wait, J.R., 1982. Geo-electromagnetism, Academic Press Inc., New York.

Winchester, J.A., Floyd, P.A., 1977. Geochemical discrimination of different magma series and their differentiation products using immobile elements. Chem. Geol. 20, 325-343.

Wingate, M.T.D., Cambbell, I.H., Harris, L.B., 2000. SHRIMP baddeleyite age for the Fraser dyke swarm, southeastern Yilgarn Craton, Western Australia. Aust. J. Earth Sci. 47, 309-313.

Worrall, L., Clarke, J.D.A., 2004. The formation of geochemical anomalies in the eastern goldfields: the role of an Eocene acid weathering event. In: Minerals Exploration Seminar: Cooperative Research Centre for Landscape Evolution and Mineral Exploration (CRC LEME) and Association of Mining and Exploration Companies (AMEC), Abstract Volume, June 2004, Perth, 23 pp.

Zindler, A., Hart, S., 1986. Chemical geodynamics. Annu. Rev. Earth Planet. Sci. 14, 493-571.

Appendix A (Digital) Regolith framework of the Albany-Fraser Orogen and SE Yilgarn margin, (González-Álvarez et al.)

Appendix B (Digital) Woodline project calcrete investigations, Albany-Fraser Province (Western Australia), (Lintern and Abdat)

Appendix C (Digital) Geochemistry, mineralogy and petrography of the Yilgarn margin/Albany-Fraser Orogen, (Sonntag)

Appendix D (Digital) Petrography and mineralogy of 15 samples from the Hercules/Atlantis prospects, Albany-Fraser Orogen, Western Australia, (Sweetapple)

Appendix E (Digital) Regolith Stratigraphy, mineralogy and geochemistry of the Neale Tenement, NE Albany-Fraser Orogen-SE Yilgarn Craton Margin, (Salama et al.)

Appendix F (Digital) Trace element mobility in a deeply weathered cover profile in the Albany-Fraser Orogen/Yilgarn Craton margin: the Hercules and Atlantis Au prospects, (González-Álvarez et al.)

Appendix G (Digital) Airborne EM in the Albany-Fraser, (Ley-Cooper)

Appendix H (Digital) H1, Evaluation of WA ASTER Geoscience products for orogeny to deposit scale geological mapping in the Albany-Fraser Orogen; H2, Salmon Gums Hylogging™ data; H3, Beadell Hercules/Atlantis Hylogging™ data; H4, Integration of multispectral ASTER and hyperspectral Hylogging™ data at Hercules and Salmon Gums, (Laukamp)

CONTACT US

t 1300 363 400
+61 3 9545 2176
e enquiries@csiro.au
w www.csiro.au

YOUR CSIRO

Australia is founding its future on science and innovation. Its national science agency, CSIRO, is a powerhouse of ideas, technologies and skills for building prosperity, growth, health and sustainability. It serves governments, industries, business and communities across the nation.

FOR FURTHER INFORMATION

CESRE /Minerals Down Under FLAGSHIP/Discovery Theme
Ignacio González-Álvarez
t +61 8 6436 8687
e Ignacio.Gonzalez-Alvarez@csiro.au
w www.csiro.au/CSIRO Earth Science and Resource Engineering-Minerals Down Under

This Report presents a summary of research funded in part by CSIRO's strategic investment in greenfields mineral exploration along cratonic boundaries in Western Australia. This research applies a multi-scale approach, which aims to support the prospectivity assessments of small to medium exploration companies during greenfields exploration, by the development of efficient exploration proxies. It also follows up on the recent Tropicana–Havana Au and the Nova magmatic Ni–Cu discoveries, by building on previous exploration experience in the southeast Yilgarn Craton margin.

This project was jointly undertaken by Minerals Research Institute of Western Australia (MRIWA), the Geological Survey of Western Australia (GSWA) and CSIRO.

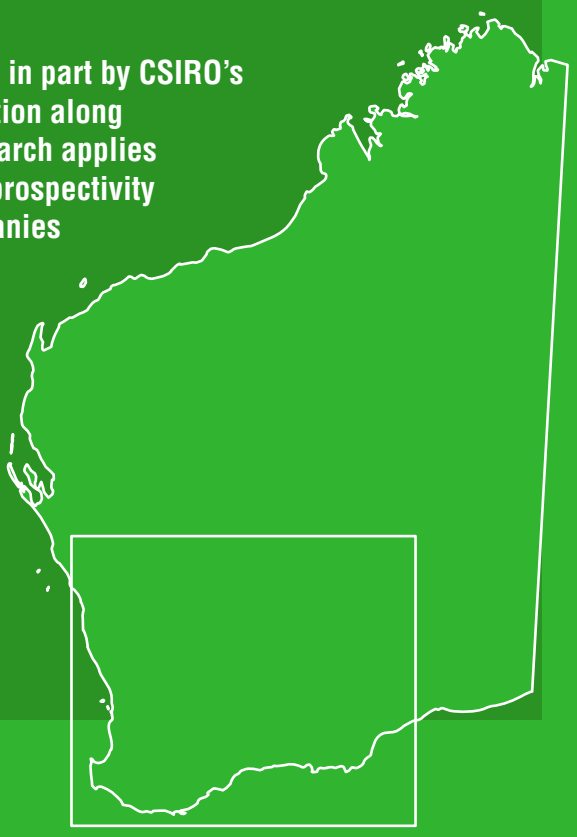

Further details of geological products and maps produced by the Geological Survey of Western Australia are available from:

Information Centre
Department of Mines and Petroleum
100 Plain Street
EAST PERTH WA 6004
Phone: (08) 9222 3459 Fax: (08) 9222 3444

www.dmp.wa.gov.au/GSWApublications

GONZÁLEZ-ÁLVAREZ et al.

GREENFIELDS GEOCHEMICAL EXPLORATION IN A REGOLITH-DOMINATED TERRAIN: THE ALBANY–FRASER OROGEN/YILGARN CRATON MARGIN

REPORT 144